Understanding Chemical and Physical Processes of Biogenic Volatile Organic Compounds in The Atmospheric Boundary Layer

by

Yang Li

A dissertation submitted in partial fulfillment
of the requirements for the degree of
Doctor of Philosophy
(Atmospheric, Oceanic and Space Sciences)
in the University of Michigan
2017

Doctoral Committee:

Associate Professor Allison L. Steiner, Chair
Senior Scientist Mary Barth, National Center for Atmospheric Research
Assistant Professor Gretchen Keppel-Aleks
Assistant Professor Kerri A. Pratt

Yang Li

yanglibj@umich.edu

ORCID iD: 0000-0003-1972-7472

DEDICATION

I dedicate this thesis to my parents, my grandparents and my husband, for giving me courage to conquer all the difficulties, for giving me strength to embrace changes in my life, and for giving me hope to chase a brighter future.

ACKNOWLEDGEMENTS

Good time always passes fast. After 5 years of doctoral study, I am deeply grateful to many people for giving me knowledge, advice, and resources, for understanding and supporting me, and for treating me like family.

I would like to express my gratitude to my advisor, Dr. Allison Steiner, who is an excellent scientist with great wisdom. She enlightened me and guided me through this thesis. Her support, patience, and encouragement gave me the power to overcome the difficulties in my research. Her professionalism is an excellent example for me to emulate. It was my great honor to be her student.

I would also like to express my gratitude to my mentor, Dr. Mary Barth. Her profound insights guided me in solving tough science questions. Her diligent and committed attitude towards science taught me how to be a good atmospheric scientist and a good human being.

I greatly appreciated my other committee members, Dr. Gretchen Keppel-Aleks and Dr. Kerri Pratt for their time to evaluate my research and to give great suggestions, making my thesis a better work. And many thanks to Dr. Ned Patton and Dr. Gao Chen for their guidance and support in helping and improving my research from multiple perspectives.

The Steiner Research Group is an awesome group and I am grateful for their support when my research or life was low. I would like to thank to Alex Bryan, Stacey Kawecki, Kirsti Ashworth, Matt Wozniak, Kevin Kuo and all my other colleagues for everything they did to make my life more beautiful and meaningful.

Many thanks to Faye Ogasawara, Darren Britten-Bozzone, Gregor Langbehn, Brian White, Melissa Terwilliger and the Advanced Research Computing team at the University of Michigan for fixing all my weird engine problems and making my life so much easier. I learned a lot from them.

Many thanks to Cheri Johnson, Sandra Pytlinski, Tonya Thompson, Rachel Long, Marti Moon and other administrative staff members in our department for all their help and making this department wonderful and feel like a big family.

I would like to thank Elizabeth Agee, the other co-founder of the Michigan-Earth Science Women's Network, for being an excellent teammate. We could not run the workshop series without her.

Special thanks to all my friends I met at the University of Michigan. They brought tons of happiness and made my life more colorful and enjoyable. They gave me help whenever I was in difficulty. I really enjoyed spending time with them. Especially during the holidays, they were the reason I didn't miss my home.

Last but not least, I want to thank my family. They gave me unconditional love and support, and encouraged me to make choices following my heart. I want to thank them for believing in me and saving me from all the down moments in my life. Without their faith in me, I would not have made it this far.

TABLE OF CONTENTS

LIST OF TABLES

LIST OF FIGURES

ABSTRACT

Understanding chemical and physical processes of biogenic volatile organic compounds in the atmospheric boundary layer

by

Yang Li

Chair: Allison L. Steiner

Biogenic volatile organic compounds (BVOC) are emitted naturally from the terrestrial biosphere and are oxidized quickly within the troposphere. These compounds play crucial roles in the formation of ozone and secondary organic aerosols (SOA) in the atmospheric boundary layer (ABL), affecting both air quality and climate. Isoprene (C_5H_8) is a relatively well-studied BVOC, emitted in large quantities with a very short atmospheric lifetime (~10 min) that is comparable to mixing timescales within the ABL. However, atmospheric regional models have difficulties in reproducing the vertical distributions of many different BVOC species. This dissertation uses two different model tools to understand the roles of chemical oxidation and turbulent transport in BVOC-dominated regions. The National Center for Atmospheric Research's Large-Eddy Simulation (LES) model is used to simulate distinct convective environments to understand the role of boundary layer turbulence on the atmospheric chemistry of key BVOC species and their oxidation products during the 2011 NASA DISCOVER-AQ field campaign. Convection plays an

important role in mixing oxygenated volatile organic compounds (OVOC) into the upper ABL, therefore, modifying the vertical structure of atmospheric oxidation capacity. I implement a new chemical mechanism in the LES to include both gas- and aqueous-phase reactions to provide the first detailed code to account for aqueous chemistry within clouds, and find that the inclusion of aqueous chemistry reduces HCHO in the cloud layer by up to 18% and increases isoprene mixing ratios, promoting segregation of reactants and reducing reaction rates in cloud layers. Using the LES as an evaluation standard, I implement a regional atmospheric chemistry model, the Weather Research and Forecasting Model coupled with Chemistry (WRF-Chem) to understand BVOC chemistry in the ABL across spatial scales. Although the WRF-Chem model is widely used to study atmospheric chemistry at regional scales, it simulates weaker turbulence than the LES, which leads to stronger segregation of isoprene and OH in the WRF-Chem simulations. Overall, this work elucidates the role of turbulence on BVOC chemistry in the ABL and suggests that competing chemical and physical processes are key for simulating BVOC oxidation in the ABL. Regional models such as WRF-Chem have difficulties in simulating these complex processes for BVOC and this may influence how we simulate and understand the oxidation capacity of the troposphere.

CHAPTER 1 Introduction

1.1. Chemistry of biogenic volatile organic compounds

The atmosphere of Earth is mainly composed of nitrogen (~78%), oxygen (~21%), argon (~0.9%), carbon dioxide and other trace gases. These trace gases have concentrations ranging from a few μmol mol^{-1} to fmol mol^{-1}, and have lifetimes varying from a few seconds to more than 1000 years depending on their chemical reactivity in the atmosphere [*Schlager et al.*, 2012]. Over time, chemical reactions in the atmosphere oxidize these compounds, leading to a complex mix of trace gases. Volatile organic compounds (VOC) are a reactive group of the short-lived trace gases that play an important role in atmospheric oxidative capacity, therefore, influencing the ability of the atmosphere to oxidize chemical compounds [*Atkinson*, 2000].

The Earth system emits large quantities and a wide variety of VOC into the troposphere [*Guenther et al.*, 2000; *Guenther et al.*, 1995]. VOC emitted directly from anthropogenic sources (e.g., fuel combustion, vehicular emissions, solvent usage in industry, etc.) and biogenic sources (e.g., vegetation, soil, ocean) are defined as primary VOC. In the terrestrial biosphere, primary biogenic VOC (BVOC) are mainly emitted by vegetation and soil, and are estimated to emit 1.2×10^{15} gC per year at the global scale, contributing about 90% to the global VOC budget [*Fuentes et al.*, 2000; *Guenther et al.*, 1995]. Even in some urban industrial environments, the importance of BVOC in atmospheric photochemical processes is comparable to anthropogenic

VOC emissions [*Goldstein and Galbally*, 2007; *Martin et al.*, 2004]. When in combination with nitrogen oxides (NO_X; $NO+NO_2$) and sunlight, VOC undergo a complex series of chemical reactions and play an important role in the formation of ozone (O_3) and secondary organic aerosols (SOA) [*Atkinson*, 2000; *Hatfield and Huff Hartz*, 2011].

Oxygenated VOC (OVOC) are an important reactive fraction of VOC. OVOC can derive from primary anthropogenic and biogenic emissions [*Sawyer et al.*, 2000; *Singh et al.*, 2001] or be formed in the atmosphere through oxidation of other primary VOC [Placet et al., 2000; Singh et al., 2001], which can be categorized as secondary VOC. OVOC are a key player in atmospheric oxidative capacity, and are estimated to comprise 30-40% of the total hydroxyl radical (OH) reactivity in urban areas [*Steiner et al.*, 2008; *Volkamer et al.*, 2010].

BVOC include isoprenoids (isoprene and monoterpenes), alkanes, alkenes, carbonyls, alcohols, esters, ethers, and acids, with isoprene and monoterpenes being the most prominent compounds, followed by alcohols and carbonyls. The emission of BVOC from vegetation is controlled by many factors, such as light, temperature, vegetation developmental stage, and stress (e.g., under injuries, air pollution, etc.). Gaps exist in investigating BVOC emission result from a lack of understanding of these control factors [*Kesselmeier and Staudt*, 1999].

The most studied BVOC species is isoprene due to its high emission rate and reactivity, which is typically about 10 minute lifetime based on reaction with the OH radical. The lifetime of these short-lived BVOC is comparable to the boundary layer turnover time in the atmosphere [*Patton et al.*, 2001]. Detailed BVOC chemical

mechanism and well-resolved turbulence are both necessary in atmospheric modeling to investigate BVOC distribution. Isoprene is highly reactive with OH, O_3, and the nitrate radical (NO_3), and their reaction pathways have been elucidated over the past three decades [*Atkinson*, 2000; *Fuentes et al.*, 2000]. The general reaction mechanism is shown [*Fuentes et al.*, 2000]:

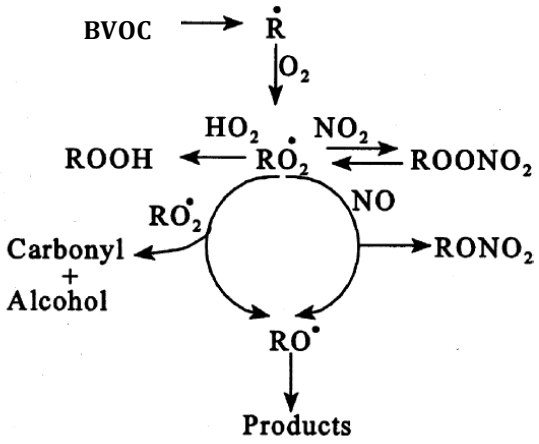

Oxidation of BVOC begins with H-atom abstraction from various C-H bonds or addition of OH, O_3 and NO_3 to the double carbon bonds to form alkyl radical, R. The reactions then proceed through the intermediate organic peroxy (RO_2). The fate of the organic peroxy depends on the ratio of nitric oxide (NO) and the hydroperoxy radical. Under high NO_X conditions, the peroxy radical reacts with NO, yielding alkoxy (RO) radicals. RO radicals can further react with O_2, then decompose or isomerize to form other BVOC oxidation products [*Fuentes et al.*, 2000]. Under low NO_X conditions, RO_2 can react with a separate HO_2 to produce peroxides (ROOH). In the case of isoprene, this is isoprene hydroxyhydroperoxides (ISOPOOH), which can form isoprene epoxydiols under low NO_X conditions and may be important for organic aerosol formation. Additionally, under low NO_X conditions, the RO_2 radical

can reach with another RO_2 to produce carbonyls and alcohols. In the overall reaction pathway, BVOC oxidation products become more oxidized and less volatile with additional oxygenated functional groups. The BVOC oxidation products have a longer lifetime (e.g., ~0.5 - 8 hours as simulated by *Li et al.* [2016]) than primarily emitted isoprene. The major primary OVOC products of isoprene include methyl vinyl ketone (MVK), methacrolein (MACR) and formaldehyde (HCHO), with their production yields estimated to be about 30-40%, 20-30%, and 50-70% respectively, [*Zhang et al.*, 2002]. The distinct formation pathways of MACR or MVK result from the carbon chain location of the OH addition [*Seinfeld et al.*, 1998].

Gas-phase oxidation of primary emitted BVOC may result in functionalized oxidation products with lower volatility, providing molecules the ability to partition to the aqueous or particle phase. For example, the BVOC primary oxidation products, MVK and MACR, can react in the aqueous phase to produce low-volatility products such as small carbonyl compounds including oxalate, glyoxal and methylglyoxal. These processes can be particularly important in cloud environments in the atmosphere. For soluble species, the extent of partitioning between gas and aqueous phases and how fast equilibrium is established are important in simulating these processes [*Betterton*, 1991]. Additionally, low-volatility products can then partition into the particle phase to form SOA following Raoult's law [*Donahue et al.*, 2006; *Hodzic et al.*, 2014], and can also dissolve into cloud droplets or aqueous particles depending on their solubility following Henry's law [*Barth et al.*, 2003], providing an important source of secondary organic aerosol (SOA) [*Blando and Turpin*, 2000; *Ervens et al.*, 2011; *Fu et al.*, 2008]. Therefore, the role of chemical processing of

BVOC in clouds is gaining increasing importance.

In addition, in-cloud aqueous-phase chemistry could influence the photochemistry of the troposphere by substantially reducing HCHO, HO_x and O_3, which further modifies BVOC concentrations in the troposphere [*Lelieveld and Crutzen*, 1991; *Lelieveld and Crutzen*, 1990]. Changes in reactive radicals (e.g., HO_x and O_3) also alter the atmospheric oxidative capacity [*Atkinson*, 2000], determining the rate of removal and therefore controlling the abundance of BVOC and other key chemical compounds in the atmosphere [*Bloss et al.*, 2005].

1.2. BVOC in the boundary layer

The atmospheric boundary layer (ABL) is defined as the part of the troposphere that is directly influenced by the presence of the Earth's surface and responds to surface forcings with a timescale of about an hour or less [*Stull*, 1988]. Figure 1.1 shows the diurnal cycle of the ABL with a well-defined structure over the land surface, where the height of the ABL varies in response to a time-dependent buoyancy forcing over the diurnal cycle (Figure 1.1). Three major components of the ABL frequently defined are the mixed layer, the residual layer, and the stable boundary layer. The mixed layer occurs during the daytime, where intense vertical mixing mixes conserved variables (e.g., potential temperature, water vapor) and generates a constant profile with height. The residual layer is formed at nighttime when the lower boundary condition forcing and the resulting turbulence decays, and has levels of some trace species the same as the recently decayed mixed layer. The stable boundary layer is characterized by statically stable air with weak

turbulence, and frequently occurs at nighttime when the lower boundary condition is at a minimum. When clouds are present in the mixed layer, the ABL is further subdivided into a cloud layer and subcloud layer.

Over land, much of the growth and evolution of the ABL are driven by buoyancy forces driven by the solar heating of the surface, which generates both latent and sensible heat fluxes that exhibit a diurnal cycle that peaks approximately around solar noon. At sunrise, convection begins to mix warm air up throughout the stable boundary layer and into the mixed layer, driving the growth of the ABL. Trace constituents left in the residual layer from previous day can be mixed back into the active daytime ABL. When the residual layer is entirely mixed into the ABL, the ABL is relatively well mixed throughout the afternoon, with turbulence decreasing in the late afternoon and ceasing after the sun goes down. The surface heat fluxes drive much of the turbulence within the ABL, which is an essential ingredient facilitating the transfer of water vapor, heat, momentum, and the diffusion of air pollutants. Turbulence kinetic energy (TKE) is a measure of the intensity of turbulence, and is directly related to the momentum, heat and moisture transport through the boundary layer.

Understanding the structure and evolution of the ABL and accurately quantifying turbulence are crucial to understand the distribution of air pollutants. After BVOC are emitted from the surface into the ABL, their fate is controlled by both physical and chemical processes. Because BVOC and their oxidation products tend to be very reactive, there can be large gradients in the mixing ratios of key chemical compounds between the free tropospheric and the ABL. Primary emissions

from the surface or entrained compounds from the free troposphere are mixed in the ABL with a growing volume throughout the day, and a decreasing volume when the buoyancy forcing shuts down and the convective boundary layer ceases to exist [*Vilà-Guerau de Arellano et al.*, 2011]. The free troposphere and ABL exchange, controlled by the evolution of boundary layer dynamics as well as the vertical structure of temperature and moisture, can be as important as the surface isoprene emission in determining the isoprene mixing ratio in the ABL [*Vilà-Guerau de Arellano et al.*, 2011]. For less reactive OVOC with longer lifetimes than primary emissions, they can reside in the ABL over the course of several days, be trapped in nocturnal residual layers and recirculated to the surface in the morning [*Forkel et al.*, 2006]. As a result, boundary layer dynamics play an important role in BVOC vertical distribution.

1.3. Limitations in current understanding of BVOC

Discrepancies between observed and modeled concentrations of isoprene and its oxidation products are still high [*Carter*, 2007; *Guenther et al.*, 2006; *Xie et al.*, 2011], and resolving this discrepancy is important for the accurate simulation of air pollutants and short-lived climate forcing agents. These discrepancies can come from several sources, as multiple processes such as emissions, chemistry, advection, vertical transport, or surface deposition are required to be simulated accurately by regional and global models.

As in most models, many physical processes implement model parameterizations to represent complex sub-grid processes. One of these

parameterizations is that of the vertical mixing scheme, which tends to be simplified in regional air quality models for computational efficiency (e.g., WRF-Chem [*Grell et al.*, 2005]; CMAQ [*Baek et al.*, 2011; *Xie et al.*, 2011]). These models frequently have difficulty in simulating OVOC in the planetary boundary layer, and tend to underestimate VOC oxidation products and fine particulate matter [*Carlton et al.*, 2010; *Steiner et al.*, 2008]. For many of the lesser studied OVOC, there are several uncertainties, including the emission of primary OVOC, the lack of OVOC observations with which to evaluate models [*Forkel et al.*, 2006; *Wang et al.*, 2014], and uncertainty in their chemical fate due to insufficient kinetic studies [*Bon et al.*, 2011; *Seco et al.*, 2013; *Sillman*, 1999; *Zheng et al.*, 2009]. From the chemistry perspective, most VOC species in the atmosphere are removed through oxidation with hydroxyl radicals, but understanding these pathways is still challenging as chemical mechanisms in atmospheric models have difficulty simulating the hydroxyl radical in chemically complex environments [*Fuchs et al.*, 2013]. Many OVOC species with low volatilities can partition into the aerosol phase (e.g., SOA formation) and understanding of these gas-to-particle transitions with their liquid-phase and heterogeneous-phase oxidation pathways is still emerging [*Mellouki et al.*, 2015; *Surratt et al.*, 2010]. Additionally, regional and global models often do not capture the complexities of boundary layer dynamics, and frequently models can simulate a decoupling between the ABL and atmospheric layers aloft [*Forkel et al.*, 2006].

Another important physical parameterization is that of convective clouds, and regional and global models have difficulties in simulating convective cumulus clouds due to uncertainties in convective parameterizations [*Gianotti et al.*, 2011;

Mapes et al., 2004; *Mauritsen et al.*, 2012]. Clouds can influence the efficacy of the aqueous process of BVOC at the cloud scale (Section 1.1), and therefore may be important in understanding oxidation in the ABL. Previous regional and global modeling studies have incorporated aqueous mechanisms including the cloud aqueous processing of organic chemical constituents (e.g., isoprene oxidation products) at varying spatial and time scales. At coarser spatial resolutions in global models (e.g., the GEOS-Chem model with a 2° latitude × 2.5° longitude resolution [*Marais et al.*, 2016]) and regional models (e.g., the regional scale Community Multiscale Air Quality (CMAQ) model with a horizontal resolution of 36 km [*Chen et al.*, 2007]), clouds are parameterized by predicting the cloud fraction within each grid. Studies using coarser resolutions with cloud parameterizations have underestimated SOA precursors as compared to observations, and this has also been attributed to a lack of a detailed cloud aqueous chemistry scheme [*Chapman et al.*, 2009; *Tuccella et al.*, 2015]. At finer regional resolutions (< 4 km), many simulations assume that clouds are resolved, as they utilize grid sizes of the same order as large clouds (km). There is still some disagreement in the literature as to the appropriate horizontal resolution at which a convective parameterization is needed. For example, *Knote et al.* [2014] used a cumulus parameterization with 4 km resolution simulations to study SOA formation. *Loughner et al.* [2014] also implemented a cumulus parameterization at 4 km to investigate the role of the Chesapeake Bay breeze on surface air quality. However, this parameterization is not used by *Loughner et al.* [2011] when the horizontal resolution is finer than 8 km. Therefore, the model resolution and its treatment of clouds are key factors in evaluating the

impacts of VOC chemistry and transport in the ABL. Accurate model representation of the turbulent motion of clouds in conjunction with sophisticated multi-phase chemistry is required to understand the fates and distributions of the BVOC species and its relevance for gas, aqueous and aerosol phase chemistry.

1.4. Atmospheric modeling tools across spatial scales

As noted above, the horizontal and vertical resolution of the model is important to understanding the physical and chemical processes that occur in the ABL. To improve the interpretation of BVOC vertical distribution and ozone evaluation, the National Center for Atmospheric Research's (NCAR) large-eddy simulation (LES) model with an online chemistry scheme is employed. The LES uses fine resolutions, with typical horizontal and vertical resolutions on the order of tens to hundreds of meters [*Moeng*, 1984]. The LES solves the Navier-Stokes equations, the conservation equation for potential temperature, the Poisson equation and the subgrid-scale kinetic energy equation for meteorological parameters. Fine grid resolution and complex turbulent closure enable the LES to resolve the energy-containing turbulent eddies in the ABL [*Moeng*, 1984]. The LES model also has an online chemical mechanism, which provides a detailed description of both gas and aqueous phase organic chemistry. Typically, the LES meteorology and chemistry are simulated with timesteps of 1.5 seconds. Overall, the LES provides an opportunity to examine BVOC chemistry coupled with ABL dynamics act a very fine spatial and temporal scale, which can help to elucidate the complex nature of ABL OVOC fate and ozone formation. Additionally, it can serve as a comparison standard for global

and regional chemical transport models and observations.

Larger-scale regional models (e.g., WRF-Chem) are essential and widely used to investigate long-term and long-range transport of air pollutants. Typical resolutions of the WRF model range from tens to thousands of kilometers in the horizontal and from 20 to 90 layers in the vertical. Because it is a community based model, WRF typically has several different parameterizations for different physical processes. One important physical parameterization for this study is the planetary boundary layer scheme, which is used to interpret how turbulent mixing alters the atmospheric status and to express the impact of subgrid-scale turbulent motions on grid-scale variables [*Shin and Hong*, 2011]. Additionally, atmospheric moist convective processes occur on spatial scales smaller than can be explicitly resolved by numerical models. A second important scheme is the cumulus parameterization, which is used to estimate the rate of subgrid-scale convective precipitation, release of latent heat, and the redistribution of heat, moisture, and momentum in the vertical due to convection [*Kain and Fritsch*, 1990]. We implement WRF-Chem with two PBL schemes (e.g., the Yonsei University (YSU) PBL scheme [*Hong et al.*, 2006] and the Mellor-Yamada-Janjic (MYJ) PBL scheme [*Janjić*, 1994]) to investigate the effects of these PBL schemes. Differences in the mixing schemes of the WRF-Chem and the LES could influence interpretation BVOC in the ABL, and in this dissertation I compare different modeling tools that provide very different representations of spatial scales to provide insight into the representation of turbulent mixing in the PBL as relevant for atmospheric chemistry.

1.5. NASA DISCOVER-AQ campaign

Aircraft data from the recent NASA DISCOVER-AQ ("Deriving Information on Surface Conditions from Column and Vertically Resolved Observations Relevant to Air Quality") field campaign can be used to understand model limitations for understanding BVOC oxidation in the PBL. These NASA missions were conducted in part to understand the formation of ozone in the ABL [*Crawford and Pickering*, 2014]. The first study took place in July 2011 in the Baltimore-Washington metropolitan area, followed by additional field campaigns in California's San Joaquin Valley (January-February 2013), Houston, TX (September 2013) and Denver, CO (July-August 2014) [*Crawford and Pickering*, 2014]. The locations were selected to target a suite of factors that influence regional air quality, including upwind emissions, transport and local anthropogenic and biogenic emissions. Based on integration of satellite observations, aircraft *in situ* profiles and surface site measurements, the DISCOVER-AQ campaigns can be used to develop an understanding of the column and surface quantities of key O_3 precursors due to variations of surface emissions, atmospheric chemistry processes and boundary layer meteorology.

Additionally, observed vertical profiles from the DISCOVER-AQ campaigns can provide insight into atmospheric oxidation of biogenic and anthropogenic species and our ability to model these variations with existing models. Figure 1.2 highlights the heterogeneity of the vertical profiles of nine VOC species measured by NASA P-3B flights in DISCOVER-AQ 2011 on July 1, 2011. These observations show that many VOC species including OVOC have vertical profiles that deviate from the

typical well-mixed assumption that is often used to describe OVOC in the PBL. Therefore, more detail of chemistry and physics in the ABL is needed, especially with respect to the role of vertical mixing in these models.

1.6. Science questions and dissertation objectives

My dissertation proposes three science questions to improve the understanding of BVOC chemistry in the PBL:

1) ***How do boundary layer dynamics affect the oxidation of BVOC in the atmosphere?***

Using the unique dataset of airborne VOC observations from the 2011 NASA DISCOVER-AQ campaign in the Baltimore-Washington area, we evaluate the relative role of transport time versus chemical lifetime to understand how key BVOC species affect the formation of tropospheric ozone. In **Chapter 2**, we select three cases representing distinct meteorological conditions during the DISCOVER-AQ 2011 campaign and implement the LES model with well-defined turbulence to evaluate the role of boundary layer dynamics on the atmospheric chemistry of BVOC.

2) ***How do in-cloud aqueous processes affect the chemistry and transport of BVOC?***

The presence of clouds adds additional complexity as many VOC are soluble in water, and a suite of aqueous phase chemical reactions can occur in cloud water. The LES model provides a unique capability to investigate the role of aqueous chemistry at the cloud-scale. In **Chapter 3**, we add an updated aqueous-phase

chemical mechanism in the LES to simulate and understand the effects of aqueous-phase chemistry on vertical distributions of key BVOC in convective environments. We present high-resolution LES-Chem simulations representing both convective transport and aqueous phase chemistry and their impact on the oxidation and distribution of organic species.

3) What horizontal and vertical spatial scales are needed to capture the physical and chemical processes that affect BVOC oxidation in regional and global atmospheric models?

LES models have up to three times more vertical levels than air quality models and use more complex turbulent closure schemes that can resolve the energy-containing turbulent eddies in the ABL. This complexity provides additional insight into the vertical transport of ozone precursor species, and serves as a comparison standard for global and regional chemical transport models and observations. In **Chapter 4**, we apply the WRF-Chem model over the 2011 DISCOVER-AQ observational region and compare results with the NCAR LES model to evaluate the WRF-Chem ability to represent BVOC vertical mixing and oxidation time scales. The comparison of the WRF-Chem simulations with the LES simulations can provide insight into the representation of turbulent mixing in the PBL as relevant for atmospheric chemistry.

Overall, the work here presents a cross-scale analysis that focuses on fine scale processes using the LES and connects these results with regional-scaling processes using WRF-Chem. The use of the LES modeling tool can provide an

accurate interpretation and evaluation of atmospheric chemistry and dynamics in the ABL. The modeling of the DISCOVER-AQ campaign provides the basis for modeling simulations in heavy pollution regions. The results presented here provide new insights into the role of turbulence in BVOC oxidation in the atmospheric boundary layer and provide steps in moving towards improving the simulation of regional air pollution.

1.7. References

Atkinson, R. (2000), Atmospheric chemistry of VOCs and NOx, *Atmos Environ*, *34*(12–14), 2063-2101, doi:http://dx.doi.org/10.1016/S1352-2310(99)00460-4.

Baek, J., Y. Hu, M. T. Odman, and A. G. Russell (2011), Modeling secondary organic aerosol in CMAQ using multigenerational oxidation of semi-volatile organic compounds, *Journal of Geophysical Research: Atmospheres*, *116*(D22), n/a-n/a, doi:10.1029/2011JD015911.

Barth, M., S. Sillman, R. Hudman, M. Jacobson, C. H. Kim, A. Monod, and J. Liang (2003), Summary of the cloud chemistry modeling intercomparison: Photochemical box model simulation, *Journal of Geophysical Research: Atmospheres*, *108*(D7).

Betterton, E. A. (1991), The partitioning of ketones between the gas and aqueous phases, *Atmospheric Environment. Part A. General Topics*, *25*(8), 1473-1477.

Blando, J. D., and B. J. Turpin (2000), Secondary organic aerosol formation in cloud and fog droplets: a literature evaluation of plausibility, *Atmos Environ*, *34*(10), 1623-1632, doi:10.1016/S1352-2310(99)00392-1.

Bloss, W. J., M. J. Evans, J. D. Lee, R. Sommariva, D. E. Heard, and M. J. Pilling (2005), The oxidative capacity of the troposphere: Coupling of field measurements of OH and a global chemistry transport model, *Faraday Discussions*, *130*, 425-436.

Bon, D. M., D. M. Bon, I. M. Ulbrich, J. A. De Gouw, and C. Warneke (2011), Measurements of volatile organic compounds at a suburban ground site (T1) in Mexico City during the MILAGRO 2006 campaign: Measurement comparison, emission ratios, and source attribution, *Atmospheric chemistry and physics*, *11*(6), 2399-2421.

Carlton, A. G., P. V. Bhave, S. L. Napelenok, E. O. Edney, G. Sarwar, R. W. Pinder, G. A. Pouliot, and M. Houyoux (2010), Model Representation of Secondary Organic Aerosol in CMAQv4.7, *Environmental Science & Technology*, *44*(22), 8553-8560, doi:10.1021/es100636q.

Carter, W. P. (2007), *Development of the SAPRC-07 chemical mechanism and updated ozone reactivity scales*, Citeseer.

Chapman, E. G., W. Gustafson Jr, R. C. Easter, J. C. Barnard, S. J. Ghan, M. S. Pekour, and J. D. Fast (2009), Coupling aerosol-cloud-radiative processes in the WRF-Chem model: Investigating the radiative impact of elevated point sources, *Atmospheric Chemistry and Physics*, *9*(3), 945-964.

Chen, J., R. Griffin, A. Grini, and P. Tulet (2007), Modeling secondary organic aerosol formation through cloud processing of organic compounds, *Atmospheric Chemistry and Physics*, *7*(20), 5343-5355.

Donahue, N., A. Robinson, C. Stanier, and S. Pandis (2006), Coupled partitioning, dilution, and chemical aging of semivolatile organics, *Environmental Science & Technology*, *40*(8), 2635-2643.

Ervens, B., B. J. Turpin, and R. J. Weber (2011), Secondary organic aerosol formation in cloud droplets and aqueous particles (aqSOA): a review of laboratory, field and model studies, *Atmos. Chem. Phys.*, *11*(21), 11069-11102, doi:10.5194/acp-11-11069-2011.

Forkel, R., O. Klemm, M. Graus, B. Rappenglück, W. R. Stockwell, W. Grabmer, A. Held, A. Hansel, and R. Steinbrecher (2006), Trace gas exchange and gas phase chemistry in a Norway spruce forest: A study with a coupled 1-dimensional canopy atmospheric chemistry emission model, *Atmos Environ*, *40, Supplement 1*(0), 28-42, doi:http://dx.doi.org/10.1016/j.atmosenv.2005.11.070.

Fu, T. M., D. J. Jacob, F. Wittrock, J. P. Burrows, M. Vrekoussis, and D. K. Henze (2008), Global budgets of atmospheric glyoxal and methylglyoxal, and implications for formation of secondary organic aerosols, *Journal of geophysical research: atmospheres*, *113*(D15).

Fuchs, H., A. Hofzumahaus, F. Rohrer, B. Bohn, T. Brauers, H. Dorn, R. Häseler, F. Holland, M. Kaminski, and X. Li (2013), Experimental evidence for efficient hydroxyl radical regeneration in isoprene oxidation, *Nature Geoscience*, *6*(12), 1023-1026.

Fuentes, J. D., L. Gu, M. Lerdau, R. Atkinson, D. Baldocchi, J. Bottenheim, P. Ciccioli, B. Lamb, C. Geron, and A. Guenther (2000), Biogenic hydrocarbons in the atmospheric boundary layer: a review, *Bulletin of the American Meteorological Society*, *81*(7), 1537-1575.

Gianotti, R. L., D. Zhang, and E. A. B. Eltahir (2011), Assessment of the Regional Climate Model Version 3 over the Maritime Continent Using Different Cumulus Parameterization and Land Surface Schemes, *Journal of Climate*, *25*(2), 638-656, doi:10.1175/JCLI-D-11-00025.1.

Goldstein, A. H., and I. E. Galbally (2007), Known and Unexplored Organic Constituents in the Earth's Atmosphere, *Environmental Science & Technology*, *41*(5), 1514-1521, doi:10.1021/es072476p.

Grell, G. A., S. E. Peckham, R. Schmitz, S. A. McKeen, G. Frost, W. C. Skamarock, and B. Eder (2005), Fully coupled "online" chemistry within the WRF model, *Atmos Environ*, *39*(37), 6957-6975, doi:http://dx.doi.org/10.1016/j.atmosenv.2005.04.027.

Guenther, A., C. Geron, T. Pierce, B. Lamb, P. Harley, and R. Fall (2000), Natural emissions of non-methane volatile organic compounds, carbon monoxide, and oxides of nitrogen from North America, *Atmos Environ*, *34*(12–14), 2205-2230, doi:http://dx.doi.org/10.1016/S1352-2310(99)00465-3.

Guenther, A., et al. (1995), A global model of natural volatile organic compound emissions, *Journal of Geophysical Research: Atmospheres*, *100*(D5), 8873-8892, doi:10.1029/94JD02950.
Guenther, A., T. Karl, P. Harley, C. Wiedinmyer, P. I. Palmer, and C. Geron (2006), Estimates of global terrestrial isoprene emissions using MEGAN (Model of Emissions of Gases and Aerosols from Nature), *Atmos. Chem. Phys.*, *6*(11), 3181-3210, doi:10.5194/acp-6-3181-2006.
Hatfield, M. L., and K. E. Huff Hartz (2011), Secondary organic aerosol from biogenic volatile organic compound mixtures, *Atmos Environ*, *45*(13), 2211-2219, doi:http://dx.doi.org/10.1016/j.atmosenv.2011.01.065.
Hodzic, A., B. Aumont, C. Knote, J. Lee‐Taylor, S. Madronich, and G. Tyndall (2014), Volatility dependence of Henry's law constants of condensable organics: Application to estimate depositional loss of secondary organic aerosols, *Geophysical Research Letters*, *41*(13), 4795-4804.
Hong, S.-Y., Y. Noh, and J. Dudhia (2006), A new vertical diffusion package with an explicit treatment of entrainment processes, *Monthly Weather Review*, *134*(9), 2318-2341.
Janjić, Z. I. (1994), The step-mountain eta coordinate model: Further developments of the convection, viscous sublayer, and turbulence closure schemes, *Monthly Weather Review*, *122*(5), 927-945.
Kain, J. S., and J. M. Fritsch (1990), A one-dimensional entraining/detraining plume model and its application in convective parameterization, *Journal of the Atmospheric Sciences*, *47*(23), 2784-2802.
Kesselmeier, J., and M. Staudt (1999), Biogenic Volatile Organic Compounds (VOC): An Overview on Emission, Physiology and Ecology, *J Atmos Chem*, *33*(1), 23-88, doi:10.1023/a:1006127516791.
Knote, C., et al. (2014), Simulation of semi-explicit mechanisms of SOA formation from glyoxal in aerosol in a 3-D model, *Atmos. Chem. Phys.*, *14*(12), 6213-6239, doi:10.5194/acp-14-6213-2014.
Lelieveld, J., and P. Crutzen (1991), The role of clouds in tropospheric photochemistry, *J Atmos Chem*, *12*(3), 229-267.
Lelieveld, J., and P. J. Crutzen (1990), Influences of cloud photochemical processes on tropospheric ozone, *Nature*, *343*(6255), 227-233.
Li, Y., M. C. Barth, G. Chen, E. G. Patton, S. W. Kim, A. Wisthaler, T. Mikoviny, A. Fried, R. Clark, and A. L. Steiner (2016), Large‐eddy simulation of biogenic VOC chemistry during the DISCOVER‐AQ 2011 campaign, *Journal of Geophysical Research: Atmospheres*, *121*(13), 8083-8105.
Loughner, C. P., D. J. Allen, K. E. Pickering, D.-L. Zhang, Y.-X. Shou, and R. R. Dickerson (2011), Impact of fair-weather cumulus clouds and the Chesapeake Bay breeze on pollutant transport and transformation, *Atmos Environ*, *45*(24), 4060-4072.
Loughner, C. P., et al. (2014), Impact of Bay-Breeze Circulations on Surface Air Quality and Boundary Layer Export, *Journal of Applied Meteorology and Climatology*, *53*(7), 1697-1713, doi:10.1175/JAMC-D-13-0323.1.
Mapes, B. E., T. T. Warner, M. Xu, and D. J. Gochis (2004), Comparison of Cumulus Parameterizations and Entrainment Using Domain-Mean Wind Divergence in a

Regional Model, *Journal of the Atmospheric Sciences*, *61*(11), 1284-1295, doi:10.1175/1520-0469(2004)061<1284:COCPAE>2.0.CO;2.
Marais, E. A., D. J. Jacob, J. L. Jimenez, P. Campuzano-Jost, D. A. Day, W. Hu, J. Krechmer, L. Zhu, P. S. Kim, and C. C. Miller (2016), Aqueous-phase mechanism for secondary organic aerosol formation from isoprene: application to the southeast United States and co-benefit of SO 2 emission controls, *Atmospheric Chemistry and Physics*, *16*(3), 1603-1618.
Martin, R. V., D. D. Parrish, T. B. Ryerson, D. K. Nicks, K. Chance, T. P. Kurosu, D. J. Jacob, E. D. Sturges, A. Fried, and B. P. Wert (2004), Evaluation of GOME satellite measurements of tropospheric NO2 and HCHO using regional data from aircraft campaigns in the southeastern United States, *Journal of Geophysical Research: Atmospheres*, *109*(D24), n/a-n/a, doi:10.1029/2004JD004869.
Mauritsen, T., B. Stevens, E. Roeckner, T. Crueger, M. Esch, M. Giorgetta, H. Haak, J. Jungclaus, D. Klocke, and D. Matei (2012), Tuning the climate of a global model, *Journal of Advances in Modeling Earth Systems*, *4*(3).
Mellouki, A., T. J. Wallington, and J. Chen (2015), Atmospheric Chemistry of Oxygenated Volatile Organic Compounds: Impacts on Air Quality and Climate, *Chemical Reviews*, *115*(10), 3984-4014, doi:10.1021/cr500549n.
Moeng, C.-H. (1984), A large-eddy-simulation model for the study of planetary boundary-layer turbulence, *Journal of the Atmospheric Sciences*, *41*(13), 2052-2062.
Patton, E., K. Davis, M. Barth, and P. Sullivan (2001), Decaying Scalars Emitted By A Forest Canopy: A Numerical Study, *Boundary-Layer Meteorol*, *100*(1), 91-129, doi:10.1023/A:1019223515444.
Placet, M., C. O. Mann, R. O. Gilbert, and M. J. Niefer (2000), Emissions of ozone precursors from stationary sources:: a critical review, *Atmos Environ*, *34*(12–14), 2183-2204, doi:http://dx.doi.org/10.1016/S1352-2310(99)00464-1.
Sawyer, R. F., R. A. Harley, S. H. Cadle, J. M. Norbeck, R. Slott, and H. A. Bravo (2000), Mobile sources critical review: 1998 NARSTO assessment, *Atmos Environ*, *34*(12–14), 2161-2181, doi:http://dx.doi.org/10.1016/S1352-2310(99)00463-X.
Schlager, H., V. Grewe, and A. Roiger (2012), Chemical Composition of the Atmosphere, in *Atmospheric Physics: Background – Methods – Trends*, edited by U. Schumann, pp. 17-35, Springer Berlin Heidelberg, Berlin, Heidelberg, doi:10.1007/978-3-642-30183-4_2.
Seco, R., J. Penuelas, I. Filella, and J. Llusia (2013), Volatile organic compounds in the western Mediterranean basin: urban and rural winter measurements during the DAURE campaign, *Atmospheric chemistry and physics*, *13*(8), 4291-4306, doi:10.5194/acp-13-4291-2013.
Seinfeld, J. H., S. N. Pandis, and K. Noone (1998), Atmospheric chemistry and physics: from air pollution to climate change, edited, AIP.
Shin, H. H., and S.-Y. Hong (2011), Intercomparison of planetary boundary-layer parametrizations in the WRF model for a single day from CASES-99, *Boundary-Layer Meteorol*, *139*(2), 261-281.
Sillman, S. (1999), The relation between ozone, NOx and hydrocarbons in urban and polluted rural environments, *Atmos Environ*, *33*(12), 1821-1845, doi:http://dx.doi.org/10.1016/S1352-2310(98)00345-8.

Singh, H., Y. Chen, A. Staudt, D. Jacob, D. Blake, B. Heikes, and J. Snow (2001), Evidence from the Pacific troposphere for large global sources of oxygenated organic compounds, *Nature*, *410*(6832), 1078-1081.

Steiner, A. L., A. L. Steiner, R. C. Cohen, R. A. Harley, and S. Tonse (2008), VOC reactivity in central California: comparing an air quality model to ground-based measurements, *Atmospheric chemistry and physics*, *8*(2), 351-368, doi:10.5194/acp-8-351-2008.

Stull, R. (1988), An Introduction to Boundary Layer Meteorology Kluwer Academic Publishers Dordrecht 666 Google Scholar.

Surratt, J. D., A. W. H. Chan, N. C. Eddingsaas, M. Chan, C. L. Loza, A. J. Kwan, S. P. Hersey, R. C. Flagan, P. O. Wennberg, and J. H. Seinfeld (2010), Reactive intermediates revealed in secondary organic aerosol formation from isoprene, *Proceedings of the National Academy of Sciences*, *107*(15), 6640-6645, doi:10.1073/pnas.0911114107.

Tuccella, P., G. Curci, G. Grell, G. Visconti, S. Crumeroylle, A. Schwarzenboeck, and A. Mensah (2015), A new chemistry option in WRF-Chem v. 3.4 for the simulation of direct and indirect aerosol effects using VBS: evaluation against IMPACT-EUCAARI data, *Geoscientific Model Development*, *8*(9), 2749-2776.

Vilà-Guerau de Arellano, J., E. G. Patton, T. Karl, K. van den Dries, M. C. Barth, and J. J. Orlando (2011), The role of boundary layer dynamics on the diurnal evolution of isoprene and the hydroxyl radical over tropical forests, *Journal of Geophysical Research: Atmospheres*, *116*(D7), n/a-n/a, doi:10.1029/2010JD014857.

Volkamer, R., P. Sheehy, L. T. Molina, and M. J. Molina (2010), Oxidative capacity of the Mexico City atmosphere – Part 1: A radical source perspective, *Atmos. Chem. Phys.*, *10*(14), 6969-6991, doi:10.5194/acp-10-6969-2010.

Wang, M., M. Shao, W. Chen, B. Yuan, S. Lu, Q. Zhang, L. Zeng, and Q. Wang (2014), A temporally and spatially resolved validation of emission inventories by measurements of ambient volatile organic compounds in Beijing, China, *Atmospheric Chemistry and Physics*, *14*(12), 5871-5891.

Xie, Y., R. Elleman, T. Jobson, and B. Lamb (2011), Evaluation of O3-NOx-VOC sensitivities predicted with the CMAQ photochemical model using Pacific Northwest 2001 field observations, *Journal of Geophysical Research: Atmospheres*, *116*(D20), n/a-n/a, doi:10.1029/2011JD015801.

Zhang, D., W. Lei, and R. Zhang (2002), Mechanism of OH formation from ozonolysis of isoprene: kinetics and product yields, *Chemical Physics Letters*, *358*(3–4), 171-179, doi:http://doi.org/10.1016/S0009-2614(02)00260-9.

Zheng, J., M. Shao, W. Che, L. Zhang, L. Zhong, Y. Zhang, and D. Streets (2009), Speciated VOC Emission Inventory and Spatial Patterns of Ozone Formation Potential in the Pearl River Delta, China, *Environmental Science & Technology*, *43*(22), 8580-8586, doi:10.1021/es901688e.

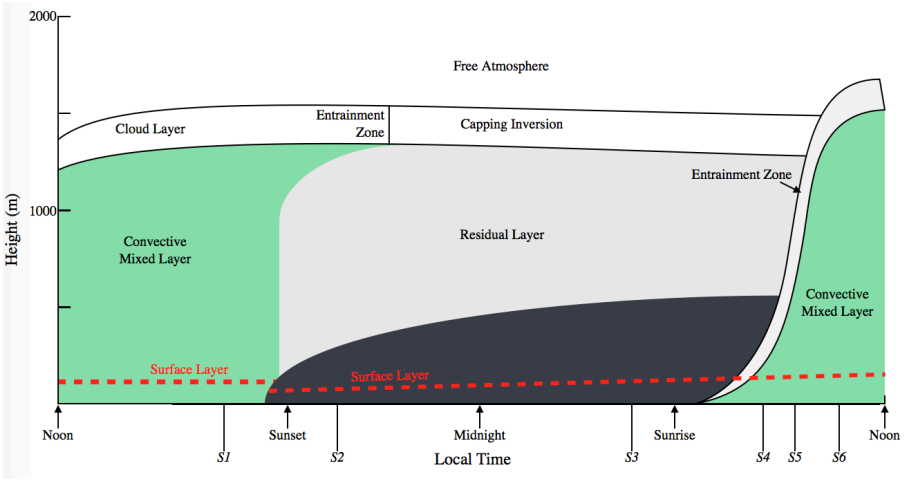

Figure 1. 1. The boundary layer in high pressure region over land consists of three major components: a turbulent mixed layer; a residual layer containing former mixed-layer air; and a nocturnal stable boundary layer of sporadic turbulence. The mixed layer can be subdivided into a cloud layer and a subcloud layer.

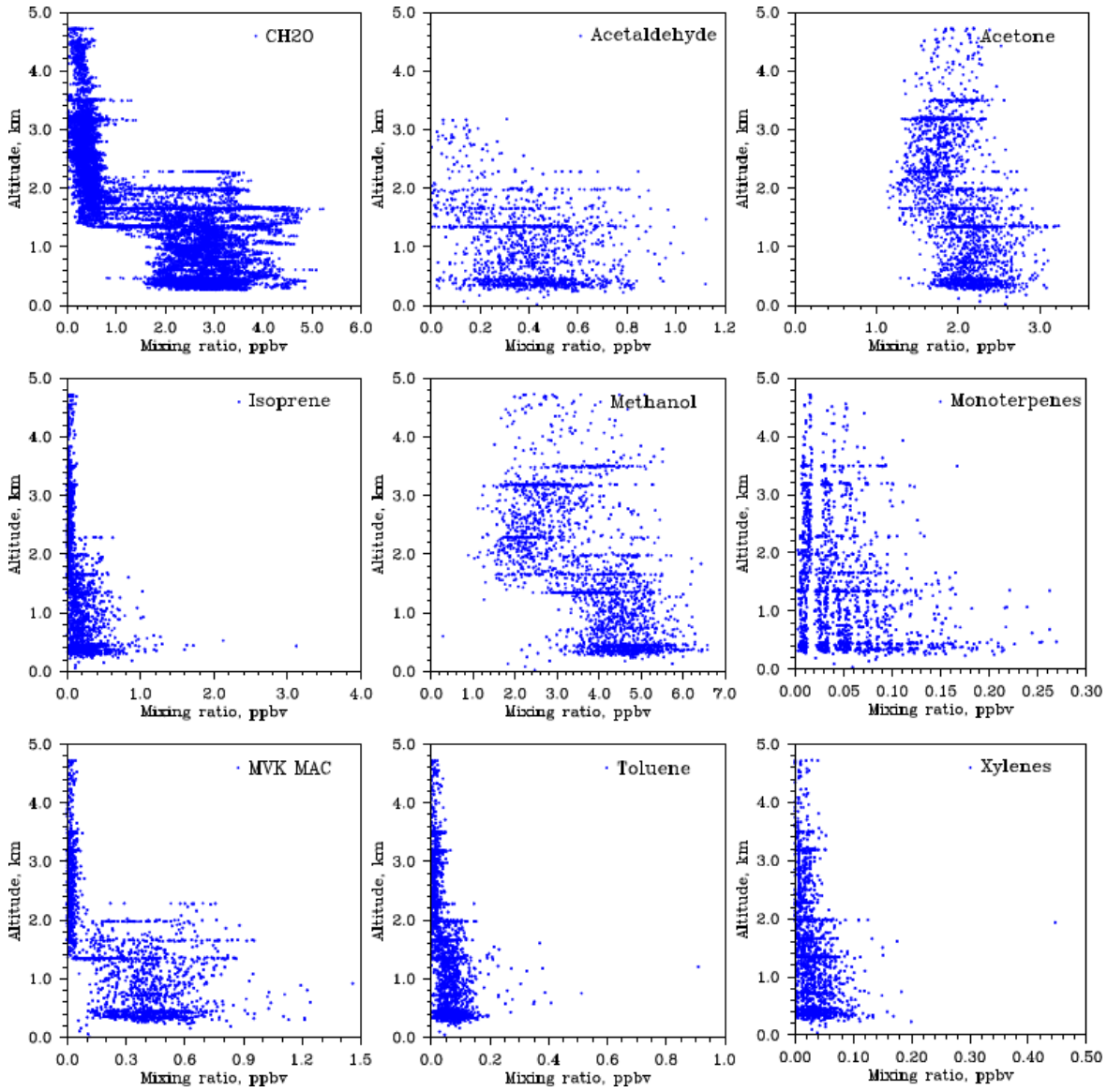

Figure 1. 2. Vertical profiles of HCHO (CH2O), acetaldehyde, acetone, isoprene, methanol, monoterpenes, MVK+MACR (MVK MAC), toluene and xylenes measured by P-3B flight on 1 July, 2011

CHAPTER 2 Large-eddy simulation of biogenic VOC chemistry during the DISCOVER-AQ 2011 campaign

Abstract

Biogenic volatile organic compounds (BVOC) are oxidized quickly in the atmosphere to form oxygenated VOC (OVOC) and play crucial roles in the formation of ozone and secondary organic aerosols. We use the National Center for Atmospheric Research's Large-Eddy Simulation (LES) model and DISCOVER-AQ 2011 flight data to understand the role of boundary layer turbulence on the atmospheric chemistry of key BVOC species and their oxidation products. We simulate three distinct convective environments during the campaign, representing fair weather conditions (Case 1: 1 July), a convective event dominated by southwesterly flow (Case 2: 11 July) and a polluted event with high temperature and convection (Case 3: 29 July). Isoprene segregation is greatest in the lower boundary layer under warm and convective conditions, reaching up to a 10% reduction in the isoprene-OH reaction rate. Under warm and convective conditions, the BVOC lifetimes lengthen due to increased isoprene emission, elevated initial chemical concentrations and OH competition. Although turbulence-driven segregation has less influence on the OVOC species, convection mixes more OVOC into the upper atmospheric boundary layer (ABL) and increases the total OH reactivity. Production and loss rates of ozone above 2 km in all the three cases indicate *in situ* ozone

formation in addition to vertical convective transport of ozone from the surface and aloft, consistent with the increased contribution of OH reactivity from OVOC. Together, these results show that total OH reactivity in the ABL increases under warmer and stronger convective conditions due to enhanced isoprene emission and the OVOC contribution to ozone formation.

2.1. Introduction

Large quantities of volatile organic compounds (VOC) are emitted into the troposphere from biogenic and anthropogenic sources. Although anthropogenic VOC dominate in megacities and urban areas [*Williams and Koppmann*, 2007], BVOC contribute about 90% to the global VOC budget [*Guenther et al.*, 1995]. Even in some urban industrial environments, the importance of BVOC in atmospheric photochemical processes is comparable to anthropogenic VOC emissions [*Goldstein and Galbally*, 2007; *Martin et al.*, 2004]. When in combination with NO_X ($NO+NO_2$) and sunlight, BVOC undergo a complex series of chemical reactions and play crucial roles in the formation of ozone (O_3) and secondary organic aerosols (SOA) [*Atkinson*, 2000; *Hatfield and Huff Hartz*, 2011].

OVOC are an important reactive fraction of VOC, and are estimated to comprise 30-40% of the total hydroxyl radical (OH) reactivity in some urban areas [*Steiner et al.*, 2008; *Volkamer et al.*, 2010]. Airborne measurements up to 12 km during INTEX-B found that OVOC accounted for up to 20% of the observed OH reactivity [*Mao et al.*, 2009], indicating its key role in the atmospheric chemistry at higher altitudes. OVOC derive from primary anthropogenic and biogenic emissions

[*Sawyer et al.*, 2000; *Singh et al.*, 2001] or can be formed in the atmosphere through oxidation of other primary VOC [*Placet et al.*, 2000; *Singh et al.*, 2001]. For example, photochemical oxidation of primary BVOC, e.g., isoprene, leads to OVOC formation [*Karl et al.*, 2009]. Formaldehyde, acetaldehyde and acetone are frequently observed to be the most abundant OVOC in urban atmospheres [*Li et al.*, 2010; *Seco et al.*, 2007], and prior studies suggest that formaldehyde can contribute more than 20% to the total hydroperoxy (HO_2) radical [*Ren et al.*, 2003] and enhance ozone formation by 4-10% [*Lei et al.*, 2009].

As the most prevalent BVOC, isoprene (C_5H_8) is highly reactive with OH, O_3, and the nitrate radical (NO_3). The major primary OVOC products of isoprene include methyl vinyl ketone (MVK), methacrolein (MACR) and formaldehyde (HCHO). When reacting with OH, isoprene forms peroxy radicals ($C_5H_7O_2$):

$$\mathbf{C_5H_8 + OH \rightarrow C_5H_7O_2} \quad \text{(R1)}$$

The fate of the isoprene peroxy radical depends on the availability of NO_X. In rural, urban, or suburban environments with NO_X emissions, OH can be recycled by reactions of peroxy radicals with NO, creating new oxidation products and forming O_3 [*Apel et al.*, 2002]:

$$\mathbf{C_5H_7O_2 + NO \rightarrow HO_2 + MVK + MACR + carbonyls} \quad \text{(R2)}$$

The oxidation processes of MVK and MACR by OH produce additional peroxy radicals ($MVKO_2$ and $MACRO_2$, respectively), which in the presence of NOx produce secondary OVOC, typically in the form of carbonyls [*Spaulding et al.*, 2003].

$$\mathbf{MVK} \xrightarrow{+\mathbf{OH}} \mathbf{MVKO_2} \xrightarrow{+\mathbf{NO}} \mathbf{carbonyls} \quad \text{(R3)}$$

$$\mathbf{MACR} \xrightarrow{+\mathbf{OH}} \mathbf{MACRO_2} \xrightarrow{+\mathbf{NO}} \mathbf{carbonyls} \quad \text{(R4)}$$

Under low NO_X conditions such as remote forest environments, isoprene peroxy radicals typically react with the hydroperoxy radical (HO_2) to form the isoprene hydroxyhydroperoxide (ISOPOOH) or other peroxy radicals (RO_2) that form peroxides, thereby reducing the product yield of MACR and MVK [*Apel et al.*, 2002].

$$\mathbf{C_5H_7O_2 + RO_2 \rightarrow peroxides} \quad \text{(R5-1)}$$

$$\mathbf{C_5H_7O_2 + HO_2 \rightarrow ISOPOOH} \quad \text{(R5-2)}$$

In both high and low NO_x environments, the oxidation of isoprene produces a suite of OVOC that can exert additional control on the oxidative capacity of the atmosphere.

Discrepancies between observed and modeled concentrations of isoprene and its oxidation products are still high [*Carter*, 2007; *Guenther et al.*, 2006; *Xie et al.*, 2011], and this could be due to the accuracy required for multiple processes (emissions, chemistry, advection, vertical transport, or surface deposition) in regional and global models. The emission of primary OVOC is highly uncertain and limited by the lack of OVOC observations [*Forkel et al.*, 2006; *Wang et al.*, 2014], and uncertainty in their chemical fate is in part due to insufficient kinetic studies [*Bon et al.*, 2011; *Seco et al.*, 2013; *Sillman*, 1999; *Zheng et al.*, 2009]. From the chemistry perspective, most VOC species in the atmosphere are removed through oxidation with hydroxyl radicals, but understanding these pathways is still challenging as

models have difficulty simulating the hydroxyl radical in chemically complex environments [*Fuchs et al.*, 2013]. In addition, many OVOC species with low volatilities can partition into the aerosol phase (e.g., SOA formation) and understanding of these gas-to-particle transitions with their liquid-phase and heterogeneous-phase oxidation pathways is still emerging [*Mellouki et al.*, 2015; *Surratt et al.*, 2010]. Boundary layer dynamics may also play an important role, as some OVOC have longer lifetimes than primary emissions and can reside in the ABL over the course of several days, be trapped in nocturnal residual layers and recirculated to the surface in the morning [*Forkel et al.*, 2006]. Additionally, regional and global models often do not capture the complexities of boundary layer dynamics, causing a decoupling between the ABL and atmospheric layers aloft [*Forkel et al.*, 2006]. A comprehensive understanding of the role of OVOC chemistry and its vertical distribution in the ABL has yet to be developed and evaluated in air quality models.

Previous studies have explored the effect of turbulence on chemistry using both models and observations. Early studies that accounted more explicitly for turbulence (e.g., second order turbulence closure, direct numerical simulations, and large-eddy simulations (LES)) found that many chemical reaction rates within the boundary layer were reduced in the presence of turbulence, due to negatively correlated concentrations and vertical velocities [*Krol et al.*, 2000; *Molemaker and Vilà-Guerau de Arellano*, 1998; *Verver et al.*, 1997]. This process has been described as the "segregation" of chemical species due to inefficient turbulent mixing. Additional studies showed that clouds can play an important role in this segregation,

with greater segregation and reaction rate reduction in clouds as simulated in LES models [*Vilà-Guerau de Arellano et al.*, 2005] and observed [*Karl et al.*, 2007]. Based on these studies, *Vinuesa and De Arellano* [2003] and *Butler et al.* [2008] added a parameterization representing segregation in chemical mechanisms, and found improved predictions related to ozone chemistry and isoprene oxidation chemistry. *Ouwersloot et al.* [2011] found that the surface isoprene emission and the surface heating also played a role in segregation based on LES simulations in the Amazon, with a 10% reaction rate reduction for isoprene and OH with homogeneous surface emission and heating and up to 20% reduction with heterogeneous surface emissions. A recent study by *Kaser et al.* [2015] found isoprene-OH segregation slowed reaction rates up to 30%, comparable to the proposed radical recycling mechanisms [*Lelieveld et al.*, 2008]. Taken together, there are multiple studies that investigate chemistry-turbulence interactions for isoprene, yet few for OVOC. This study will broaden the scope to understand the role of OVOC chemistry under different convective environments.

A typical assumption is that longer-lived species such as OVOC are well mixed within the ABL [*Borrego and Incecik*, 2012] and chemical lifetimes are much longer than turbulent mixing timescales. However, observations highlight the vertical and spatial inhomogeneities in VOC oxidation products [*Koßmann et al.*, 1996; *Velasco et al.*, 2008; *Wöhrnschimmel et al.*, 2006]. Aircraft data such as from the recent DISCOVER-AQ ("Deriving Information on Surface Conditions from Column and Vertically Resolved Observations Relevant to Air Quality") field campaign can be used to address these questions. This mission was conducted in

part to understand the distribution of key VOC species in the atmosphere and their importance for the formation of ozone in the ABL [*Crawford and Pickering*, 2014]. The first study took place in July 2011 in the Baltimore-Washington metropolitan area, followed by additional field campaigns in California's San Joaquin Valley (January-February 2013), Houston, TX (September 2013) and Denver, CO (July-August 2014) [*Crawford and Pickering*, 2014]. The locations were selected to target a suite of factors that influence regional air quality, including upwind emissions, transport and local anthropogenic and biogenic emissions. Based on integration of satellite observations, aircraft *in situ* profiles and surface site measurements, the DISCOVER-AQ campaigns are developing an understanding of the column and surface quantities of key O_3 precursors due to variations of surface emissions, atmospheric chemistry processes and boundary layer meteorology. Additionally, they provide a unique opportunity to examine multiple vertical profiles of a wide suite of atmospheric constituents to understand ABL chemistry in polluted regions.

Observed vertical profiles from the DISCOVER-AQ campaigns can provide insight into atmospheric oxidation of biogenic and anthropogenic species and our ability to model these variations with existing models. However, the simplified vertical mixing scheme in regional air quality models (e.g., CMAQ [*Baek et al.*, 2011; *Xie et al.*, 2011] or WRF-Chem [*Grell et al.*, 2005]) frequently has difficulty in simulating OVOC in the ABL, and VOC oxidation products and fine particulate matter are often underestimated in these regional and global chemical transport models as well [*Steiner et al.*, 2008; *von Kuhlmann et al.*, 2003]. In addition, global and regional models have difficulties in simulating convective cumulus clouds due to

uncertainties in convective parameterizations [*Gianotti et al.*, 2011; *Mapes et al.*, 2004; *Mauritsen et al.*, 2012]. With finer grid resolution and more complex turbulent closure, LES can resolve the energy-containing turbulent eddies in the ABL [*Moeng*, 1984]. Combined with an online chemistry scheme, LES can examine BVOC chemistry coupled with ABL dynamics accurately, elucidate the role of OVOC on regional chemistry, and serve as a comparison standard for global and regional chemical transport models and observations.

In this study, we utilize DISCOVER-AQ 2011 flight data from the Baltimore-Washington, D.C. urban area and the National Center for Atmospheric Research's (NCAR) LES model coupled to the NCAR chemical mechanism MOZART2.2 [*Kim et al.*, 2012] to simulate and understand the vertical distributions of key VOC species and their role in atmospheric composition and chemical distribution. With a more detailed chemical mechanism (52 reactants and 168 chemical reactions) than in *Ouwersloot et al.* [2011] (18 reactants and 19 chemical reactions), the LES model in this study provides an effective tool to analyze the chemistry of BVOC beyond isoprene. Three days with distinct meteorological conditions are selected to understand the role of BVOC in ozone formation within the ABL and the role of ABL dynamics in the primary and secondary oxidation of BVOC. By using the high time- and space-resolved VOC and oxidant data, we can compare the key mixing and chemical processes under similar NO_X environments (~1-2 ppbv) but different meteorological regimes. In addition, this study will fill a gap in understanding how segregation of VOC varies with temperature, humidity and the presence of clouds.

2.2. Methods

2.2.1. LES model experiment design

To understand the competing processes of boundary layer dynamics and chemistry, we use the NCAR LES model [*Moeng*, 1984; *Patton et al.*, 2005], which solves the Navier-Stokes equations, the conservation equation for potential temperature, the Poisson equation and the subgrid-scale kinetic energy equation for meteorological parameters. This version of the LES includes an online gas-phase chemical mechanism (NCAR MOZART2.2 [*Horowitz et al.*, 2003]), as implemented and described by *Kim et al.* [2012]. This mechanism includes 52 reactants and 168 chemical reactions, and here we briefly describe the biogenic VOC and oxygenated VOC chemistry relevant to this study. MACR and MVK are the major primary OVOC products of isoprene (R1 and R2). MVK then reacts with OH (R3) to produce acetaldehyde (CH_3CHO; ACETALD), whereas MACR oxidation (R4) produces hydroxyacetone (CH_3COCH_2OH; HYAC), glycolaldehyde ($HOCH_2CHO$; GLYALD) and methylglyoxal (CH_3COCHO; MGLY). Under low NOx conditions, isoprene oxidation (R5-2) also yields hydroxyhydroperoxides ($HOCH_2COOHCH_3CHCH_2$; ISOPOOH). HCHO is formed from multiple oxidation pathways, including isoprene oxidation, MVK and MACR oxidation, and also oxidation of other secondary products, e.g., GLYALD and HYAC [*Kim et al.*, 2012], and can therefore be considered both a primary oxidation and secondary oxidation product. The chemical pathways of these oxidation steps as represented in the LES are listed in Figure 2.1. For the following discussion, we categorize the VOC into (1) primary emitted BVOC (isoprene), (2) primary oxidation products (MVK, MACR and ISOPOOH), (3) dual

oxidation products (HCHO) and (4) secondary oxidation products (other OVOC species, including HYAC, GLYALD, MGLY, and ACETALD).

The simulation domain is a grid with the dimensions 14.4 km × 14.4 km × 6.4 km (96 × 96 × 96 grid points resulting in horizontal grid spacing of 150 m and vertical grid spacing of 66.67 m). This resolution is coarser than that recommended by *Sullivan and Patton* [2011], however such a sacrifice is necessary in order to incorporate the complete MOZART2.2 mechanism. At the domain sides, periodic boundary conditions are provided in the horizontal direction with no-slip conditions at the surface, and surface stress is defined by Monin-Obukhov similarity theory as in *Kim et al.* [2012]. The aspect ratio Γ (defined as D/L, where L is the domain height and D is the horizontal width of the domain) is selected to be 2.25 to allow full turbulence development independent of the periodic sidewall boundary conditions, similar to Γ values in *Brown et al.* [2002], *Sullivan and Patton* [2011], and *van der Poel et al.* [2014].

The LES domain location is centered on the DISCOVER-AQ ground site in Fair Hill, Maryland (spatial scale of domain shown in Figure 2.2), as this is a rural site with relatively high biogenic emissions and located the greatest distance from large anthropogenic sources (e.g., Baltimore metropolitan area) among the DISCOVER-AQ ground sites. Diurnal photolysis rates are calculated with offline NCAR Tropospheric Ultraviolet and Visible (TUV) Radiation Model [*Madronich and Flocke*, 1999]. The cloud module in the LES model is included to simulate realistic cloud formation and induced convection in the cloud layer.

Three distinct weather conditions are simulated to understand the

complexity of boundary layer dynamics and VOC oxidation in the ABL. The evolution of the ABL varies under different meteorological conditions, which likely affects vertical transport of BVOC. Different weather conditions may also cause changes in surface emissions of chemical species and their reaction rates, further controlling ozone formation in the atmosphere. For example, with stronger turbulence development within the ABL, longer-lived OVOC may be transported higher, causing *in situ* ozone production at a higher altitude. Thus, we design our simulations to span clear weather conditions to convective environments to test these hypotheses on BVOC mixing and chemical reactivity.

The LES uses pseudospectral methods in the horizontal direction and a second-order finite difference method in the vertical direction for advection. A sharp wave-cutoff filter is utilized to define the resolvable-scale variables, and subgrid-scale transport is parameterized using the turbulence energy model described in *Deardorff* [1980]. Dynamics is solved using a third-order Runge-Kutta scheme with a specified Courant-Fredrichs-Lewy (CFL) number, presuming that the ABL is incompressible and Boussinesq [*Sullivan and Patton*, 2011]. The full simulation time for each case is 11.5 hours, starting at 0530 LT and ending at 1700 LT. The simulation starts at 0530LT with dynamics only and when turbulent flow is established and the boundary layer dynamics have been spun up, chemical emissions and processes are then initiated at 0830 LT [*Kim et al.*, 2012]. To understand the combined effects of boundary layer dynamics and chemistry, production and loss rates (defined as the change in mixing ratio over the change in time; ppbv s^{-1}), are calculated online in the LES for each chemical species, and the

net production of individual species are calculated using Euler Backward Iterative solver based on production and loss rates with time step of 1.5 s [*Barth et al.*, 2003]. A bottom-up inert tracer emitted from the surface to the atmosphere is also included to calculate ABL height, which is defined as the height where the horizontally-averaged mixing ratio of this scalar reaches 0.5% of its surface value [*Kim et al.*, 2012; *Vilà-Guerau de Arellano et al.*, 2005]. Passive tracers undergo the same transport processes as the reactive trace gases but do not undergo chemical transformations or dry deposition, offering a reference for chemistry versus transport processes within the ABL.

2.2.2. Observations

During the July 2011 DISCOVER-AQ campaign over the Baltimore-Washington metropolitan region, several flights by NASA P-3B aircraft were conducted with *in situ* measurements in and above the ABL (ranging from 0.3 – 5 km in height), offering more complete vertical profiles than previous observations measured by tethered balloon systems [*Andronache et al.*, 1994; *Velasco et al.*, 2008]. In addition to the flights, there were six surface measurement sites at Beltsville, Padonia, Fair Hill, Aldino, Edgewood and Essex (ranging from 75-77˚W and 38.5-40˚N; Figure 2.2). High-time resolution measurements on the P3-B include Proton-Transfer-Reaction Mass Spectrometer (PTR-MS) [*Lindinger and Jordan*, 1998] measurements of several important hydrocarbons (isoprene and monoterpenes) and a suite of oxygenated VOC (acetaldehyde, acetone, methanol, MVK+MACR+ISOPOOH) as well as HCHO from the Difference Frequency Generation Absorption Spectrometer (DFGAS) [*Weibring et al.*, 2007]. Experimental values of

MVK+MACR+ISOPOOH may be overestimated due to incomplete conversion of ISOPOOH into MVK+MACR in the inlet/instrument [*Rivera-Rios et al.*, 2014]. Surface measurements of sensible and latent heat fluxes were conducted at the Edgewood site, which is located close to Fair Hill and is the only surface location with micrometeorological measurements. Surface NO_X was measured using a TECO Trace Gas Analyzer by NASA Goddard Space Flight Center at the Fair Hill site during 16 - 31 July. Surface temperature in the Fair Hill site was measured using standard EPA-approved instruments by Maryland Department of the Environment. Observational data are available through NASA DISCOVER-AQ data and information table (DISCOVER-AQ DOI: 10.5067/Aircraft/DISCOVER-AQ/Aerosol-TraceGas).

2.2.3. Case study selection and model set-up

P-3B boundary layer spiral measurements were conducted on 13 days of the campaign. As shown in Figure 2.2, the simulation domain is located within the P-3B vertical spiral in Fair Hill. We use meteorological data from the Fair Hill ground site and DISCOVER-AQ station meteorological reports (http://discover-aq.larc.nasa.gov/planning-reports_BW2011.php) to determine weather conditions during the available observational time period, and categorize days into (a) fair weather conditions (1, 2, 10, 14 and 16 July), (b) convective events (11, 20 and 22 July) and (c) polluted events with temperatures greater than 30 ˚C (20 – 22, 26 – 29 July). Figure 2.3 shows the July daily average and maximum temperatures from the Fair Hill site, and we select three of these days for model simulations to reflect different weather conditions that will likely affect VOC mixing in the ABL. Case 1 (1 July) has clear sky with moderate temperatures (daily maximum of 26.7 ˚C) and

wind speed (daytime average approximately 2 m s^{-1}), Case 2 (11 July) has slightly higher temperatures (30.6 ˚C), higher wind speeds (daytime average approximately 3 m s^{-1}) and fair weather cumulus clouds with late afternoon thunderstorms, and Case 3 (29 July) has the highest daily temperature maximum (33.3 ˚C) and moderate wind speeds (daytime average approximately 2 m s^{-1}) with afternoon cumulus clouds. Thus, Case 2 and Case 3 both have strong convective activity aloft leading to non-precipitating clouds or shallow convection.

These three days are simulated as three separate case studies with the LES model. Meteorological boundary conditions are defined with tendencies calculated in the global 1.25°× 1.25° MERRA reanalysis [*Rienecker et al.*, 2011] for three-hourly time-averaged large-scale advective forcing and radiative tendencies. We select the MERRA grid cell covering the Fair Hill site and apply the averaged large-scale forcings for altitudes lower than 1 km, between 1 km and 2 km, and higher than 2 km (Table A1). For intermediate times when reanalysis data are not available, we linearly interpolate between time steps for each of the three heights. In Case 2, MERRA large-scale water vapor tendencies above 2 km enhance moisture in the domain after 0930 LT, yet the P-3B observations indicate a persistent dry layer in the afternoon. This difference may be caused by a resolution discrepancy, e.g., the MERRA reanalysis data grid cell covers the whole Baltimore-Washington metropolitan area and represents large-scale changes, while P-3B observations represent local and more accurate conditions at the Fair Hill site. Therefore, we substitute the MERRA data above 2 km with a zero water vapor tendency to provide

realistic simulation results, and vertically interpolate between 1-2 km as in *Brown et al.* [2002].

For initial meteorological conditions, we utilize a finer resolution MERRA product (0.5° × 0.67°) for the Fair Hill location at a six-hourly time resolution to define initial profiles of potential temperature and water vapor mixing ratio (note that tendencies were not available for this resolution product). To confirm these data with other observations, we compare the MERRA initial profiles linearly interpolated to 0530 LT with sounding data at 0800 LT at two locations (Wallops Island, VA (WAL: 37.93°N, 75.48°W) and Sterling, VA (IAD: 38.98°N, 77.46°W); data from http://weather.uwyo.edu/upperair/sounding.html) and P-3B observations (Figure A1) for each simulation case. Generally, the potential temperature profiles are similar between all three data types (MERRA, soundings, and P-3B) and the LES model reproduces these profiles. For water vapor, the model initial conditions generally reproduce a realistic meteorological environment and cloud formation (Figure A1). Surface sensible and latent heat fluxes are defined from surface hourly flux measurements at the Edgewood site (Figure 2.2) and interpolated to the model time step. Generally, observations of wind direction from individual P-3B spirals above the Fair Hill site show a nearly constant wind direction with height (0.3-5 km), with some variations in individual cases as described below. Wind speeds average about 10 m s^{-1} (not shown) and the initial horizontal wind (u, v) is set to (10, 0) m s^{-1} at all levels in the LES.

For the model chemistry, we provide initial chemical concentrations and surface emissions. Initial chemical concentrations for the ABL (below 1 km) and free

atmosphere (above 3 km) are based on averaged P-3B measurements above the Fair Hill site on the case study days (Table A2). CO (200 ppbv) and CH_4 (1.7 ppmv), both important sources of peroxy radicals, are assumed constant throughout the simulation with no vertical gradients and no emissions [*Kim et al.*, 2012]. The initial vertical profiles of other chemical species not measured by the P-3B and the deposition velocities are the same for the three cases and prescribed as in *Kim et al.* [2012], with the initial profiles of these chemical species initialized with a photochemical box model and integrated from midnight to 0830 LT. The photochemical box model (the Euler Backward Iterative method described in [*Barth et al.*, 2003]) has the same chemical mechanism as in the LES simulations and provides a computationally inexpensive way to study the near-surface chemistry in the absence of fluid motion.

Surface emissions of biogenic VOC (isoprene and monoterpenes) and anthropogenic NO are included in all simulations and assumed to be horizontally homogeneous over the model domain. Other anthropogenic emissions are not included. Emissions of biogenic isoprene are based on the local MEGAN isoprene emission factor at standard conditions at Fair Hill (3.146 mg m^{-2} hr^{-1}; Figure 2.2). The diurnal pattern of isoprene emission is scaled with the solar zenith angle reflecting a radiation influence as in *Kim et al.* [2012] and modified with the temperature emission activity factor according to the time-evolving temperature for each case [*Guenther et al.*, 2006] (Figure 2.5). The temperature activity factor is defined as

$$\boldsymbol{\gamma_T = E_{opt} \times \left[\frac{C_{T_2} \times e^{\left(C_{T_1} \times x\right)}}{C_{T_2} - C_{T_1} \times \left(1 - e^{\left(C_{T_2} \times x\right)}\right)} \right]}, \quad (1)$$

where $x = \left[\left(1/T_{opt}\right) - (1/T)\right]/0.00831$, T is temperature (K), and the empirical coefficients C_{T_1} (=95), C_{T_2} (=230). E_{opt} and T_{opt} are estimated using Eqs. (2) and (3).

$$\boldsymbol{T_{opt} = 313 + \left(0.6 \times (T_{240} - 297)\right)}, \quad (2)$$

$$\boldsymbol{E_{opt} = 2.034 \times e^{\left(0.05 * (T_{24} - 297)\right)} \times e^{\left(0.05 * (T_{240} - 297)\right)}}, \quad (3)$$

T_{24} and T_{240} are the average leaf temperatures over the past 24 hours and 240 hours [*Guenther et al.*, 2006] and we define these values for each case based on hourly air temperature at the Fair Hill site. Maximum isoprene emissions are 3.15 mg m^{-2} hr^{-1}, 4.11 mg m^{-2} hr^{-1}, and 5.53 mg m^{-2} hr^{-1} for Cases 1-3, respectively. The diurnal emission of monoterpenes for all the cases is held constant during the simulation period at a rate of 0.504 mg m^{-2} hr^{-1} (Figure 2.5), as these emissions have a weak dependence on temperature and no dependence on light. Anthropogenic NO emissions for all cases are scaled from the observed diurnal pattern of surface NO_X observed at the ground-based sites during the campaign (16 – 31 July) (Figure 2.5). Based on comparison with NO emissions from the 2011 National Emissions Inventory (http://www3.epa.gov/ttnchie1/net/2011inventory.html), this scaled NO emission from the DISCOVER-AQ observations provides a chemical environment similar to the observed condition for BVOC oxidation. In general, the three cases simulate distinct meteorological environments but similar NO_X conditions, with a maximum NOx emission of 1.80 mg m^{-2} hr^{-1} for all the cases.

2.2.4. Model analysis methods

We use instantaneous P-3B measurements from all points in space and time to evaluate the average model vertical profiles from the three simulations. While the actual time of each P-3B spiral varies depending on the flight patterns, the observed spirals typically occur from noon to early afternoon. Therefore for comparison with P-3B data, LES-derived vertical profiles are created by averaging over the entire horizontal model domain between 1100-1500 LT. To investigate the time-evolution of turbulent kinetic energy, vertical profiles of turbulent kinetic energy are created by horizontally-averaging the three velocity components at an instant in time, subtracting the mean, and summing the horizontally-averaged square of the velocity fluctuations. These are averaged at 2-hour intervals starting at 0900 LT to show the diurnal progression of convection within the ABL. To examine the cloud evolution, we define the cloud top at each time step as the vertical location of the maximum liquid water height across the domain, and define the cloud base at each time step as the minimum liquid water height across the domain. The cloud fraction is defined as the horizontal fraction of vertically-integrated liquid water. Together, these variables provide information about the variability in the ABL height.

The LES simulations are initialized by meteorological and chemical conditions derived from the observations, but there are several limitations to discuss with respect to measured-modeled comparisons. From the LES perspective, the initial or boundary meteorological conditions from MERRA is limited in both space (1.25°× 1.25° for large-scale tendencies and 0.5° × 0.67° for initial θ and q profiles) and time (3- or 6- hourly depending on the product with temporal

interpolation), and may not be representative of heterogeneities within the LES domain. In addition, discrepancies between simulations and observations could be affected by the lack of a detailed surface emission inventory of anthropogenic chemical species or land surface heterogeneity in the LES. From the perspective of P-3B sampling strategy, the spirals sample a single point at a time that could capture a plume from an upwind urban region or from a strong updraft with high chemical concentrations, which cannot be reproduced by the LES using homogeneous surface conditions. Despite these limitations, the evaluation of the physical and chemical processes in the LES allows us to investigate the scientific questions stated above while recognizing these sources of error.

2.3. Model evaluation with observations

We evaluate the LES simulations in this section versus data from the P3-B flights. In general, the LES simulations are idealized in that we do not represent heterogeneous surface emissions, spatial changes in the surface energy balance, or meteorologically-driven changes in chemical boundary conditions. As a result, the comparison of the model with observations is not meant to be an exact representation of the observed conditions, but to indicate that the model is able to reproduce the observed chemical regimes. Figure 2.6 compares P-3B observations and LES simulated potential temperature (θ; K) and water vapor mixing ratio (q_v; g kg^{-1}) for the three cases. LES simulated turbulent kinetic energy (TKE; m^2 s^{-2}) is shown at four different time periods binned in 2-hour increments (Figure 2.7) to

describe the turbulent environment, and we describe the meteorological (Figure 2.6 and Figure 2.7) and chemical conditions (Figure 2.8 and Figure 2.9) for each case.

2.3.1. Case 1: Clear-sky, cool summer day (1 July 2011)

During Case 1, there is relatively clean low-level northwesterly flow with a daytime maximum temperature of 26.7 ˚C and near-surface specific humidity of 7.98 g kg^{-1}, and strong surface heating dominated by the sensible heat flux (peaking at 220 W m^{-2}; Figure 2.4a). The vertical profile of θ implies a neutral lower layer below 1.5 km during 1100-1500 LT, with a sharp inversion above (Figure 2.6a). LES predicted θ is within 1 degree of P-3B observations in the ABL, and this discrepancy increases to about 2 degrees above the ABL top. Observed q_v is reproduced within 3 g kg^{-1}, with the greatest variability between 1.6 km and 3 km (Figure 2.6b). As the day progresses, the simulated TKE increases at the surface and throughout the boundary layer, reaching up to about 3.7 m^2 s^{-2} in the afternoon (Figure 2.7a). This enhanced mixing indicates the ABL evolution, with the ABL top reaching about 2.5 km in the late afternoon. On this clear-day case, no cloud formation is simulated by the LES in the Fair Hill site, which is consistent with the lack of clouds observed by radar (http://www2.mmm.ucar.edu/imagearchive/) or the Aqua satellite (http://www-air.larc.nasa.gov/cgi-bin/ArcView/discover-aq.dc-2011?SATELLITE=1; with afternoon overpass).

Observed NO and NO_2 show well-mixed profiles below the ABL (approximately 0.1 and 0.5 ppb, respectively, below 2 km) except for a few higher mixing ratios (up to 0.6 ppb for NO and 2 ppb for NO2) at 0.3 km, and non-zero values aloft indicating their transport above the ABL (Figure 2.8a, b). The LES

captures the vertical profiles of NO and NO_2, but with slightly higher values (biases of 0.04-0.08 ppbv for NO and 0.1-0.2 ppbv for NO_2) and larger gradients below 1 km. The bias between observed and simulated NO_x could be caused by the constant NO emissions implemented in the idealized case, which does not capture the spatial or temporal variability present in the NOx emissions [*Follette-Cook et al.*, 2015]. Observed ozone concentrations vary by ~30 ppbv within and above the boundary layer, with concentrations of about 65 ppbv within the ABL during 1100-1500 LT (Figure 2.8c). The LES simulates this overall profile, but produces higher ozone concentrations throughout the boundary layer (up to 78 ppbv), which could be induced by the overestimation of NO_x. The sharp decrease of observed ozone at 2.2-3 km is likely due to large-scale meteorological factors, and could be caused by a shift in wind direction at this time and day observed on the P-3B but not reproduced by the model. Both observed and modeled isoprene has a strong concentration gradient within the ABL, with higher concentrations near the surface that decrease above the ABL, attributed to strong surface emissions and a short chemical lifetime [*Karl et al.*, 2007] (Figure 2.9a). For the longer-lived VOC species, observed MVK+MACR+ISOPOOH and HCHO are well mixed within the ABL and decrease rapidly above the ABL top. The LES captures the vertical variations of isoprene and its oxidation products within 0.7 ppbv (Figure 2.9b, c).

2.3.2. Case 2: Moderately warm day with fair weather cumulus clouds (11 July 2011)

According to DISCOVER-AQ station meteorological reports (http://discover-aq.larc.nasa.gov/planning-reports_BW2011.php), Case 2 is dominated by

southwesterly flow around the west side of the Bermuda High. In contrast to Case 1, latent heating increases up to 150 W m^{-2} at midday, accompanied by 200 W m^{-2} of sensible heat (Figure 2.4b). The Aqua satellite image on this day shows moderate cumulus clouds (Figure 2.10a). In the simulation, the daily maximum temperature peaks at 30.6 ˚C and clouds develop at around 2 km at 1100 LT. Clouds continue to grow to 4 km by the end of the simulation (Figure 2.10b), with the highest cloud fraction (37%) at around 1130 LT (Figure 2.10c).

LES predicted θ in the subcloud layer (below 2 km) is within 2 degrees of observed values (Figure 2.6c). Within the cloud layer (approximately 2-4 km in the afternoon), there are larger discrepancies of both θ and q_v, with observed q_v about 4 g kg^{-1} drier than simulated (Figure 2.6d). The difference in q_v is likely the result of both the initial profile specified in the LES (which deviates from the P-3B observations due to heterogeneity of the region covered by P-3B spirals; not shown) and the drier tendencies applied above 2 km for a realistic cloud simulation. The increase of TKE above 1 km after 1100 LT occurs within the cloud layer, indicating the development of convection. As the afternoon progresses, this convective layer deepens (Figure 2.7b) accompanied by an increase in the cloud base and cloud top height (Figure 2.10b), while near-surface TKE is lower than that in Case 1. The TKE profiles suggest that vertical mixing occurs at higher altitudes than in Case 1 (about 3.8 km) (Figure 2.7b). The evolution of TKE and clouds in Case 2 indicate a 1 km increase in ABL height from the morning to the late afternoon.

Case 2 observed NO and NO_2 concentrations are slightly higher than Case 1, by about 0.1 and 0.2 ppbv respectively (Figure 2.8d, e), which may enhance OH and

HCHO concentrations. Compared with Case 1, isoprene concentrations are about 2 ppbv higher near the surface (~0.3 km, or the lowest observations) (Figure 2.9d). This may be in part due to higher temperatures in Case 2 (32.2˚C maximum temperature compared to 29.4 ˚C for Case 1) as well as the potential advective contribution from higher source regions, e.g., locations to the southwest of the Fair Hill flight path have higher emission factors in the MEGAN inventory (Figure 2.2). Under southwesterly winds, other chemical species are also likely transported from upwind urban areas, such as Baltimore or Washington, D.C. These relatively higher levels of precursors could contribute to the enhancement in observed O_3 compared to Case 1, with observed concentrations peaking at around 93 ppbv just below the cloud base (Figure 2.8f). The overall O_3 profile is reproduced by the LES although lacks the observed O_3 vertical variation, which is likely due to spatial heterogeneity in ozone formation and the spiral sampling strategy. The 3D P-3B spirals for each day (http://www-air.larc.nasa.gov/cgi-bin/ArcView/discover-aq.dc-2011?ANALYSIS=1; not shown) show O_3 hotspots in the horizontal dimension, mostly in the southwestern section of the LES model domain, which cannot be captured by LES simulations which use horizontally homogeneous surface emissions and fluxes. In addition, the variability in the observed O_3 vertical structure could be affected by large-scale meteorology and changes in wind direction. During this case at this time, the wind direction shifted from a SSW wind carrying polluted air from urban areas cities to a WSW wind with cleaner air. As noted above, the LES cannot capture these chemistry-meteorology interactions as we use constant chemical boundary conditions.

In case 2, the secondary VOC products are fairly well-mixed within the ABL (e.g., lower than ~1km) and decrease sharply within the cloud layer. Observed MVK+MACR+ISOPOOH and HCHO are about 3 times greater than Case 1 (Figure 2.9e, f), as reflected in the difference in the precursor isoprene (Figure 2.9d). MVK+MACR+ISOPOOH and HCHO are generally underestimated by LES by up to 0.5 ppbv and 2.7 ppbv. While the initial chemical concentrations are from P-3B measurements, simulated isoprene emissions may be too low to maintain the observed atmospheric concentrations for both isoprene and its first generation products MVK+MACR+ISOPOOH and HCHO.

2.3.3. Case 3: Hot, humid day with afternoon cumulus clouds (29 July 2011)

Case 3 simulates a very hot (daytime maximum temperature 33.3 ˚C) and humid day (daily averaged q_v 16.45 g kg^{-1}) with strong convection in the late afternoon. In contrast to Cases 1 and 2, latent heating dominates the daytime surface fluxes, reaching a daily maximum of 210 Wm^{-2} (Figure 2.4c). The Aqua satellite image in Case 3 shows enhanced regional cumulus cloud activity as compared to Case 2 (Figure 2.10d). LES predicted θ is within 3 degrees of P-3B observations (Figure 2.6e). For q_v, the LES captures the dry layer at around 2.5 km but does not capture the fine structure in the vertical profile (Figure 2.6f), which may be due to the lack of surface flux heterogeneity in the LES simulations. Like Case 2, simulated TKE builds throughout the day, and vertical profiles of TKE extend up to approximately 5 km, indicating cumulus congestus clouds aloft in the simulation (Figure 2.7c). Clouds begin forming in the simulation at about 1230 LT and continue developing throughout the afternoon, with increased cloud fraction

and the cloud top reaching 5 km at 1600 LT (Figure 2.10e, f). The simulated increases in the ABL height from the morning to the afternoon are similar to those sampled by the aircraft for the three cases.

In Case 3, observed NO and NO_2 reach a maximum of 0.8 ppbv and 3.6 ppbv, respectively, and are similar to concentrations in Cases 1 and 2 as we do not simulate changes in NOx emissions between cases. The LES overestimates NO and NO_2 by 0.1 ppbv and 0.4 ppbv near 0.3-1.5 km (Figure 2.8g, h). For ozone, observed concentrations throughout the ABL are around 70 ppbv and are fairly well mixed (Figure 2.8i). The LES overpredicts O_3 by up to 20 ppbv below 3.5 km during 1100-1500 LT, which could be induced by the overestimation of NO_x. The wind direction at all heights of each P-3B spiral was nearly constant during this case and as a result, we do not see large fluctuations in the observed O_3 vertical structure.

LES captures the vertical profile of isoprene with the exception of the high observed concentrations near the surface (1-2 ppbv greater than simulated values) (Figure 2.9g). For the oxygenated species, both model and observations exhibit large vertical gradients of MVK+MACR+ISOPOOH and HCHO from the surface to about 3 km (Figure 2.9h, i). For MVK+MACR+ISOPOOH, the model compares well with the observations, with a larger standard deviation below 0.7 km. However, the observations show high MVK+MACR+ISOPOOH concentrations around 0.3 km height (up to 3.6 ppbv). This is consistent with the observed elevated isoprene and most likely due to spatially heterogeneous isoprene emissions or local, instantaneous updrafts carrying high isoprene that are not captured in the model. For HCHO, observed concentrations are slightly higher than the simulated profiles

below 1 km (Figure 2.9i). Both modeled and observed HCHO decrease from about 5 ppbv at the surface to 1 ppbv at the top of the boundary layer in near-linear fashion, suggesting strong near-surface production via chemical evolution of VOC emissions.

2.4. Discussion

As shown above, the idealized LES simulates P-3B observations and these simulations can be used to analyze the detailed chemical and ABL processes under meteorological conditions similar to those observed. Here we discuss the relative timescales of turbulent mixing versus chemistry and how this affects the overall BVOC lifetime and total OH reactivity of BVOC (Section 4.1), the role of turbulence on VOC segregation (Section 4.2), and these impacts on the formation of ozone (Section 4.3).

2.4.1. BVOC chemistry versus ABL mixing time scales

To understand the relative importance of atmospheric chemistry and ABL turbulent mixing, we compare the chemical lifetimes (τ_{CH}) of BVOC with the boundary layer turnover time (τ_T) and calculate the turbulent Damköhler number. We define the turbulent Damköhler number (Da_t) as the ratio of τ_T to τ_{CH}:

$$Da_t = \frac{\tau_T}{\tau_{CH}}, \quad (4)$$

where Da_t <1 represents slow chemistry and Da_t >1 represents fast chemistry [*Schumann*, 1989]. Based on photochemical box model calculations using surface chemical conditions (Figure A3), OH oxidation of BVOC dominates all BVOC depletion processes during 1100-1300 LT. In the current LES configuration, we

calculate τ_{CH} according to the gas-phase chemical reaction rates with OH [*Kim et al.*, 2012]:

$$\boldsymbol{\tau_{CH,X_i}} = \frac{\mathbf{1}}{\boldsymbol{k_{OH+X_i}} \times [\boldsymbol{OH}]}, \quad (5)$$

where k_{OH+Xi} is the reaction rate coefficient (cm^3 $molecules^{-1}$ s^{-1}) for each reaction of species X_i with OH, and [OH] is the ambient concentration of OH (molecules cm^{-3}). The near surface (0.3 km), midday average (1100-1300 LT) τ_{CH} for isoprene, its primary oxidation products (MVK, MCAR, ISOPOOH), its secondary oxidation products (HYAC, GLYALD, MGLY, ACETALD), and the dual oxidation product (HCHO) for the three cases are listed in Table 2.1. Simulated temperature and [OH] used in these calculations are also included in Table 2.1. BVOC in Case 2 and Case 3 exhibit longer lifetimes than Case 1. Under different meteorological conditions in the three cases, temperature likely plays a role on k_{OH+Xi}. The relationship between k_{OH+Xi} and temperature varies in the chemical mechanism depending on the chemical species [*Kim et al.*, 2012]. For example, increasing temperature will enhance reaction barriers and reduce k_{OH+Xi} for the species in Table 2.1 [*Allodi et al.*, 2008; *Kleindienst et al.*, 1982], with the absence of a temperature influence on the reaction rate coefficient for HCHO ($k_{OH+HCHO}$), GLYALD ($k_{OH+GLYALD}$) and HYAC ($k_{OH+HYAC}$). Other mechanisms, e.g., initial conditions, emissions and atmospheric stability, could also influence τ_{CH} by controlling [OH] distributions.

The turbulence turnover time (τ_T) is calculated using the ratio of the ABL's characteristic length and velocity scales:

$$\boldsymbol{\tau_T} = \frac{\boldsymbol{z_i}}{\boldsymbol{w^*}}, \quad (6)$$

where z_i is the ABL height (m), and w* is the Deardorff convective velocity scale (m s^{-1}) calculated as:

$$\boldsymbol{w^*} = \left[\frac{\boldsymbol{g}\times(\boldsymbol{SH}+\boldsymbol{0.61}\times\boldsymbol{LH})\times\boldsymbol{z_i}}{\boldsymbol{\theta}\times\boldsymbol{\rho}\times\boldsymbol{c_p}}\right]^{\boldsymbol{1/3}}, \quad (7)$$

where g is the gravitational constant (9.8 m s^{-2}), SH is the surface sensible heat flux (m K s^{-1}), LH is the surface latent heat (m s^{-1} kg kg^{-1}), ρ is the air density (kg m^{-3}), and c_p is the air heat capacity (J kg^{-1} K^{-1}). τ_T varies throughout the day, ranging from around 9-18 min in the morning to 16-26 min in the afternoon as the ABL grows and responds to increased buoyancy forcing. τ_T is greatest in the late afternoon (1600-1700 LT) for Case 3, due to the the diminished total surface buoyancy forcing reducing w* (Figure 2.11) and consistent with the lower near-surface TKE in Case 3 (Figure 2.7c).

Da_t calculated based on the midday average (1100-1300 LT) τ_{CH} at 0.3 km and τ_T for the three cases (Table 2.2) reveals that Da_t for isoprene approaches 1 in all cases, indicating similar timescales for chemical reactivity and turbulent mixing. Da_t of MACR (0.3-0.4) is lower than isoprene but much larger than the other BVOC species. We therefore compare the diurnal variations of τ_{CH} of isoprene and MACR at 0.3 km with τ_T for the three cases (Figure 2.11) to examine the relationship between their OH chemistry and turbulence in detail. τ_{CH} for isoprene ($\tau_{CH,iso}$) at 0.3 km has a lifetime comparable to τ_T. Compared to τ_T, τ_{CH} is longer in the morning but decreases as the day progresses as [OH] increases at midday. These two time scales intersect roughly around noon, with some variations between the three cases. $\tau_{CH,iso}$ is the shortest in Case 1, starting at approximately 20 minutes at the beginning of

the simulation and decreasing to 10 minutes in the middle of the day. In Cases 2 and 3, increased $\tau_{CH,iso}$ induces a later cross-over point (1200 LT in Case 2; Figure 2.11b and 1300 LT in Case 3; Figure 2.11c); in these two cases, isoprene emissions are higher than Case 1 due to warmer temperatures and higher initial VOC concentrations, producing increased competition for OH. Isoprene oxidation products MACR and MVK have slightly longer τ_{CH} than isoprene, but both have timescales that are of similar order of magnitude to τ_T (less than 100 min; Table 2.1), indicating both turbulence and chemistry play an important role in their distribution. MACR has the shortest τ_{CH} ($\tau_{CH,MACR}$) among all the OVOC evaluated here, yet there is no cross-over point in Figure 2.11 between $\tau_{CH,MACR}$ and τ_T. Longer $\tau_{CH,MACR}$ compared to $\tau_{CH,iso}$ indicates MACR and OH are more well mixed than isoprene and OH. According to the contributions of different BVOC depletion processes (Figure A3), we note the photolysis pathways of HCHO and MGLY play a comparable role to OH oxidation. Therefore, we calculate their photolysis lifetimes (Table A3) and total lifetimes (photolysis + OH reaction) (Table 2.1). Compared with the lifetimes of HCHO and MGLY against OH in Table 2.1, the total lifetimes reduce 37-38% for HCHO and 37-40% for MGLY, which are closer to the turbulence turnover time scale, indicating turbulence may have a small effect of the OH reactivity of these two species.

To further understand whether longer $\tau_{CH,iso}$ and $\tau_{CH,MACR}$ in Cases 2 and 3 results from OH competition, OH reactivity of the BVOC species at 0.3 km, 1.5 km and 2.7 km during midday is calculated as:

$$\boldsymbol{R_{OH+X_i}} = \boldsymbol{k_{OH+X_i}} \times [\boldsymbol{X_i}], \quad (8)$$

$$\boldsymbol{R_{BVOC}} = \sum \boldsymbol{R_{OH+X_i}}\,, \tag{9}$$

where $[X_i]$ is the ambient concentration of BVOC species *i* (molecules cm^{-3}) and R_{OH} is the OH reactivity (s^{-1}). Total OH reactivity of BVOC (R_{BVOC}) is the sum of the OH reactivity for all the BVOC species in Table 2.1 and shown in Figure 2.12 for three altitudes: 0.3 km to represent the near-surface, and 1.5 km and 2.7 km to show the chemical environments around the cloud base and cloud top height at midday for Case 2. In all cases, R_{BVOC} decreases with altitude from the surface to 2.7 km, consistent with the general decreasing pattern of BVOC concentrations from the surface to higher altitudes (Figure 2.9). At 0.3 km, R_{BVOC} increases from 1.44 s^{-1} in Case 1 to 4.21 s^{-1} in Case 3, due to elevated BVOC concentrations in Cases 2 and 3 (Figure 2.12). Higher R_{BVOC} in Case 2 and Case 3 causes OH competition among the VOC in the ABL. In the chemical mechanism, OH is produced mainly from O_3 photolysis, followed by the reaction between HO_2 and NO. The main source of OH loss is through reactions with isoprene, followed by CO and other VOC species [*Kim et al.*, 2012]. Given the same NO emissions and CO concentrations implemented in the three cases, OH is influenced by different initial concentrations and isoprene emissions. In general, the initial concentrations of NO_X and O_3 are comparable in all the cases, while Cases 2 and 3 have 1.5 to 3.5 times higher initial concentrations of VOC, respectively. In addition, isoprene emissions are the highest in Case 3, followed by Case 2, indicating the dominating OH depletion effects of VOC. Together, OH competition due to higher VOC concentrations decreases OH mixing ratios (Figure 2.13a) and increases OH loss rates (Figure 2.13b) at 1100-1300 LT in the ABL, and when combined with the temperature impact on reaction rates, this drives longer

lifetimes in Case 2 and Case 3 (Figure 2.11).

Additionally, clouds play an important role in the vertical distribution of the chemical species through transport, modification of photolysis rates and reduction of light-dependent emissions [*Kim et al.*, 2012]. We note that the current simulations do not include cloud-induced modulation of photolysis rates and isoprene emissions. Entrainment and enhanced oxidation capacity induced by clouds can increase the ratio of oxidation products with respect to isoprene [*Karl et al.*, 2007]. In Case 2 at both 1.5 km and 2.7 km, higher OH reactivity is triggered by higher OVOC concentrations from earlier cloud-driven convective activity from 1100-1300 LT [*Kim et al.*, 2012; *Vilà-Guerau de Arellano et al.*, 2005], while cloud formation occurs later at these two altitudes in Case 3. Therefore, the influence of convection is primarily to move additional OVOC higher in the atmosphere, increasing the oxidative capacity at higher altitudes.

Individual BVOC contributions to R_{BVOC} are shown in Figure 2.12. Vertically, from 0.3 km (Figure 2.12a, d, g) to 1.5 km (Figure 2.12b, e, h) and 2.7 km (Figure 2.12c, f, i), the R_{OH} contribution of isoprene (primary emission) ($R_{OH+Isoprene}$) decreases sharply due to near-surface chemical depletion, contributing about 25-30% at the surface to 0.5-2.5% at 2.7 km. Primary oxidation products MVK and MACR have longer chemical lifetimes than isoprene with lower near-surface contributions to total R_{OH} but similar decreasing contributions from the surface to aloft. The relatively long lifetime (> 150 min) of ISOPOOH leads to little concentration variation with altitude and increased contributions to total R_{OH} aloft. In contrast, the secondary oxidation products (ACETALD, GLYALD, MGLY and HYAC)

and HCHO show increased contributions to R_{OH} from 0.3 km to higher altitudes. For example, the increase in the ACETALD contribution can be attributed to its production from primary oxidation products and its longer lifetime. As such, these OVOC species can be interpreted as extending the influence of the highly reactive primary VOC to regions aloft, far from the primary surface source. Increased contributions to R_{OH} from OVOC are also simulated from Case 1 to Case 3, consistent with the dominating convective effects over chemical consumption.

In Cases 2 and 3, there are larger vertical variations in the R_{OH} contributions than in Case 1. For example, the decreased percentages of primary and early oxidation chain species (e.g., $R_{OH+Isoprene}$, R_{OH+MVK} and $R_{OH+MACR}$) and the increased percentages of later oxidation chain species (e.g., $R_{OH+HCHO}$ and $R_{OH+ACETALD}$) from 0.3 km to 1.5 km are larger in Case 2 and Case 3 than Case 1. Case 1 has larger near-surface TKE (maximum of 2.2 $m^2 s^{-2}$) below 1.5 km during 1100-1500 LT than Case 2 (maximum of 1.8 $m^2 s^{-2}$) and Case 3 (maximum of 1.5 $m^2 s^{-2}$), inducing a weaker transition of R_{OH} contributions from near surface to 1.5 km. In contrast, clouds increase convection aloft in Case 2 and Case 3 leading to a stronger mixing and mild gradient in R_{OH} (Figure 2.7). The similar distributions of R_{OH} contributions for oxidation products at 1.5 km and 2.7 km indicate their comparable reaction rates with OH reaching near steady state.

2.4.2. Segregation of BVOC chemistry

A metric to further understand how boundary layer turbulence affects BVOC chemistry is the intensity of segregation (I_s) between OH and a BVOC species. We analyze segregation for isoprene (primary emission; $Da_t \sim 1$) and MACR (primary

oxidation product; Da_t ~0.35) for the three cases. I_s, described as the decreased reaction rate induced by incomplete mixing, is calculated as:

$$I_s = \frac{\overline{VOC_i' \; OH'}}{\overline{VOC_i}\;\overline{OH}}, \tag{10}$$

where $\overline{\mathrm{VOC}_i'\mathrm{OH}'}$ is the horizontally-averaged covariance between VOC species i and OH, and $\overline{\mathrm{VOC}_i}$ and $\overline{\mathrm{OH}}$ are horizontally-averaged VOC and OH concentrations, respectively, while the $'$ in the numerator indicates deviation from the horizontal average [*Karl et al.*, 2007; *Schumann*, 1989; *Sykes et al.*, 1994]. I_s = 0 represents well-mixed conditions and implies zero covariance between the two species. Negative I_s indicates a decreased reaction rate due to segregation of the chemical species, with the limiting value I_s = -1 indicating the two species are completely segregated, while a positive I_s represents an increased reaction rate due to similar covariance between the two reactants [*Molemaker and Vilà-Guerau de Arellano*, 1998; *Patton et al.*, 2001; *Sykes et al.*, 1994].

We calculate I_s for isoprene and OH below 1 km (Figure 2.14a-c), as the BVOC reactivity is greatest near the isoprene emission source.. Enhanced segregation is observed for each case between noon and early afternoon, peaking at 1400 LT at 0.3 km altitude. Segregation increases slightly for Case 2 (about -0.01 more than Case 1) with the largest segregation (-0.08) in Case 3. Therefore, Case 3 shows the strongest turbulence-induced reduction of the isoprene-OH reaction rate. Focusing on the strong segregation regime of isoprene and OH (below 0.5 km), midday-averaged I_s (1100-1500 LT) of MACR and OH is compared with I_s of isoprene and OH for the three cases (Figure 2.14d-f), as the Da_t of MACR-OH could also lead to

segregation [*Patton et al.*, 2001]. I_s of MACR and OH is about a factor of 10 times weaker than isoprene and OH in all the cases, but with a similar vertical profile shape. Increased segregation of MACR and OH in Case 2 and Case 3 follows the variation of isoprene under different meteorological conditions. Despite the increase in isoprene and MACR segregation near the surface, R_{BVOC} increases due to the additional reactions of OVOC with OH as shown in Section 4.1. This suggests that other VOC can compensate for the segregation-induced reduction in oxidation and maintain the oxidative capacity of the ABL.

These results can be further understood by evaluating isoprene, MACR and OH vertical flux profiles in the strong segregation regime of isoprene and OH (below 0.5 km; Figure 2.14g-i). Fluxes are calculated as the horizontal average of the covariance between vertical velocity *w* and the individual species concentration (i.e. $w'VOC_i'$). Segregation is typically associated with organized motions in the ABL turbulence. The isoprene flux is positive (away from the surface) due to its strong surface source and the MACR flux is slightly positive yet has a near negligible signal. As isoprene oxidation is occurring at all heights within the near-surface layer, this creates a weak MACR gradient that does not enable a strong flux away from the surface. OH fluxes are negative (or towards the surface), indicating transport downwards due to formation of OH at higher altitudes within the ABL and destruction of OH via near-surface chemistry. Therefore, the lower boundary layer (<1 km) segregation for isoprene and OH is due to the fact that the downwelling motions in this region contain the majority of the OH, while isoprene emissions are largely transported upwards from the surface containing relatively low OH

concentrations. These motions in the lower boundary layer are shown with instantaneous vertical cross sections through the center of the domain of OH and isoprene (Figure A2). The segregation values for isoprene-OH of < 10% below the convective cloud layer under homogeneous surface forcings and emissions is comparable with the other studies over temperate forests [*Dlugi et al.*, 2010; *Ouwersloot et al.*, 2011].

In addition to the near-surface, we find large positive I_s of isoprene and OH near the top of the ABL (not shown), indicating isoprene and OH are transported together to the free troposphere with initially very low concentrations. As shown in Figure A2, the transport motions of isoprene and OH are consistent with convection near the top of the ABL, with the hot spots of the vertical velocity *w* in Cases 2 and 3 also indicating cloud formation. This positive correlation is consistent with the results in *Ouwersloot et al.* [2011]. While we do not have the appropriate data to determine segregation from the P3-B observations, this result suggests that subcloud segregation may decrease the reactivity of highly reactive VOC (e.g., with lifetimes equivalent of less than isoprene) by as much as 10 %.

To quantify the influence of turbulence on lifetimes of isoprene and MACR, their effective τ_{CH} (τ_{eCH}) can be re-calculated using the gas-phase chemical reaction rates with OH modified by segregation [*Patton et al.*, 2001]:

$$\boldsymbol{\tau_{eCH,X_i}} = \frac{\mathbf{1}}{\boldsymbol{k_{OH+X_i}}\times(\mathbf{1}+\boldsymbol{I_{s,OH+X_i}})\times[\boldsymbol{OH}]}, \tag{11}$$

where $I_{s,OH+X_i}$ is the segregation intensity between OH and X_i. τ_{eCH} of isoprene and MACR for the three cases are listed in Table 2.3, which are also calculated during

midday (1100-1300 LT) at 0.3 km to compare with their original lifetimes in Table 2.1. Lifetimes of isoprene and MACR both increase due to segregation, with larger lifetime variations in isoprene.

2.4.3. Vertical distribution of ozone production/loss

Here, we assess the effect of turbulence on BVOC oxidation to ozone production, formation and loss. Simulated and observed ozone concentrations are 60-80 ppbv up to approximately the top of the domain, with discrepancies likely due to those in differences in measured and modeled NO_X and VOC (Figure 2.8 and Figure 2.9). In each case at 1500-1700 LT, production and loss rates are approximately two times higher than at 1100-1300 LT at 1-2.5 km (Figure 2.15), consistent with a stronger convective environment and increased photo-oxidation producing more O_3 from OVOC precursors in the afternoon. Near-surface net ozone production in Case 2 is higher than Case 1, providing support to the hypothesis that higher observed ozone concentrations in Case 2 are in part due to transport of precursors from upwind polluted cities under southwesterly winds. Case 3 has the largest simulated near-surface net production rate (reaching up to 0.005 ppbv s^{-1}) at 1100-1300 LT. Ozone production and loss occurs up to 3 km in Case 1, 4.5 km in Case 2, and 3.6 km in Case 3, similar to the maximum heights reached by TKE evolution (Figure 2.7). Stronger TKE in Case 2 and Case 3 transports ozone precursors into the convective cloud layer (Figure 2.8 and Figure 2.9), indicating *in situ* ozone production, mostly occurring within the clouds, due to convectively transported precursors in the model (Figure 2.15). This *in situ* ozone production is an important supplement to other potential sources of ABL ozone at higher altitudes,

e.g., downward mixing of ozone from the free troposphere, and long-range advection of ozone and its precursors. Enhanced ozone production rates at 0.3 km, 1.5 km and 2.7 km during 1100-1300 LT in Case 2 and Case 3 are all consistent with the increased R_{OH} contributions described in Section 4.1, with transported OVOC species dominating at the two high altitudes.

2.5. Conclusions

We evaluate the role of boundary layer dynamics on the atmospheric chemistry of BVOC during the DISCOVER-AQ 2011 campaign using a LES-chemistry model with well-defined turbulence. Because these eddies are highly resolved on a scale that may be relevant for fast BVOC chemistry, the LES simulations capture this relationship more accurately than coarser resolution models without coupling between turbulence and chemistry. Data analysis of the DISCOVER-AQ flights and ground-based observations provides the basis for modeling simulations. We select three cases during the campaign representing realistic meteorological conditions in the boundary layer ranging from a cool, clear sky day to a hot, humid day with cumulus clouds. With moderate resolution in the LES model, simulated meteorological environments, including potential temperature and water vapor mixing ratio of each cases, reproduce P-3B observations in all the simulated cases. Generally, simulated concentrations of the chemical species compare well with P-3B observations.

Consistent with other studies, we find that the chemical lifetime of highly reactive primary emissions such as isoprene are on the same scale of the boundary

layer turnover time, suggesting that accurate knowledge of ABL mixing is essential for understanding the oxidation of isoprene. By evaluating BVOC segregation, we find clear diurnal and vertical variations of segregation for isoprene and OH that peak at a 10% rate reduction around 1400 local time at 0.3 km under warm and convective environments. For the next most reactive BVOC product, MACR, the segregation is about ten times lower than isoprene, suggesting that reactant segregation itself is not significant for most OVOC in the ABL.

While turbulence does not directly affect OVOC reaction rates, turbulent mixing affects the OVOC species in ways that alter the overall oxidative capacity of the ABL. When temperature and convection increase, we simulate longer lifetimes for the representative BVOC species in the ABL resulting from a competition for OH radicals. The effect of more vigorous turbulence on chemistry is analyzed with OH reactivity at three heights (0.3 km, 1.5 km and 2.7 km) and the production and loss of ozone. Larger vertical variations in the OH reactivity contributions in Case 2 and Case 3 are consistent with the convective environments represented by the evolution of TKE. Cases 2 and 3 have higher temperatures, more water vapor, and cumulus clouds that increase transport of OVOC aloft, explaining the higher OH reactivity in these cases at 1.5 km and 2.7 km altitudes. Overall, this mixes more OVOC into the upper PBL and allows its reaction with OH, thereby increasing the oxidative capacity of the PBL. The production and loss rates of ozone follow TKE evolution, suggesting that transport of ozone precursors and *in situ* ozone production yield active ozone production and loss processes aloft under warm and convective environments (e.g., Cases 2 and 3). Consistent with the simulated

increase in BVOC lifetimes, higher concentrations of BVOC that typically occur under warmer, convective meteorological conditions lead to an increase in the total OH reactivity and an increase in OVOC contributions to the OH reactivity and ozone production aloft.

Acknowledgments

This research is supported by NASA Earth and Space Science Fellowship (NESSF) NNX13AN76H. The National Center for Atmospheric Research is sponsored by the National Science Foundation. We gratefully acknowledge Kenneth Davis, Chin-Hoh Moeng, and Peter Sullivan for initiation of the study and the development of the NCAR LES model. DISCOVER-AQ 2011 campaign data are obtained through DISCOVER-AQ DOI: 10.5067/Aircraft/DISCOVER-AQ/Aerosol-TraceGas. The PTR-MS measurements aboard the NASA P-3B were supported by the Austrian Federal Ministry for Transport, Innovation and Technology (bmvit) through the Austrian Space Applications Programme (ASAP) of the Austrian Research Promotion Agency (FFG). Tomas Mikoviny was supported by an appointment to the NASA Postdoctoral Program at the Langley Research Center, administered by Oak Ridge Associated Universities through a contract with NASA. We gratefully acknowledge Si-Chee Tsay (NASA Goddard Space Flight Center) for providing NO_X measurements, and Edwin Gluth (Maryland Department of the Environment) for providing Surface temperature in the Fair Hill site. MERRA IC/BC data are obtained through the Modeling and Assimilation Data and Information Services Center (MDISC) (http://disc.sci.gsfc.nasa.gov/daac-bin/DataHoldings.pl). For data from model runs in this paper, please contact Yang Li (University of Michigan; yanglibj@umich.edu).

This manuscript was published on *Journal of Geophysical Research: Atmospheres,* and is currently under review. We acknowledge the co-authors, Mary C. Barth, Gao Chen, Edward G. Patton, Si-Wan Kim, Armin Wisthaler, Tomas Mikoviny, Alan Fried, Richard Clark and Allison L. Steiner, for providing guidance on this work.

2.6. References

Allodi, M. A., K. N. Kirschner, and G. C. Shields (2008), Thermodynamics of the hydroxyl radical addition to isoprene, *The Journal of Physical Chemistry A*, *112*(30), 7064-7071.

Andronache, C., W. L. Chameides, M. O. Rodgers, J. Martinez, P. Zimmerman, and J. Greenberg (1994), Vertical distribution of isoprene in the lower boundary layer of the rural and urban southern United States, *Journal of Geophysical Research: Atmospheres*, *99*(D8), 16989-16999, doi:10.1029/94JD01027.

Apel, E. C., et al. (2002), Measurement and interpretation of isoprene fluxes and isoprene, methacrolein, and methyl vinyl ketone mixing ratios at the PROPHET site during the 1998 Intensive, *Journal of Geophysical Research: Atmospheres*, *107*(D3), ACH 7-1-ACH 7-15, doi:10.1029/2000JD000225.

Atkinson, R. (2000), Atmospheric chemistry of VOCs and NOx, *Atmos Environ*, *34*(12–14), 2063-2101, doi:http://dx.doi.org/10.1016/S1352-2310(99)00460-4.

Baek, J., Y. Hu, M. T. Odman, and A. G. Russell (2011), Modeling secondary organic aerosol in CMAQ using multigenerational oxidation of semi-volatile organic compounds, *Journal of Geophysical Research: Atmospheres*, *116*(D22), n/a-n/a, doi:10.1029/2011JD015911.

Barth, M., S. Sillman, R. Hudman, M. Jacobson, C. H. Kim, A. Monod, and J. Liang (2003), Summary of the cloud chemistry modeling intercomparison: Photochemical box model simulation, *Journal of Geophysical Research: Atmospheres*, *108*(D7).

Barth, M. C., S. Sillman, R. Hudman, M. Z. Jacobson, C. H. Kim, A. Monod, and J. Liang (2003), Summary of the cloud chemistry modeling intercomparison: Photochemical box model simulation, *Journal of Geophysical Research: Atmospheres*, *108*(D7), n/a-n/a, doi:10.1029/2002JD002673.

Betterton, E. A. (1991), The partitioning of ketones between the gas and aqueous phases, *Atmospheric Environment. Part A. General Topics*, *25*(8), 1473-1477.

Blando, J. D., and B. J. Turpin (2000), Secondary organic aerosol formation in cloud and fog droplets: a literature evaluation of plausibility, *Atmos Environ*, *34*(10), 1623-1632, doi:10.1016/S1352-2310(99)00392-1.

Bloss, W. J., M. J. Evans, J. D. Lee, R. Sommariva, D. E. Heard, and M. J. Pilling (2005), The oxidative capacity of the troposphere: Coupling of field measurements of OH and a global chemistry transport model, *Faraday Discussions*, *130*, 425-436.

Bon, D. M., D. M. Bon, I. M. Ulbrich, J. A. De Gouw, and C. Warneke (2011), Measurements of volatile organic compounds at a suburban ground site (T1) in Mexico City during the MILAGRO 2006 campaign: Measurement comparison, emission ratios, and source attribution, *Atmospheric chemistry and physics*, *11*(6), 2399-2421.

Borrego, C., and S. Incecik (2012), *Air Pollution Modeling and Its Application XVI*, Springer US.

Brown, A. R., et al. (2002), Large-eddy simulation of the diurnal cycle of shallow cumulus convection over land, *Quarterly Journal of the Royal Meteorological Society*, *128*(582), 1075-1093, doi:10.1256/003590002320373210.

Butler, T. M., D. Taraborrelli, C. Brühl, H. Fischer, H. Harder, M. Martinez, J. Williams, M. G. Lawrence, and J. Lelieveld (2008), Improved simulation of isoprene oxidation chemistry with the ECHAM5/MESSy chemistry-climate model: lessons from the GABRIEL airborne field campaign, *Atmos. Chem. Phys.*, *8*(16), 4529-4546, doi:10.5194/acp-8-4529-2008.

Carlton, A. G., P. V. Bhave, S. L. Napelenok, E. O. Edney, G. Sarwar, R. W. Pinder, G. A. Pouliot, and M. Houyoux (2010), Model Representation of Secondary Organic Aerosol in CMAQv4.7, *Environmental Science & Technology*, *44*(22), 8553-8560, doi:10.1021/es100636q.

Carter, W. P. (2007), *Development of the SAPRC-07 chemical mechanism and updated ozone reactivity scales*, Citeseer.

Chapman, E. G., W. Gustafson Jr, R. C. Easter, J. C. Barnard, S. J. Ghan, M. S. Pekour, and J. D. Fast (2009), Coupling aerosol-cloud-radiative processes in the WRF-Chem model: Investigating the radiative impact of elevated point sources, *Atmospheric Chemistry and Physics*, *9*(3), 945-964.

Chen, J., R. Griffin, A. Grini, and P. Tulet (2007), Modeling secondary organic aerosol formation through cloud processing of organic compounds, *Atmospheric Chemistry and Physics*, *7*(20), 5343-5355.

Deardorff, J. (1980), Stratocumulus-capped mixed layers derived from a three-dimensional model, *Boundary-Layer Meteorol*, *18*(4), 495-527, doi:10.1007/BF00119502.

Dlugi, R., et al. (2010), Turbulent exchange and segregation of HOx radicals and volatile organic compounds above a deciduous forest, *Atmos. Chem. Phys.*, *10*(13), 6215-6235, doi:10.5194/acp-10-6215-2010.

Donahue, N., A. Robinson, C. Stanier, and S. Pandis (2006), Coupled partitioning, dilution, and chemical aging of semivolatile organics, *Environmental Science & Technology*, *40*(8), 2635-2643.

Ervens, B., B. J. Turpin, and R. J. Weber (2011), Secondary organic aerosol formation in cloud droplets and aqueous particles (aqSOA): a review of laboratory, field and model studies, *Atmos. Chem. Phys.*, *11*(21), 11069-11102, doi:10.5194/acp-11-11069-2011.

Follette-Cook, M. B., K. E. Pickering, J. H. Crawford, B. N. Duncan, C. P. Loughner, G. S. Diskin, A. Fried, and A. J. Weinheimer (2015), Spatial and temporal variability of

trace gas columns derived from WRF/Chem regional model output: Planning for geostationary observations of atmospheric composition, *Atmos Environ*, *118*, 28-44.
Forkel, R., O. Klemm, M. Graus, B. Rappenglück, W. R. Stockwell, W. Grabmer, A. Held, A. Hansel, and R. Steinbrecher (2006), Trace gas exchange and gas phase chemistry in a Norway spruce forest: A study with a coupled 1-dimensional canopy atmospheric chemistry emission model, *Atmos Environ*, *40, Supplement 1*(0), 28-42, doi:http://dx.doi.org/10.1016/j.atmosenv.2005.11.070.
Fu, T. M., D. J. Jacob, F. Wittrock, J. P. Burrows, M. Vrekoussis, and D. K. Henze (2008), Global budgets of atmospheric glyoxal and methylglyoxal, and implications for formation of secondary organic aerosols, *Journal of geophysical research: atmospheres*, *113*(D15).
Fuchs, H., A. Hofzumahaus, F. Rohrer, B. Bohn, T. Brauers, H. Dorn, R. Häseler, F. Holland, M. Kaminski, and X. Li (2013), Experimental evidence for efficient hydroxyl radical regeneration in isoprene oxidation, *Nature Geoscience*, *6*(12), 1023-1026.
Fuentes, J. D., L. Gu, M. Lerdau, R. Atkinson, D. Baldocchi, J. Bottenheim, P. Ciccioli, B. Lamb, C. Geron, and A. Guenther (2000), Biogenic hydrocarbons in the atmospheric boundary layer: a review, *Bulletin of the American Meteorological Society*, *81*(7), 1537-1575.
Gianotti, R. L., D. Zhang, and E. A. B. Eltahir (2011), Assessment of the Regional Climate Model Version 3 over the Maritime Continent Using Different Cumulus Parameterization and Land Surface Schemes, *Journal of Climate*, *25*(2), 638-656, doi:10.1175/JCLI-D-11-00025.1.
Goldstein, A. H., and I. E. Galbally (2007), Known and Unexplored Organic Constituents in the Earth's Atmosphere, *Environmental Science & Technology*, *41*(5), 1514-1521, doi:10.1021/es072476p.
Grell, G. A., S. E. Peckham, R. Schmitz, S. A. McKeen, G. Frost, W. C. Skamarock, and B. Eder (2005), Fully coupled "online" chemistry within the WRF model, *Atmos Environ*, *39*(37), 6957-6975, doi:http://dx.doi.org/10.1016/j.atmosenv.2005.04.027.
Guenther, A., C. Geron, T. Pierce, B. Lamb, P. Harley, and R. Fall (2000), Natural emissions of non-methane volatile organic compounds, carbon monoxide, and oxides of nitrogen from North America, *Atmos Environ*, *34*(12–14), 2205-2230, doi:http://dx.doi.org/10.1016/S1352-2310(99)00465-3.
Guenther, A., et al. (1995), A global model of natural volatile organic compound emissions, *Journal of Geophysical Research: Atmospheres*, *100*(D5), 8873-8892, doi:10.1029/94JD02950.
Guenther, A., T. Karl, P. Harley, C. Wiedinmyer, P. I. Palmer, and C. Geron (2006), Estimates of global terrestrial isoprene emissions using MEGAN (Model of Emissions of Gases and Aerosols from Nature), *Atmos. Chem. Phys.*, *6*(11), 3181-3210, doi:10.5194/acp-6-3181-2006.
Hatfield, M. L., and K. E. Huff Hartz (2011), Secondary organic aerosol from biogenic volatile organic compound mixtures, *Atmos Environ*, *45*(13), 2211-2219, doi:http://dx.doi.org/10.1016/j.atmosenv.2011.01.065.

Hodzic, A., B. Aumont, C. Knote, J. Lee‐Taylor, S. Madronich, and G. Tyndall (2014), Volatility dependence of Henry's law constants of condensable organics: Application to estimate depositional loss of secondary organic aerosols, *Geophysical Research Letters*, *41*(13), 4795-4804.

Hong, S.-Y., Y. Noh, and J. Dudhia (2006), A new vertical diffusion package with an explicit treatment of entrainment processes, *Monthly Weather Review*, *134*(9), 2318-2341.

Horowitz, L. W., et al. (2003), A global simulation of tropospheric ozone and related tracers: Description and evaluation of MOZART, version 2, *Journal of Geophysical Research: Atmospheres*, *108*(D24), 4784, doi:10.1029/2002JD002853.

Janjić, Z. I. (1994), The step-mountain eta coordinate model: Further developments of the convection, viscous sublayer, and turbulence closure schemes, *Monthly Weather Review*, *122*(5), 927-945.

Kain, J. S., and J. M. Fritsch (1990), A one-dimensional entraining/detraining plume model and its application in convective parameterization, *Journal of the Atmospheric Sciences*, *47*(23), 2784-2802.

Karl, T., A. Guenther, A. Turnipseed, G. Tyndall, P. Artaxo, and S. Martin (2009), Rapid formation of isoprene photo-oxidation products observed in Amazonia, *Atmospheric Chemistry and Physics*, *9*(20), 7753-7767.

Karl, T., A. Guenther, R. J. Yokelson, J. Greenberg, M. Potosnak, D. R. Blake, and P. Artaxo (2007), The tropical forest and fire emissions experiment: Emission, chemistry, and transport of biogenic volatile organic compounds in the lower atmosphere over Amazonia, *Journal of Geophysical Research: Atmospheres (1984–2012)*, *112*(D18).

Kaser, L., et al. (2015), Chemistry – turbulence interactions and mesoscale variability influence the cleansing efficiency of the atmosphere, *Geophysical Research Letters*, n/a-n/a, doi:10.1002/2015GL066641.

Kesselmeier, J., and M. Staudt (1999), Biogenic Volatile Organic Compounds (VOC): An Overview on Emission, Physiology and Ecology, *J Atmos Chem*, *33*(1), 23-88, doi:10.1023/a:1006127516791.

Kim, S. W., M. C. Barth, and M. Trainer (2012), Influence of fair-weather cumulus clouds on isoprene chemistry, *Journal of Geophysical Research. Atmospheres*, *117*(1), doi:http://dx.doi.org/10.1029/2011JD017099.

Kleindienst, T. E., G. W. Harris, and J. N. Pitts (1982), Rates and temperature dependences of the reaction of hydroxyl radical with isoprene, its oxidation products, and selected terpenes, *Environmental Science & Technology*, *16*(12), 844-846, doi:10.1021/es00106a004.

Knote, C., et al. (2014), Simulation of semi-explicit mechanisms of SOA formation from glyoxal in aerosol in a 3-D model, *Atmos. Chem. Phys.*, *14*(12), 6213-6239, doi:10.5194/acp-14-6213-2014.

Koßmann, M., H. Vogel, B. Vogel, R. Vögtlin, U. Corsmeier, F. Fiedler, O. Klemm, and H. Schlager (1996), The composition and vertical distribution of volatile organic compounds in southwestern Germany, eastern France and northern Switzerland during the TRACT campaign in September 1992, *Physics and Chemistry of the Earth*, *21*(5–6), 429-433, doi:http://dx.doi.org/10.1016/S0079-1946(97)81137-8.

Krol, M. C., M. J. Molemaker, and J. V. G. de Arellano (2000), Effects of turbulence and heterogeneous emissions on photochemically active species in the convective boundary layer, *Journal of Geophysical Research: Atmospheres*, *105*(D5), 6871-6884, doi:10.1029/1999JD900958.

Lei, W., M. Zavala, B. De Foy, and R. Volkamer (2009), Impact of primary formaldehyde on air pollution in the Mexico City Metropolitan Area, *Atmospheric chemistry and physics*, *9*(7), 2607-2618.

Lelieveld, J., et al. (2008), Atmospheric oxidation capacity sustained by a tropical forest, *Nature*, *452*(7188), 737-740, doi:http://www.nature.com/nature/journal/v452/n7188/suppinfo/nature06870_S1.html.

Lelieveld, J., and P. Crutzen (1991), The role of clouds in tropospheric photochemistry, *J Atmos Chem*, *12*(3), 229-267.

Lelieveld, J., and P. J. Crutzen (1990), Influences of cloud photochemical processes on tropospheric ozone, *Nature*, *343*(6255), 227-233.

Li, Y., M. C. Barth, G. Chen, E. G. Patton, S. W. Kim, A. Wisthaler, T. Mikoviny, A. Fried, R. Clark, and A. L. Steiner (2016), Large‐eddy simulation of biogenic VOC chemistry during the DISCOVER‐AQ 2011 campaign, *Journal of Geophysical Research: Atmospheres*, *121*(13), 8083-8105.

Li, Y., M. Shao, S. Lu, C.-C. Chang, and P. K. Dasgupta (2010), Variations and sources of ambient formaldehyde for the 2008 Beijing Olympic games, *Atmos Environ*, *44*(21–22), 2632-2639, doi:http://dx.doi.org/10.1016/j.atmosenv.2010.03.045.

Lindinger, W., and A. Jordan (1998), Proton-transfer-reaction mass spectrometry (PTR-MS): on-line monitoring of volatile organic compounds at pptv levels, *Chemical Society Reviews*, *27*(5), 347-375, doi:10.1039/A827347Z.

Loughner, C. P., D. J. Allen, K. E. Pickering, D.-L. Zhang, Y.-X. Shou, and R. R. Dickerson (2011), Impact of fair-weather cumulus clouds and the Chesapeake Bay breeze on pollutant transport and transformation, *Atmos Environ*, *45*(24), 4060-4072.

Loughner, C. P., et al. (2014), Impact of Bay-Breeze Circulations on Surface Air Quality and Boundary Layer Export, *Journal of Applied Meteorology and Climatology*, *53*(7), 1697-1713, doi:10.1175/JAMC-D-13-0323.1.

Madronich, S., and S. Flocke (1999), The Role of Solar Radiation in Atmospheric Chemistry, in *Environmental Photochemistry*, edited by P. Boule, pp. 1-26, Springer Berlin Heidelberg, doi:10.1007/978-3-540-69044-3_1.

Mao, J., et al. (2009), Airborne measurement of OH reactivity during INTEX-B, *Atmos. Chem. Phys.*, *9*(1), 163-173, doi:10.5194/acp-9-163-2009.

Mapes, B. E., T. T. Warner, M. Xu, and D. J. Gochis (2004), Comparison of Cumulus Parameterizations and Entrainment Using Domain-Mean Wind Divergence in a Regional Model, *Journal of the Atmospheric Sciences*, *61*(11), 1284-1295, doi:10.1175/1520-0469(2004)061<1284:COCPAE>2.0.CO;2.

Marais, E. A., D. J. Jacob, J. L. Jimenez, P. Campuzano-Jost, D. A. Day, W. Hu, J. Krechmer, L. Zhu, P. S. Kim, and C. C. Miller (2016), Aqueous-phase mechanism for secondary organic aerosol formation from isoprene: application to the southeast United States and co-benefit of SO 2 emission controls, *Atmospheric Chemistry and Physics*, *16*(3), 1603-1618.

Martin, R. V., D. D. Parrish, T. B. Ryerson, D. K. Nicks, K. Chance, T. P. Kurosu, D. J. Jacob, E. D. Sturges, A. Fried, and B. P. Wert (2004), Evaluation of GOME satellite measurements of tropospheric NO2 and HCHO using regional data from aircraft campaigns in the southeastern United States, *Journal of Geophysical Research: Atmospheres*, *109*(D24), n/a-n/a, doi:10.1029/2004JD004869.

Mauritsen, T., B. Stevens, E. Roeckner, T. Crueger, M. Esch, M. Giorgetta, H. Haak, J. Jungclaus, D. Klocke, and D. Matei (2012), Tuning the climate of a global model, *Journal of Advances in Modeling Earth Systems*, *4*(3).

Mellouki, A., T. J. Wallington, and J. Chen (2015), Atmospheric Chemistry of Oxygenated Volatile Organic Compounds: Impacts on Air Quality and Climate, *Chemical Reviews*, *115*(10), 3984-4014, doi:10.1021/cr500549n.

Moeng, C.-H. (1984), A large-eddy-simulation model for the study of planetary boundary-layer turbulence, *Journal of the Atmospheric Sciences*, *41*(13), 2052-2062.

Molemaker, M. J., and J. Vilà-Guerau de Arellano (1998), Control of Chemical Reactions by Convective Turbulence in the Boundary Layer, *Journal of the Atmospheric Sciences*, *55*(4), 568-579, doi:10.1175/1520-0469(1998)055<0568:COCRBC>2.0.CO;2.

Ouwersloot, H. G., J. Vilà-Guerau de Arellano, C. C. van Heerwaarden, L. N. Ganzeveld, M. C. Krol, and J. Lelieveld (2011), On the segregation of chemical species in a clear boundary layer over heterogeneous land surfaces, *Atmos. Chem. Phys.*, *11*(20), 10681-10704, doi:10.5194/acp-11-10681-2011.

Patton, E., K. Davis, M. Barth, and P. Sullivan (2001), Decaying Scalars Emitted By A Forest Canopy: A Numerical Study, *Boundary-Layer Meteorol*, *100*(1), 91-129, doi:10.1023/A:1019223515444.

Patton, E. G., P. P. Sullivan, and C.-H. Moeng (2005), The Influence of Idealized Heterogeneity on Wet and Dry Planetary Boundary Layers Coupled to the Land Surface, *Journal of the Atmospheric Sciences*, *62*(7), 2078-2097, doi:10.1175/JAS3465.1.

Placet, M., C. O. Mann, R. O. Gilbert, and M. J. Niefer (2000), Emissions of ozone precursors from stationary sources:: a critical review, *Atmos Environ*, *34*(12–14), 2183-2204, doi:http://dx.doi.org/10.1016/S1352-2310(99)00464-1.

Ren, X., et al. (2003), OH and HO2 Chemistry in the urban atmosphere of New York City, *Atmos Environ*, *37*(26), 3639-3651, doi:http://dx.doi.org/10.1016/S1352-2310(03)00459-X.

Rienecker, M. M., et al. (2011), MERRA: NASA's Modern-Era Retrospective Analysis for Research and Applications, *Journal of Climate*, *24*(14), 3624-3648, doi:10.1175/JCLI-D-11-00015.1.

Rivera-Rios, J. C., et al. (2014), Conversion of hydroperoxides to carbonyls in field and laboratory instrumentation: Observational bias in diagnosing pristine versus anthropogenically controlled atmospheric chemistry, *Geophysical Research Letters*, *41*(23), 8645-8651, doi:10.1002/2014GL061919.

Sawyer, R. F., R. A. Harley, S. H. Cadle, J. M. Norbeck, R. Slott, and H. A. Bravo (2000), Mobile sources critical review: 1998 NARSTO assessment, *Atmos Environ*, *34*(12–14), 2161-2181, doi:http://dx.doi.org/10.1016/S1352-2310(99)00463-X.

Schlager, H., V. Grewe, and A. Roiger (2012), Chemical Composition of the Atmosphere, in *Atmospheric Physics: Background – Methods – Trends*, edited by U. Schumann, pp. 17-35, Springer Berlin Heidelberg, Berlin, Heidelberg, doi:10.1007/978-3-642-30183-4_2.

Schumann, U. (1989), Large-eddy simulation of turbulent diffusion with chemical reactions in the convective boundary layer, *Atmospheric Environment (1967)*, *23*(8), 1713-1727, doi:http://dx.doi.org/10.1016/0004-6981(89)90056-5.

Seco, R., J. Peñuelas, and I. Filella (2007), Short-chain oxygenated VOCs: Emission and uptake by plants and atmospheric sources, sinks, and concentrations, *Atmos Environ*, *41*(12), 2477-2499, doi:http://dx.doi.org/10.1016/j.atmosenv.2006.11.029.

Seco, R., J. Penuelas, I. Filella, and J. Llusia (2013), Volatile organic compounds in the western Mediterranean basin: urban and rural winter measurements during the DAURE campaign, *Atmospheric chemistry and physics*, *13*(8), 4291-4306, doi:10.5194/acp-13-4291-2013.

Seinfeld, J. H., S. N. Pandis, and K. Noone (1998), Atmospheric chemistry and physics: from air pollution to climate change, edited, AIP.

Shin, H. H., and S.-Y. Hong (2011), Intercomparison of planetary boundary-layer parametrizations in the WRF model for a single day from CASES-99, *Boundary-Layer Meteorol*, *139*(2), 261-281.

Sillman, S. (1999), The relation between ozone, NOx and hydrocarbons in urban and polluted rural environments, *Atmos Environ*, *33*(12), 1821-1845, doi:http://dx.doi.org/10.1016/S1352-2310(98)00345-8.

Singh, H., Y. Chen, A. Staudt, D. Jacob, D. Blake, B. Heikes, and J. Snow (2001), Evidence from the Pacific troposphere for large global sources of oxygenated organic compounds, *Nature*, *410*(6832), 1078-1081.

Spaulding, R. S., G. W. Schade, A. H. Goldstein, and M. J. Charles (2003), Characterization of secondary atmospheric photooxidation products: Evidence for biogenic and anthropogenic sources, *Journal of Geophysical Research: Atmospheres*, *108*(D8), n/a-n/a, doi:10.1029/2002JD002478.

Steiner, A. L., A. L. Steiner, R. C. Cohen, R. A. Harley, and S. Tonse (2008), VOC reactivity in central California: comparing an air quality model to ground-based measurements, *Atmospheric chemistry and physics*, *8*(2), 351-368, doi:10.5194/acp-8-351-2008.

Stull, R. (1988), An Introduction to Boundary Layer Meteorology Kluwer Academic Publishers Dordrecht 666 Google Scholar.

Sullivan, P. P., and E. G. Patton (2011), The Effect of Mesh Resolution on Convective Boundary Layer Statistics and Structures Generated by Large-Eddy Simulation, *Journal of the Atmospheric Sciences*, *68*(10), 2395-2415, doi:10.1175/JAS-D-10-05010.1.

Surratt, J. D., A. W. H. Chan, N. C. Eddingsaas, M. Chan, C. L. Loza, A. J. Kwan, S. P. Hersey, R. C. Flagan, P. O. Wennberg, and J. H. Seinfeld (2010), Reactive intermediates revealed in secondary organic aerosol formation from isoprene, *Proceedings of the National Academy of Sciences*, *107*(15), 6640-6645, doi:10.1073/pnas.0911114107.

Sykes, R. I., S. F. Parker, D. S. Henn, and W. S. Lewellen (1994), Turbulent Mixing with Chemical Reaction in the Planetary Boundary Layer, *Journal of Applied Meteorology*, *33*(7), 825-834, doi:10.1175/1520-0450(1994)033<0825:TMWCRI>2.0.CO;2.

Tuccella, P., G. Curci, G. Grell, G. Visconti, S. Crumeroylle, A. Schwarzenboeck, and A. Mensah (2015), A new chemistry option in WRF-Chem v. 3.4 for the simulation of direct and indirect aerosol effects using VBS: evaluation against IMPACT-EUCAARI data, *Geoscientific Model Development*, *8*(9), 2749-2776.

van der Poel, E. P., R. Ostilla-Mónico, R. Verzicco, and D. Lohse (2014), Effect of velocity boundary conditions on the heat transfer and flow topology in two-dimensional Rayleigh-B\'enard convection, *Physical Review E*, *90*(1), 013017.

Velasco, E., C. Márquez, E. Bueno, R. Bernabé, A. Sánchez, O. Fentanes, H. Wöhrnschimmel, B. Cárdenas, A. Kamilla, and S. Wakamatsu (2008), Vertical distribution of ozone and VOCs in the low boundary layer of Mexico City, *Atmospheric chemistry and Physics*, *8*(12), 3061-3079.

Verver, G. H. L., H. Van Dop, and A. A. M. Holtslag (1997), Turbulent mixing of reactive gases in the convective boundary layer, *Boundary-Layer Meteorol*, *85*(2), 197-222, doi:10.1023/A:1000414710372.

Vilà-Guerau de Arellano, J., S. W. Kim, M. C. Barth, and E. G. Patton (2005), Transport and chemical transformations influenced by shallow cumulus over land, *Atmos. Chem. Phys.*, *5*(12), 3219-3231, doi:10.5194/acp-5-3219-2005.

Vilà-Guerau de Arellano, J., E. G. Patton, T. Karl, K. van den Dries, M. C. Barth, and J. J. Orlando (2011), The role of boundary layer dynamics on the diurnal evolution of isoprene and the hydroxyl radical over tropical forests, *Journal of Geophysical Research: Atmospheres*, *116*(D7), n/a-n/a, doi:10.1029/2010JD014857.

Vinuesa, J.-F., and J. V.-G. De Arellano (2003), Fluxes and (co-)variances of reacting scalars in the convective boundary layer, *Tellus B*, *55*(4), 935-949, doi:10.1046/j.1435-6935.2003.00073.x.

Volkamer, R., P. Sheehy, L. T. Molina, and M. J. Molina (2010), Oxidative capacity of the Mexico City atmosphere – Part 1: A radical source perspective, *Atmos. Chem. Phys.*, *10*(14), 6969-6991, doi:10.5194/acp-10-6969-2010.

von Kuhlmann, R., M. G. Lawrence, P. J. Crutzen, and P. J. Rasch (2003), A model for studies of tropospheric ozone and nonmethane hydrocarbons: Model description and ozone results, *Journal of Geophysical Research: Atmospheres*, *108*(D9), n/a-n/a, doi:10.1029/2002JD002893.

Wang, M., M. Shao, W. Chen, B. Yuan, S. Lu, Q. Zhang, L. Zeng, and Q. Wang (2014), A temporally and spatially resolved validation of emission inventories by measurements of ambient volatile organic compounds in Beijing, China, *Atmospheric Chemistry and Physics*, *14*(12), 5871-5891.

Weibring, P., D. Richter, J. G. Walega, and A. Fried (2007), First demonstration of a high performance difference frequency spectrometer on airborne platforms, *Opt. Express*, *15*(21), 13476-13495, doi:10.1364/OE.15.013476.

Williams, J., and R. Koppmann (2007), Volatile Organic Compounds in the Atmosphere: An Overview, in *Volatile Organic Compounds in the Atmosphere*, edited, pp. 1-32, Blackwell Publishing Ltd, doi:10.1002/9780470988657.ch1.

Wöhrnschimmel, H., C. Márquez, V. Mugica, W. A. Stahel, J. Staehelin, B. Cárdenas, and S. Blanco (2006), Vertical profiles and receptor modeling of volatile organic compounds over Southeastern Mexico City, *Atmos Environ*, *40*(27), 5125-5136.

Xie, Y., R. Elleman, T. Jobson, and B. Lamb (2011), Evaluation of O3-NOx-VOC sensitivities predicted with the CMAQ photochemical model using Pacific Northwest 2001 field observations, *Journal of Geophysical Research: Atmospheres*, *116*(D20), n/a-n/a, doi:10.1029/2011JD015801.

Zhang, D., W. Lei, and R. Zhang (2002), Mechanism of OH formation from ozonolysis of isoprene: kinetics and product yields, *Chemical Physics Letters*, *358*(3–4), 171-179, doi:http://doi.org/10.1016/S0009-2614(02)00260-9.

Zheng, J., M. Shao, W. Che, L. Zhang, L. Zhong, Y. Zhang, and D. Streets (2009), Speciated VOC Emission Inventory and Spatial Patterns of Ozone Formation Potential in the Pearl River Delta, China, *Environmental Science & Technology*, *43*(22), 8580-8586, doi:10.1021/es901688e.

Crawford, J. H., and Pickering, K. E., (2014), Air & Waste Management Association, *The Magazine for Environmental Managers,* 1-47.

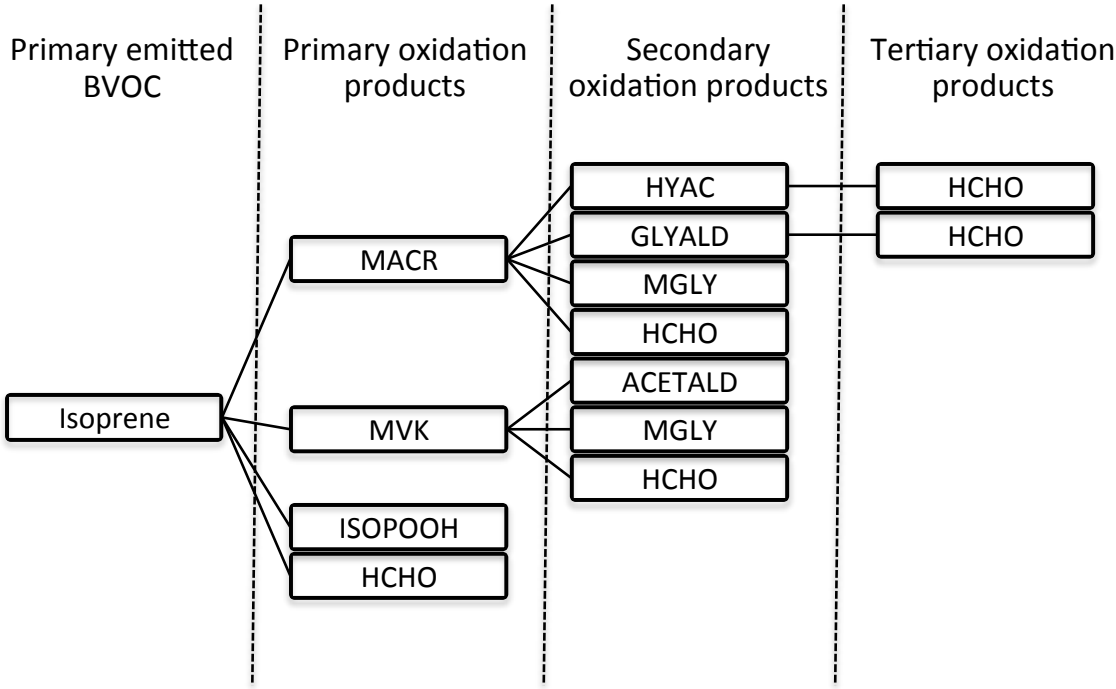

Figure 2. 1. Chemical oxidation pathways of the biogenic volatile organic compound (BVOC) species simulated in the LES model.

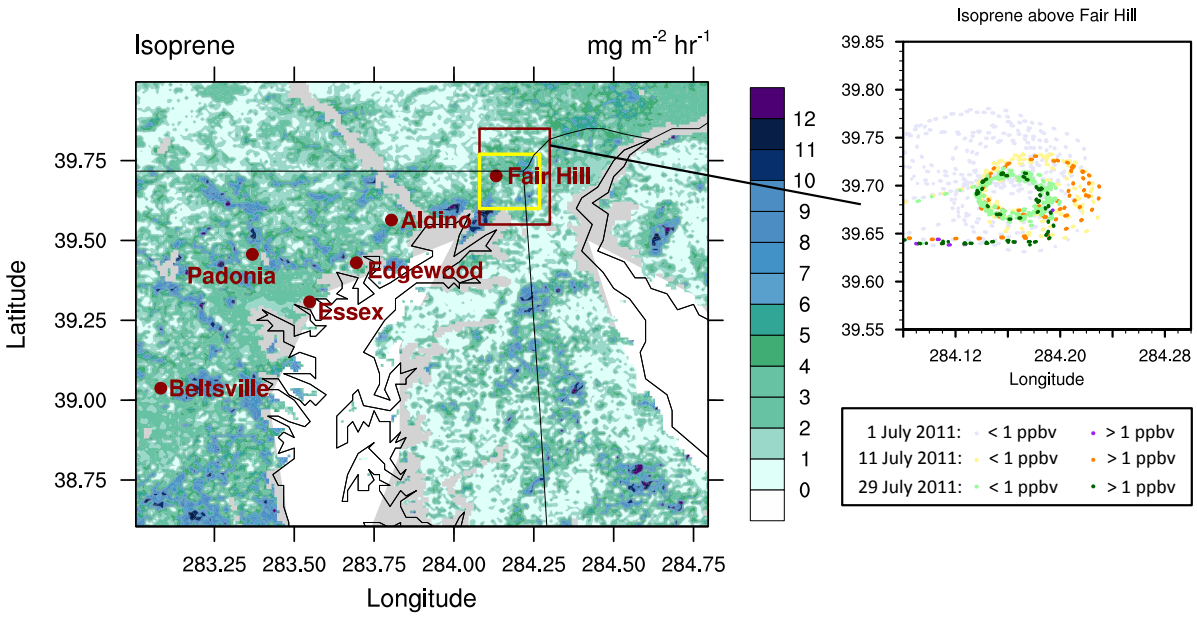

Figure 2. 2. The spatial distribution of isoprene emission factors (mg m^{-2} hr^{-1}) at standard conditions for the MEGAN canopy-scale model [*Guenther et al.*, 2006] (contour map; left) with ground-based DISCOVER-AQ sites (red dots) and the LES simulation domain (yellow box). P-3B spirals above the Fair Hill region (red box; left) are shown in the right figure, with specific measurement locations on each simulation day, with Case 1 in purple (1 July 2011), Case 2 in orange (11 July 2011), and Case 3 in green (29 July 2011). Lighter colors represent isoprene concentrations below 1 ppbv, and darker colors represent isoprene concentrations above 1 ppbv.

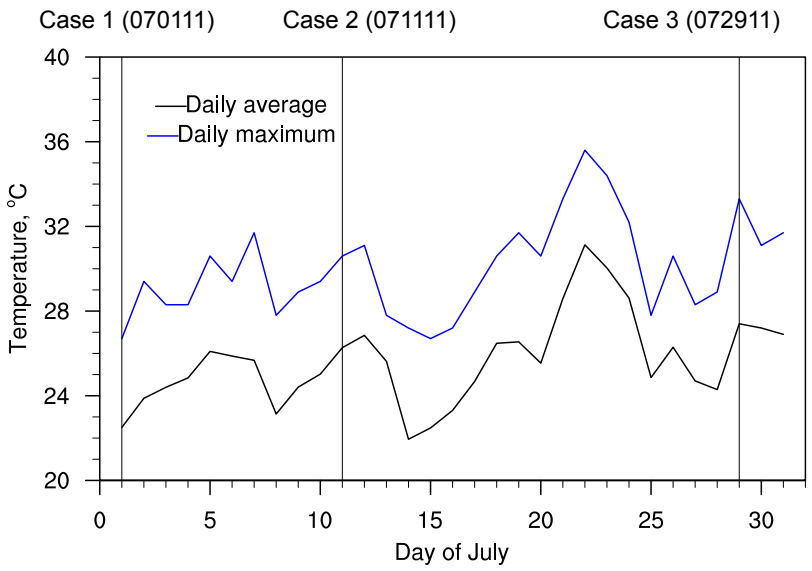

Figure 2. 3. Daily average and maximum temperature (°C) at the Fair Hill ground site during the DISCOVER-AQ campaign. Vertical lines represent the three selected case studies: Case 1 (1 July 2011; clear), Case 2 (11 July 2011; convection) and Case 3 (29 July 2011; high temperature and convection).

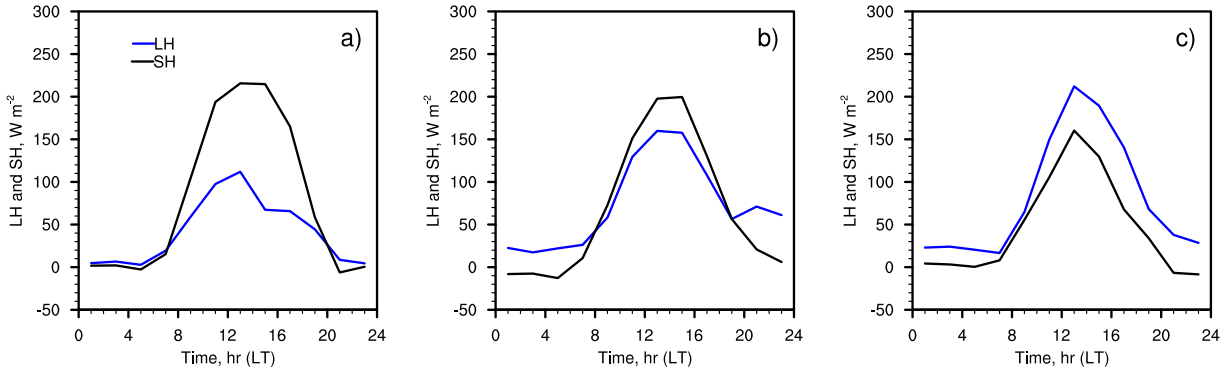

Figure 2. 4. Observed surface sensible heat (SH; W m^{-2}; black) and latent heat (LH; W m^{-2}; blue) fluxes from the Edgewood site used as lower boundary conditions for (a) Case 1, (b) Case 2 and (c) Case 3.

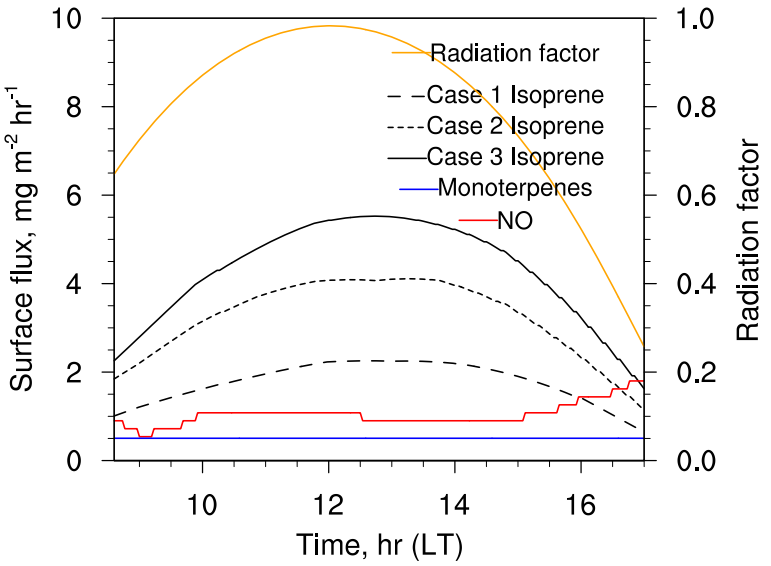

Figure 2. 5. Diurnal surface fluxes (mg m^{-2} hr^{-1}) of isoprene, NO and monoterpenes in the LES simulations, and radiation factor (unitless) for scaling isoprene emission in all the cases. Isoprene varies for each case based on changes in surface temperature, while NO and monoterpenes are the same for each simulation case.

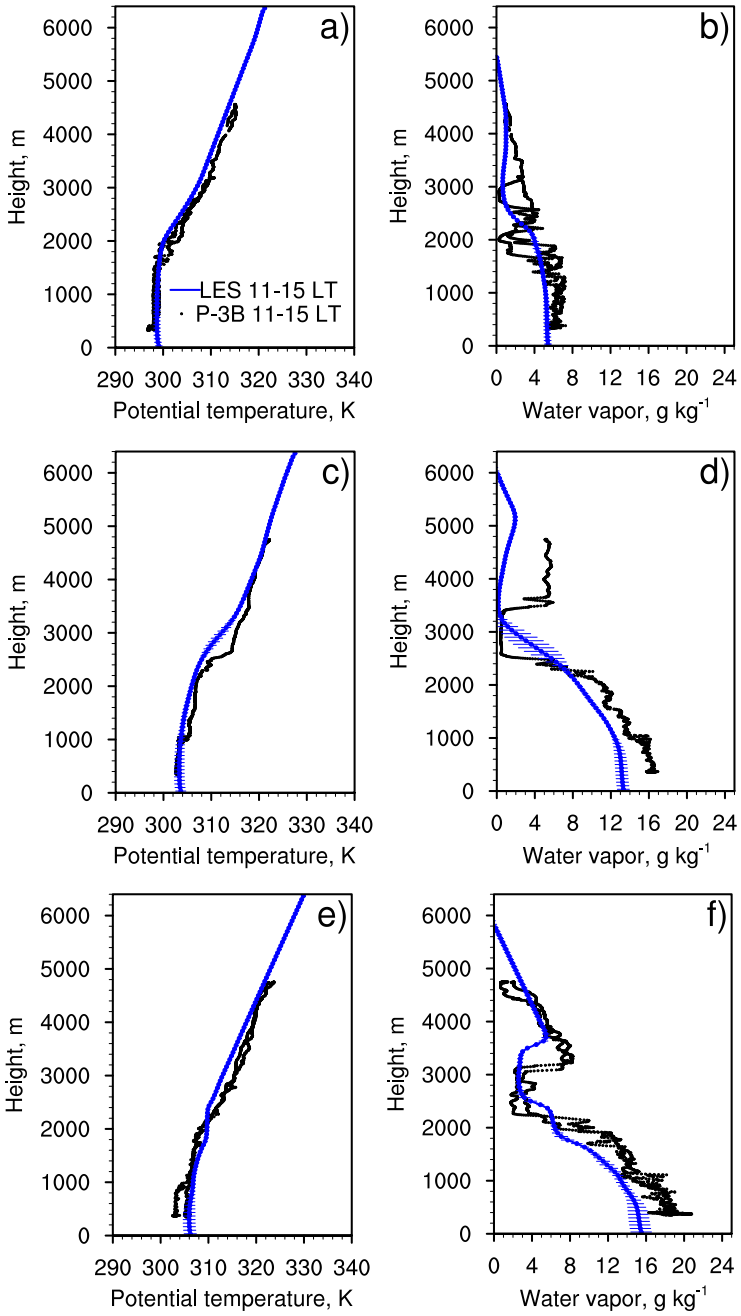

Figure 2. 6. Comparison between P-3B observations (black dots) and domain-average modeled (blue lines with horizontal bars representing the spatial standard deviation) vertical profiles of potential temperature (K) (a, c, e) and water vapor mixing ratio (g kg^{-1}) (b, d, f) for the three cases (Case 1: a, b; Case 2: c, d; Case 3: e, f)

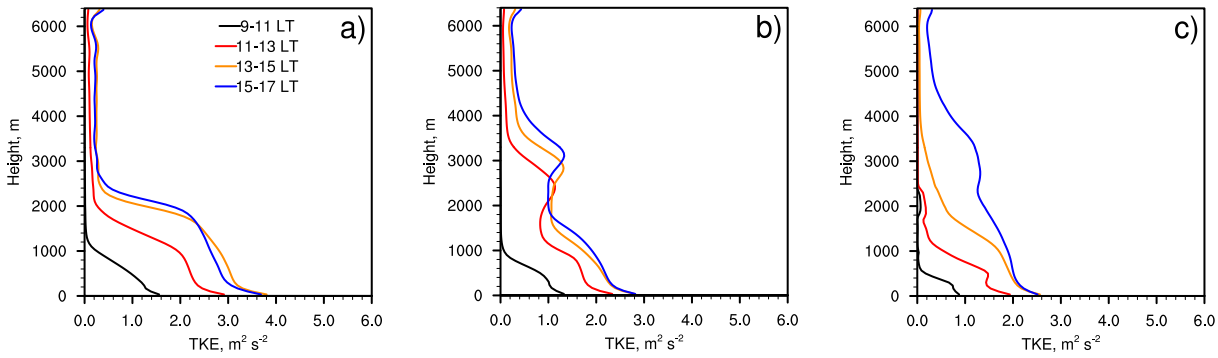

Figure 2. 7. Domain-average simulated vertical profiles of turbulent kinetic energy (m^2 s^{-2}) for (a) Case 1, (b) Case 2 and (c) Case 3.

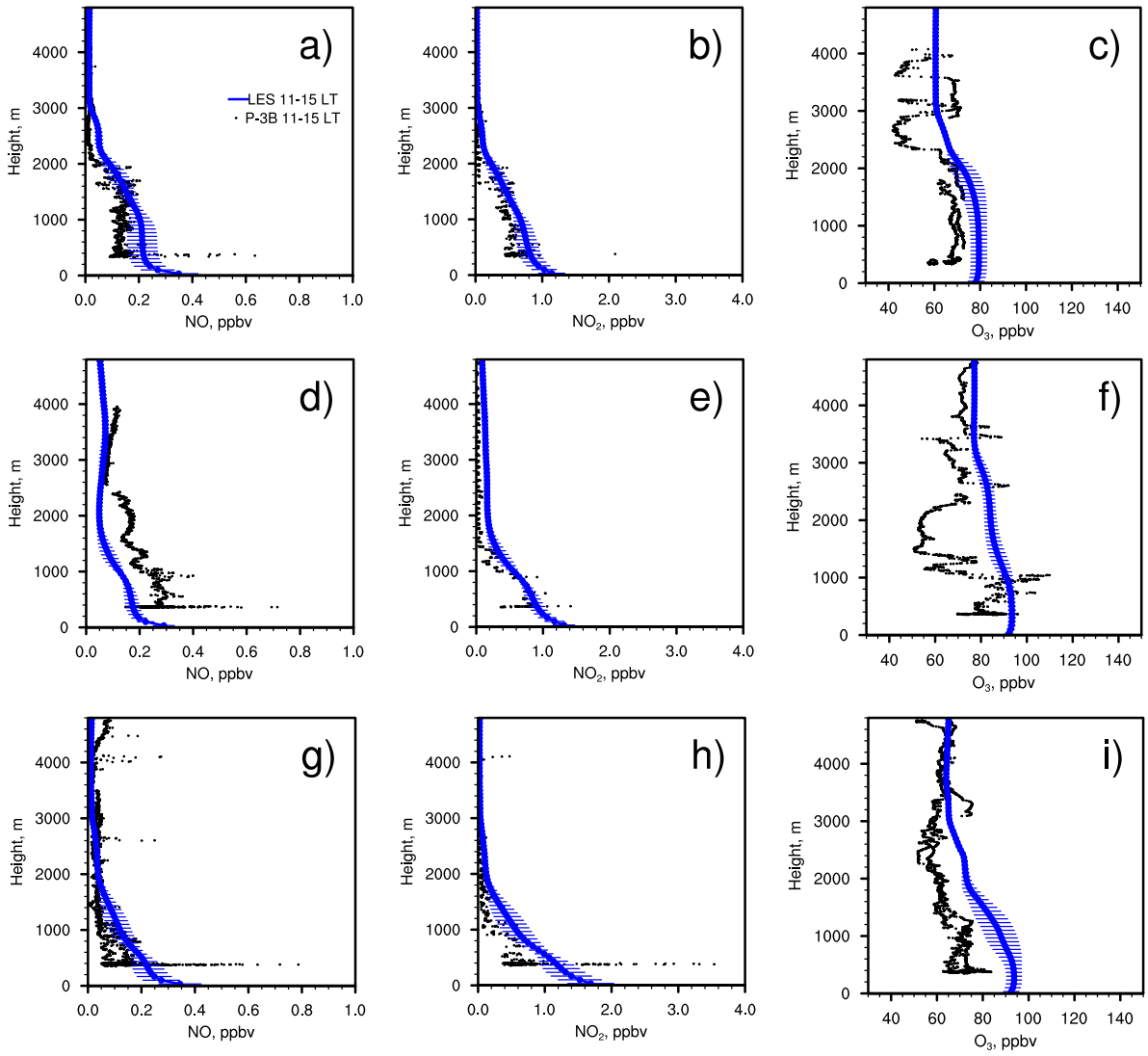

Figure 2. 8. Comparison between P-3B observations (black dots) and domain-average modeled (blue lines with horizontal bars representing the spatial standard deviation) NO (ppbv) (a, d, g), NO_2 (ppbv) (b, e, h) and O_3 (ppbv) (c, f, i) during 1100-1500 LT for the three cases (Case 1: a-c; Case 2: d-f; Case 3: g-i)

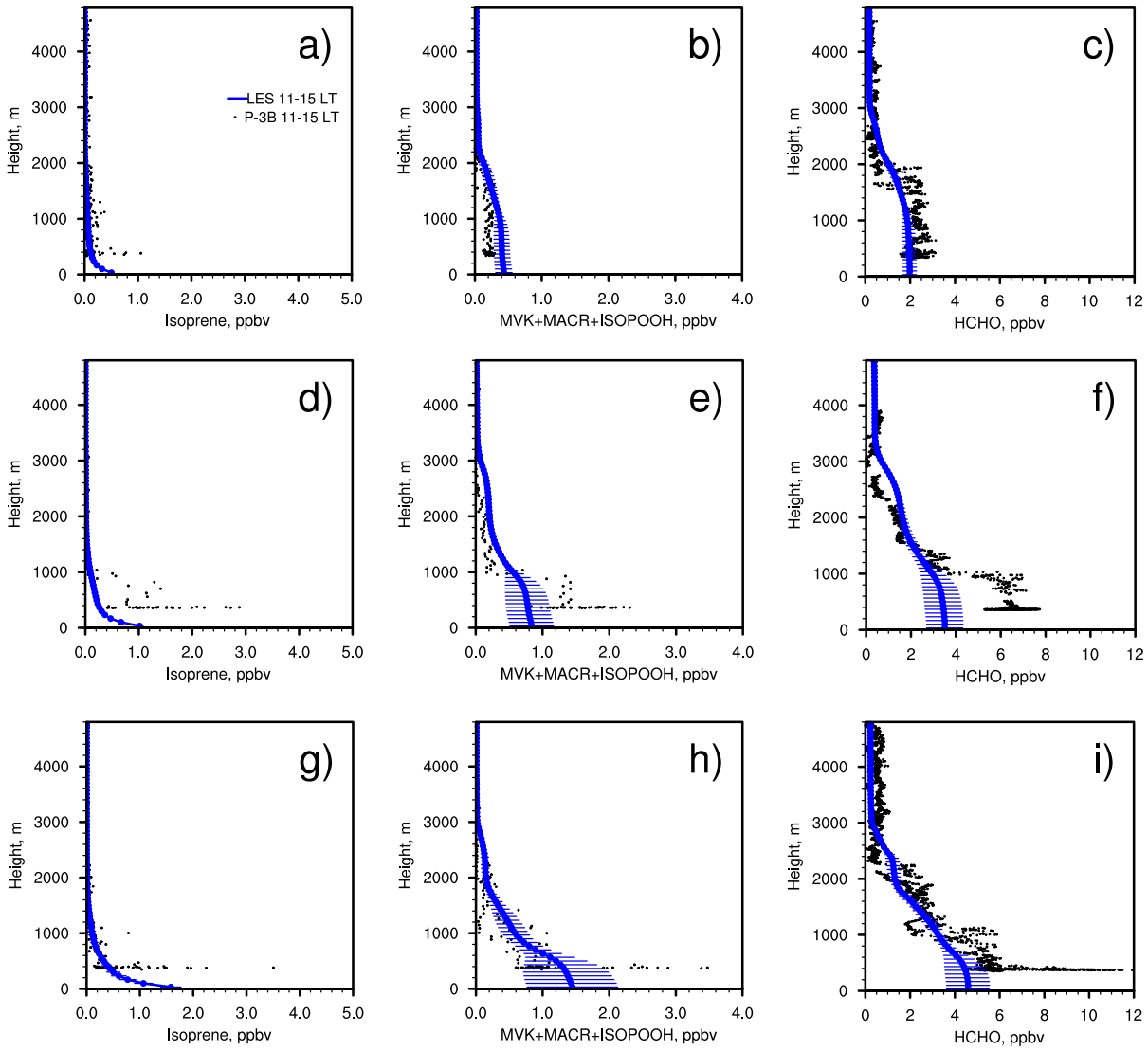

Figure 2. 9. Comparison between P-3B observations (black dots) and domain-average modeled (blue lines with horizontal bars representing the spatial standard deviation) isoprene (ppbv) (a, d, g), MVK+MACR+ISOPOOH (ppbv) (b, e, h) and HCHO (ppbv) (c, f, i) during 1100-1500 LT for the three cases (Case 1: a-c; Case 2: d-f; Case 3: g-i)

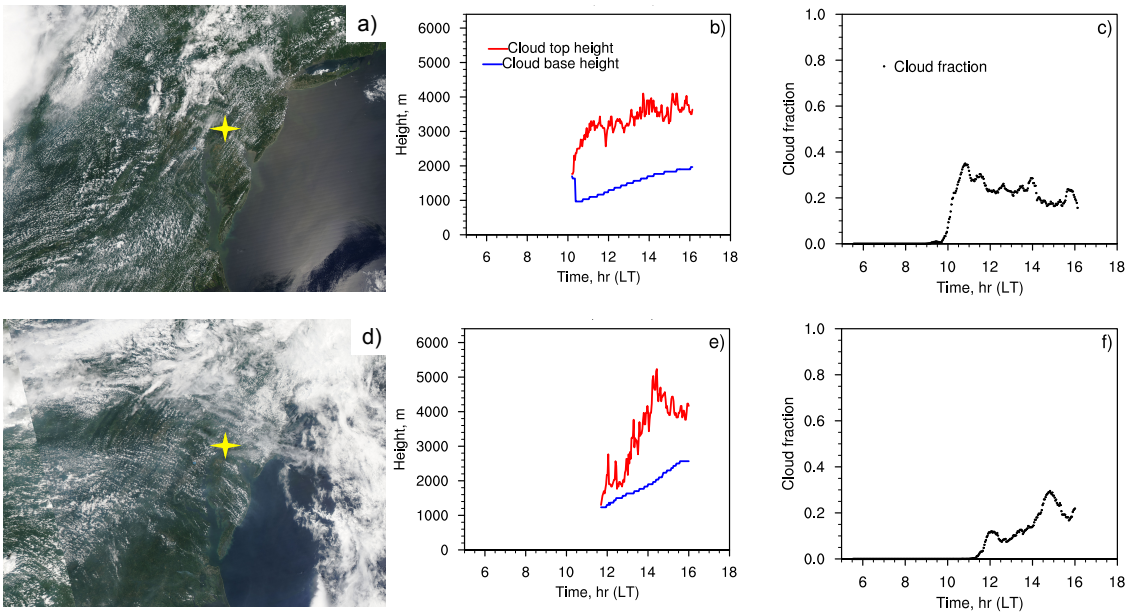

Figure 2. 10. Aqua satellite cloud images (http://www-air.larc.nasa.gov/cgi-bin/ArcView/discover-aq.dc-2011?SATELLITE=1) with Fair Hill location noted (yellow star) for (a) Case 2 and (d) Case 3, simulated temporal evolution of the cloud top and base heights (m) for (b) Case 2 and (e) Case 3, and the cloud fraction (unitless) (c) for Case 2 and (f) Case 3. Cloud top, base and fraction are defined in Section 2.4.

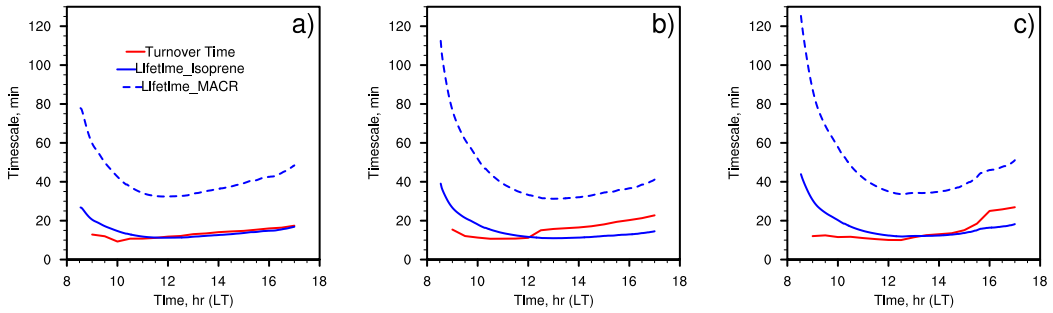

Figure 2. 11. Comparison of diurnal turnover time (τ_T) and chemical lifetimes of isoprene ($\tau_{CH,\,iso}$) and MACR ($\tau_{CH,\,MACR}$) at 0.3 km height for (a) Case 1, (b) Case 2 and (c) Case 3.

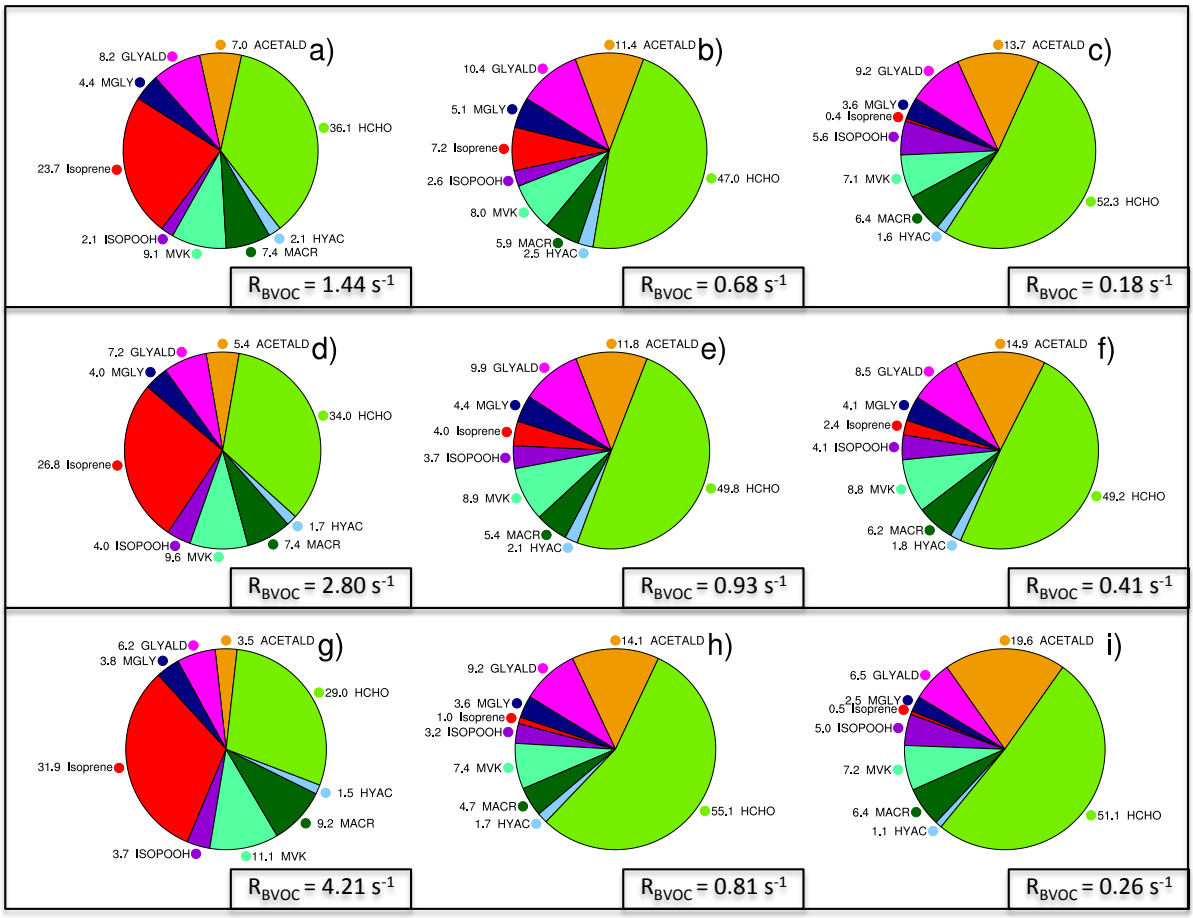

Figure 2. 12. LES simulated OH reactivity contribution percentages (%) and total BVOC+OH reactivity (R_{BVOC}) (black box) of the BVOC species at 0.3 km (a, d, g), 1.5 km (b, e, h) and 2.7 km (c, f, i) during midday (1100-1300 LT) for the three cases (Case 1: a-c; Case 2: d-f; Case 3: g-i)

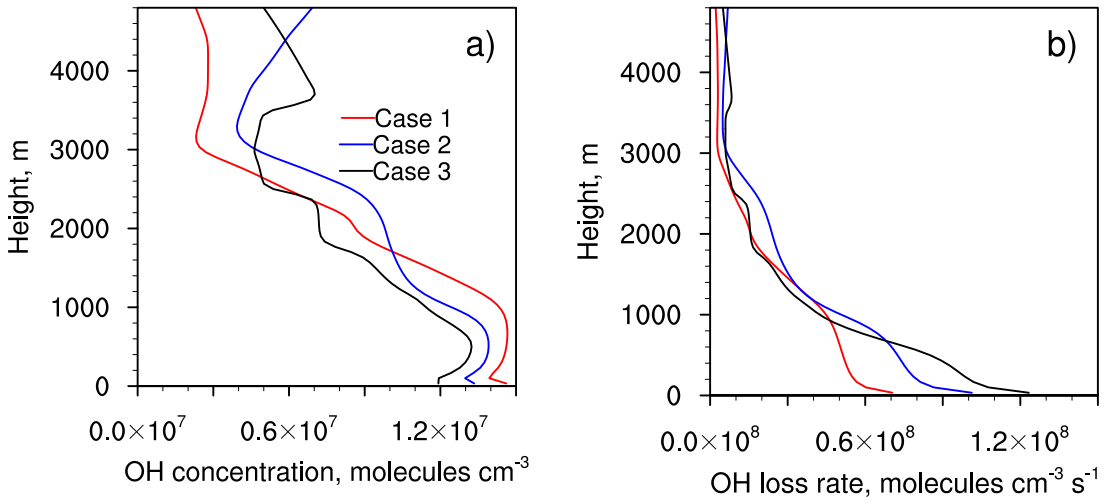

Figure 2. 13. LES simulated domain-average OH concentration (a) and loss rate (b) during midday (1100-1300 LT) for the three cases.

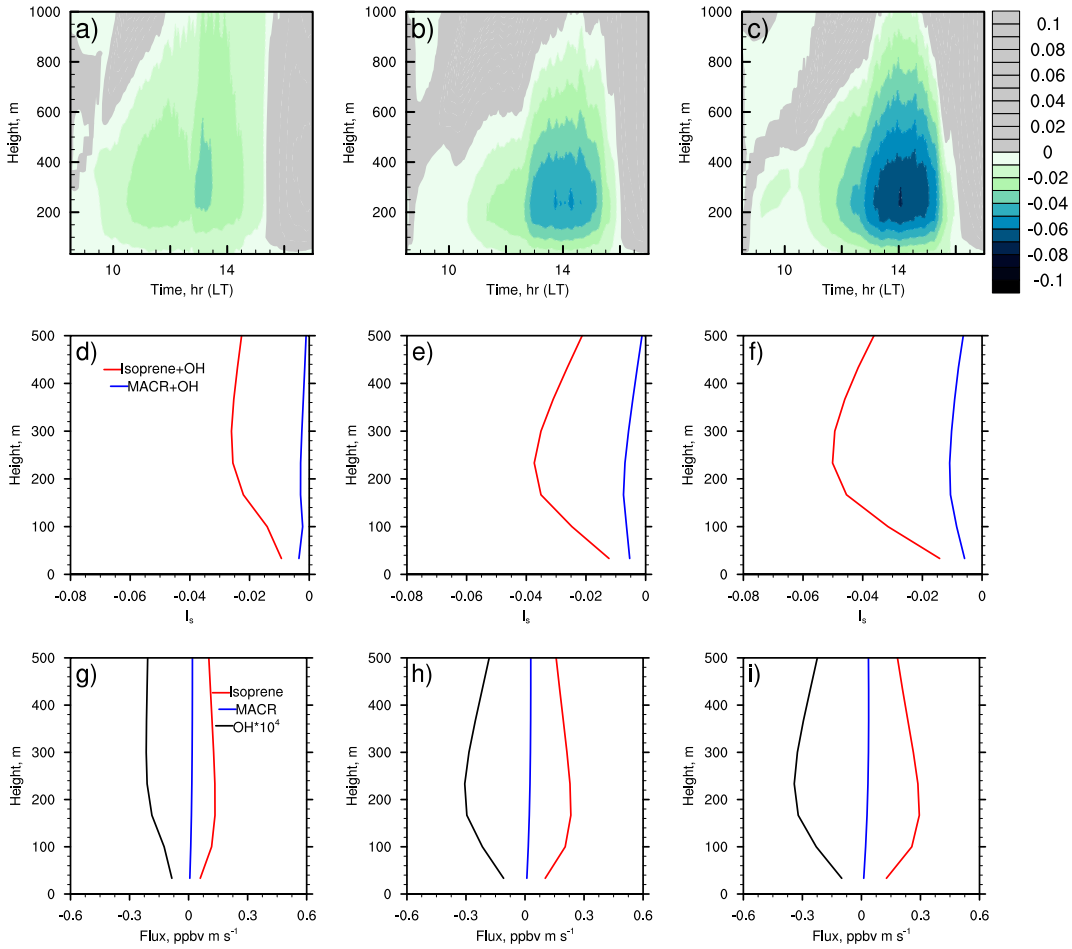

Figure 2. 14. LES simulated temporal evolution of I_s for isoprene and OH (a-c), near surface vertical profiles of horizontal- and temporal- (1100-1500 LT) averaged I_s for isoprene and OH, MACR and OH (d-f), and fluxes of isoprene, MACR, OH (g-i) for the three cases (Case 1: a, d, g; Case 2: b, e, h; Case 3: c, f, i)

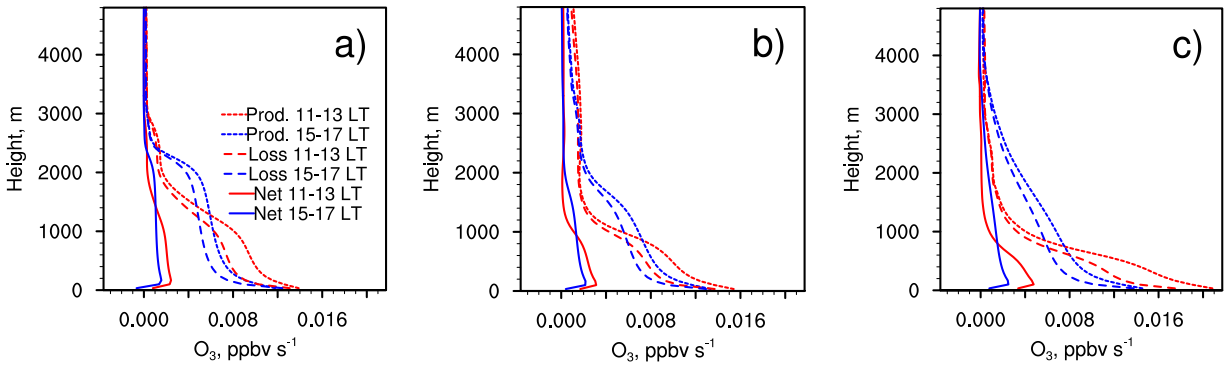

Figure 2. 15. LES simulated production (short dashed lines), loss (long dashed lines) and net gain (solid lines) rates of O_3 for (a) Case 1, (b) Case 2 and (c) Case 3.

Table 2. 1 Modeled midday (1100-1300 LT) lifetimes of selected chemical species according to their reaction rates with OH and total lifetimes (calculated based on photolysis and reaction with OH) of HCHO and MGLY at 0.3 km for the three cases. Values shown are horizontal- (across the model domain) and temporal- (1100-1300 LT) averages at 0.3 km, with plus and minus one standard deviation.

	Lifetime (τ_{CH}, min)		
	Case 1	Case 2	Case 3
Isoprene	11.39 ± 0.17	12.26 ± 0.93	13.13 ± 1.10
MACR	32.88 ± 0.50	35.01 ± 2.70	37.27 ± 3.19
MVK	60.57 ± 0.89	65.33 ± 4.92	70.07 ± 5.83
ISOPOOH	153.55 ± 2.34	163.63 ±12.60	174.31 ±14.87
HCHO	115.57 ± 1.82	121.97 ± 9.55	129.22 ±11.24
HYAC	385.22 ± 6.08	406.57 ±31.83	430.75 ±37.46
GLYALD	115.57 ± 1.82	121.97 ± 9.55	129.22 ±11.24
MGLY	80.69 ± 1.12	88.64 ± 6.47	96.07 ± 7.70
ACETALD	81.29 ± 1.23	86.83 ± 6.66	92.63 ± 7.87
	Parameters for lifetime calculation		
Temperature (K)	292.66 ± 0.42	296.88 ± 0.56	299.33 ± 0.73
OH (molecules cm^{-3})	1.44e+7 ± 2.22e+5	1.37e+7 ± 1.04e+6	1.30e+7 ± 1.08e+6
	Total lifetime (τ_{CH}, min)		
HCHO	73.48	76.24	79.69
MGLY	49.63	52.65	55.55

Table 2. 2 Modeled turbulent Damköhler number (Da_t) of selected chemical species at 0.3 km during midday (1100-1300 LT) for the three cases. τ_T values shown are horizontal- (across the model domain) and temporal- (1100-1300 LT) averages at 0.3 km, with plus and minus one standard deviation. Da_t values are calculated based on these τ_T averages and the τ_{CH} averages from Table 2.1.

	Da_t (unitless)		
Isoprene	1.03	1.04	0.81
MACR	0.36	0.36	0.29
MVK	0.19	0.19	0.15
ISOPOOH	0.10	0.10	0.08
HCHO	0.08	0.08	0.06
HYAC	0.03	0.03	0.02
GLYALD	0.10	0.10	0.08
MGLY	0.15	0.14	0.11
ACETALD	0.14	0.15	0.11
	τ_T for Da_t calculation		
τ_T (min)	11.79 ± 0.89	12.70 ± 2.48	10.63 ± 0.62

Table 2. 3 Segregation modified midday (1100-1300 LT) lifetimes of isoprene and MACR at 0.3 km for the three cases. Values shown are horizontal- (across the model domain) and temporal- (1100-1300 LT) averages at 0.3 km, with plus and minus one standard deviation.

	Lifetime (τ_{CH}, min)		
	Case 1	Case 2	Case 3
Isoprene	11.70 ± 0.18	12.54 ± 0.87	13.57 ± 1.00
MACR	32.96 ± 0.51	35.08 ± 2.66	37.52 ± 3.16

CHAPTER 3 Impact of in-cloud aqueous processes on the chemistry and transport of biogenic volatile organic compounds

Abstract

We investigate the impacts of cloud aqueous processes on the chemistry and transport of biogenic volatile organic compounds (BVOC) using the National Center for Atmospheric Research's large-eddy simulation code with an updated chemical mechanism that includes both gas- and aqueous-phase reactions. We simulate transport and chemistry for a meteorological case with a diurnal pattern of non-precipitating cumulus clouds from the Baltimore-Washington area DISCOVER-AQ campaign. We evaluate two scenarios with and without aqueous-phase chemical reactions. In the cloud layer (2-3 km), the addition of aqueous phase reactions decreases HCHO by 18% over the domain due to its solubility and the fast depletion from aqueous reactions, resulting in a corresponding decrease in radical oxidants. This radical decrease increases isoprene and MACR (100% and 15%, respectively) in the cloud layer. Aqueous-phase reactions can modify the turbulence-induced controls on reaction rates between OH and BVOC by changing the sign of the segregation intensity, causing up to 55% reduction in the isoprene-OH reaction rate and 40% for the MACR-OH reaction when clouds are present. Analysis of the isoprene-OH covariance budget shows the chemistry term is the primary driver of

the strong segregation in clouds, triggered by the decrease in OH. Organic acids are formed only through aqueous-phase reactions. Turbulence mixes these compounds on short time scales, with the near-surface mixing ratios of these acids reaching 20% of the mixing ratios in the cloud layer within one hour of cloud formation.

3.1. Introduction

Clouds affect the chemical composition of the troposphere by various chemical and physical processes (e.g., *Ervens* [2015]; *Tost et al.* [2010]). Aqueous-phase reactions in clouds provide an additional pathway for altering the composition in and near clouds, creating unique intermediates such as ions and hydrated species that are distinct from the products created from gas-phase only chemistry [*Ervens*, 2015]. The convective motion in clouds transports temperature and water vapor vertically [*Cotton et al.*, 1995], and chemical constituents in the atmospheric boundary layer (ABL) (e.g., *Barth et al.* [2007]; *Vilà-Guerau de Arellano et al.* [2005]).

Investigations into acid rain production highlighted the importance of in-cloud aqueous-phase chemistry. Many observational studies showed the importance of sulfate formation from the aqueous-phase oxidation of sulfur dioxide (SO_2) (e.g., *Bower et al.* [1999]; *Hegg and Hobbs* [1979; 1981; 1982]; *Husain* [1989]; *Husain et al.* [2004]; *Laj et al.* [1997]). Based on box modeling studies, *Chameides* [1984] and *Jacob* [1986] found the in-cloud acidity affected not only the generation of inorganic acids (e.g., sulfuric acid), but also the formation of organic acids. Early regional chemistry transport models were developed to study the regional-scale transport,

chemistry and deposition of the chemical constituents contributing to acid rain based on parameterized chemical reactions and cloud processes [*Carmichael and Peters*, 1986; *Chang et al.*, 1987]. *Lelieveld and Crutzen* [1990] and *Lelieveld and Crutzen* [1991] found in-cloud aqueous-phase chemistry could influence the photochemistry of the troposphere by reducing HCHO, HO_x and O_3 substantially (15-70% for HCHO, 10-70% for HO_x and 35-45% for O_3). However, *Liang and Jacob* [1997] used a lower but more realistic cloud liquid water and a lower Henry's law constant for CH_3O_2 and simulated less than 3% reduction in O_3 due to cloud chemistry. Similarly, *Barth et al.* [2002] showed a 6% O_3 reduction caused by aqueous chemistry and cloud radiative effects. Up until this point, only CH_4 and HCHO chemistry were included to investigate the in-cloud aqueous chemistry of organic trace species.

The role of chemical processing of organic compounds in clouds is gaining increasing importance because of the implications of these organic compounds to form secondary organic aerosol (SOA). *Sempére and Kawamura* [1994] studied wet precipitation and aerosols in the atmosphere with observations, suggesting the importance of oxygenated organics (e.g., oxalic acid, glyoxal, methylglyoxal) for the formation of SOA in aqueous chemistry. *Jacob and Wofsy* [1988] found isoprene gas and aqueous chemistry provided an important atmospheric source of formic acid, methacrylic acid and pyruvic acid over the Amazon forest. Further laboratory studies [*Carlton et al.*, 2007; *Ervens et al.*, 2003] confirmed that the aqueous-phase photooxidation of organics (e.g., glyoxal) is a potential global and regional source of SOA, and regional scale modeling showed that inclusion of cloud processing of

isoprene oxidation products (e.g., glyoxal, methylglyoxal) improved correlations between modeled and aircraft-observed organic aerosols [*Carlton et al.*, 2008]. *Epstein and Nizkorodov* [2012] identified aqueous photolysis sinks of VOC and found that aqueous photolysis is an important sink for glyceraldehyde and pyruvic acid. Other studies [*Chen et al.*, 2007; *Ervens et al.*, 2011; *Lim et al.*, 2010] confirmed the importance of aqueous-phase processes in forming SOA-precursor organic acids (e.g., hydroxyacetic acid, glyoxylic acid, oxalic acid and pyruvic acid), but these studies were limited in that the vertical mixing in their simulations were parameterized and assumed each grid cell was well mixed.

In this study, we focus on the gas and aqueous chemistry of BVOC as the they are ubiquitous [*Guenther et al.*, 1995] and reactive in the atmosphere [*Goldstein and Galbally*, 2007]. BVOC play a crucial role in the formation of O_3 through a series of photochemical reactions in the presence of NO_x ($NO + NO_2$), and also control the oxidizing capacity of the atmosphere through OH and HO_2 radical chemistry [*Atkinson*, 2000; *Lelieveld et al.*, 2008]. Gas-phase oxidation of primary emitted BVOC may result in functionalized products with lower volatility that have the ability to partition to the aqueous phase. For example, the BVOC primary oxidation products, methyl vinyl ketone (MVK) and methacrolein (MACR), can react in the aqueous phase to produce low-volatility products (e.g., small carbonyl compounds including oxalate, glyoxal and methylglyoxal), providing an important source of secondary organic aerosol (SOA) [*Blando and Turpin*, 2000; *Ervens et al.*, 2011; *Fu et al.*, 2008]. *Couvidat et al.* [2012] included gas/aqueous equilibrium and aqueous-phase chemical reactions of isoprene dihydroxyepoxides (IEPOX) in their

hydrophilic/hydrophobic organic model (H^2O) and simulated a significant SOA increase. The efficacy of this process at the cloud scale and its importance in regional and global models are still poorly understood. Because these reactions are occurring in clouds, accurate model representation of clouds, turbulence and multi-phase chemistry is required to understand the fates and distributions of the BVOC species and its relevance for SOA formation.

Representing the physical processes within clouds requires a wide range of spatial (micrometers to kilometers) and temporal scales [*Hozumi et al.*, 1982; *Leriche et al.*, 2013; *Plank*, 1969]. Efficient upward transport in convective clouds occurs on timescales of minutes to hours, much faster than the timescale of days to reach the upper troposphere by advection or diffusion [*Barth et al.*, 2001; *Tost et al.*, 2010]. A range of spatial scales have been used to investigate cloud-chemistry interactions, ranging from zero-dimensional box modeling of coupled gas- and aqueous-phase chemistry (e.g., *Barth et al.* [2003]; *Chameides* [1984]) up to three-dimensional regional models with parameterized cloud processes to study acid rain and aerosol formation [*Chang et al.*, 1987; *Chapman et al.*, 2009]. Prior regional and global three-dimensional modeling studies have incorporated aqueous mechanisms including the cloud aqueous processing of organic chemical constituents (e.g., isoprene oxidation products) at varying spatial and time scales. At coarser spatial resolutions in global models (e.g., the GEOS-Chem model with a 2° latitude × 2.5° longitude resolution [*Fu et al.*, 2009; *Marais et al.*, 2016]) and regional models (e.g., the regional scale Community Multiscale Air Quality (CMAQ) model with a horizontal resolution of 36 km [*Chen et al.*, 2007]), clouds are parameterized by

predicting the cloud fraction within each grid. At finer regional resolutions (< 4 km), many simulations assume that clouds are resolved and utilize grid sizes of the same order as large clouds (km), and solve the meteorology and chemistry on the order of minutes. For example, previous studies implemented the Weather Research and Forecasting model coupled with Chemistry (WRF-Chem) at cloud-resolving scales (~2 km), but found a low bias in reproducing SOA precursors caused by a lack of detailed cloud aqueous chemistry scheme [*Chapman et al.*, 2009; *Tuccella et al.*, 2015]. *Berg et al.* [2015] and *Wang et al.* [2015] improved the WRF-Chem treatment of cloud aqueous chemistry for sub-grid parameterized convective clouds for coarser resolutions (10 km and 36 km horizontal grid resolutions, respectively) to compensate for the computational expense. In all of these studies, the model resolution and its treatment of clouds are key factors in evaluating the impacts of cloud processes on VOC chemistry and transport. However, these studies are limited by the lack of a combination between an accurate representation of the turbulent motion of clouds in conjunction with sophisticated multi-phase chemistry.

Because most atmospheric reactions are driven by kinetics, the proximity of molecules is required for chemical reactions to occur. Further, because dispersion within the ABL is controlled primarily by ABL-scale eddies, incomplete mixing becomes important for reactions when the reaction rate is similar to the turbulent mixing rate [*Schumann*, 1989; *Sykes et al.*, 1994]. As a result, segregation, defined as the reduction in chemical reaction rates caused by incomplete mixing (e.g., *Krol et al.* [2000]), can occur for fast reactions within the ABL. In clouds, the partitioning of soluble species into the aqueous phase affects the interstitial gas phase mixing

ratios and potential reaction rates. Segregation can also happen between soluble species and less soluble species. For example, because HO_2 is taken up by cloud water and NO is insoluble, the reaction rate between NO and HO_2 may decrease due to segregation, reducing the recycling rate of HO_2 to OH and the production of gas-phase OH, thereby further suppressing ozone (O_3) formation and altering other oxidants in the atmosphere [*Lelieveld and Crutzen*, 1990]. Many studies have investigated the intensity of segregation in dry boundary layers using observations and models with gas chemistry only, and found a turbulence-induced reduction in their reaction rates in the sub-cloud layer (e.g., *Kim et al.* [2016], *Krol et al.* [2000], *Molemaker and Vilà-Guerau de Arellano* [1998] and *Ouwersloot et al.* [2011]). *Vilà-Guerau de Arellano et al.* [2005] discussed the segregation induced by clouds using a LES without aqueous chemistry and attributed all segregation to cloud transport. *Kim et al.* [2004] also found enhanced segregation in shallow cumulus clouds and proposed in-cloud aqueous processes could play an important role in segregation, although aqueous reactions were not included in their simulations. Therefore, a model with high resolution and detailed gas and aqueous chemical mechanisms are required to study the effects of clouds on chemistry in convective environments.

In this study, we utilize the National Center for Atmospheric Research's (NCAR) large-eddy simulation (LES) model coupled to the NCAR gas-phase chemical mechanism MOZART2.2 [*Kim et al.*, 2012] (which will hereafter be called: LES-Chem). We add an updated aqueous-phase chemical mechanism (*Barth et al.* [2003], *Barth et al.* [2016], *Herrmann et al.* [2010] and *Herrmann et al.* [2015]) to simulate and understand the effects of aqueous-phase chemistry on vertical distributions of

key BVOC species, such as isoprene and its gas-phase oxidation products, in convective environments. LES-Chem has vertical and horizontal resolutions that can resolve the energy-containing turbulent eddies in the ABL [*Moeng*, 1984], and the coupled online chemical mechanism provides a detailed description of gas and aqueous phase organic chemistry. In this manuscript, we present high-resolution LES-Chem simulations representing both convective transport and aqueous phase chemistry and their impact on the oxidation and distribution of organic species. As far as we are aware, this study represents the first to include aqueous chemistry in a LES to study the interplay between ABL dynamics and chemistry.

3.2. Methods

3.2.1. Simulation Design

We use the NCAR LES [*Moeng*, 1984; *Patton et al.*, 2005] with an online chemical mechanism [*Kim et al.*, 2016; *Kim et al.*, 2012; *Li et al.*, 2016] to study the impacts of clouds on gas and aqueous chemistry. *Li et al.* [2016] simulated cloud and chemical composition evolution with this model for the NASA DISCOVER-AQ Baltimore-Washington campaign for three different meteorological case studies, including one clear case and two convective cases. We select case 2 from those experiments (11 July 2011, 0530-1430 LT), as it has a clear diurnal pattern of non-precipitating cumulus clouds with the cloud fraction peaking around 40% at midday [*Li et al.*, 2016]. This specific case provides an unique opportunity to examine the BVOC distribution and chemistry under convective conditions.

In this simulation, *Li et al.* [2016] used meteorological initial and boundary

conditions from the global MERRA reanalysis [*Rienecker et al.*, 2011], and chemical initial and boundary conditions from averaged NASA P-3B measurements above the Fair Hill, Maryland site on the case study day. While the *Li et al.* [2016] study used a model domain of 14.4 km × 14.4 km × 6.4 km (96 × 96 × 96 grid points with horizontal grid spacing of 150 m and vertical grid spacing of 66.67 m), here we use a lower domain height (4.8 km) and test three horizontal resolutions (see section 2.2). The 4.8 km domain height allows full turbulence development independent of the top boundary [*Li et al.*, 2016] and captures the varying cloud layers ranging from 1 km to 4 km altitudes. These simulations do not include the interaction between radiation and clouds, and use observed surface forcings and the MERRA reanalysis radiative tendencies to account for the impact of radiation changes over the diurnal cycle. The simulation is performed with a fixed time step of 1.5 s, and meteorological simulations begin at 0530 LT with chemistry initiated at 0830 LT. *Li et al.* [2016] provide further details of the LES meteorological configuration.

The gas-phase chemistry mechanism is based on the NCAR gas-phase chemical mechanism MOZART2.2 [*Horowitz et al.*, 2003] as implemented by *Kim et al.* [2012]. It includes 64 reactants and 168 reactions. Although the isoprene chemistry does not include the most recent research (e.g., *Paulot et al.* [2009]; *Paulot et al.* [2012]), a comparison of the mechanism used here with an updated isoprene mechanism using a photochemical box model finds consistent behavior between the two mechanisms for the relationship between NO_x and OH [*Kim et al.,* 2016]. The aqueous-phase chemical mechanism (Table 3.1) is based on *Barth et al.* [2003] and *Barth et al.* [2016]. For the current LES-Chem study, we updated

reactions and rate constants based on *Ervens et al.* [2008], *Herrmann et al.* [2010] and *Herrmann et al.* [2015] and added organic acid formation in the aqueous phase based on *Ervens et al.* [2008]. Henry's law equilibrium constants (Table 3.2) are based on *Sander* [2015] and *Sander et al.* [2011]. Accommodation coefficients (Table 3.2) are based on *McNeill et al.* [2012]. Details on the calculations of chemical production and loss for the LES chemical mechanism are provided in the Supporting Information. The method used to partition trace gas mixing ratios between the gas and aqueous phases works well for both low and high solubility gases, but it overestimates OH aqueous-phase concentrations, which are controlled by the chemistry and mass transfer rather than the Henry's Law equilibrium. Therefore the conclusions drawn here from the OH chemical budget are qualitative rather than quantitative. Isoprene emissions are calculated based on the solar zenith angle and temperature [*Guenther et al.*, 2006] and anthropogenic VOC emissions are not included in these simulations.

We categorize the BVOC species following *Li et al.* [2016] as (1) primary emitted BVOC (isoprene), (2) primary oxidation products [MVK, MACR and isoprene hydroxyhydroperoxide (ISOPOOH)], (3) dual-oxidation products [produced by both the primary emitted BVOC and the oxidation products, such as formaldehyde (HCHO)], and (4) secondary oxidation products [produced by the primary oxidation products, including hydroxyacetone (HYAC), glycolaldehyde (GLYALD), methylglyoxal (MGLY), and acetaldehyde (ACETALD)]. To understand aqueous processes, we also categorize the VOC species according to the Henry's law constants as (1) insoluble species (isoprene), (2) slightly soluble species (MACR,

ACETALD, MVK and ISOPOOH with a $K_H^{\ominus}$ range of 4.8-300 M atm^{-1}), (3) moderately soluble species (HYAC, HCHO, MGLY and GLYALD with a $K_H^{\ominus}$ range of 3230-7700 M atm^{-1}) and (4) highly soluble organic acids [hydroxyacetic acid (GLYCAC), formic acid (HCOOH), glyoxylic acid (GLYOXAC), pyruvic acid (PYRAC), and oxalic acid (OXALAC) with a $K_H^{\ominus}$ range of 8900-5.0×10^8 M atm^{-1}].

3.2.2. Comparison of Three LES Resolutions

For a given set of initial conditions and forcing, *Sullivan and Patton* [2011] investigated the sensitivity and convergence of the LES and found simulations with 256^3 mesh points (with a $\Delta x \times \Delta y \times \Delta z$ of 20 m × 20 m × 8 m) or more were needed to estimate the high-order moments of conserved scalars from the resolved LES flow fields and resolve sharp gradients in scalars such as temperature. Based on these resolution tests, a higher LES resolution than that implemented by *Li et al.* [2016] may be necessary to accurately resolve the turbulent environment. Based on the fixed domain (14.4 km × 14.4 km × 4.8 km) described above, we test three mesh resolutions to examine the numerical convergence of the idealized LES simulations in the absence of chemistry.

Three resolutions were tested with a constant spacing for each mesh: (1) 96^3 grid points, representing a $\Delta x \times \Delta y \times \Delta z$ of 150 m × 150 m × 50 m, (2) 192^3 grid points, representing a $\Delta x \times \Delta y \times \Delta z$ of 75 m × 75 m × 25 m, and (3) 320^3 grid points, representing 45 m × 45 m × 15 m, to capture a range of resolutions within our computational resources. In these three varying-resolution simulations, clouds in the 192^3 and 320^3 simulations exhibit similar evolution patterns (Figure 3.1). As in

Li et al. [2016], the cloud top is defined as the maximum height where liquid water is present in the domain and the cloud base is defined as the minimum height where liquid water is present (Figure 3.1a). The cloud fraction is the horizontal fraction of the domain containing vertically integrated liquid water (or LWP>0; Figure 3.1b). Clouds in the 192^3 and 320^3 simulations develop around 1045 LT (Figure 3.1a) and reach the highest fraction (47%) at around 1130 LT (Figure 3.1b). Clouds in the 96^3 simulation form slightly earlier (Figure 3.1a), and the cloud fraction in the 96^3 simulation diverges from the other two simulations with higher resolutions (Figure 3.1b). Cloud fraction diverges (<10%) between the 192^3 and 320^3 simulations after 1200 LT (Figure 3.1b), with the 320^3 simulation simulating a slightly higher fraction.

As in the statistical analysis of *Sullivan and Patton* [2011], we select three time periods to compare the behaviors of the three resolutions after the turbulence is spun-up, representing (1) clear weather conditions before cloud formation (1000 LT), (2) a convective condition with peak cloud fraction (1200 LT), and (3) a weaker convective environment with dissipating clouds (1300 LT). For each vertical level, the mean values represent horizontally-averaged quantities (over the entire horizontal domain) that are temporally-averaged for 30-minute time periods surrounding the desired time (i.e., 0945-1015 LT, 1145-1215 LT and 1245-1315 LT). To investigate turbulent quantities, we define a fluctuation as a quantity's deviation from its instantaneous horizontal average.

To investigate the resolution dependence of the LES in simulating turbulence, we examine the total (resolved plus subgrid-scale, SGS) quantities of important

meteorological statistics, including liquid water potential temperature flux (WH), total water (vapor plus liquid) specific humidity flux (WQ), and turbulent kinetic energy (TKE). We note that liquid water potential temperature and total water specific humidity are conserved when undergoing reversible processes [*Deardorff*, 1976]. SGS contributions to WH, WQ, and TKE are estimated using a SGS eddy viscosity model [*Deardorff*, 1980].

The variation of WH, WQ and TKE from 1000 LT, 1200 LT to 1300 LT (Figure 3.2) is consistent with the cloud evolution in Figure 3.1. Cloud development at the two later times produces larger fluxes and TKE at high altitudes (1-3 km, Figure 3.2d-i). At 1200 LT and 1300 LT, WH, WQ and TKE show more divergence between simulations with different resolutions. In general, WH and TKE profiles show better convergence between the two finer-mesh simulations (192^3 and 320^3; Figure 3.2d, f, g, i). At 1300 LT, we find stronger WQ in coarser resolution simulations and weaker WQ in finer simulations (Figure 3.2h). Those discrepancies within 1 - 3 km highlight the resolution sensitivity of the LES, indicating that coarser model resolutions may overestimate moisture transport by clouds and thus potentially overestimate aqueous chemical reaction rates within cloud layers.

In summary, the statistics effectively converge with the 192^3 mesh resolution or higher, although there are some minor differences between the 192^3 and 320^3 mesh resolutions. We also note that these tests do not necessarily reflect resolution independence for the chemical reactants, however there is little difference between the 96^3 and 192^3 grids for the vertical profiles of reactive species such as isoprene

and chemical segregation values (<2%, results not shown). The high computational expense associated with including both gas- and aqueous-phase reactions makes the 320^3 grid mesh simulations impractical to perform within our available resources. We therefore select the 192^3 mesh for our simulations investigating the importance of aqueous-phase chemistry within clouds.

3.2.3. Simulations and Sampling Methods

To understand the importance of including aqueous-phase reactions in the LES chemical scheme, we simulate two scenarios using the meteorological environment and the 192^3 resolution including: (1) with gas phase chemistry only and aqueous-phase reactions turned off (scenario 1: NOAQU), and (2) with both gas- and aqueous-phase reactions (scenario 2: AQU).

We focus on changes in the chemistry and transport of BVOC caused by introducing aqueous-phase reactions. Aqueous-phase reactions occur only in liquid water present in the cloud layer (Figure 3.1a). To capture these small-structure changes where clouds are present, we select a cloudy column within the model domain for analysis of the impact of aqueous chemistry. We select a vertical column with high liquid water path (LWP) based on visual inspection at a time of peak cloud fraction (1200 LT in this case), hereinafter called the "cloudy column." This column has LWP larger than 160 g m^{-2} and is selected to highlight the detailed chemical processes occurring within clouds. This cloudy column is defined by $25 \times 25 \times 192$ grid points representing a 1875 m × 1875 m × 4800 m region. The column remains spatially fixed over time, thus clouds evolve within the column. We evaluate the

vertical profile within the column by horizontally-averaging over the cloudy column's horizontal extent and time-averaging over 30-minute intervals. To understand the temporal impacts of aqueous phase chemistry on the chemical species in the cloud layer , we evaluate aqueous chemistry in the 2-3 km altitude layer of the cloudy column and over the domain, respectively. In addition, an instantaneous vertical cross section of the LES domain that intersects with the center of the selected cloudy column is analyzed to compare and understand the meteorological versus chemical factors on BVOC mixing ratios and resulting chemistry.

3.3. Results

3.3.1. Meteorology

For both the NOAQU and AQU simulations, the meteorological initial conditions and forcing parameters are identical, as we make no changes to the meteorology between the simulations. In the simulation, clouds continually form and dissipate beginning at 1045 LT, with a cloud fraction ranging from 0% to 47% over the course of the simulation (Figure 3.1b). Cloud base is at 1.5 km and the cloud top reaches 3.5 km in the early afternoon (Figure 3.1a), with peak cloud fractions between 1100-1230 LT (Figure 3.1b). From 1000 LT to 1400 LT, ABL development is observed through the profiles of potential temperature (θ; K) and TKE ($m^2\ s^{-2}$) (Figure 3.3a, b). The ABL height is defined as the height where a bottom-up inert tracer emitted from the surface has a horizontal model domain averaged mixing ratio that is 0.5% of its surface value [*Kim et al.*, 2012; *Vilà-Guerau de Arellano et al.*, 2005]. The ABL height is around 1 km at 1000-1100 LT and starts

to increase rapidly after 1200 LT, reaching up to 3 km at 1400 LT. In the sub-cloud layer, near-surface θ increases about 5 K over this time period, while θ at 3 km decreases about 5 K, leading to a less stable atmospheric environment. TKE increases with time as surface heat fluxes increase throughout the day, with the largest values in the subcloud layer and a second local maximum emerging in the cloud layer (1-3.5 km) from 12-14 LT. Total water specific humidity (q; g kg^{-1}) decreases near surface but increases aloft based on initial profiles provided by reanalysis and sonde data (Figure 3.3c). Liquid water specific humidity (q_l; g kg^{-1}) increases at 1200 LT between 1-3 km, matching the convective environment indicated by strong TKE at this height (Figure 3.3d).

3.3.2. Cloud Sampling

Following the cloud sampling methods in section 2.3, we select a 30-minute period at 1200 LT (1145-1215 LT) with peak cloud fraction (Figure 3.1a) to identify a region of the domain with high liquid water. Figure 3.4a shows the horizontal distribution of the 30-minute averaged liquid water path (LWP) centered at 1200 LT. The domain primarily has LWP less than 200 g m^{-2}, a value within the expected range for shallow cumulus clouds (e.g., *Lenderink et al.* [2004]). A few high LWP regions are also observed in Figure 3.4a, indicating regions with deeper clouds and higher liquid water content. We select a region with high LWP (>240 g m^{-2}) to analyze the variations of BVOC under different phases of cloud evolution (Figure 3.4a; red box). The temporal evolution of q_l in this cloudy column (Figure 3.4b) shows temporally intermittent clouds from 1.5 km to 3.5 km altitude and therefore

our analysis of BVOC temporal variations in this cloudy column focuses on the 2-3 km altitude region (Figure 3.4b, grey dashed lines) (Section 4.1).

We use an instantaneous *x*-*z* cross section of meteorological and chemical variables at 1200 LT to study the effects of vertical transport of liquid water on chemical constituents. The instantaneous vertical cross section of q_l shows a cloud cluster (Figure 3.4c) with q_l of 1.6-2.0 g kg^{-1} in the main cloud region and higher mixing ratios at the top of the cloud. The cloud cluster has strong upward motion (w = 4 to 7 m s^{-1}) inside the clouds (Figure 3.4d), and weak downdrafts observed near cloud edges.

3.3.3. Vertical profiles of chemical species

For the AQU simulation, we investigate horizontally- and 30-minute averaged vertical profiles of isoprene (Figure 3.5a), primary isoprene oxidation products (Figure 3.5b-d) and HCHO (Figure 3.5e), together with OH, HO_2, RO_2, NO_2 and NO (Figure 3.5f-j). RO_2 is calculated as the sum of all the organic peroxy radicals in the LES chemical scheme. The mixing ratio profiles of the chemical variables display the total mixing ratio, or the sum of gas plus aqueous phase mixing ratios. The distribution of species in the ABL depends on both chemistry and turbulent mixing and here we discuss the vertical distribution of BVOC, HOx and NOx as simulated by the LES.

Emitted from the surface, isoprene rapidly reacts with OH in the gas phase. Mixing ratios are highest near the emissions source and then decrease rapidly with height due to chemical loss. Additionally, this decrease with height increases as OH

production increases during the day (e.g., from 1000 LT to 1400 LT). After 1100 LT, a small amount of isoprene is transported upward above cloud base (Figure 3.5 a), due in part to the strong upward motions in clouds.

Generally, isoprene oxidation products (MACR, MVK, HCHO and ISOPOOH) have vertical gradients with higher mixing ratios near the surface reflecting the near-surface isoprene source (Figure 3.5 b-e). In the morning (1000 LT) above 1km, MACR, MVK and HCHO mixing ratios are elevated due to the chemical initial conditions from P-3B measurements, representing observed oxidation products in a residual layer aloft. These mixing ratios are then depleted largely from 1000 LT to 1400 LT due to reactions with OH below 3 km (Figure 3.5 b, c, e). MACR, MVK and HCHO have longer lifetimes than isoprene, resulting in well-mixed mixing ratios below the cloud base (~1 km). About an hour after cloud formation, the vertical profiles of MACR, MVK and HCHO are also well mixed in the cloud layer (1-3 km) with lower mixing ratios. In contrast to the other BVOC oxidation products, ISOPOOH mixing ratios increase during the daytime. Its longer lifetime compared with the other BVOC species in Figure 3.5 [*Li et al.*, 2016] allows ABL motions to transport ISOPOOH aloft beginning at 1200 LT (Figure 3.5d).

OH mixing ratios are mainly controlled by photochemistry, thus its vertical profile (Figure 3.5f) reflects OH sources and sinks. Mixing ratios are lower near the surface (where reaction of OH and isoprene dominates) and higher aloft (details of OH sources and sinks are presented in section 4.2). As in *Li et al.* [2016], diurnal photolysis rates are calculated offline with the NCAR Tropospheric Ultraviolet and

Visible (TUV) Radiation Model [*Madronich and Flocke*, 1999]. TUV-calculated photolysis rates peak at around 1315 LT in the simulations, leading to OH increasing beyond local noon. HO_2 vertical profiles are similar to OH due to fast conversion reactions between OH and HO_2 (Figure 3.5g). NO_2 vertical profiles (Figure 3.5i) show decreasing near-surface mixing ratios and increasing upward transport from 1000 LT to 1400 LT. Atmospheric photochemical conversion between NO and NO_2 leads to a similar variation of NO vertical profiles (Figure 3.5j) as NO_2.

3.4. Effects of Aqueous Chemistry on Chemistry in the ABL

To investigate the impacts of aqueous-phase reactions on BVOC, we evaluate the two simulations with (AQU) and without (NOAQU) aqueous-phase reactions for the vertical changes of total (gas + aqueous) mixing ratios at 1200 LT and the temporal evolution within the cloud layer (2-3 km) for the cloudy column and the entire LES domain. The changes due to aqueous chemistry in the cloudy column reflect the effects of aqueous processes in clouds, and the domain-wide changes evaluate aqueous chemistry effects on a regional scale. Segregation between the key BVOC species and OH are also calculated and compared with prior studies.

To obtain average vertical profiles in the cloudy column, mixing ratios at each model level are horizontally averaged over the column region and temporally averaged for the 30-minute time period centered on the desired time (i.e., 1145-1215 LT). Similarly, domain-wide vertical profiles are averaged horizontally over the entire LES simulation domain. To study the temporal evolution of the chemical species, their mixing ratios are horizontally averaged over the column region or the

domain, and then vertically averaged for all grid points spanning the 2-3 km altitude region. Spatial standard deviations are applied only on the averaged quantities related to the cloudy column, reflecting the magnitude of mixing ratio variations relative to this average over the horizontal extent of the cloudy column and the 2-3 km region at each time interval.

3.4.1. In-cloud Temporal Evolution of Chemistry

We investigate the temporal variations within the 2-3 km altitude layer of the selected cloudy column (Figure 3.4a) and the whole domain over the time period of dominant cloud formation. In the cloudy column, three cloud clusters develop at around 1200 LT, 1300 LT and 1330 LT (Figure 3.4b). Clouds lead to strong upward transport, increasing mixing ratios that correspond to q_l variation and updrafts (Figure 3.4d). BVOC and oxidant mixing ratios in the cloud layer change on a similar time scale as q_l, with mixing ratios of the two simulations diverging when q_l increases (Figure 3.6).

Prior to cloud development at 2-3 km, the isoprene mixing ratio is very low (~ 5 pptv), similar to isoprene mixing ratios simulated by [*Kim et al.*, 2012]. As clouds develop in the column, convective motion transports isoprene upward and isoprene mixing ratios increase up to 140 pptv (i.e., when $q_l > 0$ g kg^{-1}). Isoprene mixing ratios quickly decrease when clouds dissipate or exit the predefined column (Figure 3.6a), which could be due to its fast reaction with OH. When looking beyond the cloudy column to the full domain, the domain-wide averaged q_l (~0.05 g kg^{-1} peak

values) is much lower than the cloudy column (~0.2-0.6 g kg^{-1} peak values) yet domain-averaged isoprene increases by about ~10 pptv at 2-3 km (Figure 3.6e).

MACR decreases from 1030 LT to 1130 LT before cloud formation due to its gas-phase reaction with OH, and reaches 30 pptv by midday. Similar to isoprene, MACR mixing ratios increase within convective updrafts and decrease in the absence of clouds (Figure 3.6b). Domain-averaged MACR increases 15% in the AQU simulation as compared to the NOAQU simulation (Figure 3.6f). In the AQU simulation, OH reductions (Figure 3.6c) slow BVOC oxidation rates and increase the peak mixing ratios of isoprene and MACR slightly higher than the NOAQU simulation (Figure 3.6a, b).

The mixing ratios of OH increase from 1030 LT to 1430 LT due to photochemical production during midday (Figure 3.6c). In the NOAQU simulation, OH increases sharply when q_l increases, then decreases after each cloud event. In the AQU simulation, OH decreases by up to 25% of the NOAQU simulation values when q_l increases, signifying the effects of adding aqueous-phase reactions in the AQU simulation (Figure 3.6c; Table 3.1). Gas-phase chemistry also contributes to its depletion; for example, segregation of NO and HO_2 induced by their solubility differences reduces OH production in the presence of clouds. However, the gas phase contribution is much smaller than contributions from aqueous phase chemistry (discussed in section 4.2). The BVOC lifetime (according to their reaction rates with OH) is inversely proportional to the OH mixing ratio [*Li et al.*, 2016]. Therefore, the 25% OH decrease within the cloudy column in the AQU simulation

leads to a 33% increase of BVOC lifetimes in clouds. Domain-averaged OH shows a smaller divergence between the AQU and the NOAQU simulations (Figure 3.6g), which could result from regions without the OH decrease in the AQU simulation or without the OH enhancement in the NOAQU simulation, eliminating the accumulated effects of aqueous processes. HCHO concentrations are initialized at ~2 ppbv in the 2-3 km cloud layer based on P-3B observations. However, the model lacks emissions of anthropogenic VOC that would contribute to HCHO formation, therefore concentrations decrease between 0830-1145 LT. After cloud formation, HCHO shows a relatively constant mixing ratio (1.2 ppbv) when q_l decreases to zero in the NOAQU simulation (Figure 3.6d), indicating a balance of its photochemical sources and sinks. Adding aqueous-phase reactions (AQU simulation) decreases the HCHO mixing ratio by 0.2 ppbv (17%), due to its solubility and fast consumption by aqueous-phase OH. This reduction is similar to decreasing HCHO mixing ratios simulated with aqueous chemistry by *Lelieveld and Crutzen* [1991], *Barth et al.* [2003], and others (e.g. *Chameides and Davis* [1982], *Chameides* [1984] or *Jacob* [1986]). The lifetime of HCHO is longer than isoprene, MACR and OH [*Li et al.*, 2016]; therefore, aqueous chemistry could also have an accumulated effect on HCHO variation. Including aqueous-phase processes not only decreases HCHO when clouds exist, but also steadily decreases mixing ratios in the cloud layer over the course of the simulation. Domain-wide HCHO variations also show an accumulated effect of aqueous processes, with an 18% decrease in the AQU simulation compared to the NOAQU simulation at 1430 LT (Figure 3.6h). Compared with the updated chemical mechanism with both gas- and aqueous- phase reactions, this suggests that gas-

phase only mechanisms may overestimate HCHO by about 18% in the early afternoon during convective cloud events. We note that anthropogenic emissions are not included in these simulations and this could affect the magnitude of in-cloud HCHO changes.

ISOPOOH shows an increasing trend over time (not shown), signifying an accumulation of this BVOC oxidation product in the cloud layer due to its longer lifetime than isoprene, MACR, MVK and the HO_x species [*Li et al.*, 2016]. No difference between the two simulations is observed for the ISOPOOH time series (Figure 3.6g), indicating that aqueous chemistry does not affect ISOPOOH mixing ratios. We note that ISOPOOH is treated as slightly soluble in the LES. We use a deposition velocity of 0.909 cm s^{-1} for ISOPOOH in the simulations, which is lower than the deposition velocity of 1.5±0.4 cm s^{-1} used by *Wolfe et al.* [2015] for ISOPOOH+ isoprene dihydroxyepoxides (IEPOX). Compared with the NOAQU simulation, NO_x also show enhanced mixing rations in the AQU simulation (not shown), resulted from a decrease of HO_x.

3.4.2. Effects of Aqueous Chemistry on the Profiles of Chemical Species

Vertical profiles of total (gas plus aqueous) mixing ratios of key BVOC species, oxidation products, and oxidants horizontally-averaged reveal differences between the two simulations in the cloudy (q_l > 0 g kg^{-1}) layer from 1 to 3 km (Figure 3.7). In the cloudy column (Figure 3.7a-d), isoprene mixing ratios increase about 20 pptv in the cloud layer (1-3 km) when aqueous chemistry is included (Figure 3.7a). In addition, MACR increases 15 pptv (about 20%; Figure 3.7b) and mixing ratios of OH

and HCHO decrease up to 20-25% due to the aqueous-phase reactions (Figure 3.7c, d). As was shown with the temporal evolution of HCHO (Figure 3.6d), aqueous-phase chemistry depletes HCHO and reduces HCHO mixing ratios in the cloudy column by 20% compared to gas-phase only chemistry (Figure 3.7d). Compared with the cloudy column, domain-wide profiles show smaller changes in the chemical species between the AQU and the NOAQU simulations (Figure 3.7e-h), with about a 14% increase for MACR, 18% decrease for OH and 18% decrease for HCHO.

To understand the effects of aqueous chemistry on the key chemical species, we focus on the cloudy column where the impacts are the greatest. The decrease of OH with the addition of aqueous chemistry mainly results from the rapid oxidation of HCHO in clouds (Figure 3.8). In the NOAQU simulation, OH is chemically produced through reactions of HO_2 and NO, and O_3 photolysis (Figure 3.8a), and is depleted primarily through reaction with CO and HCHO (Figure 3.8b). Compared with the total (sum of aqueous- and gas- phase) production and loss rates in the NOAQU simulation (Figure 3.8a, b), the total OH production rate increases slightly (about 5%) in the cloud layer in the AQU simulation, and the total loss rate increases about 30% on average (Figure 3.8c, d), leading to a net loss in OH production. While the aqueous-phase O_3 + HO_2 reaction is an important pathway that increases the OH production in the cloudy column (about 10%) (Figure 3.8c), it is offset by the aqueous HCHO oxidation with OH, which is the dominant loss pathway for OH and contributes more than 90% of the change in the OH loss in the cloud layer. This is followed by the aqueous-phase reaction of OH and CH_3OH, which contributes about 30% of the change in the OH loss (Figure 3.8d), although we note that the high

mixing ratios of CH_3OH (~6.5 ppbv measured by P-3B in the ABL) at the Fair Hill site in the 2011 DISCOVER-AQ campaign contribute to the importance of this reaction in the budget. Other primary loss pathways for OH are the aqueous-phase reactions of OH and GLYALD, OH and HCOOH, and OH and MGLY, contributing about 8%, 5% and 2% of the change in the OH loss in the cloud layer, respectively (Figure 3.8d). These results for OH sources and losses are qualitative only, because the LES model was configured such that Henry's Law equilibrium is used to estimate OH aqueous-phase concentrations, resulting in higher OH aqueous-phase concentrations than found by other models (e.g., *Tilgner et al.* [2013]). HO_2 dissolves in the aqueous phase more easily than OH, which further suppresses gas-phase reactions that reform OH [*Chameides and Davis*, 1982]. For example, the OH production rate through the reaction of HO_2 and NO decreases by about 10% in the AQU simulation (Figure 3.8c) compared with that in the NOAQU simulation (Figure 3.8a). These results suggest that the lack of aqueous-phase reactions could overestimate OH in the cloud layer. We note that because aqueous chemistry changes the vertical gradient of each species, turbulent transport may also play a role in decreasing OH; however, this term contributes less than 1% to the OH decrease (not shown) and is therefore small compared to aqueous HCHO oxidation.

Decreased oxidants lower the reaction rates of the BVOC chemistry, resulting in increased mixing ratios of isoprene and its primary oxidation products (e.g., MVK and MACR). ISOPOOH has a longer lifetime (2.7 hr with respect to OH gas-phase oxidation [*Li et al.*, 2016]) than other species like MACR and MVK, and is only slightly soluble in the aqueous phase. ISOPOOH mixing ratios are similar in the two

simulations (not shown), reflecting the lack of aqueous-phase reaction of ISOPOOH and the similar gas-phase net production rates of ISOPOOH calculated under both scenarios (Figure S1).

3.4.3. Segregation

Understanding chemical production and loss rates is crucial to interpret the oxidation and vertical distribution of the BVOC species. However, these chemical reactions are influenced by turbulent mixing caused by eddies at various scales, from the Kolmogorov to the ABL scale. Numerical models that do not resolve turbulence typically ignore the effects of turbulent mixing by assuming constituents are well mixed. The LES resolves the energy-containing turbulent scales of motion thereby permitting investigation of the effects of insufficient mixing on chemical production and loss rates.

We calculate the intensity of segregation (I_s) between OH and the BVOC species to study the impact of aqueous-phase chemistry on turbulence-induced modification to their overall reaction rate. I_s is calculated as:

$$I_s = \frac{\overline{VOC_\iota' \; OH'}}{\overline{VOC_\iota}\,\overline{OH}}, \qquad (2)$$

which is the covariance between a BVOC species and OH ($\overline{\mathrm{VOC}_\iota' \mathrm{OH}'}$, where the overbar represents a horizontal average across the entire LES domain, and the $'$ represents a deviation from that average) divided by the product of the horizontally-averaged BVOC ($\overline{\mathrm{VOC}_\iota}$) and OH ($\overline{\mathrm{OH}}$). Negative I_s indicates a reduction in the reaction rate due to segregation of the reactants and positive I_s represents an

increase in the reaction rate [*Karl et al.*, 2007; *Li et al.*, 2016; *Molemaker and Vilà-Guerau de Arellano*, 1998; *Verver et al.*, 1997].

We calculate I_s for OH and isoprene and OH and MACR over the entire LES domain for the two simulations at each time step. Domain-wide influences of segregation can be used to study the turbulence-induced impacts at a scale comparable to regional atmospheric chemistry models (~14 km). Because a cloud fraction larger than 30% is maintained in the domain after cloud formation (Figure 3.1b), continuous positive or negative I_s values are calculated in the cloud layer (Figure 3.9). In the NOAQU simulation, positive I_s values in the cloud layer (Figure 3.9a, b) indicate higher reaction rates between OH and the BVOC species than one would predict in the absence of turbulence consistent with *Ouwersloot et al.* [2011] analysis of OH-isoprene segregation. Strong positive I_s occurs near or above the top of the clouds (Figure 3.9a, b). The positive correlations are predominantly due to chemical transformations (Figure 3.10a) leading to the very low mixing ratios of these species in the free troposphere (Figure 3.5), which will be further discussed below using the covariance budget. In our case with non-precipitating clouds, adding aqueous-phase chemistry leads to a decrease in the reaction rates of OH and isoprene by about 20-40%, consistent with an up to 39±7% reduction of the isoprene-OH reaction rate in the cloud layer observed by *Karl et al.* [2007], and OH and MACR by about 10% in the cloud layer over the domain. We note the relatively low mixing ratios of isoprene at this altitude (Figure 3.7a), suggesting that the impact of the isoprene-OH segregation should not significantly change peroxy radical production at this altitude. In the AQU simulation, the reactions of OH and

MVK, OH and MGLY, OH and ACETALD, and NO and HO_2 also exhibit negative I_s in the cloud layer over the domain (Figure S2). The impacts of turbulence on the reaction rates of OH and MVK, OH and MGLY, and NO and HO_2 are comparable spatially but weaker in magnitude (5-10%) than on the reaction of OH and MACR, and the impact on reaction rate of OH and ACETALD is minor (<5%).

To understand the processes controlling segregation between isoprene and OH in the modeling domain, we calculate the covariance budget as follows:

$$\partial\langle\overline{(C_5H_8)'(OH)'}\rangle/\partial t = -\langle\overline{w'(C_5H_8)'}\partial\overline{(OH)}/\partial z\rangle - \langle\overline{w'(OH)'}\partial\overline{(C_5H_8)}/\partial z\rangle - \partial\langle\overline{w'(C_5H_8)'(OH)'}/\partial z\rangle - \langle\overline{(C_5H_8)'(\partial\tau_{wOH}/\partial z)}\rangle - \left\langle\overline{(OH)'\left(\partial\tau_{wC_5H_8}/\partial z\right)}\right\rangle + \partial\langle\overline{(C_5H_8)'(OH)'}\rangle/\partial t\,|_{chem} \quad (3)$$

where $'$ indicates deviation from the horizontal average, the overline denotes horizontal average, angle brackets denote the time average, and τ_{wOH} and $\tau_{wC_5H_8}$ denote the subgrid stress for OH and C_5H_8, respectively [*Kim et al.*, 2004; *Moeng and Sullivan*, 1994]. The term on the left hand side is the tendency of covariance between isoprene and OH, while the terms on the right hand side show how this covariance is generated. The first two terms on the right hand side are the gradient production of the covariance between isoprene and OH, the third term represents the turbulent transport of the two species, and the fourth and fifth terms are SGS diffusion terms [*Schumann*, 1989; *Vinuesa and De Arellano*, 2003]. The last term on the right hand side is the net production/destruction of covariance from

chemical transformations, which is calculated as the residual of the covariance budget.

The covariance budget is important in understanding the processes controlling segregation. Figure 3.10 shows the profiles of the budget terms horizontally-averaged over the model domain at 1200 LT under the NOAQU and AQU simulations. In the NOAQU simulation, gradient production enhances the covariance of isoprene and OH below the cloud base (around 1 km), while turbulent transport increases the covariance near surface (below 0.2 km) (Figure 3.10a). The chemistry term also increases the covariance near surface, indicating an increase in segregation. Because of the rapid chemistry near the surface, SGS chemistry may be important to the isoprene-OH segregation [*Vinuesa et al.*, 2006; *Vinuesa and Porté-Agel*, 2005], but SGS chemistry is currently neglected. The SGS diffusion term in the NOAQU simulation shifts from negative to positive below 0.5 km, with a relatively small contribution to the covariance budget. In the cloud layer (around 1-3 km), chemistry becomes the main contributor to the covariance budget while other terms are all negligible (Figure 3.10a).

The contributions of the different budget terms are similar below the cloud base (around 1 km) between the two scenarios (Figure 3.10a, b). At cloud base in AQU, there is a strong increase in the contributions from chemistry and turbulent transport (Figure 3.10b), matching the positive I_s values at the cloud base at around 1200 LT (Figure 3.9c). The positive I_s results from the positive covariance of gas-phase OH and isoprene mixing ratios at that height, due in part to the strong upward

motions in clouds. In the cloud layer (around 1-3 km), chemistry drives a positive correlation in the NOAQU simulation (Figure 3.10a) but increases segregation in the AQU simulation (Figure 3.10b), which supports our previous discussion regarding the importance of including aqueous-phase reactions in section 4.1 and 4.2. The covariance budget is also calculated at 1330 LT, and the results are similar to the budget calculated at 1200 LT (not shown).

Based on the importance of chemistry in cloud layers, we further investigate the profiles of I_s for reactions of isoprene and OH, MACR and OH, and their fluxes averaged over the entire horizontal domain and over a 30-minute period at 1200 LT for the two scenarios (Figure 3.11). The magnitude of segregation in the cloud layer is similar between the NOAQU and AQU simulations, but with opposite sign (Figure 3.11a, b). While the OH chemical lifetime is estimated to be very short (~1 s in the gas phase), it is likely that OH survives in the atmosphere longer than one might expect from solely a chemistry perspective because of turbulence-induced segregation of reactants (i.e., insufficient mixing as quantified by I_s); an effect which results in a vertical flux of OH despite its short chemical lifetime. Resolved vertical flux profiles of isoprene and MACR are similar between the two simulations (Figure 3.11c, d), yet there is a large decrease in the vertical flux of OH in the cloud layer due to its aqueous chemistry (dominated by HCHO) (Figure 3.11e). This suggests that the loss of OH through aqueous chemistry is the dominant driver of the change in the sign of segregation in the cloud layer.

Instantaneous vertical cross sections of OH and isoprene under the two scenarios (Figure S3) also show the importance of changes in OH on the segregation in clouds. Consistent with the liquid water vertical cross section (Figure 3.4c), OH mixing ratios in clouds are higher than the surrounding atmosphere in the NOAQU simulation. In the AQU simulation, OH mixing ratios decrease within the cloud cluster. Vertical motion within the cloud transports isoprene upward under both scenarios, but in the AQU simulation isoprene mixing ratios are slightly higher due to aqueous reactions that consume substantial OH. While strong segregation between isoprene and OH in the cloud layer reduces reaction rates by 20-40%, the low isoprene mixing ratios in the cloud layer (< 0.10 ppbv) indicate this will likely not significantly decrease the overall chemical loss rate of isoprene in the ABL.

In this study, the LES with aqueous chemistry simulated segregation reduces reaction rates of isoprene and OH by about 10% near the surface, and by about 20-40% in the cloud layer. *Ouwersloot et al.* [2011] simulated similar near-surface segregation for isoprene and OH (10%) with homogeneous surface emission, and found an up to 20% reduction in isoprene-OH reaction rates with heterogeneous surface emissions. Other uncertainties, such as chemical mechanisms, emissions uncertainties and the alteration of photolysis rates by clouds are known to influence BVOC reaction rates at a similar or greater magnitude. This work quantifies the chemistry-turbulence interaction rate under convective conditions, which improves our understanding of effects of chemical and mixing on the key chemical species.

3.4.4. Formation and Transport of Organic Acids

The addition of aqueous phase reactions from Table 3.1 introduces the formation of aqueous-phase organic acids. These compounds (e.g., HCOOH, GLYCAC, GLYOXAC, OXALAC and PYRAC) form only through aqueous-phase reactions in the LES chemical mechanism, therefore their mixing ratios are zero in the NOAQU simulation. Once formed in the aqueous phase, they can be oxidized by OH and H_2O_2. The remaining acids enter the gas phase as liquid cloud water evaporates, thereby influencing mixing ratios in both phases. The dominant organic acids are HCOOH, which is mainly formed through the aqueous OH oxidation of HCHO, and GLYCAC (Figure 3.12), which is produced by the OH oxidation of a third-generation isoprene oxidation product GLYALD (Table 3.1). Other acids formed in the mechanism are GLYOXAC (produced from the OH oxidation of CHOCHO) and PYRAC and OXALAC, formed from MGLY (Table 3.1).

Mixing ratios of these organic acids averaged over the simulation domain increase gradually in the cloud layer (2-3 km) after clouds develop at about 1030 LT (Figure 3.1). The organic acids accumulate over the afternoon and are mixed down towards the surface by turbulence resulting in a gradual increase of near-surface mixing ratios. Due to fast turbulence mixing with a turnover time of the ABL of ~13 min [*Li et al.*, 2016], near-surface mixing ratios reach about 20% of the mixing ratios in the cloud layer within one hour after cloud formation, which occurs at around 1200 LT when the first cloud cluster develops (Figure 3.4b). The mixing ratios of HCOOH, GLYCAC, GLYOXAC, OXALAC and PYRAC in the cloud layer then increase to 560 pptv, 100 pptv, 3.9 pptv, 0.26 pptv and 25 pptv at 1430 LT, with their near-

surface mixing ratios reaching up to 320 pptv, 70 pptv, 2.5 pptv, 0.15 pptv and 10 pptv, respectively, eventually reaching about 50% of their mixing ratios in the cloud layer. These mixing ratios are within the expected range of their measured or simulated values in the atmosphere (e.g., *Ervens et al.* [2011]; *Jardine et al.* [2010]; *Lim et al.* [2010]). Vertical profiles of organic acids are consistent with their observed vertical structures with peak values aloft (e.g., HCOOH measured by *Chapman et al.* [1995]). Overall, the LES results suggest that organic acids that are formed in clouds can mix within the boundary layer on the time scale of one hour (Figure 3.12), indicating the importance of convection and turbulence in understanding the formation and fate of these compounds.

3.5. Conclusions

In this study, we investigate the impacts of cloud aqueous processes on the chemistry and transport of BVOC using a LES model with an updated chemical mechanism including both gas- and aqueous-phase reactions. We design the experiments based on a meteorological case with a diurnal pattern of non-precipitating cumulus clouds from the Baltimore-Washington area DISCOVER-AQ campaign [*Li et al.*, 2016]. We test three mesh resolutions in the LES and find acceptable convergence of the meteorological profiles with the 192^3 mesh resolution with 25 m grid height. Using this resolution, we simulate two scenarios with and without aqueous-phase reactions to understand the importance of including aqueous-phase reactions in the boundary layer in BVOC-dominated environments.

In cloud-dominated regions with no aqueous chemistry (NOAQU simulation), mixing ratios of all chemical species increase inside the cloud compared to outside the cloud, indicating the importance of convection in transporting surface-emitted species or species produced near the surface to regions aloft. Including aqueous chemical reactions (AQU simulations) decreases HCHO up to 18% over the domain due to its solubility and the aqueous-phase oxidation by OH, which subsequently results in consumption of the HO_x species. These results suggest that omitting aqueous-phase reactions in the chemical mechanism could overestimate HO_x and HCHO in the cloud layer. As a result of decreasing HO_x, mixing ratios of isoprene and MACR increase over the domain (100% and 15%, respectively) in the cloud layer when aqueous-phase reactions are included in the chemical mechanism.

Turbulence-resolving simulation (e.g., LES) provides information on whether reactants are well mixed or segregated, which affects reactivity in the ABL. Aqueous-phase chemistry changes the sign of the covariance between BVOC (e.g., isoprene) and OH from positive to negative, producing segregation between BVOC and OH and therefore slower effective reaction rates. We find that aqueous chemistry can increase the intensity of segregation between OH and the BVOC species by up to 20-40% for the isoprene-OH reaction and 10% for MACR-OH reaction. Analysis of the covariance budget shows that the strong segregation in clouds is mainly driven by the chemical reactivity term, triggered by the decrease in OH through aqueous phase consumption.

Organic acids, noted SOA precursors formed in clouds via aqueous reactions,

are included in the LES chemical mechanism. Our simulations show that these acids accumulate as the afternoon and cloud conditions progress. Turbulent mixing leads to enhanced near-surface mixing ratios of organic acids, reaching about 20% of the mixing ratios in the cloud layer within one hour after cloud formation, with the percentages increasing up to 50% at the end of the simulation (1430 LT).

Overall, this study quantifies the effect of aqueous chemistry on gas-phase chemistry and reactivity for a particular set of initial conditions and forcing. We emphasize that the conclusions presented are based on LES simulations with homogeneous surface conditions and a simplified emission inventory without anthropogenic VOC emissions. Heterogeneous surface emissions for isoprene, the inclusion of anthropogenic VOC, and representing higher order VOC chemistry require further exploration.

Acknowledgments

This research is supported by NASA Earth and Space Science Fellowship (NESSF) NNX13AN76H and the Barbour Scholarship at the University of Michigan. The National Center for Atmospheric Research is sponsored by the National Science Foundation. We gratefully acknowledge the NCAR Graduate Visitor Program for supporting the collaboration and the development of the NCAR LES model. This manuscript was submitted to *Journal of Geophysical Research: Atmospheres,* and is currently under review. We acknowledge the co-authors, Mary C. Barth, Edward G. Patton and Allison L. Steiner, for providing guidance on this work.

3.6. References

Atkinson, R. (2000), Atmospheric chemistry of VOCs and NOx, *Atmos Environ*, *34*(12–14), 2063-2101, doi:http://dx.doi.org/10.1016/S1352-2310(99)00460-4.

Barth, M., M. Bela, A. Fried, P. Wennberg, J. Crounse, J. St Clair, N. Blake, D. Blake, C. Homeyer, and W. Brune (2016), Convective transport and scavenging of peroxides by thunderstorms observed over the central US during DC3, *Journal of Geophysical Research: Atmospheres*, *121*(8), 4272-4295.

Barth, M., S. Sillman, R. Hudman, M. Jacobson, C. H. Kim, A. Monod, and J. Liang (2003), Summary of the cloud chemistry modeling intercomparison: Photochemical box model simulation, *Journal of Geophysical Research: Atmospheres*, *108*(D7).

Barth, M. C., P. G. Hess, and S. Madronich (2002), Effect of marine boundary layer clouds on tropospheric chemistry as analyzed in a regional chemistry transport model, *Journal of Geophysical Research: Atmospheres*, *107*(D11), AAC 7-1-AAC 7-12, doi:10.1029/2001JD000468.

Barth, M. C., et al. (2007), Cloud-scale model intercomparison of chemical constituent transport in deep convection, *Atmos. Chem. Phys.*, *7*(18), 4709-4731, doi:10.5194/acp-7-4709-2007.

Barth, M. C., A. L. Stuart, and W. C. Skamarock (2001), Numerical simulations of the July 10, 1996, Stratospheric-Tropospheric Experiment: Radiation, Aerosols, and Ozone (STERAO)-Deep Convection experiment storm: Redistribution of soluble tracers, *Journal of Geophysical Research: Atmospheres*, *106*(D12), 12381-12400, doi:10.1029/2001JD900139.

Berg, L., M. Shrivastava, R. Easter, J. Fast, E. Chapman, Y. Liu, and R. Ferrare (2015), A new WRF-Chem treatment for studying regional-scale impacts of cloud processes on aerosol and trace gases in parameterized cumuli, *Geoscientific Model Development*, *8*(2), 409-429.

Blando, J. D., and B. J. Turpin (2000), Secondary organic aerosol formation in cloud and fog droplets: a literature evaluation of plausibility, *Atmos Environ*, *34*(10), 1623-1632, doi:10.1016/S1352-2310(99)00392-1.

Bower, K., T. Choularton, M. Gallagher, R. Colvile, K. Beswick, D. Inglis, C. Bradbury, B. Martinsson, E. Swietlicki, and O. Berg (1999), The great dun fell experiment 1995: An overview, *Atmospheric research*, *50*(3), 151-184.

Carlton, A. G., B. J. Turpin, K. E. Altieri, S. Seitzinger, A. Reff, H.-J. Lim, and B. Ervens (2007), Atmospheric oxalic acid and SOA production from glyoxal: Results of aqueous photooxidation experiments, *Atmos Environ*, *41*(35), 7588-7602.

Carlton, A. G., B. J. Turpin, K. E. Altieri, S. P. Seitzinger, R. Mathur, S. J. Roselle, and R. J. Weber (2008), CMAQ model performance enhanced when in-cloud secondary organic aerosol is included: comparisons of organic carbon predictions with measurements, *Environmental science & technology*, *42*(23), 8798-8802.

Carmichael, G. R., and L. K. Peters (1986), A second generation model for regional-scale transport/chemistry/deposition, *Atmospheric Environment (1967)*, *20*(1), 173-188.

Chameides, W. L. (1984), The photochemistry of a remote marine stratiform cloud, *Journal of Geophysical Research: Atmospheres*, *89*(D3), 4739-4755.
Chameides, W. L., and D. D. Davis (1982), The free radical chemistry of cloud droplets and its impact upon the composition of rain, *Journal of Geophysical Research: Oceans*, *87*(C7), 4863-4877, doi:10.1029/JC087iC07p04863.
Chang, J., R. Brost, I. Isaksen, S. Madronich, P. Middleton, W. Stockwell, and C. Walcek (1987), A three‐dimensional Eulerian acid deposition model: Physical concepts and formulation, *Journal of Geophysical Research: Atmospheres*, *92*(D12), 14681-14700.
Chapman, E. G., W. Gustafson Jr, R. C. Easter, J. C. Barnard, S. J. Ghan, M. S. Pekour, and J. D. Fast (2009), Coupling aerosol-cloud-radiative processes in the WRF-Chem model: Investigating the radiative impact of elevated point sources, *Atmospheric Chemistry and Physics*, *9*(3), 945-964.
Chapman, E. G., D. V. Kenny, K. M. Busness, J. M. Thorp, and C. W. Spicer (1995), Continuous airborne measurements of gaseous formic and acetic acids over the western North Atlantic, *Geophysical Research Letters*, *22*(4), 405-408, doi:10.1029/94GL03023.
Chen, J., R. Griffin, A. Grini, and P. Tulet (2007), Modeling secondary organic aerosol formation through cloud processing of organic compounds, *Atmospheric Chemistry and Physics*, *7*(20), 5343-5355.
Cotton, W. R., G. D. Alexander, R. Hertenstein, R. L. Walko, R. L. McAnelly, and M. Nicholls (1995), Cloud venting — A review and some new global annual estimates, *Earth-Science Reviews*, *39*(3–4), 169-206, doi:http://dx.doi.org/10.1016/0012-8252(95)00007-0.
Deardorff, J. (1976), Clear and cloud-capped mixed layers, their numerical simulation, structure and growth and parameterization, paper presented at Seminars on the Treatment of the Boundary Layer in Numerical Weather Prediction.
Deardorff, J. (1980), Stratocumulus-capped mixed layers derived from a three-dimensional model, *Boundary-Layer Meteorol*, *18*(4), 495-527, doi:10.1007/BF00119502.
Ervens, B. (2015), Modeling the Processing of Aerosol and Trace Gases in Clouds and Fogs, *Chemical Reviews*, *115*(10), 4157-4198.
Ervens, B., A. G. Carlton, B. J. Turpin, K. E. Altieri, S. M. Kreidenweis, and G. Feingold (2008), Secondary organic aerosol yields from cloud‐processing of isoprene oxidation products, *Geophysical Research Letters*, *35*(2).
Ervens, B., S. Gligorovski, and H. Herrmann (2003), Temperature-dependent rate constants for hydroxyl radical reactions with organic compounds in aqueous solutions, *Physical Chemistry Chemical Physics*, *5*(9), 1811-1824.
Ervens, B., B. J. Turpin, and R. J. Weber (2011), Secondary organic aerosol formation in cloud droplets and aqueous particles (aqSOA): a review of laboratory, field and model studies, *Atmos. Chem. Phys.*, *11*(21), 11069-11102, doi:10.5194/acp-11-11069-2011.

Fu, T.-M., D. J. Jacob, and C. L. Heald (2009), Aqueous-phase reactive uptake of dicarbonyls as a source of organic aerosol over eastern North America, *Atmos Environ*, *43*(10), 1814-1822.
Fu, T. M., D. J. Jacob, F. Wittrock, J. P. Burrows, M. Vrekoussis, and D. K. Henze (2008), Global budgets of atmospheric glyoxal and methylglyoxal, and implications for formation of secondary organic aerosols, *Journal of geophysical research: atmospheres*, *113*(D15).
Goldstein, A. H., and I. E. Galbally (2007), Known and Unexplored Organic Constituents in the Earth's Atmosphere, *Environmental Science & Technology*, *41*(5), 1514-1521, doi:10.1021/es072476p.
Guenther, A., et al. (1995), A global model of natural volatile organic compound emissions, *Journal of Geophysical Research: Atmospheres*, *100*(D5), 8873-8892, doi:10.1029/94JD02950.
Guenther, A., T. Karl, P. Harley, C. Wiedinmyer, P. I. Palmer, and C. Geron (2006), Estimates of global terrestrial isoprene emissions using MEGAN (Model of Emissions of Gases and Aerosols from Nature), *Atmos. Chem. Phys.*, *6*(11), 3181-3210, doi:10.5194/acp-6-3181-2006.
Hegg, D. A., and P. V. Hobbs (1979), The homogeneous oxidation of sulfur dioxide in cloud droplets, *Atmospheric Environment (1967)*, *13*(7), 981-987.
Hegg, D. A., and P. V. Hobbs (1981), Cloud water chemistry and the production of sulfates in clouds, *Atmospheric Environment (1967)*, *15*(9), 1597-1604.
Hegg, D. A., and P. V. Hobbs (1982), Measurements of sulfate production in natural clouds, *Atmospheric Environment (1967)*, *16*(11), 2663-2668.
Herrmann, H., D. Hoffmann, T. Schaefer, P. Bräuer, and A. Tilgner (2010), Tropospheric aqueous‐phase free‐radical chemistry: Radical sources, spectra, reaction kinetics and prediction tools, *ChemPhysChem*, *11*(18), 3796-3822.
Herrmann, H., T. Schaefer, A. Tilgner, S. A. Styler, C. Weller, M. Teich, and T. Otto (2015), Tropospheric aqueous-phase chemistry: kinetics, mechanisms, and its coupling to a changing gas phase, *Chemical reviews*, *115*(10), 4259-4334.
Horowitz, L. W., et al. (2003), A global simulation of tropospheric ozone and related tracers: Description and evaluation of MOZART, version 2, *Journal of Geophysical Research: Atmospheres*, *108*(D24), 4784, doi:10.1029/2002JD002853.
Hozumi, K., T. Harimaya, and C. Magono (1982), The size distribution of cumulus clouds as a function of cloud amount, *Journal of the Meteorological Society of Japan*, *60*(2), 691-699.
Husain, L. (1989), A technique for determining in‐cloud formation of SO4, *Geophysical research letters*, *16*(1), 57-60.
Husain, L., B. Ghauri, K. Yang, A. R. Khan, and O. Rattigan (2004), Application of the SO 4 2−/Se tracer technique to study SO 2 oxidation in cloud and fog on a time scale of minutes, *Chemosphere*, *54*(2), 177-183.
Jacob, D. J. (1986), Chemistry of OH in remote clouds and its role in the production of formic acid and peroxymonosulfate, *Journal of Geophysical Research: Atmospheres*, *91*(D9), 9807-9826.
Jacob, D. J., and S. C. Wofsy (1988), Photochemistry of biogenic emissions over the Amazon forest, *Journal of Geophysical Research: Atmospheres*, *93*(D2), 1477-1486.

Jardine, K. J., E. D. Sommer, S. R. Saleska, T. E. Huxman, P. C. Harley, and L. Abrell (2010), Gas Phase Measurements of Pyruvic Acid and Its Volatile Metabolites, *Environmental Science & Technology*, *44*(7), 2454-2460, doi:10.1021/es903544p.
Karl, T., A. Guenther, R. J. Yokelson, J. Greenberg, M. Potosnak, D. R. Blake, and P. Artaxo (2007), The tropical forest and fire emissions experiment: Emission, chemistry, and transport of biogenic volatile organic compounds in the lower atmosphere over Amazonia, *Journal of Geophysical Research: Atmospheres (1984–2012)*, *112*(D18).
Kim, S.-W., M. C. Barth, and C.-H. Moeng (2004), The effect of shallow cumulus convection on the segregation of chemical reactants, paper presented at 16th Symposium on Boundary Layers and Turbulence.
Kim, S. W., M. Barth, and M. Trainer (2016), Impact of turbulent mixing on isoprene chemistry, *Geophysical Research Letters*, *43*(14), 7701-7708.
Kim, S. W., M. C. Barth, and M. Trainer (2012), Influence of fair-weather cumulus clouds on isoprene chemistry, *Journal of Geophysical Research. Atmospheres*, *117*(1), doi:http://dx.doi.org/10.1029/2011JD017099.
Krol, M. C., M. J. Molemaker, and J. V. G. de Arellano (2000), Effects of turbulence and heterogeneous emissions on photochemically active species in the convective boundary layer, *Journal of Geophysical Research: Atmospheres*, *105*(D5), 6871-6884, doi:10.1029/1999JD900958.
Laj, P., S. Fuzzi, M. Facchini, G. Orsi, A. Berner, C. Kruisz, W. Wobrock, A. Hallberg, K. Bower, and M. Gallagher (1997), Experimental evidence for in-cloud production of aerosol sulphate, *Atmos Environ*, *31*(16), 2503-2514.
Lelieveld, J., et al. (2008), Atmospheric oxidation capacity sustained by a tropical forest, *Nature*, *452*(7188), 737-740, doi:http://www.nature.com/nature/journal/v452/n7188/suppinfo/nature06870_S1.html.
Lelieveld, J., and P. Crutzen (1991), The role of clouds in tropospheric photochemistry, *J Atmos Chem*, *12*(3), 229-267.
Lelieveld, J., and P. J. Crutzen (1990), Influences of cloud photochemical processes on tropospheric ozone, *Nature*, *343*(6255), 227-233.
Lenderink, G., A. Siebesma, S. Cheinet, S. Irons, C. G. Jones, P. Marquet, F. M. üLLER, D. Olmeda, J. Calvo, and E. Sanchez (2004), The diurnal cycle of shallow cumulus clouds over land: A single‐column model intercomparison study, *Quarterly Journal of the Royal Meteorological Society*, *130*(604), 3339-3364.
Leriche, M., J. P. Pinty, C. Mari, and D. Gazen (2013), A cloud chemistry module for the 3-D cloud-resolving mesoscale model Meso-NH with application to idealized cases, *Geosci. Model Dev.*, *6*(4), 1275-1298, doi:10.5194/gmd-6-1275-2013.
Li, Y., M. C. Barth, G. Chen, E. G. Patton, S. W. Kim, A. Wisthaler, T. Mikoviny, A. Fried, R. Clark, and A. L. Steiner (2016), Large‐eddy simulation of biogenic VOC chemistry during the DISCOVER‐AQ 2011 campaign, *Journal of Geophysical Research: Atmospheres*, *121*(13), 8083-8105.
Liang, J., and D. J. Jacob (1997), Effect of aqueous phase cloud chemistry on tropospheric ozone, *Journal of Geophysical Research: Atmospheres*, *102*(D5), 5993-6001.

Lim, Y. B., Y. Tan, M. J. Perri, S. P. Seitzinger, and B. J. Turpin (2010), Aqueous chemistry and its role in secondary organic aerosol (SOA) formation, *Atmos. Chem. Phys.*, *10*(21), 10521-10539, doi:10.5194/acp-10-10521-2010.
Madronich, S., and S. Flocke (1999), The Role of Solar Radiation in Atmospheric Chemistry, in *Environmental Photochemistry*, edited by P. Boule, pp. 1-26, Springer Berlin Heidelberg, doi:10.1007/978-3-540-69044-3_1.
Marais, E. A., D. J. Jacob, J. L. Jimenez, P. Campuzano-Jost, D. A. Day, W. Hu, J. Krechmer, L. Zhu, P. S. Kim, and C. C. Miller (2016), Aqueous-phase mechanism for secondary organic aerosol formation from isoprene: application to the southeast United States and co-benefit of SO 2 emission controls, *Atmospheric Chemistry and Physics*, *16*(3), 1603-1618.
McNeill, V. F., J. L. Woo, D. D. Kim, A. N. Schwier, N. J. Wannell, A. J. Sumner, and J. M. Barakat (2012), Aqueous-Phase Secondary Organic Aerosol and Organosulfate Formation in Atmospheric Aerosols: A Modeling Study, *Environmental Science & Technology*, *46*(15), 8075-8081, doi:10.1021/es3002986.
Moeng, C.-H. (1984), A large-eddy-simulation model for the study of planetary boundary-layer turbulence, *Journal of the Atmospheric Sciences*, *41*(13), 2052-2062.
Moeng, C.-H., and P. P. Sullivan (1994), A Comparison of Shear- and Buoyancy-Driven Planetary Boundary Layer Flows, *Journal of the Atmospheric Sciences*, *51*(7), 999-1022, doi:doi:10.1175/1520-0469(1994)051<0999:ACOSAB>2.0.CO;2.
Molemaker, M. J., and J. Vilà-Guerau de Arellano (1998), Control of Chemical Reactions by Convective Turbulence in the Boundary Layer, *Journal of the Atmospheric Sciences*, *55*(4), 568-579, doi:10.1175/1520-0469(1998)055<0568:COCRBC>2.0.CO;2.
Ouwersloot, H. G., J. Vilà-Guerau de Arellano, C. C. van Heerwaarden, L. N. Ganzeveld, M. C. Krol, and J. Lelieveld (2011), On the segregation of chemical species in a clear boundary layer over heterogeneous land surfaces, *Atmos. Chem. Phys.*, *11*(20), 10681-10704, doi:10.5194/acp-11-10681-2011.
Patton, E. G., P. P. Sullivan, and C.-H. Moeng (2005), The Influence of Idealized Heterogeneity on Wet and Dry Planetary Boundary Layers Coupled to the Land Surface, *Journal of the Atmospheric Sciences*, *62*(7), 2078-2097, doi:10.1175/JAS3465.1.
Paulot, F., J. D. Crounse, H. G. Kjaergaard, A. Kürten, J. M. S. Clair, J. H. Seinfeld, and P. O. Wennberg (2009), Unexpected epoxide formation in the gas-phase photooxidation of isoprene, *Science*, *325*(5941), 730-733.
Paulot, F., D. Henze, and P. Wennberg (2012), Impact of the isoprene photochemical cascade on tropical ozone, *Atmospheric Chemistry and Physics*, *12*(3), 1307-1325.
Plank, V. G. (1969), The size distribution of cumulus clouds in representative Florida populations, *Journal of Applied Meteorology*, *8*(1), 46-67.
Rienecker, M. M., et al. (2011), MERRA: NASA's Modern-Era Retrospective Analysis for Research and Applications, *Journal of Climate*, *24*(14), 3624-3648, doi:10.1175/JCLI-D-11-00015.1.
Sander, R. (2015), Compilation of Henry's law constants (version 4.0) for water as solvent, *Atmospheric Chemistry & Physics*, *15*(8).

Sander, S. P., et al. (2011), Chemical kinetics and photochemical data for use in atmospheric studies: Evaluation number 17*Rep. JPL Publication 10-6*, Jet Propulsion Laboratory, Pasadena, CA.
Schumann, U. (1989), Large-eddy simulation of turbulent diffusion with chemical reactions in the convective boundary layer, *Atmospheric Environment (1967)*, *23*(8), 1713-1727, doi:http://dx.doi.org/10.1016/0004-6981(89)90056-5.
Sempére, R., and K. Kawamura (1994), Comparative distributions of dicarboxylic acids and related polar compounds in snow, rain and aerosols from urban atmosphere, *Atmos Environ*, *28*(3), 449-459.
Sullivan, P. P., and E. G. Patton (2011), The Effect of Mesh Resolution on Convective Boundary Layer Statistics and Structures Generated by Large-Eddy Simulation, *Journal of the Atmospheric Sciences*, *68*(10), 2395-2415, doi:10.1175/JAS-D-10-05010.1.
Sykes, R. I., S. F. Parker, D. S. Henn, and W. S. Lewellen (1994), Turbulent Mixing with Chemical Reaction in the Planetary Boundary Layer, *Journal of Applied Meteorology*, *33*(7), 825-834, doi:10.1175/1520-0450(1994)033<0825:TMWCRI>2.0.CO;2.
Tilgner, A., P. Bräuer, R. Wolke, and H. Herrmann (2013), Modelling multiphase chemistry in deliquescent aerosols and clouds using CAPRAM3. 0i, *J Atmos Chem*, *70*(3), 221-256.
Tost, H., M. G. Lawrence, C. Brühl, P. Jöckel, G. T. The, and S.-O. D. A. T. The (2010), Uncertainties in atmospheric chemistry modelling due to convection parameterisations and subsequent scavenging, *Atmos. Chem. Phys.*, *10*(4), 1931-1951, doi:10.5194/acp-10-1931-2010.
Tuccella, P., G. Curci, G. Grell, G. Visconti, S. Crumeroylle, A. Schwarzenboeck, and A. Mensah (2015), A new chemistry option in WRF-Chem v. 3.4 for the simulation of direct and indirect aerosol effects using VBS: evaluation against IMPACT-EUCAARI data, *Geoscientific Model Development*, *8*(9), 2749-2776.
Verver, G. H. L., H. Van Dop, and A. A. M. Holtslag (1997), Turbulent mixing of reactive gases in the convective boundary layer, *Boundary-Layer Meteorol*, *85*(2), 197-222, doi:10.1023/A:1000414710372.
Vilà-Guerau de Arellano, J., S. W. Kim, M. C. Barth, and E. G. Patton (2005), Transport and chemical transformations influenced by shallow cumulus over land, *Atmos. Chem. Phys.*, *5*(12), 3219-3231, doi:10.5194/acp-5-3219-2005.
Vinuesa, J.-F., and J. V.-G. De Arellano (2003), Fluxes and (co-)variances of reacting scalars in the convective boundary layer, *Tellus B*, *55*(4), 935-949, doi:10.1046/j.1435-6935.2003.00073.x.
Vinuesa, J.-F., F. Porté-Agel, S. Basu, and R. Stoll (2006), Subgrid-scale modeling of reacting scalar fluxes in large-eddy simulations of atmospheric boundary layers, *Environmental Fluid Mechanics*, *6*(2), 115-131.
Vinuesa, J. F., and F. Porté‐Agel (2005), A dynamic similarity subgrid model for chemical transformations in large‐eddy simulation of the atmospheric boundary layer, *Geophysical research letters*, *32*(3).
Wang, K., Y. Zhang, K. Yahya, S.-Y. Wu, and G. Grell (2015), Implementation and initial application of new chemistry-aerosol options in WRF/Chem for simulating

secondary organic aerosols and aerosol indirect effects for regional air quality, *Atmos Environ*, *115*, 716-732.

Wolfe, G., T. Hanisco, H. Arkinson, T. Bui, J. Crounse, J. Dean‐Day, A. Goldstein, A. Guenther, S. Hall, and G. Huey (2015), Quantifying sources and sinks of reactive gases in the lower atmosphere using airborne flux observations, *Geophysical Research Letters*, *42*(19), 8231-8240.

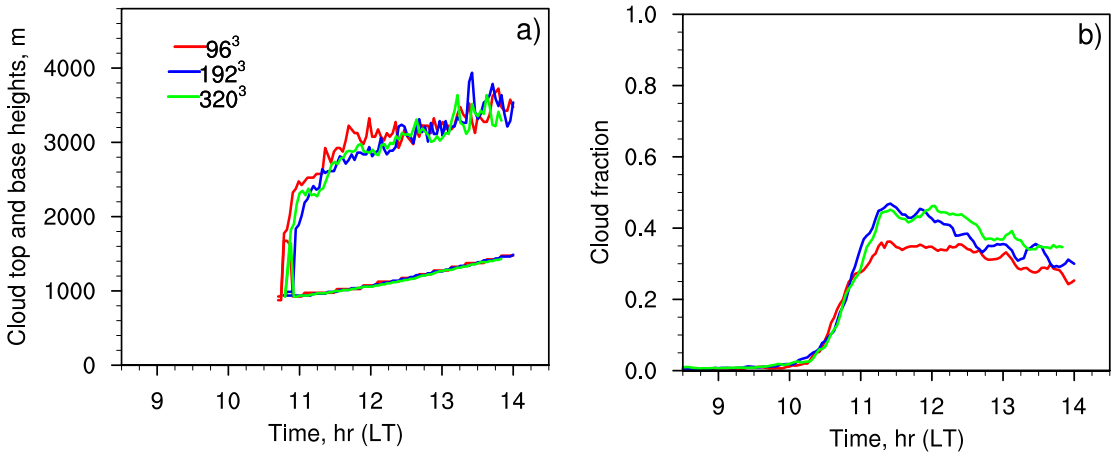

Figure 3. 1. Temporal evolution of domain maximum cloud top and base heights (a) and the cloud fraction (unitless) (b) over the model domain for the three simulations with grid points of 96^3, 192^3, 320^3.

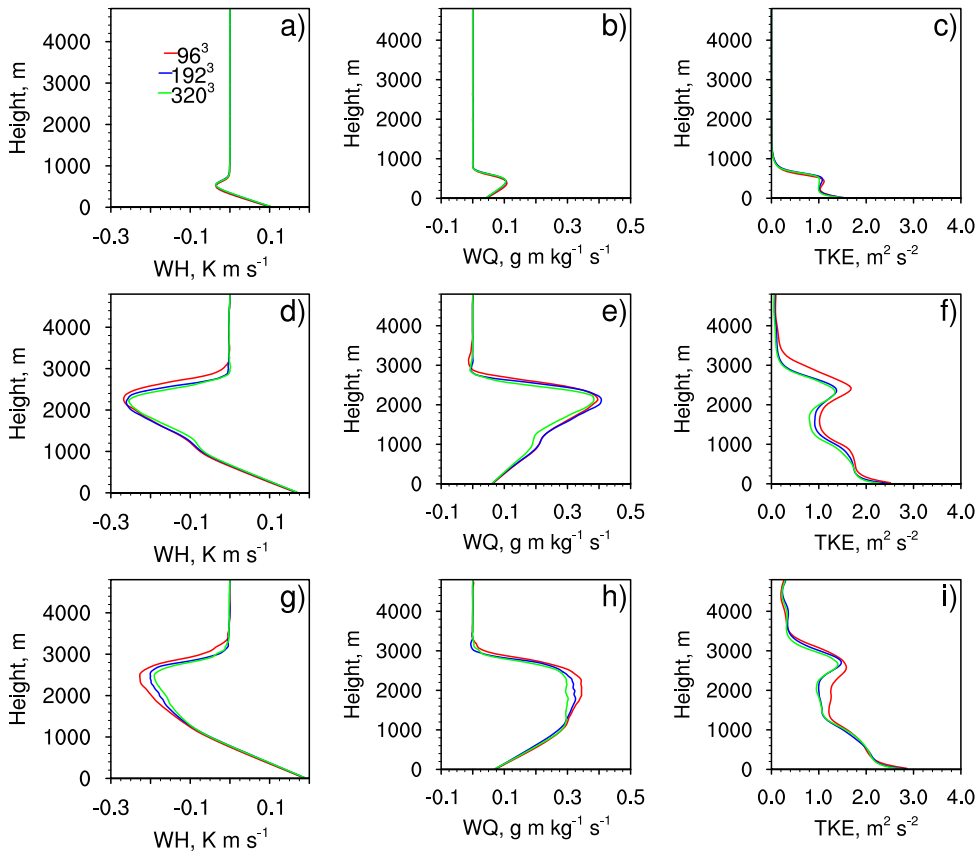

Figure 3. 2. Vertical profiles of total (resolved plus SGS) quantities of liquid water potential temperature flux (WH; a, d, g), total water (vapor plus liquid) specific humidity flux (WQ; b, e, h), and turbulent kinetic energy (TKE; c, f, i) horizontally averaged over the model domain and averaged over a 30-minute period at 1000 LT (a, b, c), 1200 LT (d, e, f) and 1300 LT (g, h, i) for the three simulations with grid points of 96^3, 192^3, 320^3.

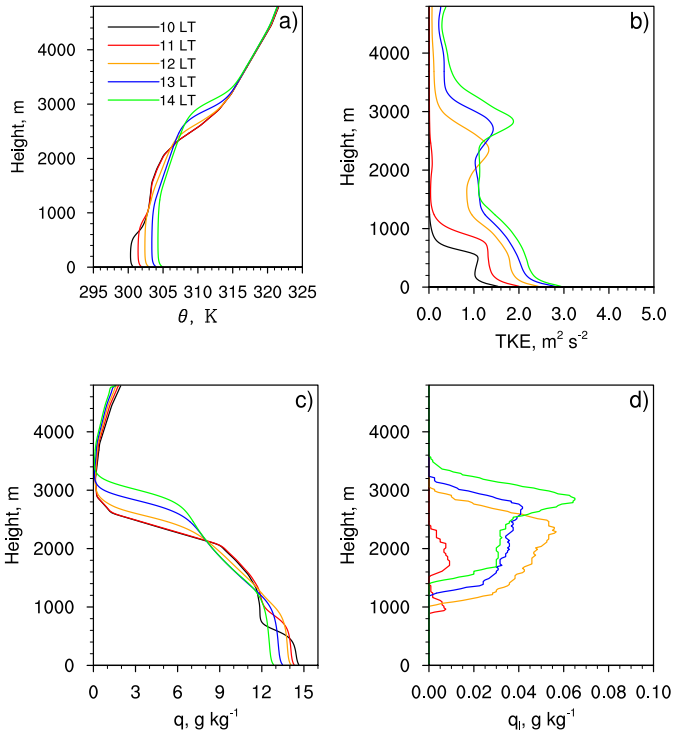

Figure 3. 3. Horizontally-averaged over the domain vertical profiles of θ (a), TKE (b), q (c) and q_l (d) averaged over a 30-minute period at 1000 LT, 1100 LT, 1200 LT, 1300 LT and 1400 LT for the simulation with grid points of 192^3.

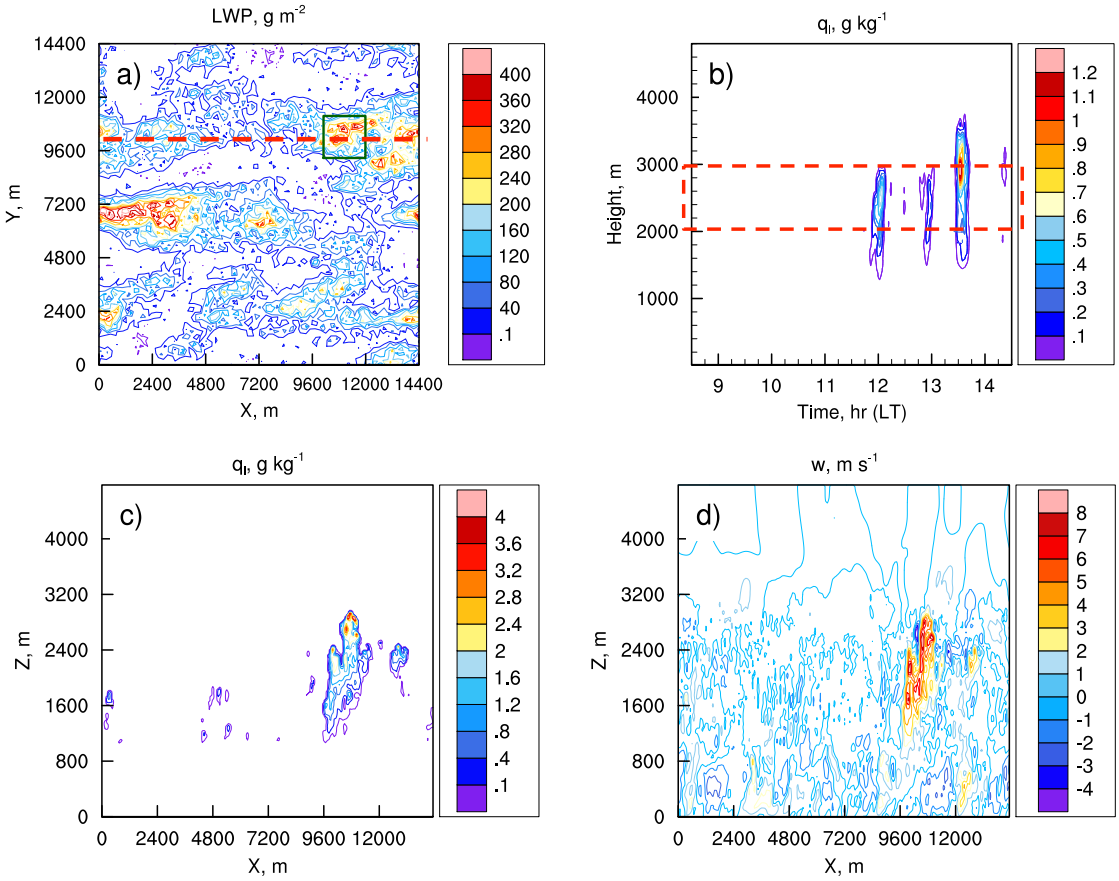

Figure 3. 4. Horizontal contour map of LWP averaged over a 30-minute period at 1200 LT (a) with a selected domain of high liquid water content ("cloudy column"; green box). Temporal evolution of q_l averaged in the cloudy column is shown in (b) with the red dashed box marking the altitude range in the cloud layer (2-3 km) for averaging. (c) and (d) show instantaneous vertical cross sections, cutting through the center of the high liquid water column as marked by the red dashed line in (a), of q_l and w at 1200 LT.

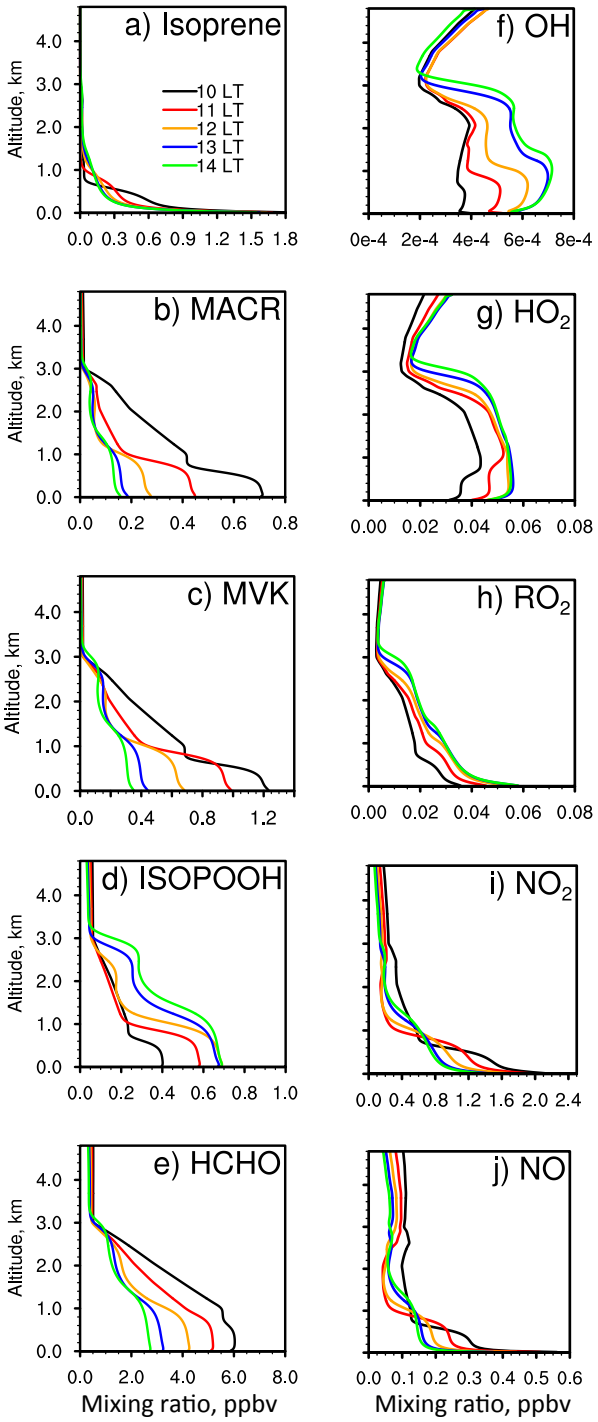

Figure 3. 5. Horizontally-averaged over the domain vertical profiles of isoprene (a), MACR (b), MVK (c), ISOPOOH (d), HCHO (e), OH (f), HO_2 (g), RO_2 (h), NO_2 (i) and NO (j) averaged over a 30-minute period at 1000 LT, 1100 LT, 1200 LT, 1300 LT and 1400 LT for the AQU simulation.

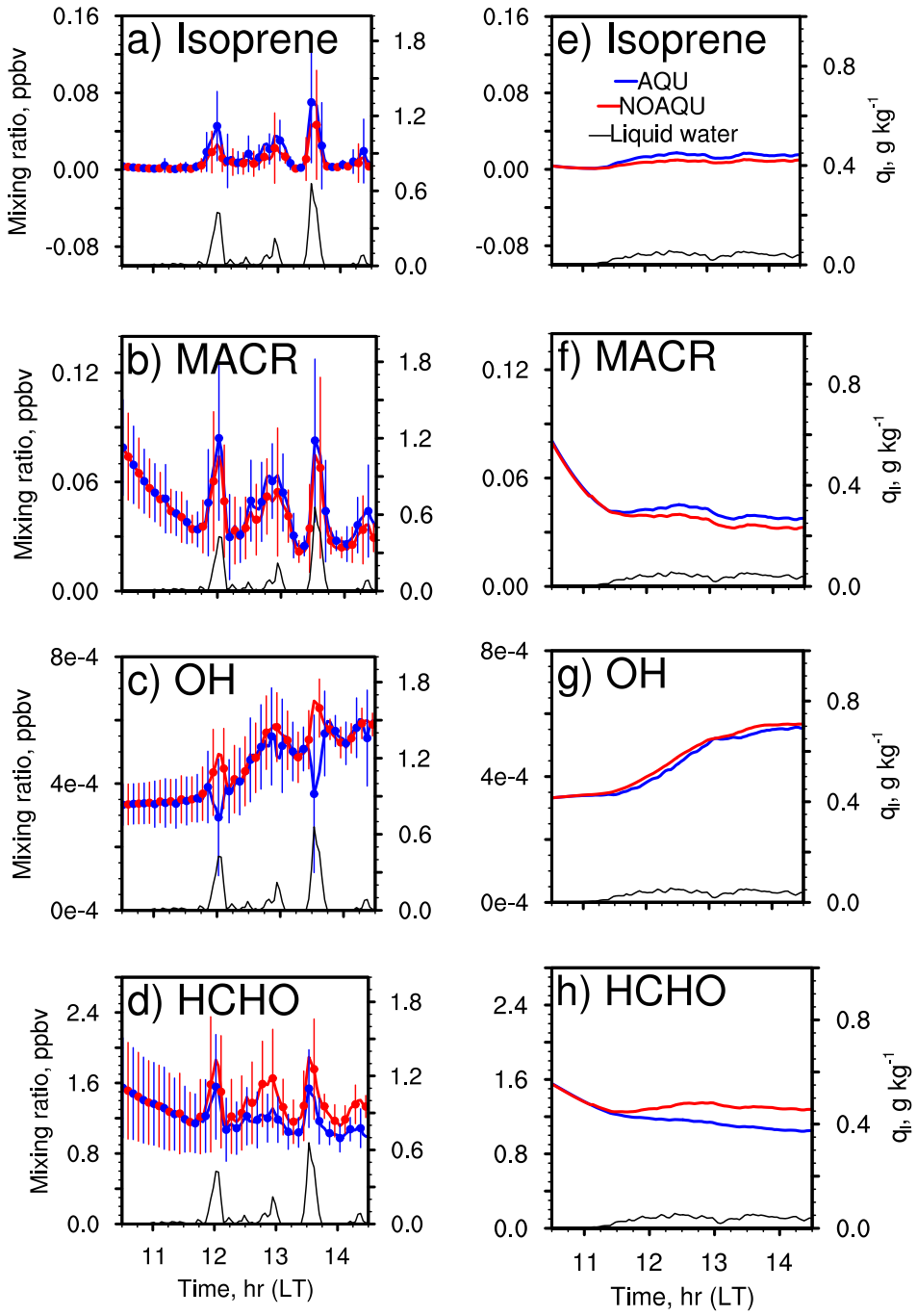

Figure 3. 6. Temporal evolution averaged in the cloudy column (a-d) and averaged over the domain (e-h) of the cloud layer (2-3 km) of total (gas + liquid) isoprene (a, e), MACR (b, f), OH (c, g), HCHO (d, h) and q_l for the NOAQU and AQU simulations, with vertical bars representing the spatial standard deviation.

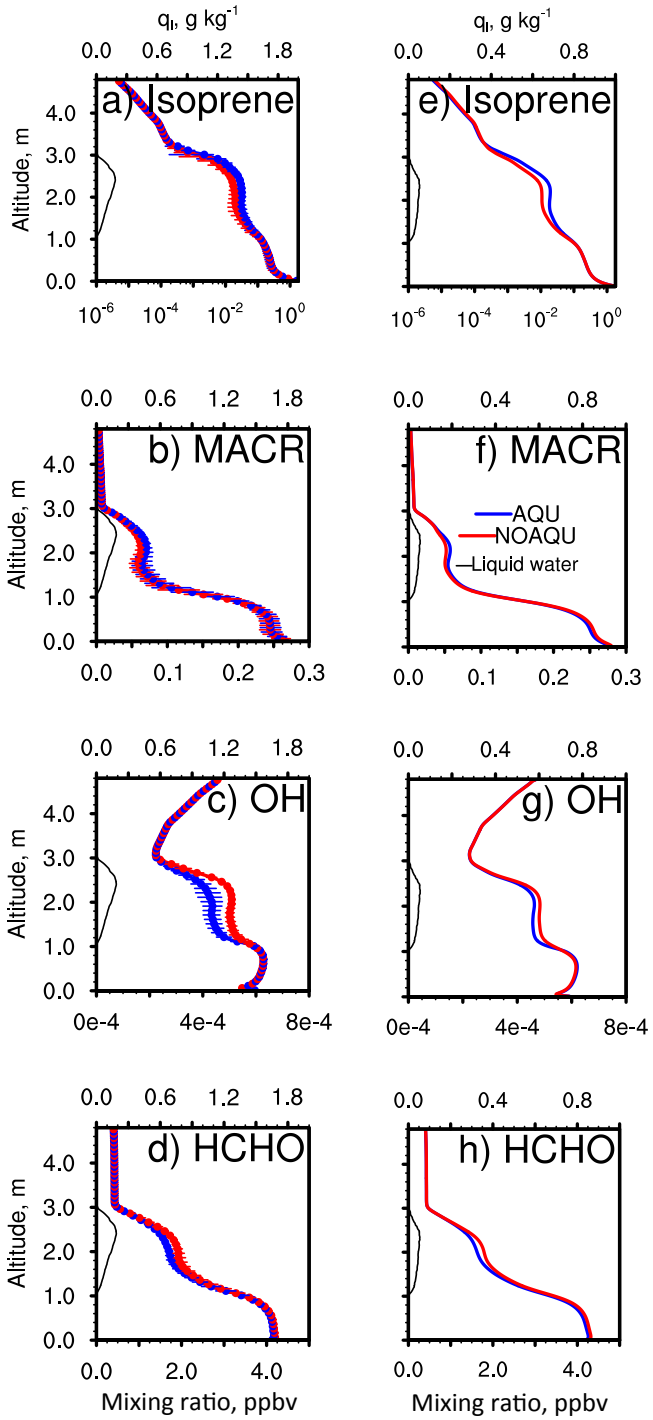

Figure 3. 7. Vertical profiles horizontally-averaged over the cloudy column (marked in Figure 3.4a) (a-d) and over the domain (e-h) of isoprene (a, e), MACR (b, f), OH (c, g), HCHO (d, h) and q_l averaged over a 30-minute period at 1200 LT for the NOAQU and AQU simulations. Horizontal bars represent the spatial standard deviation.

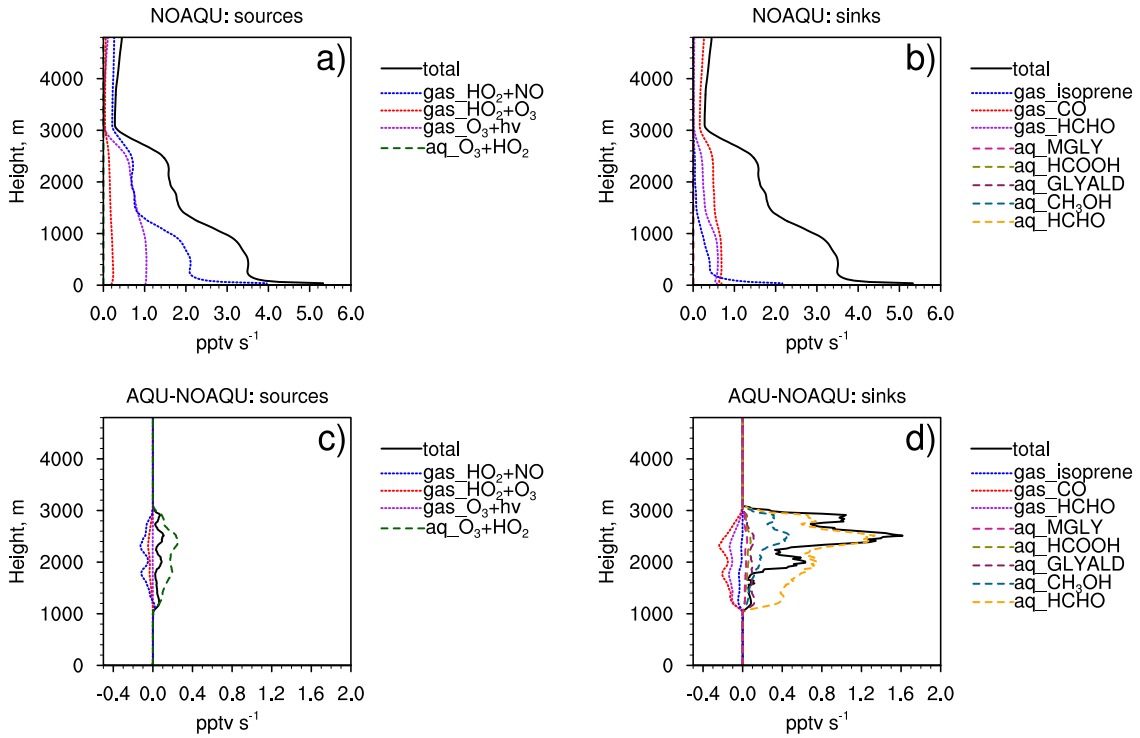

Figure 3. 8. Horizontally-averaged over the cloudy column production (a) and loss rates (b) of OH in the cloudy column at 1200 LT for the NOAQU simulation (a-b), and the changes (AQU-NOAQU) in the production (c) and loss rates (d) after including aqueous phase chemistry (c-d) in the AQU simulation.

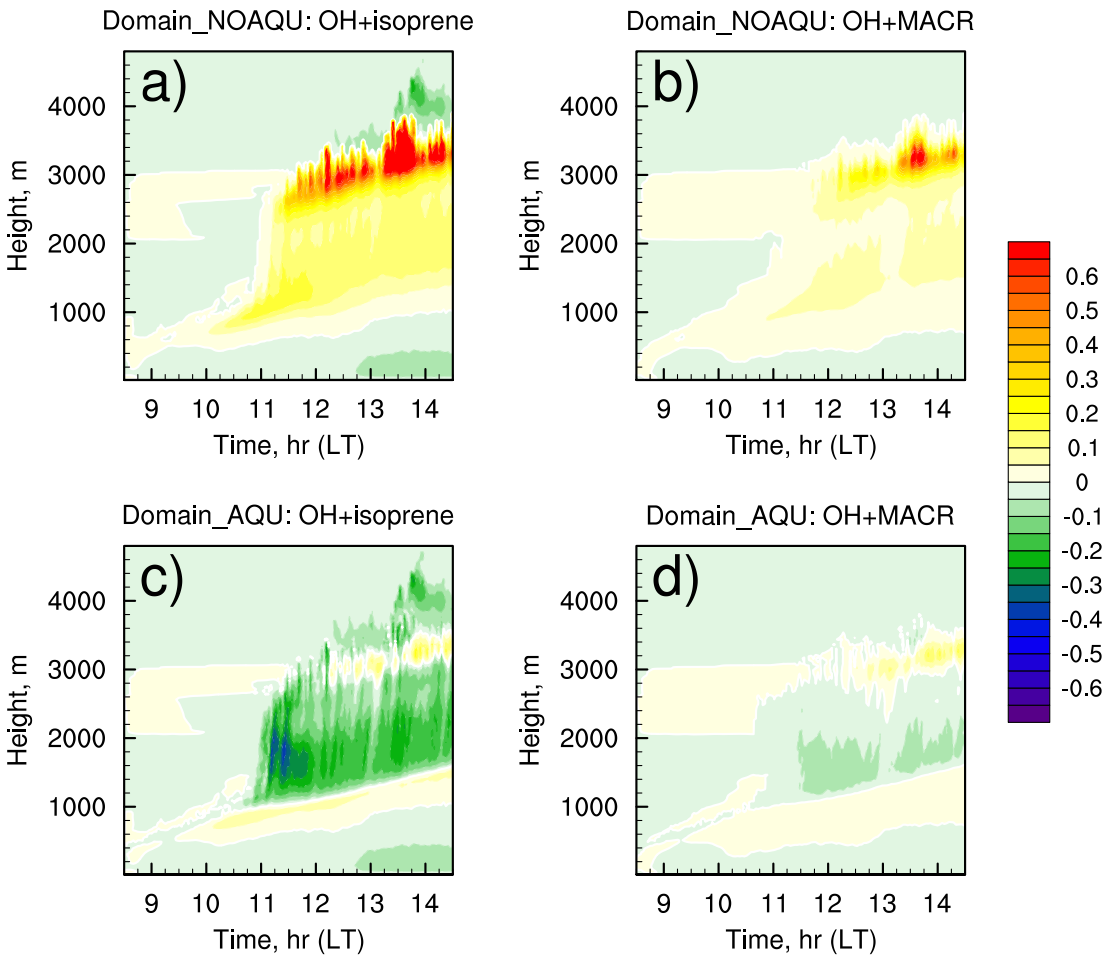

Figure 3. 9. Temporal evolution of I_s over the domain for OH + isoprene (a, c) and OH + MACR (b, d) for the NOAQU (a, b) and AQU (c, d) simulations.

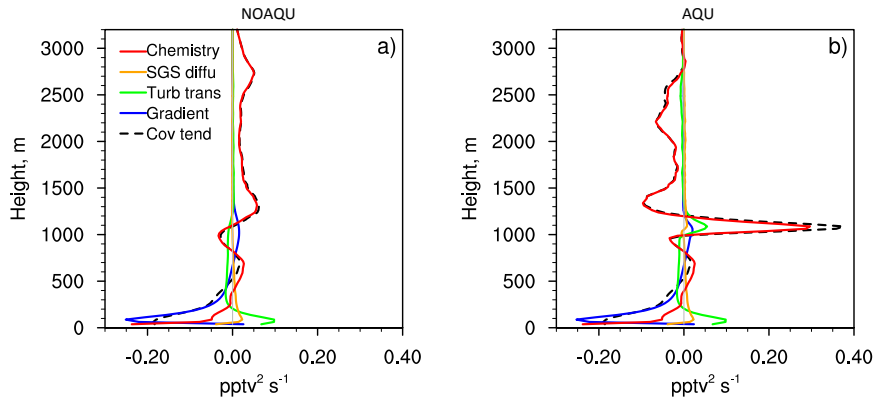

Figure 3. 10. Horizontally-averaged over the domain vertical profiles of covariance budget (black dashed line), including the sum of two gradient terms (blue), a turbulent transport term (green), the sum of two subgrid-scale diffusion terms (orange) and a chemistry term (red), averaged over a 30-minute period at 1200 LT for the NOAQU (a) and AQU (b) simulations. The grey line marks the zero value.

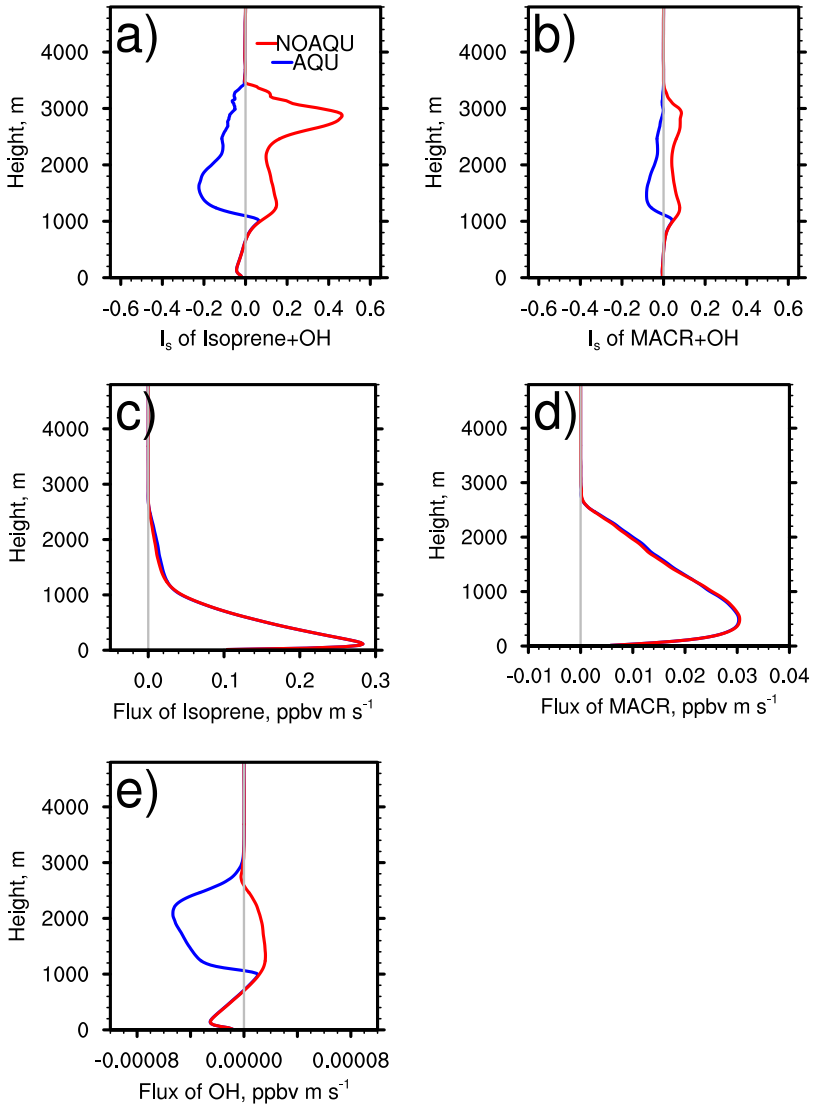

Figure 3. 11. Horizontally-averaged over the domain vertical profiles of I_s for isoprene and OH, MACR and OH (a, b), and fluxes of isoprene, MACR and OH (c-e) averaged over a 30-minute period at 1200 LT for the NOAQU and AQU simulations. The grey lines mark the zero values of I_s and fluxes.

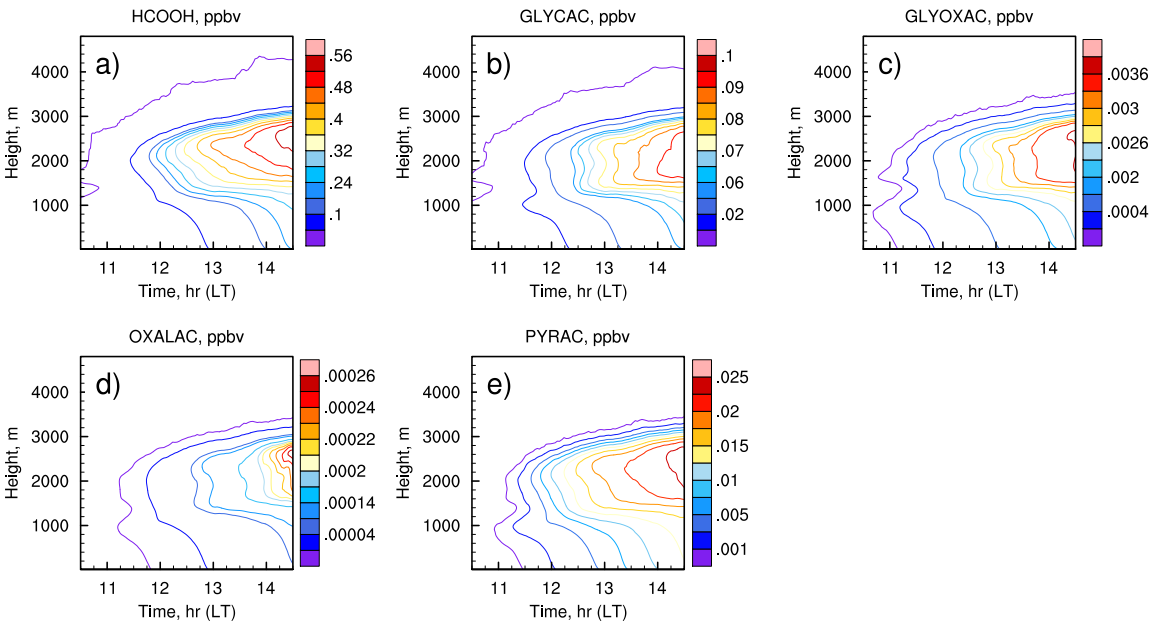

Figure 3. 12. Temporal evolution of horizontally-averaged over the domain HCOOH (a), GLYCAC (b), GLYOXAC (c), OXALAC (d) and PYRAC (e) for the AQU simulation.

Table 3. 1. Aqueous-Phase Reactions[a]

Number	Reaction	k_{298}	E/R
A1	$O_3 + h\nu + H_2O \rightarrow H_2O_2 + O_2$		
A2	$H_2O_2 + h\nu \rightarrow 2\ OH$		
A3	$HCHO + OH + O_2 \rightarrow HCOOH + HO_2$	1.0×10^{9}	1000
A4[b]	$HCOOH + OH + O_2 \rightarrow CO_2 + HO_2 + H_2O$	1.3×10^{8}	1000
A5	$CH_3O_2 + O_2^- + H_2O \rightarrow CH_3OOH + OH^- + O_2$	5.0×10^{7}	1600
A6	$CH_3OOH + OH \rightarrow CH_3O_2 + H_2O$	2.4×10^{7}	1700
A7	$CH_3OOH + OH \rightarrow CH_3(OH)_2 + HO_2$	6.0×10^{6}	1700
A8[b]	$HO_2 + HO_2 \rightarrow H_2O_2 + O_2$	8.3×10^{5}	2720
A9	$OH + OH \rightarrow H_2O_2$	5.2×10^{9}	1500
A10	$O_3 + HO_2 \rightarrow OH + 2O_2$	1.5×10^{9}	2200
A11	$O_3 + OH \rightarrow HO_2 + O_2$	3.0×10^{9}	1500
A12	$H_2O_2 + OH \rightarrow HO_2 + H_2O$	3.0×10^{7}	1700
A13	$OH + HO_2 \rightarrow H_2O + O_2$	1.0×10^{10}	1500
A14	$CO_2 + 2OH^- \rightarrow CO_3^{2-} + H_2O$	1.0×10^{7}	1500
A15	$CO_2 + HO_2 + 2OH^- \rightarrow H_2O_2 + CO_3^{2-} + OH$	1.5×10^{6}	1500
A16	$CO_3^{2-} + H_2O_2 + OH \rightarrow HO_2 + CO_2 + 2OH^-$	8.0×10^{5}	2800
A17	$CO_3^{2-} + HO_2 \rightarrow CO_2 + OH^- + O_2^-$	4.0×10^{8}	1500
A18	$NO_3 + HO_2 \rightarrow HNO_3 + O_2$	1.0×10^{9}	1500
A19	$N_2O_5 + H_2O \rightarrow 2\ HNO_3$	1.0×10^{20}	0
A20	$SO_2 + H_2O_2 \rightarrow SO_4^{2-} + 2H^+$	7.2×10^{7}	4000
A21[b]	$SO_2 + 2O_3 \rightarrow SO_4^{2-} + 2O_2$	2.4×10^{4}	0
A22	$OH + CHOCHO \rightarrow HO_2 + GLYOXAC$	9.2×10^{8}	1200
A23[b]	$OH + GLYOXAC \rightarrow HO_2 + OXALAC$	3.6×10^{8}	1000
A24	$OH + MGLY \rightarrow HO_2 + 0.92\ PYRAC + 0.08\ GLYOXAC$	6.1×10^{8}	1400
A25	$OH + GLYALD \rightarrow HO_2 + GLYCAC$	1.2×10^{9}	0
A26	$OH + GLYCAC \rightarrow HO_2 + GLYOXAC$	1.2×10^{9}	0
A27[b]	$OH + OXALAC \rightarrow HO_2 + 2\ CO_2 + H_2O$	1.4×10^{6}	0
A28[b]	$OH + PYRAC \rightarrow HO_2 + ACETAC + H_2O$	3.2×10^{8}	1800
A29[b]	$OH + ACETAC \rightarrow HO_2 + 0.15\ HCHO + 0.85\ GLYALD + H_2O$	1.5×10^{7}	1330
A30	$CH_3O_2 + CH_3O_2 \rightarrow HCHO + CH_3OH + O_2$	1.7×10^{8}	2200
A31	$OH + ACETALD + O_2 \rightarrow HO_2 + ACETAC$	3.6×10^{9}	580
A32	$OH + HYAC + O_2 \rightarrow HO_2 + MGLY + H_2O$	1.3×10^{8}	0
A33	$2OH + CHOCHO \rightarrow 2\ HCOOH$	5.0×10^{3}	0
A34	$H_2O_2 + CHOCHO \rightarrow 2\ HCOOH$	1.0	0
A35[b]	$H_2O_2 + GLYOXAC \rightarrow HCOOH + CO_2 + H_2O$	9.0×10^{-1}	0
A36	$H_2O_2 + HCOOH \rightarrow CO_2 + 2H_2O$	2.0×10^{-1}	0
A37[b]	$H_2O_2 + OXALAC \rightarrow 2\ CO_2 + 2H_2O$	1.1×10^{-1}	0
A38[b]	$H_2O_2 + PYRAC \rightarrow ACETAC + CO_2 + H_2O$	1.1×10^{-1}	0
A39	$OH + CH_3OH \rightarrow CH_2OH + H_2O$	9.0×10^{8}	0
A40	$OH + CH_3COCH_3 + O_2 \rightarrow CH_3COCH_2O_2 + H_2O$	1.3×10^{8}	0
A41	$OH + isoprene + O_2 \rightarrow ISOPO_2 + H_2O$	1.4×10^{10}	0
A42	$OH + MACR + O_2 \rightarrow CH_3COCHO_2CH_2OH + H_2O$	9.4×10^{9}	1200

A43	OH + MVK + O_2 → $CH_3COCHO_2CH_2OH$ + H_2O	7.3×10^{9}	1400
A44	O_3 + MACR → MGLY + HCHO + 0.70 H_2O_2	2.4×10^{4}	2900
A45	O_3 + MVK → 0.75 MGLY + HCHO + 0.24 PYRAC + 0.69 H_2O_2	4.4×10^{4}	2200

[a]Reaction rates are calculated using equation $k = k_{298}\times e^{\left[\frac{E}{R}\left(\frac{1}{298}-\frac{1}{T}\right)\right]}$. The units are s^{-1} for the photolysis rates and $M^{-1}\ s^{-1}$ for the second-order reactions.

[b]The reaction family is solved for using the dissociation constants [*Ervens et al.*, 2008] to partition between ions.

[c]The mechanism names are explained as:

Isoprene: C_5H_8

$ISOPO_2$: peroxy radical derived from OH + isoprene or $HOCH_2COOCH_3CHCH_2$

ISOPOOH: hydroxyhydroperoxide or $HOCH_2COOHCH_3CHCH_2$

MACR: methacrolein or CH_2CCH_3CHO

MVK: methyl vinyl ketone or $CH_2CHCOCH_3$

HYAC: hydroxyacetone or CH_3COCH_2OH

GLYALD: glycolaldehyde or $HOCH_2CHO$

MGLY: methylglyoxal or CH_3COCHO

ACETALD: acetaldehyde or CH_3CHO

GLYCAC: hydroxyacetic acid or $HOCH_2COOH$

GLYOXAC: glyoxylic acid or CHOCOOH

PYRAC: pyruvic acid or $CH_3COCOOH$

OXALAC: oxalic acid or HOOCCOOH

ACETAC: acetic acid or CH_3COOH

Table 3. 2. Henry's law constants and accommodation coefficients for trace gases that dissolve in water as a solvent

Chemical species	Accommodation coefficient	$K_H^{\ominus}$, M atm^{-1}	$-d \ln K_H / d(1/T)$, K
O_3	0.00053	1.03×10^{-2}	2830
NO_2	0.00063	1.2×10^{-2}	2360
NO	0.005	1.91×10^{-3}	1790
HNO_3	0.2	2.6×10^{6}	8700
H_2O_2	0.02	8.44×10^{4}	7600
CH_3OOH	0.0038	3.0×10^{2}	5280
HCHO	0.2	3.23×10^{3}	7100
SO_2	0.11	1.23	3120
OH	0.05	3.9×10^{1}	0
CH_3CO_3	0.02	1.0×10^{-1}	0
HNO_4	0.2	1.2×10^{4}	6900
HO_2	0.2	6.9×10^{2}	0
N_2O_5	0.005	1.0×10^{12}	0
NO_3	0.001	3.8×10^{-2}	0
CH_3O_2	0.05	2.7	2030
$CH_3CO_3NO_2$	0.02	2.8	5730
$CH_2CCH_3CO_3NO_2$	0.02	1.7	0
MACR[a]	0.02	4.8	4300
MVK[a]	0.02	2.6×10^{1}	4800
ACETALD[a]	0.03	1.29×10^{1}	5890
C_3H_6OHOOH	0.05	3.36×10^{2}	5995
CH_3COOOH	0.02	8.37×10^{2}	5310
CHOCHO	0.023	4.19×10^{5}	7480
C_2H_5OOH	0.05	3.36×10^{2}	5995
GLYALD[a]	0.023	4.1×10^{4}	4600
MGLY[a]	0.023	3.4×10^{3}	7500
$CH_2CCH_3CHONO_2CH_2OH$	0.02	1.0×10^{3}	0
$HOCH_2CCH_3CHCHO$	0.03	3.0×10^{4}	9200
CH_3OH	0.015	2.03×10^{2}	9240
CH_3COCH_3	0.02	2.78×10^{1}	5530
$C_{10}H_{18}O_3$	0.05	3.0×10^{2}	5280
$CH_3COCHOOHCH_2OH$	0.05	3.0×10^{2}	5280
HYAC[a]	0.02	7.7×10^{3}	0
CH_3COCH_2OOH	0.05	3.0×10^{2}	5280
$HOCH_2COOHCH_3CHCHOH$	0.05	3.0×10^{2}	5280
ISOPOOH[a]	0.05	3.0×10^{2}	5280
HCOOH	0.012	8.9×10^{3}	6100
SO_4^{2-}	0.2	1.0×10^{12}	0
CO_2	0.05	3.6×10^{-2}	2200
CO_3^{2-}	0.1	1.0×10^{12}	0

CH_3COOH	0.019	5.5×10^3	0
GLYCAC[a]	0.019	2.83×10^4	0
GLYOXAC[a]	0.019	1.0×10^4	0
PYRAC[a]	0.019	3.1×10^5	5088
OXALAC[a]	0.019	5.0×10^8	0

[a]The mechanism names are explained as:
MACR: methacrolein or CH_2CCH_3CHO
MVK: methyl vinyl ketone or $CH_2CHCOCH_3$
HYAC: hydroxyacetone or CH_3COCH_2OH
GLYALD: glycolaldehyde or $HOCH_2CHO$
MGLY: methylglyoxal or CH_3COCHO
ACETALD: acetaldehyde or CH_3CHO
GLYCAC: hydroxyacetic acid or $HOCH_2COOH$
GLYOXAC: glyoxylic acid or CHOCOOH
PYRAC: pyruvic acid or $CH_3COCOOH$
OXALAC: oxalic acid or HOOCCOOH
ISOPOOH: hydroxyhydroperoxide or $HOCH_2COOHCH_3CHCH_2$

CHAPTER 4 Comparing turbulent mixing of biogenic VOC across model scales

Abstract

In regional atmospheric chemistry models, the vertical transport of chemical constituents is influenced by many factors, including the horizontal and vertical grid resolution, planetary boundary layer (PBL) schemes, and the use of cumulus parameterization to represent sub-grid scale cloud processes. Here, we use the Weather Research and Forecasting Model coupled with Chemistry (WRF-Chem) to evaluate the simulation of vertical mixing in the PBL and its impact on gas-phase chemistry. We design a series of WRF-Chem simulations of varying resolutions and parameterizations to understand the impacts of various factors on simulating BVOC vertical distributions. Simulations are evaluated using the NCAR Large Eddy Simulation (LES) model and the NASA P-3B measurements over the Baltimore-Washington region. Meteorologically, we find WRF-Chem simulations with finer resolutions (e.g., 4 km and 1.33 km) produce a later cloud formation in the afternoon. The selection of boundary layer parameterization can further affect BVOC vertical mixing, with the Yonsei University (YSU) PBL scheme simulating higher PBL height and higher well-mixed BVOC profiles. However, overall these resolution and parameterization differences do not lead to a large discrepancy in simulated BVOC vertical distributions. By comparing with LES simulations, we find WRF-Chem

simulates much weaker vertical mixing which leads to stronger segregation of isoprene and OH near the surface than the LES simulations.

4.1. Introduction

Large quantities and a wide variety of volatile organic compounds (VOC) are emitted into the troposphere from biogenic sources [*Guenther et al.*, 2000; *Guenther et al.*, 1995]. In the terrestrial biosphere, primary biogenic volatile organic compounds (BVOC) are estimated to be 1.2×10^{15} gC per year at the global scale, an amount equivalent to global methane emissions [*Fuentes et al.*, 2000; *Guenther et al.*, 1995]. In the presence of NO_X ($NO+NO_2$) and sunlight, BVOC play a crucial role in the formation of ozone (O_3) and secondary organic aerosols (SOA) through a complex series of photochemical reactions [*Atkinson*, 2000]. Oxygenated VOC (OVOC), an important reactive fraction of VOC, are also formed as secondary products in many of these photochemical reactions [*Singh et al.*, 2001]. Accurate model representation of the chemical and physical processes of BVOC and the pathways of BVOC to form ozone and SOA in the planetary boundary layer (PBL) is fundamental to our understanding of air pollution events. Recently, studies have focused on understanding BVOC oxidation pathways under low NOx conditions (e.g., *Paulot et al.* [2009] and *Taraborrelli et al.* [2012]) and new pathways that elucidate the role of isoprene and other oxygenated VOC in aerosol formation pathways have been identified.

Despite changes in chemical mechanisms, many atmospheric chemistry models

still have difficulties in representing isoprene mixing ratios as well as ozone mixing ratios in high isoprene regions [*Fiore et al.*, 2005; *Horowitz et al.*, 2007; *Squire et al.*, 2015]. In many model evaluations, vertical mixing is attributed as a driver of measured-modeled discrepancies [*Castellanos et al.*, 2011; *Loughner et al.*, 2011]. The lifetimes of different BVOC species vary over a range of several minutes to several hours [*Li et al.*, 2016], with the BVOC oxidation products having longer atmospheric lifetimes than primary biogenic emissions such as isoprene. The reacting time scale of the short-lived BVOC species (e.g., isoprene with a lifetime of 11-13 min [*Li et al.*, 2016]) are similar to the turbulence turnover time scale in the ABL, indicating the importance in accurately simulating meteorological parameters that drive turbulent mixing. Regional air quality models (e.g., the Community Multiscale Air Quality (CMAQ) model [*Xie et al.*, 2011] or the Weather Research and Forecasting Model coupled with Chemistry (WRF-Chem) [*Grell et al.*, 2005]) frequently have difficulties in simulating OVOC in the PBL due to simplified vertical mixing schemes [*Carlton et al.*, 2010; *von Kuhlmann et al.*, 2003]. For example, the failure to capture the complexities of the PBL dynamics causes a decoupling of OVOC between the PBL and atmospheric layers aloft [*Forkel et al.*, 2006]. In addition, most moderate resolution atmospheric models have difficulties representing convective cumulus clouds due to uncertainties in convective parameterizations [*Chen et al.*, 2007], therefore impeding the study of OVOC aqueous-phase processing in clouds and aerosol water to form SOA [*Li et al.*, submitted].

Previous studies by *Li et al.* [2016] and *Li et al.* [submitted] used the National Center for Atmospheric Research's (NCAR) large-eddy simulation (LES) model to

investigate the role of BVOC in the boundary layer and found the LES can reproduce the observed BVOC vertical profiles during the 2011 NASA DISCOVER-AQ field campaign, which provided observations throughout the PBL. The LES model has fine resolution on the order of tens to hundreds of meters and complex turbulent closure, which can resolve the energy-containing turbulent eddies in the PBL [*Moeng*, 1984]. However, these LES characteristics increase the computational expense and limit the application of the LES to small geographical regions as well as short time scales (e.g., several hours) when simulating the atmospheric processes. To investigate long-term and long-range transport of air pollutants, large-scale regional models (e.g., WRF-Chem) are essential and widely used. In this study, we aim to simulate the BVOC vertical mixing using the WRF-Chem model [*Grell et al.*, 2005], and then use the NCAR LES model [*Li et al.*, 2016; *Moeng*, 1984] with well-resolved turbulence to evaluate WRF-Chem simulations.

The resolution of regional models also plays an important role in representing the fine spatial structure of the PBL [*Mass et al.*, 2002], which then affects the transport of the chemical species. *Loughner et al.* [2011] performed high-resolution (up to 1.3 km horizontal resolution) WRF simulations to illustrate that WRF-Chem can simulate the complex local-scale bay-breeze circulations, finding that high resolution improves the representation of vertical mixing and PBL venting in the model. *Tie et al.* [2010] performed WRF simulations at four resolutions (3, 6, 12, and 24 km) and found that the simulation of ozone was improved versus observations with increasingly higher spatial resolutions. The improvements in representing convective transport and atmospheric chemistry associated with the enhancement

of model resolution suggests that increasing model resolution will likely be important in simulating the oxidation and distribution of BVOC in regional models.

In this study, we apply the WRF-Chem model over the 2011 DISCOVER-AQ observational region and compare results with the NCAR LES model to evaluate the WRF-Chem ability to represent BVOC vertical mixing and oxidation time scales. With different horizontal resolutions implemented in the WRF-Chem simulations, we aim to understand the effects of resolution on vertical distributions of key BVOC species and their role on BVOC oxidation. In addition, two PBL schemes (e.g., the Yonsei University (YSU) PBL scheme [*Hong et al.*, 2006] and the Mellor-Yamada-Janjic (MYJ) PBL scheme [*Janjić*, 1994]) coupled with the WRF-Chem model are also implemented and compared to investigate the effects of these PBL schemes on vertical mixing. The effects of WRF-Chem resolution and physical parameterizations are discussed in Section 3. Secondly, we evaluate the finest resolution WRF-Chem simulation (1.3 km) against the LES simulations (Section 4). Finally, we compare the simulation of segregation of isoprene chemistry between the various model simulations to understand the role of vertical mixing on the oxidation of isoprene (Section 5). While we note that there are many inherent and irreconcilable differences between the LES and WRF-Chem simulations, the comparison presented here can provide insight into the representation of turbulent mixing in the PBL as relevant for atmospheric chemistry.

4.2. Methods

4.2.1. WRF-Chem simulation design

We implement the WRF-Chem model [*Grell et al.*, 2005] version 3.7.1 to investigate the impacts of different model scales on BVOC distributions for the NASA DISCOVER-AQ Baltimore-Washington campaign. Physical parameterizations in this model are listed in Table 4.1. We select the chemical mechanism of the Model for Ozone and Related Chemical Tracers, version 4 (MOZART-4, [*Emmons et al.*, 2010]) and the Model for Simulating Aerosol Interactions and Chemistry with four size bins (MOSAIC, [*Zaveri et al.*, 2008]) to calculate gas- and particle- phase chemical reactions, as this is closest in mechanisms to that implemented in the LES. This chemical mechanism includes an updated isoprene oxidation scheme and a detailed treatment of monoterpenes [*Knote et al.*, 2014]. Photolysis rates coupled with the chemical mechanism are calculated using the fast Tropospheric Ultraviolet-Visible (fTUV) module [*Tie et al.*, 2003].

We focus on 11 July 2011 observations from the NASA DISCOVER-AQ campaign to evaluate the WRF-Chem simulations. This observational day has a clear diurnal pattern of non-precipitating cumulus clouds as simulated with the LES model with chemistry by *Li et al.* [2016]. At coarser grid scales (e.g., > 4km horizontal resolution), convection in WRF-Chem simulations is typically parameterized using cumulus parameterizations. At finer resolutions (4km and lower), convection can be explicitly resolved although there is some disagreement in the community on this determination at 4 km [*Bryan et al.*, 2003; *Weisman et al.*, 1997]. This case provides a unique opportunity to study the impacts of resolution

on PBL mixing under convective conditions, which further influence BVOC distributions. WRF-Chem simulations start at 0600 UTC on 10 July 2011 and end at 0000 UTC on 12 July 2011 to allow boundary layer dynamics to spin up before the analysis date (i.e., 11 July 2011).

We perform the WRF-Chem simulations with a one-way nested domain at three horizontal resolutions of 12 km, 4 km and 1.33 km with dimensions of 175 × 175, 172 × 220 and 169 × 169 grid cells, respectively, on a Lambert conformal conic projection (Figure 4.1). The 12 km resolution parent domain covers the Southeastern US, the 4 km resolution nested domain covers the Maryland region, and the 1.33 km resolution nested domain covers the DISCOVER-AQ 2011 observational sites. We use 72 vertical levels from the surface to 100 hPa for all three simulations. One third of the vertical levels (e.g., the lowest 24 levels) are located within the PBL to resolve boundary layer processes. We select an interior region with identical latitudinal and longitudinal ranges for all three domains to analyze the effects of different resolutions, hereinafter called the "analysis region" that encompasses the P-3B observations at the Fair Hill site (Figure 4.1). The analysis region includes 4 × 5, 13 × 16 and 40 × 47 grid cells for the 12 km, 4 km and 1.33 km resolution domains, respectively.

The varying resolution simulations are performed with fixed time steps of 60 s, 20 s and 20 s for meteorology and 180 s, 60 s and 60 s for chemistry, for the 12, 4 and 1.3 km domains, respectively. We also tested shorter time steps for meteorology (e.g., 8 s) and chemistry (e.g., 24 s and 8 s) but found no significant improvement in

simulating meteorological factors or chemical mixing ratios and therefore the results with shorter time steps are not discussed here. Meteorological initial and lateral boundaries in the simulations with 12 km resolution are initialized and forced by the North American Regional Reanalysis (NARR) at a 32 km resolution and at 6-hour time intervals. Chemical initial and boundary conditions are forced by 6 hourly MOZART-4/GOES-5 simulations [*Emmons et al.*, 2010]. We use the 2011 National Emission Inventory (NEI 2011) to provide anthropogenic emissions and the Model of Emissions of Gases and Aerosols from Nature (MEGAN) [*Guenther et al.*, 2006] for biogenic isoprene emissions.

4.2.2. WRF-Chem PBL parameterization sensitivity simulations

Accurately resolving turbulent mixing is of essential importance for the dispersion of chemical emissions and simulating the chemical reactions in the atmosphere. To evaluate the representation of turbulent mixing by different PBL parameterization schemes, we perform the WRF-Chem simulations for all the three resolutions using the YSU PBL scheme [*Hong et al.*, 2006] and the MYJ PBL scheme [*Janjić*, 1994], respectively. YSU is a nonlocal scheme with first-order closure, that explicitly represents entrainment at the top of the PBL [*Hong et al.*, 2006]. MYJ is a local scheme with a 1.5-order closure and an equation for prognosis of turbulent kinetic energy (TKE) [*Janjić*, 1994]. For both PBL simulations, we implement the Grell-Freitas cumulus convective parameterization to simulate subgrid clouds in the domain with 12 km horizontal resolution. The simulations with 4 km and 1.33 km do not include a cumulus parameterization as these resolutions are thought to accurately capture sub-grid cloud formation, although there is still some

disagreement in the literature on the justification of using cumulus convective parameterization on 4 km horizontal resolution [*Bryan et al.*, 2003; *Weisman et al.*, 1997]. For example, *Knote et al.* [2014] used cumulus parameterization for a 4 km resolution simulation to study SOA formation. *Loughner et al.* [2014] also implemented a cumulus parameterization at 4 km to investigate the role of the Chesapeake Bay breeze on surface air quality. However, this parameterization is not used by *Loughner et al.* [2011] when the horizontal resolution is finer than 8 km. Therefore, we perform an additional 4km simulation with the cumulus parameterization turned on to compare the two simulations.

4.2.3. LES simulations

To evaluate the WRF-Chem simulations, we use the NCAR LES simulation for the same time period (11 July 2011) [*Li et al.*, 2016]. In the LES, a sharp wave-cutoff filter is utilized to define the resolvable-scale variables, and subgrid-scale transport is parameterized using the turbulence energy model described in *Deardorff* [1980]. Dynamics is solved using a third-order Runge-Kutta scheme with a specified Courant-Fredrichs-Lewy (CFL) number, presuming that the ABL is incompressible and Boussinesq [*Sullivan and Patton*, 2011]. The simulation starts at 0530LT with dynamics only. Chemical emissions and processes are then initiated at 0830 LT after the boundary layer dynamics have been spun up [*Kim et al.*, 2012].

However, we note that there are many fundamental differences between the LES experimental set-up and that of WRF. The first is the lower boundary conditions. Surface heat fluxes (e.g., sensible heat flux and latent heat flux) are very important

in PBL evolution, which can further influence the formation of cumulus clouds. The *Li et al.* [2016] study uses observed hourly surface sensible and latent heat fluxes from the Edgewood site (located close to Fair Hill) for the lower surface boundary condition. Surface heat fluxes are simulated prognostically in WRF-Chem by the Noah Land Surface Model and they will respond to changes in incoming solar radiation due to clouds and soil moisture conditions after precipitation. The WRF-Chem simulated sensible and latent heat fluxes averaged over the analysis region show positive biases as compared to the ground measurements at the Edgewood site used in the LES model [*Li et al.*, 2016]. Figure 4.2 compares surface heat fluxes simulated by Noah in WRF-Chem with ground measurements at the Edgewood site and used in the LES simulation [*Li et al.*, 2016]. Sensible heat flux used in WRF-Chem is about 90 W m^{-2} higher than in the LES model, while latent heat flux is about 110 W m^{-2} higher than in the LES model. To eliminate these differences in evaluating WRF-Chem simulations, we perform an additional LES simulation (LES_SHLH; Table 4.2) using the Noah simulated sensible and latent heat fluxes (Figure 4.2; Table 4.2).

For the lower chemical boundary conditions, the LES included homogeneous surface emissions of isoprene, monoterpenes and nitric oxide (NO), where biogenic isoprene emissions were based on the local MEGAN isoprene emission factor at Fair Hill at standard conditions [*Guenther et al.*, 2006] and scaled by the solar zenith angle and the temperature emission activity factor to provide a diurnal cycle [*Li et al.*, 2016]. NO emissions were scaled from the diurnal pattern of surface NO_X observed at the ground-based sites during the DISCOVER-AQ campaign. The homogenous surface condition implemented in the LES simulations is unlike WRF-

Chem simulations, which implement the NEI with a strong spatial heterogeneity to the emissions.

A second major difference between the LES and WRF-Chem simulations is the implementation of chemical and physical lateral boundary conditions. For the LES simulations, *Li et al.* [2016] defined meteorological boundary conditions with tendencies calculated by the global 1.25°× 1.25° MERRA reanalysis for three-hourly time-averaged large-scale forcings, and utilized a finer resolution MERRA product (0.5° × 0.67°) at a six-hourly time resolution to define initial profiles of potential temperature and water vapor mixing ratio [*Rienecker et al.*, 2011]. The initial profiles were also verified with sounding data at two locations (Wallops Island, VA (WAL: 37.93°N, 75.48°W) and Sterling, VA (IAD: 38.98°N, 77.46°W)) and P-3B observations, providing realistic initial conditions for the LES simulations. For WRF-Chem, lateral meteorological boundary conditions are from the NARR and updated every six hours. For chemical conditions, WRF-Chem chemical boundary conditions are forced by 6 hourly MOZART-4/GOES-5 simulations, while the LES chemical initial conditions are from P-3B observations.

A third difference is the chemical mechanisms implemented in the two different model types. The LES chemical mechanism is based on the NCAR chemical mechanism MOZART2.2 [*Kim et al.*, 2012] and the WRF-Chem mechanism is the MOZART- MOSAIC mechanism. While their gas phase oxidation pathways for isoprene are similar, the chemical mechanism in the LES does not include SOA formation pathways. Additionally, the LES mechanism does not explicitly include

aromatic emissions or aromatic chemistry, and the photochemical processes related to anthropogenic VOC that are included in WRF-Chem could change the distribution of oxidant radicals (e.g., HO_X), therefore, further modifying BVOC vertical distribution.

4.3. Evaluation of WRF-Chem parameterizations and resolution

4.3.1. Meteorology

To understand the meteorological factors simulated by the WRF-Chem model using different resolutions and different PBL schemes, we first compare the temporal evolution of potential temperature (θ) vertical profiles horizontally averaged over the analysis region in Figure 4.3. Based on the changes in temperature gradient, we can determine the appropriate location of the PBL height. The 12 km YSU simulation (YSU_12km; Table 4.2) simulates a higher PBL than the MYJ simulation (Figure 4.3a, d). For example, the PBL height at 1500 LT in the YSU_12 km simulation is about 2 km, but is 1.6 km in the MYJ_12 km simulation (Figure 4.3a, d). We also compare the θ differences between the WRF-Chem simulations using 4 km or 1.33 km resolutions with those using 12 km resolution in the analysis region (Figure 4.3b, c, e, f). The θ differences are within the range of -1.2 to 1.2 K, with large decreases aloft up to 1.2 K at around 3 km and increases below 2.5 km in the YSU simulations, and 2 km in the MYJ simulations during 1500-2000 LT. This suggests that the finer resolution simulations and simulations that include the cumulus parameterization produce a colder environment aloft but a warmer environment near the surface, which may promote surface emissions or reactions of some BVOC species.

These temperature differences are likely driven by changes in liquid water (q_l) formation due to different treatment of water vapor condensation. The MYJ PBL simulations show an earlier formation of non-precipitation clouds at lower altitudes based on the distribution of q_l, and tend to form more liquid water than with the YSU scheme (Figure 4.4). The differences in PBL height, temperature and liquid water between the simulations using the YSU scheme and the MYJ scheme are consistent with the comparisons in *Xie et al.* [2012] and *Hu et al.* [2010], which found the YSU scheme yields warmer and drier daytime PBLs. The MYJ scheme implements local treatment of large-scale eddies, preventing a deeper mixing of the PBL [*Hu et al.*, 2010]. As resolution increases (e.g., with the resolutions of 4 km and 1.33 km), clouds evolve at later times and water vapor condenses to liquid droplets (Figure 4.4b, c, e, f), consistent with a colder atmosphere aloft (Figure 4.3b, c, e, f).

The simulations can be more easily compared with the liquid water path (LWP) averaged over the analysis region for all WRF-Chem simulations (Figure 4.5). Simulations with 12 km resolution produce high LWP peaks in the early morning (~0600 LT). However, the finer resolution simulations (e.g., 4 km and 1.33 km) without cumulus parameterizations simulate high LWP peaks in the late afternoon (~1800 LT). In Figure 4.5a, we also compare LWP from a simulation with 4 km resolution and YSU scheme and with cumulus parameterization (YSU_4 km_cumu). Liquid water generated from this YSU_4 km_cumu simulation is comparable to the 12 km resolution, but is much lower than other simulations with 4 km and 1.33 km resolutions without cumulus parameterization. The large LWP difference between

the two 4 km simulations highlights the differences that are driven by the implementation of a cumulus parameterization.

4.3.2. Chemistry

Based on the WRF-Chem simulations with different resolutions, we investigate the changes in vertical profiles of the primary emitted isoprene and secondary BVOC (e.g., methyl vinyl ketone (MVK), methacrolein (MACR) and isoprene hydroxyhydroperoxide (ISOPOOH)), OH, NO_2 and O_3, which are important chemical species in understanding ozone (O_3) formation. Those profiles are horizontally averaged over the analysis region, and are also evaluated using P-3B measurements (Figure 4.6). Isoprene profiles show no discernable difference in simulations with different resolutions and PBL schemes, and both simulated and P-3B observed isoprene profiles show a strong gradient within the PBL. Simulated near-surface (below 1 km) isoprene mixing ratios are lower than P-3B measurements (Figure 4.6a, f), which could result from the heterogeneity of P-3B sampling strategy, where some flight paths may pass over the high isoprene emission region not represented by WRF-Chem MEGAN emissions. MACR, MVK and ISOPOOH are primary isoprene oxidation products, and WRF-Chem simulates well-mixed profiles up to 3.4 km in the simulations with YSU scheme and up to 3.2 km with MYJ scheme, which show large discrepancies from their P-3B measured profiles (Figure 4.6b, g). The reasons for the well-mixed MVK+MACR+ISOPOOH profiles and the discrepancies from P-3B observations are discussed below. OH and NO_2 are also mixed higher in the YSU simulations than the MYJ simulations (Figure 4.6c, e, h, j), matching with the higher PBL heights simulated with the YSU scheme (Figure 4.3). The higher mixed ozone

precursors result in the higher mixed O_3 profiles (Figure 4.6d, i). Near-surface O_3 mixing ratios simulated by WRF-Chem are within the P-3B measurement range. However, simulated O_3 mixing ratios above 2 km show a negative bias deviating from the well-mixed O_3 vertical profiles measured by P-3B.

In Figure 4.6, the WRF-Chem resolution affects the vertical distributions of NO_2 and OH, showing the strongest gradients simulated with 1.33 km resolution using both YSU and MYJ schemes. NO_2 profiles simulated with 1.33 km resolution compare well with P-3B observations near the surface (Figure 4.6e, j), suggesting that the increase in resolution provides a better representation of reactive chemistry in the boundary layer. Higher near-surface NO_2 mixing ratio induces higher near-surface OH simulated with 1.33 km resolution (Figure 4.6c, h).

4.4. Comparison of WRF-Chem and LES simulations

To understand the limitation of WRF-Chem in interpreting vertical mixing, we use the LES with well-resolved turbulence to evaluate the WRF-Chem simulation. We note there are numerous differences between the NCAR LES model and the WRF-Chem model, as detailed in Section 2.3. Although the evaluation of WRF-Chem simulations using the LES is qualitative, the comparison can provide insight into the representation of turbulent mixing of BVOC in the PBL due to the limited observations in this atmospheric region. To provide the best comparison of surface conditions, we select a region with similar physical and chemical surface characteristics. For isoprene, we select a region that has similar isoprene emissions for both the LES and WRF-Chem (~46 mol km^{-2} hr^{-1} and 38 mol km^{-2} hr^{-1},

respectively). For physical conditions, we compare the revised LES simulation (LES_SHLH) and the simulation by *Li et al.* [2016] with P-3B measurements. In general, we compare the compare only the 1.33 km MYJ WRF-Chem simulation, as the θ and q_l in the 1.33 km YSU and MYJ schemes show similar vertical variations (Figure 4.3 and Figure 4.4). Additionally, the MYJ simulations predict TKE, which is a useful comparison of turbulence with the LES.

4.4.1. Meteorology evaluation

Comparing the two LES simulations (LES and LES_SHLH), higher surface heat fluxes induce a more dynamic atmosphere. The mixed layer, as represented by θ profiles and high TKE values, extends about 20% higher with the modified sensible and latent heat fluxes than the original LES simulation (Figure 4.7a, d). q_v is also transported higher (up to 4 km) in the LES_SHLH simulation. Although using the same surface forcing as in the LES_SHLH simulation, WRF-Chem simulates a lower θ (~10 K) near the surface with less temporal variation from 9-17 LT than the LES (Figure 4.7a, d, g), indicating a stable daytime environment simulated by WRF-Chem. This is consistent with the lower TKE (~50%; Figure 4.7i) than simulated by the LES (Figure 4.7c, f). Observed P-3B θ profiles are more consistent with the LES results and show large discrepancy (~8 K) from the WRF-Chem simulations. q_v profiles for WRF-Chem also have less temporal variation than the LES, and show higher values near the surface (2-3 g kg^{-1}) but lower values aloft (2-4 g kg^{-1}) than the LES (Figure 4.7b, e, h). P-3B observed q_v profiles show discrepancies from both the LES and the WRF-Chem models (~4 g kg^{-1} and 2 g kg^{-1} near the surface, respectively), which could be due to heterogeneity of the region covered by P-3B spirals or the

simulation of moisture aloft during cloud processes. Low q_v aloft in the WRF-Chem simulation (Figure 4.7h) could result from a lack of mixing above the PBL, consistent with the lower TKE simulated by WRF-Chem and from the difference in the boundary conditions used in these models. TKE as simulated by WRF-Chem is about 1-2 $m^2 s^{-2}$ lower near the surface than the LES and is near zero above 2 km (Figure 4.7i).

Vertical velocity (*w*) is another important meteorological factor in determining BVOC vertical transport, and we compare *w* horizontal contours to examine the differences simulated by the WRF-Chem and the LES. Although we choose our highest resolution WRF-Chem simulations (1.33 km resolutions), we note the order of magnitude resolution difference between WRF-Chem and LES (150 m resolution [*Li et al.*, 2016]). At two atmospheric heights (0.3 km and 2km), WRF-Chem *w* horizontal contours show little variation in both space and time, with *w* values within the range of -0.5-0.5 m s^{-1} (Figure 4.8a-d). With well-resolved turbulence in the LES simulations, *w* at 0.3 km shows large fluctuations (-2.5 to 3 m s^{-1}) even when aggregated to the 1.33 km resolution, with detailed structure marking the strong upward transport regions and the downward transport regions (Figure 4.8e). At 2 km, upward transport is weaker than at 0.3 km except for a few regions with strong upward motion (Figure 4.8f). With higher surface heat fluxes, the LES model simulates stronger *w* at both 0.3 and 2 km (-3.5 to 4 m s^{-1}) (Figure 4.8g, h), matching stronger TKE (Figure 4.7c, f).

4.4.2. Vertical mixing of chemical species

We compare the vertical profiles of BVOC and other key ozone precursors for the two WRF-Chem simulations with 1.33 km resolution, the two LES simulations and P-3B measurements (Figure 4.9). We also include formaldehyde (HCHO) because it is produced by the oxidation of the primary emitted BVOC, secondary oxidation products, as well as anthropogenic emissions. Generally, the LES simulates low near-surface (below 1 km) mixing ratios of isoprene, HCHO as well as NO_2 as compared to WRF-Chem simulations (Figure 4.9a, b, e, f). Although surface heat fluxes were increased in the LES_SHLH simulation, this has a relatively small impact on the vertical mixing of BVOC species. For example, changes in the TKE budget between LES and LES_SHLH in the surface layer are 25% compared to the original LES simulation, however, the chemical species shown here are only transported a little higher than the original simulation.

Comparing with the 50% TKE difference between the WRF-Chem simulations and the LES simulations in Section 4.1, the difference in isoprene or NO_2 vertical profiles primarily results from stronger vertical mixing in the LES simulations, which transports more chemical species upward. For HCHO, the lack of anthropogenic VOC emission sources in the LES simulations also contributes to the large discrepancies (~2 ppb) of HCHO near the surface (Figure 4.9f). These ozone precursors also influence OH mixing ratios and hence ozone. The LES simulates higher OH than the WRF-Chem, resulting in higher mixing ratios of OH and O_3 aloft in the LES simulations (Figure 4.9c, d).

The LES simulated vertical profiles of MVK+MACR+ISOPOOH show larger gradients than the WRF-Chem simulations, with the LES simulated mixing ratio decreasing from about 1 ppbv at the surface to 0.5 ppbv at 2 km while the mixing ratio from WRF-Chem is maintained at about 0.5 ppbv from the surface to 2 km (Figure 4.9b). However, WRF-Chem simulates a more stable atmosphere temporally and vertically according to the TKE profiles in Section 4.1, with near zero TKE above 2 km (Figure 4.7i). This suggests that there is not sufficient mixing to transport MVK+MACR+ISOPOOH aloft in the WRF-Chem simulations. Therefore, we also examine the chemical initial conditions used in the WRF-Chem simulations (Figure 4.10), which shows a high mixing ratio aloft of MVK+MACR+ISOPOOH and HCHO, as well as other species (e.g., isoprene and NO_2) (Figure 4.10). Unlike the LES simulations that were initialized from the P-3B observations, it appears that the bias aloft in WRF-Chem derives not from vertical mixing but from the boundary conditions from the MOZART4-GEOS5 simulations. The lack of vertical mixing then amplifies the effect of initial chemical conditions in the WRF-Chem simulations, causing persistent high BVOC values aloft.

4.4.3. Segregation

One metric for evaluating how mixing influences BVOC chemistry in the WRF-Chem versus LES simulations is the intensity of segregation (I_s) between OH and a BVOC species (e.g., isoprene) as:

$$I_s = \frac{\overline{VOC_i' \, OH'}}{\overline{VOC_i}\,\overline{OH}}, \qquad (1)$$

where $\overline{\mathrm{VOC}_i{}'\mathrm{OH}'}$ is the horizontally-averaged covariance between VOC species i and OH, and $\overline{\mathrm{VOC}_i}$ and $\overline{\mathrm{OH}}$ are horizontally-averaged VOC and OH mixing ratios, respectively, while the $'$ in the numerator indicates deviation from the horizontal average [*Karl et al.*, 2007; *Schumann*, 1989]. I_s is described as the decreased reaction rate induced by incomplete mixing, with 0 representing well-mixed conditions, a negative value indicating a decreased reaction rate due to segregation of the chemical species (with the limiting value I_s = -1 indicating the two species are completely segregated), and a positive value representing an increased reaction rate due to similar covariance between the two reactants [*Molemaker and Vilà-Guerau de Arellano*, 1998; *Patton et al.*, 2001]. In the past, we have evaluated how this segregation rate changes under convective conditions [*Li et al.*, 2016] and with the addition of aqueous chemistry in clouds [*Li et al.*, submitted].

Here we investigate temporal evolution of I_s for OH and isoprene in the analysis region from the WRF-Chem simulations with 1.33 km resolution and compare with the original LES simulation [*Li et al.*, 2016]. The WRF-Chem simulations (Figure 4.11a, b) show clear PBL development, with higher PBL height in the YSU simulation than the MYJ simulation. Within the PBL, negative I_s indicates a decrease in the reaction rate of isoprene + OH. Above the PBL in the afternoon, positive I_s indicates an increase in their reaction rate. The positive I_s region in the WRF-Chem simulations follows the cloud evolution shown in Figure 4.4. However, there is an increase in segregation in the cloud layer at about 2.5 km in the afternoon, which coincides with the weakened vertical mixing in this region simulated by WRF-Chem. Near the surface, WRF-Chem simulates stronger

segregation (I_s = -0.2) than the LES (I_s = -0.1), indicating an additional 10% decrease in the reaction rate of isoprene + OH simulated by WRF-Chem, consistent with the lower TKE simulated by WRF-Chem (Figure 4.7). Overall, the reduced mixing in WRF-Chem further separates parcels of air that contain OH than the LES and increases the segregation values. It is important to note again that WRF-Chem uses heterogeneous surface condition, which may be an important factor in the calculation of segregation across the region. As in the *Ouwersloot et al.* [2011] study, heterogeneous surface emissions further reduced the reaction rate of isoprene and OH by 10% compared with a homogeneous surface emission. Therefore, the heterogeneous surface condition used in WRF-Chem could also contribute to the stronger segregation in the WRF-Chem simulations.

4.5. Conclusions

In this study, we investigate vertical mixing of BVOC as simulated by the WRF-Chem model and use the NCAR LES model and the NASA P-3B measurements to evaluate chemical and physical processes in the planetary boundary layer. Through a suite of WRF-Chem sensitivity simulations with varying resolutions (e.g., 12 km, 4 km and 1.33 km), PBL schemes (YSU and MYJ) and cumulus parameterization options, we can understand the role of WRF-Chem physical parameterizations and the representation of turbulence and its impact on chemistry for a regional scale model.

Compared with WRF-Chem simulations with 12 km resolution, the finer resolution simulations (e.g., 4 km and 1.33 km) generate a later cloud formation in

the afternoon, resulting in a colder environment in the same region. The difference in liquid water can further induce a discrepancy of in-cloud mixing of up to 20%. This indicates that resolution could change the interpretation of the impact of mixing on BVOC chemistry, with stronger segregation simulated with finer resolutions. Consistent with previous studies, we find WRF-Chem simulations using the YSU PBL scheme simulate a higher and drier PBL than using the MYJ scheme. However, despite these differences in the meteorology, the PBL scheme change has little impact on the vertical distribution of BVOC and isoprene segregation.

Direct comparison of the LES and WRF-Chem simulations is a challenge due to the numerous differences between the modeling frameworks, including chemical and physical parameterizations, lower boundary conditions, and lateral meteorological and chemical boundary conditions. Because the LES model can resolve the energy-containing turbulence and simulate more accurate vertical mixing, it is a useful tool to provide a qualitative evaluation of vertical mixing as simulated by the WRF-Chem model. Compared with the LES, the WRF-Chem simulates weaker TKE (~1-2 m^2 s^{-2} lower near the surface) and w (~±3.5 m s^{-1}) regardless of physical parameterization changes. The comparatively low vertical mixing amplifies the effect of initial chemical conditions in the WRF-Chem simulations, which causes persistent high mixing ratios of some BVOC aloft (e.g., the secondary maximum of MVK+MACR+ISOPOOH near 2 km). The weakened mixing in the WRF-Chem simulations causes stronger segregation of isoprene and OH near the surface than the LES, indicating that regional model estimates of segregation are not as well-represented as those simulated by a finer resolution model. Consistent with

previous regional air quality modeling studies [*Carlton et al.*, 2010; *von Kuhlmann et al.*, 2003], we find vertical mixing scheme in WRF-Chem fail to represent the vertical mixing of BVOC and other key chemical species, causing a large bias when comparing with measurements.

Acknowledgments

This research is supported by NASA Earth and Space Science Fellowship (NESSF) NNX13AN76H and the Barbour Scholarship at the University of Michigan. We acknowledge the co-authors, Mary C. Barth and Allison L. Steiner, for providing guidance on this work.

4.6. References

Atkinson, R. (2000), Atmospheric chemistry of VOCs and NOx, *Atmos Environ*, *34*(12–14), 2063-2101, doi:http://dx.doi.org/10.1016/S1352-2310(99)00460-4.

Bryan, G. H., J. C. Wyngaard, and J. M. Fritsch (2003), Resolution requirements for the simulation of deep moist convection, *Monthly Weather Review*, *131*(10), 2394-2416.

Carlton, A. G., P. V. Bhave, S. L. Napelenok, E. O. Edney, G. Sarwar, R. W. Pinder, G. A. Pouliot, and M. Houyoux (2010), Model Representation of Secondary Organic Aerosol in CMAQv4.7, *Environmental Science & Technology*, *44*(22), 8553-8560, doi:10.1021/es100636q.

Castellanos, P., L. T. Marufu, B. G. Doddridge, B. F. Taubman, J. J. Schwab, J. C. Hains, S. H. Ehrman, and R. R. Dickerson (2011), Ozone, oxides of nitrogen, and carbon monoxide during pollution events over the eastern United States: An evaluation of emissions and vertical mixing, *Journal of Geophysical Research: Atmospheres*, *116*(D16).

Chen, J., R. Griffin, A. Grini, and P. Tulet (2007), Modeling secondary organic aerosol formation through cloud processing of organic compounds, *Atmospheric Chemistry and Physics*, *7*(20), 5343-5355.

Deardorff, J. (1980), Stratocumulus-capped mixed layers derived from a three-dimensional model, *Boundary-Layer Meteorol*, *18*(4), 495-527, doi:10.1007/BF00119502.

Emmons, L. K., L. K. Emmons, S. Walters, P. G. Hess, and J. F. Lamarque (2010), Description and evaluation of the Model for Ozone and Related chemical Tracers,

version 4 (MOZART-4), *Geoscientific model development*, *3*(1), 43-67, doi:10.5194/gmd-3-43-2010.
Fiore, A. M., L. W. Horowitz, D. W. Purves, H. Levy, M. J. Evans, Y. Wang, Q. Li, and R. M. Yantosca (2005), Evaluating the contribution of changes in isoprene emissions to surface ozone trends over the eastern United States, *Journal of Geophysical Research: Atmospheres*, *110*(D12).
Forkel, R., O. Klemm, M. Graus, B. Rappenglück, W. R. Stockwell, W. Grabmer, A. Held, A. Hansel, and R. Steinbrecher (2006), Trace gas exchange and gas phase chemistry in a Norway spruce forest: A study with a coupled 1-dimensional canopy atmospheric chemistry emission model, *Atmos Environ*, *40, Supplement 1*(0), 28-42, doi:http://dx.doi.org/10.1016/j.atmosenv.2005.11.070.
Fuentes, J. D., L. Gu, M. Lerdau, R. Atkinson, D. Baldocchi, J. Bottenheim, P. Ciccioli, B. Lamb, C. Geron, and A. Guenther (2000), Biogenic hydrocarbons in the atmospheric boundary layer: a review, *Bulletin of the American Meteorological Society*, *81*(7), 1537-1575.
Grell, G. A., S. E. Peckham, R. Schmitz, S. A. McKeen, G. Frost, W. C. Skamarock, and B. Eder (2005), Fully coupled "online" chemistry within the WRF model, *Atmos Environ*, *39*(37), 6957-6975, doi:http://dx.doi.org/10.1016/j.atmosenv.2005.04.027.
Guenther, A., C. Geron, T. Pierce, B. Lamb, P. Harley, and R. Fall (2000), Natural emissions of non-methane volatile organic compounds, carbon monoxide, and oxides of nitrogen from North America, *Atmos Environ*, *34*(12–14), 2205-2230, doi:http://dx.doi.org/10.1016/S1352-2310(99)00465-3.
Guenther, A., et al. (1995), A global model of natural volatile organic compound emissions, *Journal of Geophysical Research: Atmospheres*, *100*(D5), 8873-8892, doi:10.1029/94JD02950.
Guenther, A., T. Karl, P. Harley, C. Wiedinmyer, P. I. Palmer, and C. Geron (2006), Estimates of global terrestrial isoprene emissions using MEGAN (Model of Emissions of Gases and Aerosols from Nature), *Atmos. Chem. Phys.*, *6*(11), 3181-3210, doi:10.5194/acp-6-3181-2006.
Hong, S.-Y., Y. Noh, and J. Dudhia (2006), A new vertical diffusion package with an explicit treatment of entrainment processes, *Monthly Weather Review*, *134*(9), 2318-2341.
Horowitz, L. W., A. M. Fiore, G. P. Milly, R. C. Cohen, A. Perring, P. J. Wooldridge, P. G. Hess, L. K. Emmons, and J. F. Lamarque (2007), Observational constraints on the chemistry of isoprene nitrates over the eastern United States, *Journal of Geophysical Research: Atmospheres*, *112*(D12).
Hu, X.-M., J. W. Nielsen-Gammon, and F. Zhang (2010), Evaluation of three planetary boundary layer schemes in the WRF model, *Journal of Applied Meteorology and Climatology*, *49*(9), 1831-1844.
Janjić, Z. I. (1994), The step-mountain eta coordinate model: Further developments of the convection, viscous sublayer, and turbulence closure schemes, *Monthly Weather Review*, *122*(5), 927-945.
Karl, T., A. Guenther, R. J. Yokelson, J. Greenberg, M. Potosnak, D. R. Blake, and P. Artaxo (2007), The tropical forest and fire emissions experiment: Emission, chemistry, and transport of biogenic volatile organic compounds in the lower

atmosphere over Amazonia, *Journal of Geophysical Research: Atmospheres (1984–2012)*, *112*(D18).
Kim, S. W., M. C. Barth, and M. Trainer (2012), Influence of fair-weather cumulus clouds on isoprene chemistry, *Journal of Geophysical Research. Atmospheres*, *117*(1), doi:http://dx.doi.org/10.1029/2011JD017099.
Knote, C., et al. (2014), Simulation of semi-explicit mechanisms of SOA formation from glyoxal in aerosol in a 3-D model, *Atmos. Chem. Phys.*, *14*(12), 6213-6239, doi:10.5194/acp-14-6213-2014.
Li, Y., M. C. Barth, G. Chen, E. G. Patton, S. W. Kim, A. Wisthaler, T. Mikoviny, A. Fried, R. Clark, and A. L. Steiner (2016), Large‐eddy simulation of biogenic VOC chemistry during the DISCOVER‐AQ 2011 campaign, *Journal of Geophysical Research: Atmospheres*, *121*(13), 8083-8105.
Loughner, C. P., D. J. Allen, K. E. Pickering, D.-L. Zhang, Y.-X. Shou, and R. R. Dickerson (2011), Impact of fair-weather cumulus clouds and the Chesapeake Bay breeze on pollutant transport and transformation, *Atmos Environ*, *45*(24), 4060-4072.
Loughner, C. P., et al. (2014), Impact of Bay-Breeze Circulations on Surface Air Quality and Boundary Layer Export, *Journal of Applied Meteorology and Climatology*, *53*(7), 1697-1713, doi:10.1175/JAMC-D-13-0323.1.
Mass, C. F., D. Ovens, K. Westrick, and B. A. Colle (2002), Does increasing horizontal resolution produce more skillful forecasts?, *Bulletin of the American Meteorological Society*, *83*(3), 407-430.
Moeng, C.-H. (1984), A large-eddy-simulation model for the study of planetary boundary-layer turbulence, *Journal of the Atmospheric Sciences*, *41*(13), 2052-2062.
Molemaker, M. J., and J. Vilà-Guerau de Arellano (1998), Control of Chemical Reactions by Convective Turbulence in the Boundary Layer, *Journal of the Atmospheric Sciences*, *55*(4), 568-579, doi:10.1175/1520-0469(1998)055<0568:COCRBC>2.0.CO;2.
Ouwersloot, H. G., J. Vilà-Guerau de Arellano, C. C. van Heerwaarden, L. N. Ganzeveld, M. C. Krol, and J. Lelieveld (2011), On the segregation of chemical species in a clear boundary layer over heterogeneous land surfaces, *Atmos. Chem. Phys.*, *11*(20), 10681-10704, doi:10.5194/acp-11-10681-2011.
Patton, E., K. Davis, M. Barth, and P. Sullivan (2001), Decaying Scalars Emitted By A Forest Canopy: A Numerical Study, *Boundary-Layer Meteorol*, *100*(1), 91-129, doi:10.1023/A:1019223515444.
Paulot, F., J. D. Crounse, H. G. Kjaergaard, A. Kürten, J. M. S. Clair, J. H. Seinfeld, and P. O. Wennberg (2009), Unexpected epoxide formation in the gas-phase photooxidation of isoprene, *Science*, *325*(5941), 730-733.
Rienecker, M. M., et al. (2011), MERRA: NASA's Modern-Era Retrospective Analysis for Research and Applications, *Journal of Climate*, *24*(14), 3624-3648, doi:10.1175/JCLI-D-11-00015.1.
Schumann, U. (1989), Large-eddy simulation of turbulent diffusion with chemical reactions in the convective boundary layer, *Atmospheric Environment (1967)*, *23*(8), 1713-1727, doi:http://dx.doi.org/10.1016/0004-6981(89)90056-5.

Singh, H., Y. Chen, A. Staudt, D. Jacob, D. Blake, B. Heikes, and J. Snow (2001), Evidence from the Pacific troposphere for large global sources of oxygenated organic compounds, *Nature*, *410*(6832), 1078-1081.

Squire, O., A. Archibald, P. Griffiths, M. Jenkin, D. Smith, and J. Pyle (2015), Influence of isoprene chemical mechanism on modelled changes in tropospheric ozone due to climate and land use over the 21st century, *Atmospheric Chemistry and Physics*, *15*(9), 5123-5143.

Sullivan, P. P., and E. G. Patton (2011), The Effect of Mesh Resolution on Convective Boundary Layer Statistics and Structures Generated by Large-Eddy Simulation, *Journal of the Atmospheric Sciences*, *68*(10), 2395-2415, doi:10.1175/JAS-D-10-05010.1.

Taraborrelli, D., M. Lawrence, J. Crowley, T. Dillon, S. Gromov, C. Groß, L. Vereecken, and J. Lelieveld (2012), Hydroxyl radical buffered by isoprene oxidation over tropical forests, *Nature Geoscience*, *5*(3), 190-193.

Tie, X., G. Brasseur, and Z. Ying (2010), Impact of model resolution on chemical ozone formation in Mexico City: application of the WRF-Chem model, *Atmospheric Chemistry and Physics*, *10*(18), 8983-8995.

Tie, X., S. Madronich, S. Walters, R. Zhang, P. Rasch, and W. Collins (2003), Effect of clouds on photolysis and oxidants in the troposphere, *Journal of Geophysical Research: Atmospheres*, *108*(D20), n/a-n/a, doi:10.1029/2003JD003659.

von Kuhlmann, R., M. G. Lawrence, P. J. Crutzen, and P. J. Rasch (2003), A model for studies of tropospheric ozone and nonmethane hydrocarbons: Model description and ozone results, *Journal of Geophysical Research: Atmospheres*, *108*(D9), n/a-n/a, doi:10.1029/2002JD002893.

Weisman, M. L., W. C. Skamarock, and J. B. Klemp (1997), The resolution dependence of explicitly modeled convective systems, *Monthly Weather Review*, *125*(4), 527-548.

Xie, B., J. C. Fung, A. Chan, and A. Lau (2012), Evaluation of nonlocal and local planetary boundary layer schemes in the WRF model, *Journal of Geophysical Research: Atmospheres*, *117*(D12).

Xie, Y., R. Elleman, T. Jobson, and B. Lamb (2011), Evaluation of O3-NOx-VOC sensitivities predicted with the CMAQ photochemical model using Pacific Northwest 2001 field observations, *Journal of Geophysical Research: Atmospheres*, *116*(D20), n/a-n/a, doi:10.1029/2011JD015801.

Zaveri, R. A., R. C. Easter, J. D. Fast, and L. K. Peters (2008), Model for Simulating Aerosol Interactions and Chemistry (MOSAIC), *Journal of Geophysical Research: Atmospheres*, *113*(D13), n/a-n/a, doi:10.1029/2007JD008782.

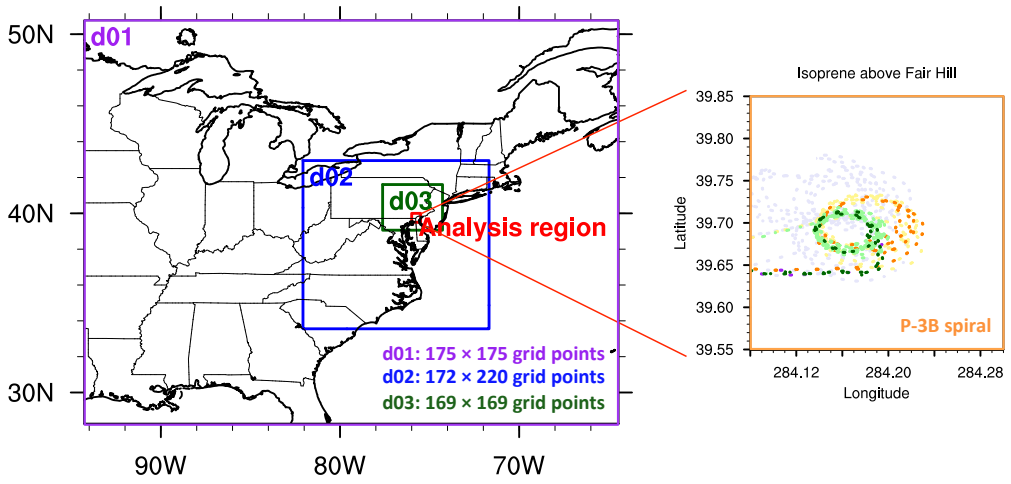

Figure 4. 1. Domains of the WRF-Chem simulations with 12 km (d01; purple box), 4 km (d02; blue box), 1.33 km (d03; green box) resolutions and the analysis region (red box). The analysis region (red box) covers the P-3B spirals above the Fair Hill observation site (as in *Li et al. [2016]*; orange box; right figure), with specific measurement locations on each simulation day (1 July 2011: purple; 11 July 2011: orange; 29 July 2011: green). Lighter colors represent isoprene mixing ratios below 1 ppbv, and darker colors represent isoprene mixing ratios above 1 ppbv.

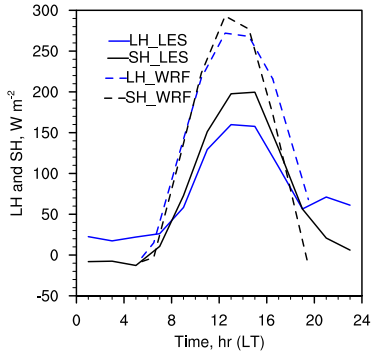

Figure 4. 2. Comparison of surface sensible heat (SH; W m^{-2}; black) and latent heat (LH; W m^{-2}; blue) fluxes between the ground observations at the Edgewood site in the 2011 DISCOVER-AQ campaign used in the LES model [*Li et al.,* 2016] (solid lines) and the horizontal averages over the analysis region from the Noah Land Surface Model implemented in the WRF-Chem simulations at 1.33 km resolution (dashed lines).

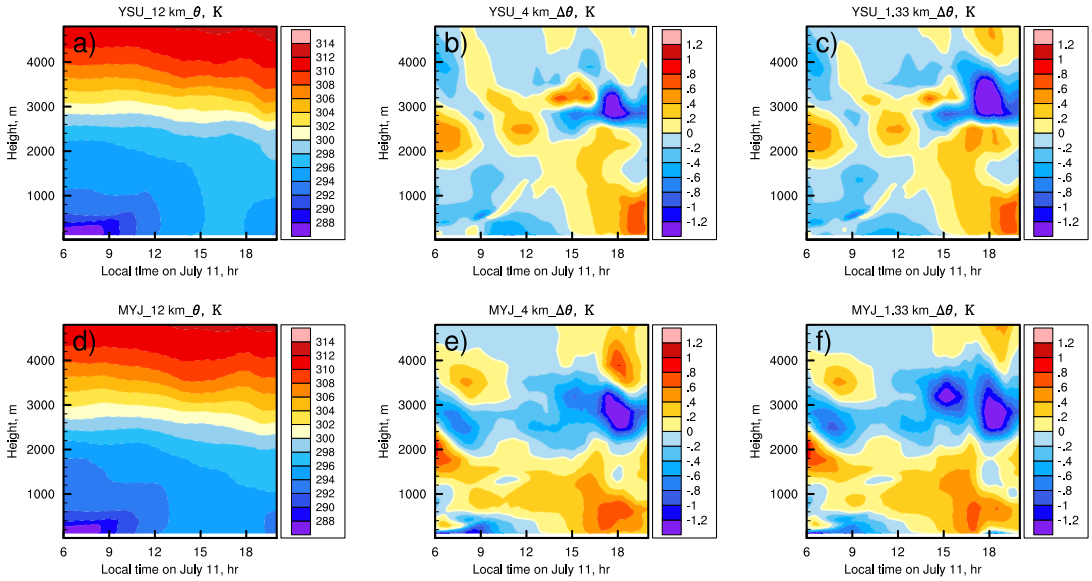

Figure 4. 3. Temporal evolution of θ averaged over the analysis region for the WRF-Chem simulations with the resolution of 12 km (a, d), and the differences of θ (Δθ) between the 12 km and 4 km simulations (b, e) and between the 12km and 1.33 km simulations (c, f) using the YSU (a-c) and the MYJ (d-f) PBL schemes.

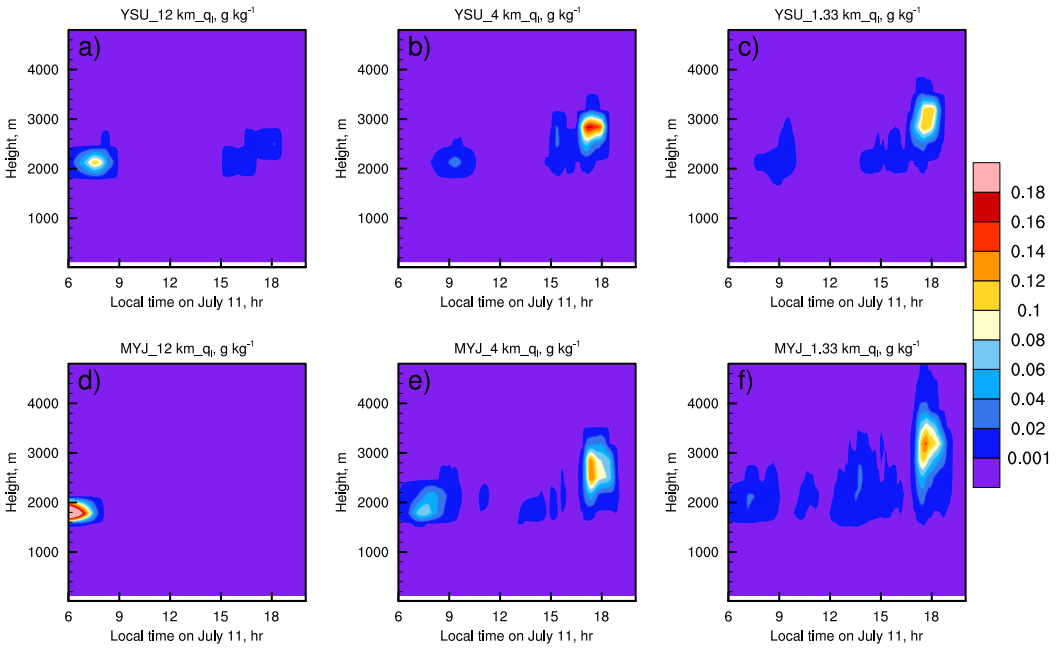

Figure 4. 4. Temporal evolution of WRF-Chem q_l averaged over the analysis region with resolutions of 12 km (a, d), 4 km (b, e) and 1.33 km (c, f) using the YSU (a-c) and the MYJ (d-f) PBL schemes.

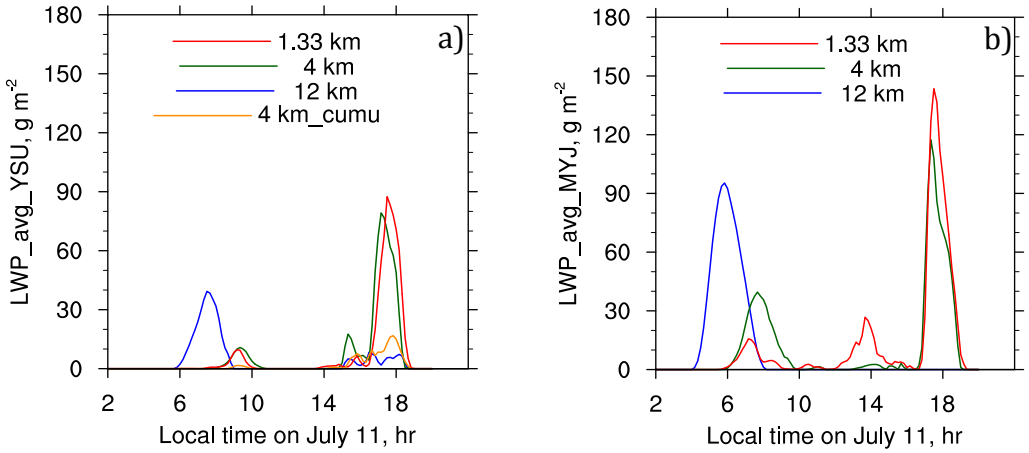

Figure 4. 5. Temporal evolution of liquid water path (LWP) horizontally-averaged over the analysis region for the WRF-Chem simulations at resolutions of 12 km (blue), 4 km (green) and 1.33 km (red) using the YSU (a) and the MYJ (b) PBL schemes. The left figure (a) also includes the LWP temporal evolution simulated at the resolution of 4 km using a cumulus parameterization (orange).

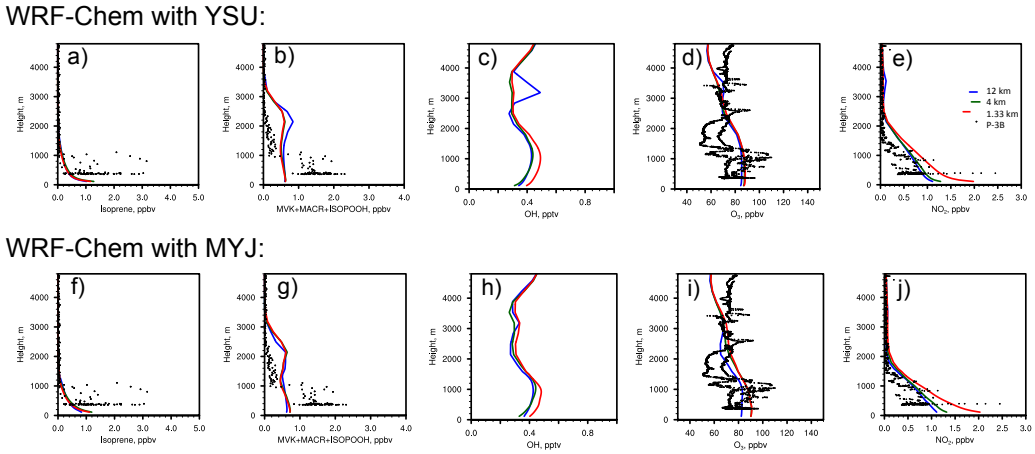

Figure 4. 6. Comparison of afternoon (1300-1700 LT) P-3B observations (black dots) and WRF-Chem horizontally-averaged over the analysis region (solid lines) isoprene, MVK+MACR+ISOPOOH, OH, O_3 and NO_2 with resolutions of 12 km (blue), 4 km (green) and 1.33 km (red) using the YSU (a-e) and the MYJ (f-j) PBL schemes.

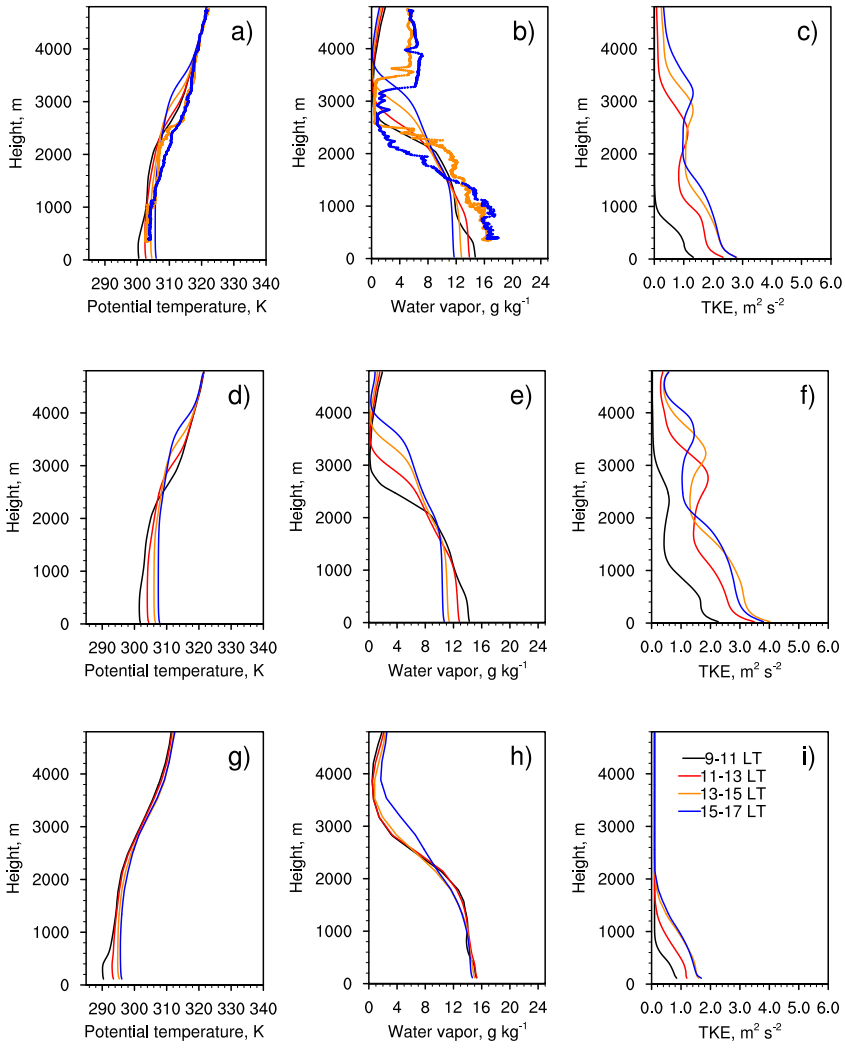

Figure 4. 7. Vertical profiles of potential temperature (θ; K) (a, d, g), water vapor mixing ratio (q_v; g kg^{-1}) (b, e, h) and turbulent kinetic energy (TKE; m^2 s^{-2}) (c, f, i) from P-3B observations at Fair Hill (dots; a-c), domain-average LES simulations with original (lines; a-c) and modified sensible and latent heat (lines; d-f), and horizontally-average over the analysis region WRF-Chem simulations with 1.33 km resolution using the MYJ PBL scheme (lines; g-i).

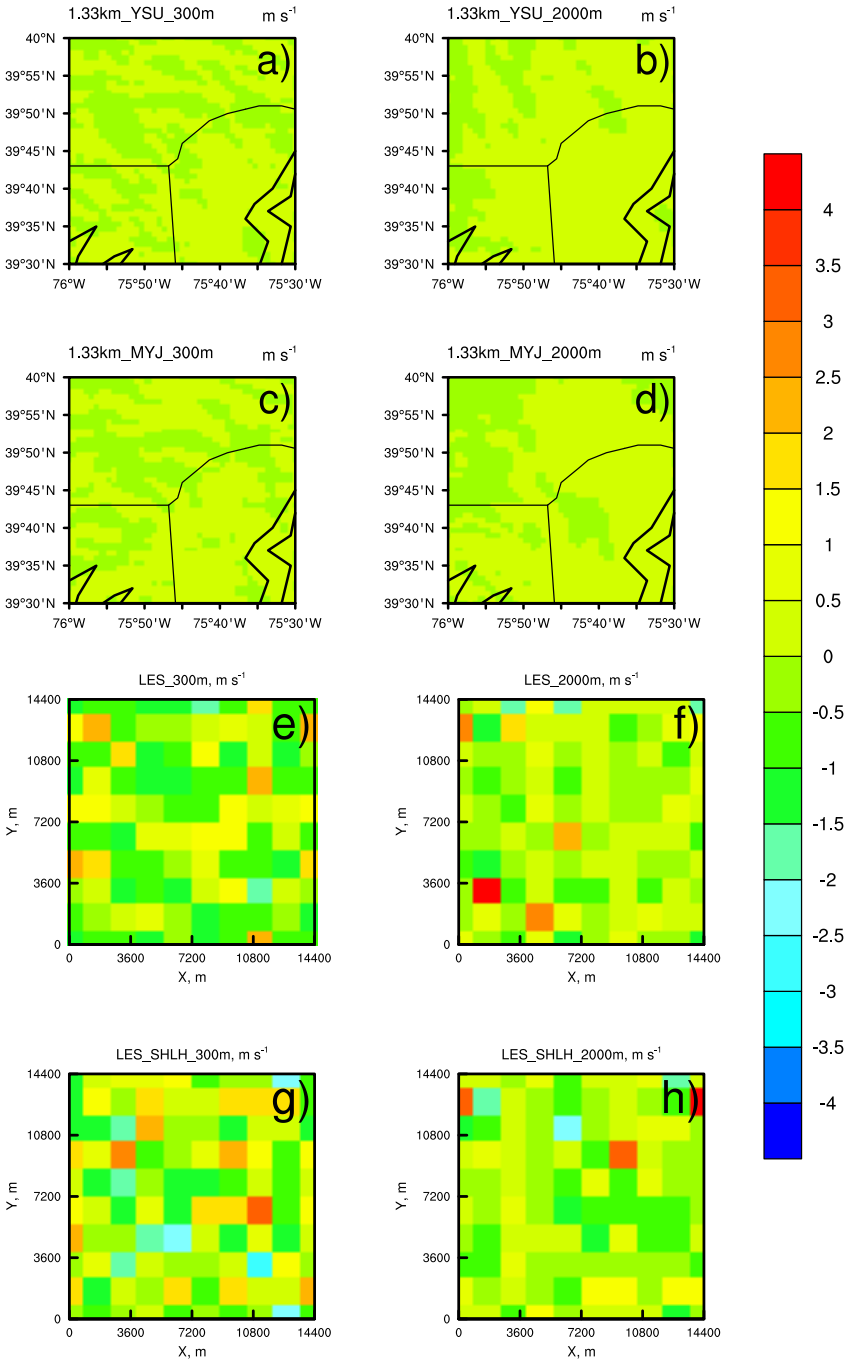

Figure 4. 8. Comparison of instantaneous horizontal cross sections of vertical velocity (w) at two altitudes (300 m: a, c, e, g; 2000 m: b, d, f, h) at 1200 LT over the analysis region from the WRF-Chem simulations with 1.33 km resolution using the YSU scheme (a, b) and the MYJ scheme (b, c), and aggregated to 1.33 km resolution over the domain from the LES simulations with original (e, f) and modified sensible heat and latent heat fluxes (g, h).

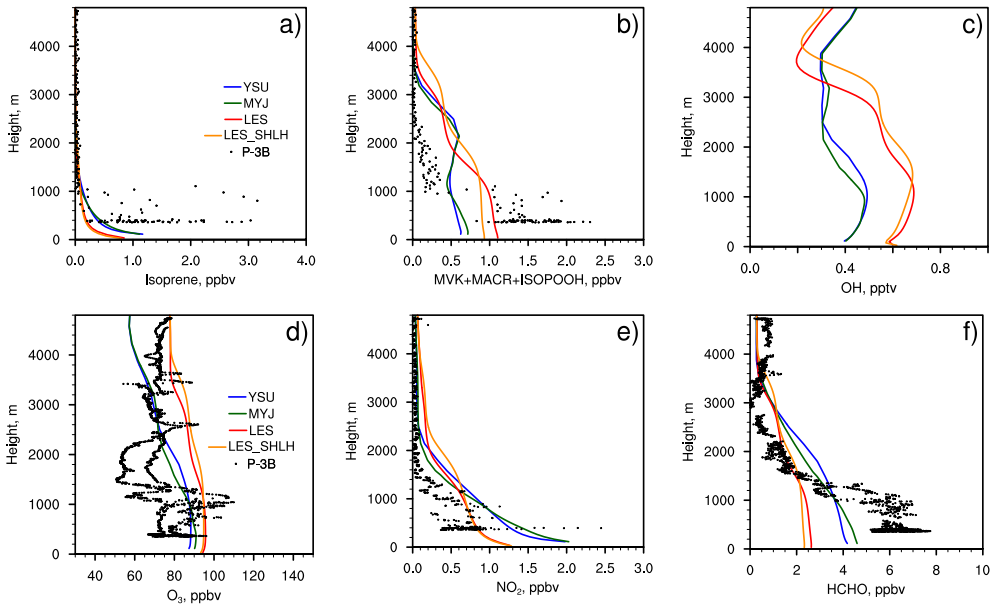

Figure 4. 9. Afternoon (1300-1700 LT) vertical profiles of isoprene (a), MVK+MACR+ISOPOOH (b), OH (c), O_3 (d), NO_2 (e) and HCHO (f) from P-3B observations at Fair Hill (black dots), horizontally-averaged WRF-Chem simulations with 1.33 km resolution using the YSU (blue lines) and the MYJ (green lines) PBL schemes, and domain-average LES simulations with original (red lines) and modified (orange lines) sensible and latent heat.

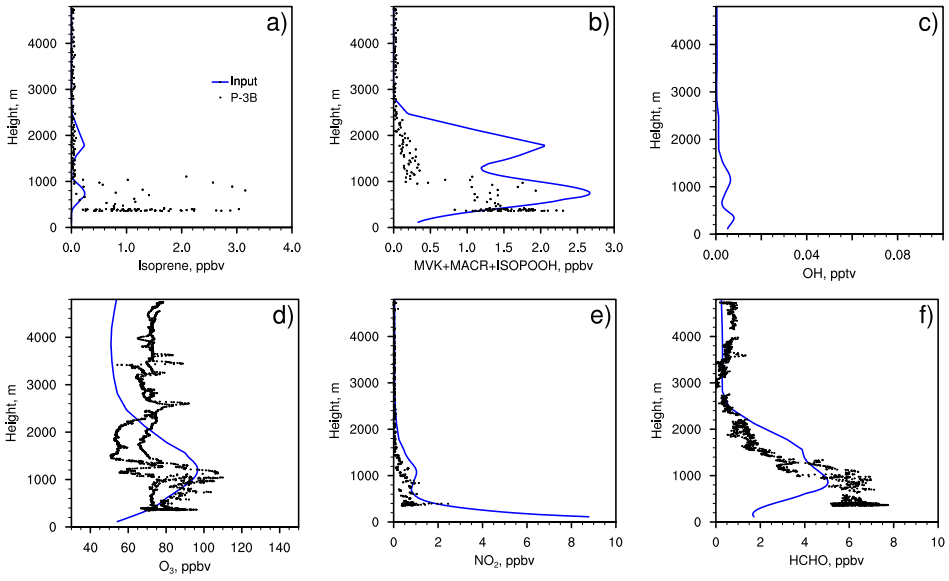

Figure 4. 10. Afternoon (1300-1700 LT) vertical profiles of isoprene (a), MVK+MACR+ISOPOOH (b), OH (c), O3 (d), NO2 (e) and HCHO (f) from P-3B observations at Fair Hill (black dots) and WRF-Chem chemical boundary conditions (blue lines).

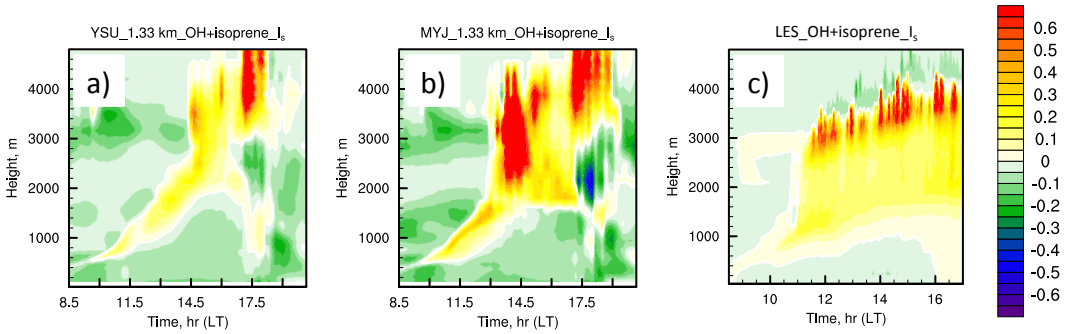

Figure 4. 11. Temporal evolution of I_S for OH + isoprene (horizontally-averaged over the analysis region) for the WRF-Chem simulations with the resolution of 1.33 km (a, b) using the YSU (a) and the MYJ (b) PBL schemes, and for the original LES simulation (c).

Table 4. 1. Physical and chemical parameterizations in WRF-Chem

Process	Method
Cloud microphysics	Morrison double-moment scheme
Radiation	RRTMG short- and longwave
Land surface	Noah Land Surface Model
Planetary boundary layer	YSU/MYJ
Cumulus	Grell-Freitas scheme
Chemical mechanism	MOZART-MOSAIC-4 aerosol bins
Anthropogenic emissions	NEI 2011
Biogenic emissions	MEGAN

Table 4. 2. Summary of WRF-Chem and LES simulations

WRF-Chem simulations	
Name	Simulation description
YSU_12 km	With 12 km resolution using the YSU PBL scheme
YSU_4 km	With 4 km resolution using the YSU PBL scheme
YSU_1.33 km	With 1.33 km resolution using the YSU PBL scheme
YSU_4 km_cumu	With 4 km resolution using the YSU PBL scheme and with
MYJ_12 km	With 12 km resolution using the MYJ PBL scheme
MYJ_4 km	With 4 km resolution using the MYJ PBL scheme
MYJ_1.33 km	With 1.33 km resolution using the MYJ PBL scheme
LES simulations	
LES	With model setup as in *Li et al.* [2016]
LES_SHLH	With modified sensible and latent heat as used in WRF-Chem

CHAPTER 5 Conclusions and Future Work

Biogenic volatile organic compounds (BVOC) are a key driver of tropospheric atmospheric chemistry and play an important role in the formation of ozone, aerosols and the oxidation capacity of the atmosphere. In this dissertation, we examine the role of BVOC in both the chemical and physical processes in the atmospheric boundary layer (ABL) to understand their transport, reactivity and ultimate fate. These processes are important to assess the contribution of BVOC to the formation of ozone (O_3) and secondary organic aerosol (SOA), therefore allowing us to study their impacts on the Earth's climate system and to develop strategies to effectively reduce oxidant precursors.

5.1. Summary of dissertation conclusions

This dissertation implements a suite of modeling tools across spatial scales (a Large Eddy Simulation model, and the WRF-Chem regional model) and aircraft data focused in the planetary boundary layer (the NASA DISCOVER-AQ observations) to investigate and interpret convective mixing and its impact on the vertical distribution of BVOC concentrations and their resulting impact on atmospheric oxidation. Primary findings of each chapter are described below.

Chapter 2: *How do boundary layer dynamics affect the oxidation of BVOC in the atmosphere?*

Short-lived BVOC have a lifetime comparable to the timescales of turbulent mixing in the ABL. Capturing the complexity of boundary layer dynamics is crucial in understanding BVOC oxidation in the atmosphere. We evaluate the role of boundary layer dynamics on the atmospheric chemistry of BVOC during the DISCOVER-AQ 2011 campaign using a LES model. The LES simulations provide a better simulation of turbulence than coarser resolution models without coupling between turbulence and chemistry because eddies are highly resolved [*Li et al.*, 2016; *Moeng*, 1984] on a scale relevant for fast BVOC chemistry.

We select three cases during the campaign ranging from a clear sky day to a hot, humid day with cumulus clouds. With the LES model, we find 1) simulated meteorological environments reproduce P-3B observations in the selected cases; 2) the chemical lifetime of isoprene, a highly reactive primary BVOC, is on the same timescale of the boundary layer turbulent mixing, suggesting accurate knowledge of ABL mixing is essential for understanding BVOC oxidation; 3) segregation induced by incomplete mixing causes an up to 10% reduction in the reaction rate of isoprene and OH, indicating a potential bias in understanding the formation of O_3 and SOA initiated by the isoprene reactions; 4) turbulent mixing transports more OVOC aloft that alters the overall oxidative capacity of the ABL; and 5) higher BVOC mixing ratios typically occur under warmer, convective meteorological conditions, leading to an increase in the total OH reactivity and an increase in OVOC contributions to the OH reactivity and O_3 production aloft. The findings improve our understanding that O_3 at higher altitudes in the troposphere arise not only from transport caused by convection or advection, but also can be attributed to the oxidation of OVOC species.

Chapter 3: *How do in-cloud aqueous processes affect the chemistry and transport of biogenic volatile organic compounds?*

Functionalized oxidation products formed by BVOC oxidation have lower volatility and can partition to the aqueous phase if liquid water is present in the atmosphere. Aqueous chemistry of some of these OVOC species (e.g., organic acids, carbonyls) in cloud droplets and particulate water has recently been shown to provide an important pathway for SOA formation. However, most assessment tools such as regional and global models have difficulties in simulating convective cumulus clouds due to uncertainties in convective parameterizations [*Gianotti et al.*, 2011; *Mapes et al.*, 2004; *Mauritsen et al.*, 2012]. These models also frequently underestimate BVOC oxidation products due to a lack of detailed multi-phase BVOC chemical mechanism at cloud-scale resolution [*Tuccella et al.*, 2015]. In this chapter, we develop the LES model to include an updated gas- and aqueous-phase chemical mechanism to simulate and understand the efficacy of the aqueous process of BVOC at the cloud scale. I update the chemical mechanism to include 64 reactants and 168 reactions that account for aqueous reactions of BVOC oxidation products and formation of organic acids. The combination of detailed chemical mechanism and well-resolved turbulent scheme improve our understanding of BVOC oxidation and provide a basis for future SOA studies.

We design the experiments based on a meteorological case with a diurnal pattern of non-precipitating cumulus clouds from the Baltimore-Washington area DISCOVER-AQ campaign [*Li et al.*, 2016]. We find that 1) adding aqueous chemistry

reduces HCHO in the cloud layer by up to 18%, reducing OH, which further increases OH-reactive VOC such as isoprene and decreases the atmospheric oxidative capacity; 2) adding aqueous-phase reactions induces a segregation of reactants and reduced reaction rates in cloud layers, particularly for isoprene; and 3) in-cloud formation of organic acids increases their mixing ratios throughout the boundary layer, providing a basis to study SOA formation from these precursors. This signifies the importance of aqueous processes in modifying the vertical distribution of BVOC in the PBL, especially under convective environments with high cloud fraction. Overall, this study quantifies the effect of aqueous chemistry on gas-phase chemistry and reactivity using a newly developed modeling tool.

Chapter 4: *What horizontal and vertical spatial scales are needed to capture the physical and chemical processes that affect BVOC oxidation in regional and global atmospheric models?*

While LES model simulations are useful for understanding fine scale turbulence and its impact on atmospheric chemistry, their simulations are limited in both space and time. It is computationally challenging to apply these models to broader spatial regions and longer time periods that are necessary to fully understand tropospheric chemistry. The simplified vertical mixing schemes typically implemented in regional air quality models (e.g., WRF-Chem [*Grell et al.*, 2005]; CMAQ [*Baek et al.*, 2011; *Xie et al.*, 2011]) frequently have difficulty in simulating OVOC in the planetary boundary layer, and underestimate VOC oxidation products and fine particulate matter [*Carlton et al.*, 2010; *Steiner et al.*, 2008]. To

evaluate the physical and chemical processes that are important in scaling up to broader spatial extents, we investigate vertical mixing of BVOC as simulated by the WRF-Chem model and compare with LES model simulations and the NASA P-3B measurements to evaluate these processes in a regional model. Through a suite of WRF-Chem sensitivity simulations of varying horizontal resolution (e.g., 12 km, 4 km and 1.33 km), PBL parameterizations and cumulus parameterization options, we identify key factors that are important in understanding chemical and physical aspects of turbulence and BVOC chemistry across spatial scales. We find 1) WRF-Chem simulations with finer resolutions generate a later cloud formation and a higher liquid water specific humidity; 2) WRF-Chem simulations have weaker vertical mixing than simulated by the LES, although this does not have significant impacts on the ozone formation chemistry; and 3) weaker vertical mixing causes stronger segregation of isoprene and OH in the WRF-Chem simulations than the LES. Overall, this suggests WRF-Chem has difficulties in simulating the complex processes for BVOC and this may influence how we understand the oxidative capacity in the atmosphere.

When implementing the two model tools (i.e., the LES and the WRF-Chem), we note several sources of important differences between the modeling methods, such as the treatment of the physical lower boundary conditions, gas-phase chemical mechanisms, differences in the anthropogenic and biogenic emissions, the alteration of photolysis rates by clouds and simplification in aqueous chemistry. All of these factors are likely to have strong impacts on the different representation of physical and chemical processes in the atmosphere. Additionally, each of these

processes also has considerable uncertainty as well. For example, each of these processes are known to influence BVOC reaction rates at varying magnitudes, ranging from differences on the order of 10-20% (e.g., the differences in the chemical mechanisms) and a factor of 2 or 3 (e.g., the uncertainties in biogenic VOC emissions). This work provides a first attempt to quantify the interactions between atmospheric physics and chemistry using two very different modeling techniques under different weather conditions, improving our understanding of the relative impacts of physical mixing versus chemical interaction.

5.2. Applications and future research questions

By integrating aircraft *in situ* profiles and surface site measurements from the DISCOVER-AQ campaign, this research synthesizes both atmospheric dynamics and chemistry using the LES tool at fine spatial scales. The LES model combined with online chemistry allows examination of the coupling between atmospheric chemistry and dynamics, representing an integrated and holistic view of atmospheric science. The results are used to inform modeling at the regional scale (e.g., WRF-Chem) and improve our understanding of isoprene chemistry in the atmospheric boundary layer. The effects of turbulent mixing on BVOC vertical distribution and segregation of reactants induced by incomplete mixing also provides insight to global modeling studies.

Above, the many differences between the WRF-Chem regional model with the LES model were noted, including surface conditions, ABL mixing schemes and gas and aqueous chemical mechanisms. Comparison of these models provides

guidance on examining the impacts of model interpretations on ABL mixing and BVOC distribution. The discrepancy in simulated ABL mixing could result from initial and boundary conditions, and also from distinct PBL mixing schemes used in different models. Future studies could implement heterogeneous chemical emissions and surface heating fluxes in the LES, and apply the same dataset of initial chemical (e.g., P-3B observation) and meteorological (MERRA reanalysis) conditions to drive the simulations in each model. By reducing the impacts of these factors, we focus more on how different mixing schemes interpret ABL mixing processes. For example, the WRF-Chem model can be implemented with different PBL schemes, such as the Yonsei University (YSU) PBL scheme and the Mellor-Yamada-Janjic (MYJ) PBL scheme. YSU is a nonlocal scheme with first-order closure, while MYJ is a local scheme with a 1.5-order closure and an equation for prognosis of turbulent kinetic energy (TKE). Understanding how the YSU scheme, the MYJ scheme and the LES interpret the ABL mixing is crucial to learn how the ABL mixing processes further affect BVOC distribution essentially.

Chemically, the model development that integrates gas-phase and aqueous-phase chemistry provides basis to study secondary organic aerosol (SOA) precursors. This work is important in understanding the role of isoprene in the formation of SOA. Although this dissertation does not simulate the particle phase, the results from the gas- and aqueous-phase chemistry are extremely important for understanding SOA. Low-volatility OVOC from isoprene oxidation can partition into the particle phase to form SOA [*Donahue et al.*, 2006; *Hodzic et al.*, 2014], and can also dissolve into cloud droplets or aqueous particles depending on their solubility

[*Barth et al.*, 2003]. Further oxidation of OVOC in the aqueous phase affects the chemistry of radical and other oxidant species, and produces lower volatility products that may contribute as an additional source of SOA [*Lim et al.*, 2005]. Accurate model representation of the chemical and physical processes of OVOC and the pathways of OVOC to form SOA in the ABL is fundamental to our understanding of air pollution events and to the predictability of the effects of VOC emissions changes on SOA. The work presented in Chapter 3 provides an important example of the role of cloud processing of BVOC and its potential importance for simulating these processes at broader spatial scales. Many developments are needed in the chemical mechanisms of the WRF-Chem and the LES. Although the MOZART-MOSAIC chemical mechanism utilized with the WRF-Chem model has advanced isoprene gas chemistry, aqueous reactions in this mechanism are still preliminary. Future studies could develop the aqueous chemistry mechanism in the WRF-Chem based on the updated gas- and aqueous- phase chemical scheme in the LES. Because aqueous processes play an important role in SOA formation, improving aqueous chemistry in the WRF-Chem would enhance its ability in simulating SOA in a regional scale. In addition, the addition of anthropogenic emissions in the LES and the development of SOA formation processes is also necessary to simulate a more realistic environment and to extend the implementation of the LES to urban polluted regions. These improvements in both the regional model and the LES model would allow the study of more complicated atmospheric processes and investigate the advantages and disadvantages of different model tools.

Air quality is a human health and environmental issue that must be addressed. Over the continental United States, total anthropogenic VOC and NO_X emissions have been decreasing over the past several decades [*Simon et al.*, 2015], changing the chemistry of ozone formation and placing more emphasis on the biogenic VOC chemistry and its contribution to organic aerosol. Understanding atmospheric chemistry across different chemical regimes is still an important issue, and many existing gas-phase mechanisms still struggle to simulate isoprene and ozone formation correctly [*Fiore et al.*, 2005; *Horowitz et al.*, 2007; *Squire et al.*, 2015; *Travis et al.*, 2016]. In many cases, boundary layer mixing schemes are identified as a key area where more understanding is needed [*Forkel et al.*, 2006; *Lin and McElroy*, 2010]. The work presented in this dissertation focuses specifically fills this gap and works to understand the role of coupled chemical and meteorological processes that improve our understanding of tropospheric chemistry.

5.3. References

Baek, J., Y. Hu, M. T. Odman, and A. G. Russell (2011), Modeling secondary organic aerosol in CMAQ using multigenerational oxidation of semi-volatile organic compounds, *Journal of Geophysical Research: Atmospheres*, *116*(D22), n/a-n/a, doi:10.1029/2011JD015911.

Barth, M., S. Sillman, R. Hudman, M. Jacobson, C. H. Kim, A. Monod, and J. Liang (2003), Summary of the cloud chemistry modeling intercomparison: Photochemical box model simulation, *Journal of Geophysical Research: Atmospheres*, *108*(D7).

Carlton, A. G., P. V. Bhave, S. L. Napelenok, E. O. Edney, G. Sarwar, R. W. Pinder, G. A. Pouliot, and M. Houyoux (2010), Model Representation of Secondary Organic Aerosol in CMAQv4.7, *Environmental Science & Technology*, *44*(22), 8553-8560, doi:10.1021/es100636q.

Donahue, N., A. Robinson, C. Stanier, and S. Pandis (2006), Coupled partitioning, dilution, and chemical aging of semivolatile organics, *Environmental Science & Technology*, *40*(8), 2635-2643.

Fiore, A. M., L. W. Horowitz, D. W. Purves, H. Levy, M. J. Evans, Y. Wang, Q. Li, and R. M. Yantosca (2005), Evaluating the contribution of changes in isoprene emissions to surface ozone trends over the eastern United States, *Journal of Geophysical Research: Atmospheres*, *110*(D12).

Forkel, R., O. Klemm, M. Graus, B. Rappenglück, W. R. Stockwell, W. Grabmer, A. Held, A. Hansel, and R. Steinbrecher (2006), Trace gas exchange and gas phase chemistry in a Norway spruce forest: A study with a coupled 1-dimensional canopy atmospheric chemistry emission model, *Atmos Environ*, *40, Supplement 1*(0), 28-42, doi:http://dx.doi.org/10.1016/j.atmosenv.2005.11.070.

Gianotti, R. L., D. Zhang, and E. A. B. Eltahir (2011), Assessment of the Regional Climate Model Version 3 over the Maritime Continent Using Different Cumulus Parameterization and Land Surface Schemes, *Journal of Climate*, *25*(2), 638-656, doi:10.1175/JCLI-D-11-00025.1.

Grell, G. A., S. E. Peckham, R. Schmitz, S. A. McKeen, G. Frost, W. C. Skamarock, and B. Eder (2005), Fully coupled "online" chemistry within the WRF model, *Atmos Environ*, *39*(37), 6957-6975, doi:http://dx.doi.org/10.1016/j.atmosenv.2005.04.027.

Hodzic, A., B. Aumont, C. Knote, J. Lee‐Taylor, S. Madronich, and G. Tyndall (2014), Volatility dependence of Henry's law constants of condensable organics: Application to estimate depositional loss of secondary organic aerosols, *Geophysical Research Letters*, *41*(13), 4795-4804.

Horowitz, L. W., A. M. Fiore, G. P. Milly, R. C. Cohen, A. Perring, P. J. Wooldridge, P. G. Hess, L. K. Emmons, and J. F. Lamarque (2007), Observational constraints on the chemistry of isoprene nitrates over the eastern United States, *Journal of Geophysical Research: Atmospheres*, *112*(D12).

Li, Y., M. C. Barth, G. Chen, E. G. Patton, S. W. Kim, A. Wisthaler, T. Mikoviny, A. Fried, R. Clark, and A. L. Steiner (2016), Large‐eddy simulation of biogenic VOC

chemistry during the DISCOVER‐AQ 2011 campaign, *Journal of Geophysical Research: Atmospheres*, *121*(13), 8083-8105.
Lim, H.-J., A. G. Carlton, and B. J. Turpin (2005), Isoprene Forms Secondary Organic Aerosol through Cloud Processing: Model Simulations, *Environmental Science & Technology*, *39*(12), 4441-4446, doi:10.1021/es048039h.
Lin, J.-T., and M. B. McElroy (2010), Impacts of boundary layer mixing on pollutant vertical profiles in the lower troposphere: Implications to satellite remote sensing, *Atmos Environ*, *44*(14), 1726-1739, doi:http://doi.org/10.1016/j.atmosenv.2010.02.009.
Mapes, B. E., T. T. Warner, M. Xu, and D. J. Gochis (2004), Comparison of Cumulus Parameterizations and Entrainment Using Domain-Mean Wind Divergence in a Regional Model, *Journal of the Atmospheric Sciences*, *61*(11), 1284-1295, doi:10.1175/1520-0469(2004)061<1284:COCPAE>2.0.CO;2.
Mauritsen, T., B. Stevens, E. Roeckner, T. Crueger, M. Esch, M. Giorgetta, H. Haak, J. Jungclaus, D. Klocke, and D. Matei (2012), Tuning the climate of a global model, *Journal of Advances in Modeling Earth Systems*, *4*(3).
Moeng, C.-H. (1984), A large-eddy-simulation model for the study of planetary boundary-layer turbulence, *Journal of the Atmospheric Sciences*, *41*(13), 2052-2062.
Simon, H., A. Reff, B. Wells, J. Xing, and N. Frank (2015), Ozone Trends Across the United States over a Period of Decreasing NOx and VOC Emissions, *Environmental Science & Technology*, *49*(1), 186-195, doi:10.1021/es504514z.
Squire, O., A. Archibald, P. Griffiths, M. Jenkin, D. Smith, and J. Pyle (2015), Influence of isoprene chemical mechanism on modelled changes in tropospheric ozone due to climate and land use over the 21st century, *Atmospheric Chemistry and Physics*, *15*(9), 5123-5143.
Steiner, A. L., A. L. Steiner, R. C. Cohen, R. A. Harley, and S. Tonse (2008), VOC reactivity in central California: comparing an air quality model to ground-based measurements, *Atmospheric chemistry and physics*, *8*(2), 351-368, doi:10.5194/acp-8-351-2008.
Travis, K. R., et al. (2016), Why do models overestimate surface ozone in the Southeast United States?, *Atmos. Chem. Phys.*, *16*(21), 13561-13577, doi:10.5194/acp-16-13561-2016.
Tuccella, P., G. Curci, G. Grell, G. Visconti, S. Crumeroylle, A. Schwarzenboeck, and A. Mensah (2015), A new chemistry option in WRF-Chem v. 3.4 for the simulation of direct and indirect aerosol effects using VBS: evaluation against IMPACT-EUCAARI data, *Geoscientific Model Development*, *8*(9), 2749-2776.
Xie, Y., R. Elleman, T. Jobson, and B. Lamb (2011), Evaluation of O3-NOx-VOC sensitivities predicted with the CMAQ photochemical model using Pacific Northwest 2001 field observations, *Journal of Geophysical Research: Atmospheres*, *116*(D20), n/a-n/a, doi:10.1029/2011JD015801.

Appendices

Appendix A

Supplementary Figures for Chapter 2

Contents of this file

Figures A1 to A3

Tables A1 to A3

Introduction

This supporting information provides figures and tables that introduce meteorological (Figure A1, Table A1) and chemical conditions (Table A2) used in the simulations. Vertical cross sections of chemical species and vertical velocity are shown to better understand segregation of isoprene and OH (Figure A2). The bar chart (Figure A3) and the photolysis lifetime table (Table A3) are used as a supplement to show the reactivity of the BVOC species.

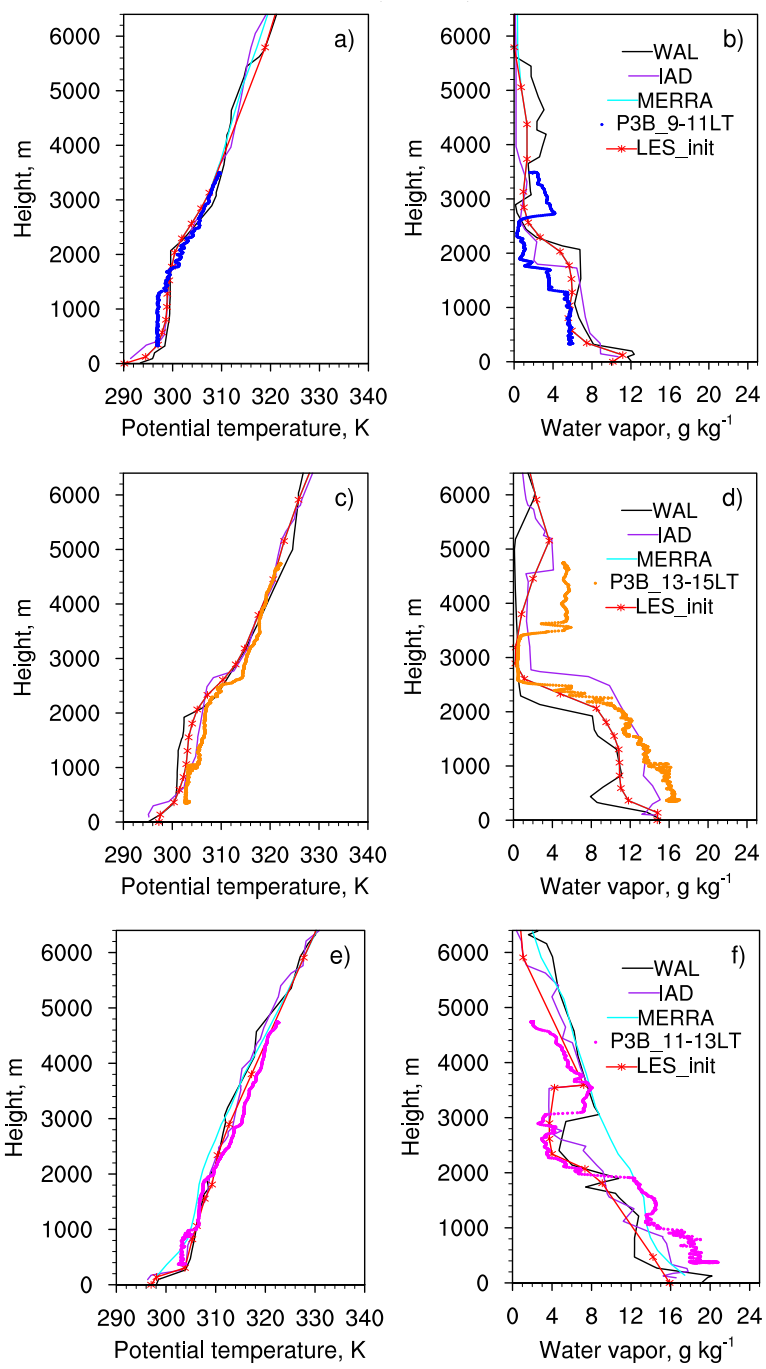

Figure A 1. Comparison of potential temperature (K) (a, c, e) and water vapor mixing ratio (g kg^{-1}) (b, d, f) of the initial profiles at 0530 LT used in LES (red), interpolated 0530 LT profiles derived from 6-hourly finer resolution (0.5° × 0.67°) MERRA data (cyan), sounding data at 0800 LT from WAL (black) and IAD (purple) sites, and the earliest P-3B observed profiles (0900-1100 LT for Case 1, 1300-1500 LT for Case 2 and 1100-1300 LT for Case 3) for the three cases (Case 1: a, b; Case 2: c, d; Case 3: e, f).

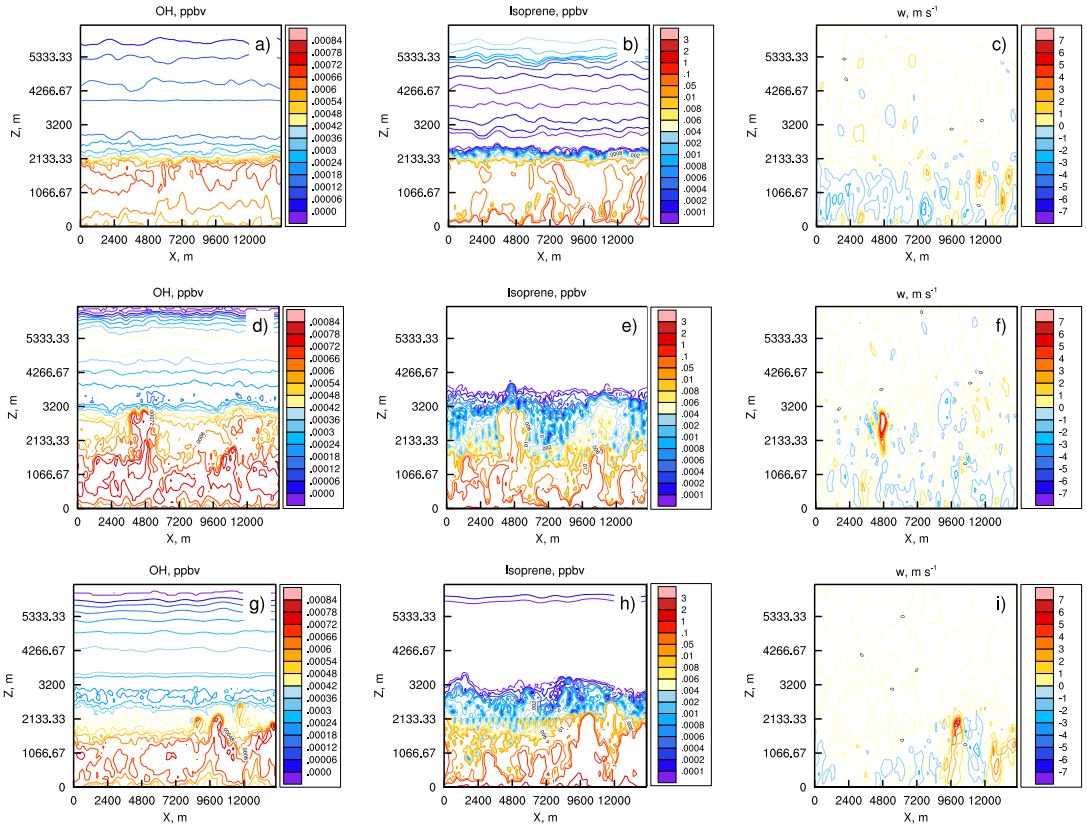

Figure A 2. LES simulated instantaneous vertical cross section of OH (a, d, g), isoprene (b, e, h) and vertical velocity w (c, f, i) in the middle of the domain at 1400 LT for the three cases (Case 1: a-c; Case 2: d-f; Case 3: g-i).

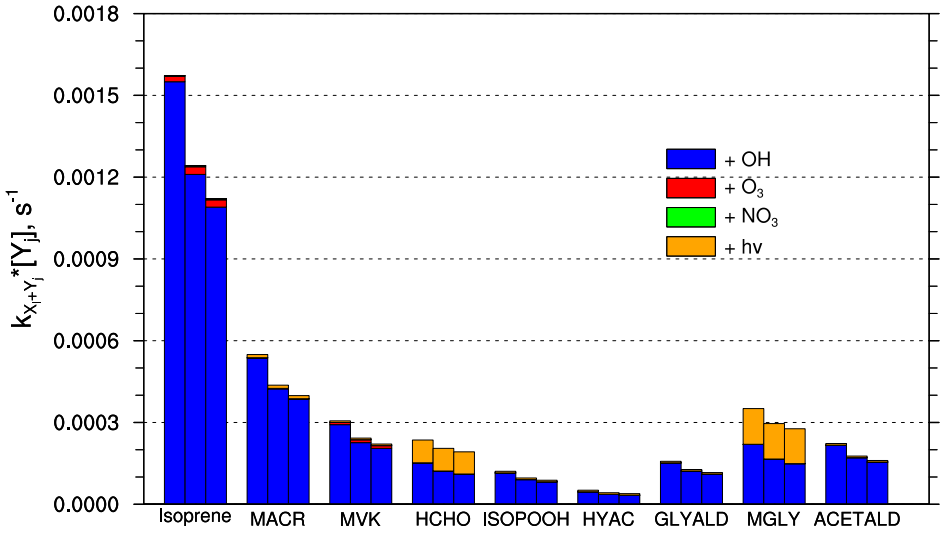

Figure A 3. Photochemical box model simulated $k_{Xi+Yj} * [Y_j]$ (s^{-1}) during 1100-1300 LT (with three vertical bars for each BVOC species representing the values for the three cases), where k_{Xi+Yj} is the reaction rate coefficient for each reaction of BVOC species X_i with Y_j and $[Y_j]$ is the ambient concentration of OH, O_3, or NO_3, k_{Xi+Yj} is the photolysis rate and $[Y_j]$ is 1 for the photolysis pathway.

Case 1		Potential temperature tendency ($K\ h^{-1}$)			Water vapor tendency ($g\ kg^{-1}\ h^{-1}$)			Radiative tendency ($K\ h^{-1}$)		
Time										
LT, hr	UTC, hr	0-1 km	1-2 km	> 2 km	0-1 km	1-2 km	> 2 km	0-1 km	1-2 km	> 2 km
3.5	7.5	-0.190	0.005	-0.143	-0.124	-0.236	-0.129	-0.193	-0.091	-0.078
6.5	10.5	-0.164	-0.016	0.014	-0.362	-0.222	-0.124	-0.112	-0.071	-0.062
9.5	13.5	-0.125	-0.019	0.077	-0.273	-0.325	-0.038	0.051	-0.008	-0.018
12.5	16.5	-0.139	-0.043	0.117	-0.046	-0.233	0.053	0.097	0.030	0.000
15.5	19.5	-0.154	-0.097	0.206	0.066	-0.056	0.044	0.055	0.030	-0.002
18.5	22.5	-0.068	-0.031	0.125	0.086	-0.008	0.034	-0.061	-0.025	-0.032
Case 2		Potential temperature tendency ($K\ h^{-1}$)			Water vapor tendency ($g\ kg^{-1}\ h^{-1}$)			Radiative tendency ($K\ h^{-1}$)		
Time										
LT, hr	UTC, hr	0-1 km	1-2 km	> 2 km	0-1 km	1-2 km	> 2 km	0-1 km	1-2 km	> 2 km
3.5	7.5	0.142	Interpolated	0.000	0.184	Interpolated	0.000	-0.172	Interpolated	0.000
6.5	10.5	0.125	Interpolated	0.000	0.231	Interpolated	0.000	-0.117	Interpolated	0.000
9.5	13.5	0.005	Interpolated	0.000	0.204	Interpolated	0.000	0.038	Interpolated	0.000
12.5	16.5	-0.003	Interpolated	0.000	0.156	Interpolated	0.000	0.086	Interpolated	0.000
15.5	19.5	-0.051	Interpolated	0.000	0.154	Interpolated	0.000	0.008	Interpolated	0.000
18.5	22.5	0.001	Interpolated	0.000	0.086	Interpolated	0.000	-0.121	Interpolated	0.000
Case 3		Potential temperature tendency ($K\ h^{-1}$)			Water vapor tendency ($g\ kg^{-1}\ h^{-1}$)			Radiative tendency ($K\ h^{-1}$)		
Time										
LT, hr	UTC, hr	0-1 km	1-2 km	> 2 km	0-1 km	1-2 km	> 2 km	0-1 km	1-2 km	> 2 km
3.5	7.5	0.239	0.065	-0.096	0.310	0.081	-0.079	-0.042	-0.013	-0.088
6.5	10.5	0.156	0.053	0.125	0.239	0.043	-0.166	-0.040	-0.033	-0.077
9.5	13.5	0.120	0.078	0.028	0.060	0.014	-0.102	0.054	-0.018	-0.016
12.5	16.5	0.126	0.088	-0.188	0.039	-0.205	-0.312	0.063	0.010	0.014
15.5	19.5	0.342	0.350	-0.146	-0.111	0.097	-0.172	-0.008	-0.006	0.010
18.5	22.5	0.420	0.339	-0.189	-0.159	0.521	0.240	-0.142	-0.063	-0.036

Table A 1. Meteorological boundary conditions for the three LES cases derived from 3-hourly 1.25° × 1.25° MERRA reanalysis data at the Fair Hill site (39.71°N, 75.87°W).

	Case 1		Case 2		Case 3	
Chemical species	Boundary layer (ppbv)	Free atmosphere (ppbv)	Boundary layer (ppbv)	Free atmosphere (ppbv)	Boundary layer (ppbv)	Free atmosphere (ppbv)
O3	59.96	60.44	74.57	73.47	69.48	65.45
NO2_NCAR	1.49	0.02	1.87	0.39	1.14	0.05
NO	0.45	0.02	0.21	0.03	0.20	0.02
HNO3_TD-LIF	0.83	0.08	1.39	0.50	1.69	0.56
CH2O_DFGAS	2.70	0.39	7.29	0.54	6.75	0.51
Isoprene	0.27	0.03	0.93	0.02	0.62	0.01
Monoterpenes	0.06	0.01	0.11	0.01	0.09	0.00
MVK+MAC+ISOPOOH	0.47	0.01	1.79	0.02	1.23	0.01
Acetaldehyde	0.46	0.05	1.23	0.28	1.03	0.22
Methanol	4.65	3.23	6.53	2.45	6.92	1.64
Acetone	2.16	1.91	4.95	2.39	4.37	1.98

Table A 2. Initial concentrations (ppbv) for the PBL (below 1 km) and free atmosphere (above 3 km) of P-3B measured chemical species for the three LES cases. Data derived from P-3B measurements from the Fair Hill spiral.

	Photolysis lifetime (τ_{CH}, min)		
	Case 1	Case 2	Case 3
HCHO	201.79 ± 8.91	203.38 ± 9.39	207.92 ± 10.46
MGLY	128.94 ± 4.15	129.67 ± 4.35	131.70 ± 4.85

Table A 3. Modeled midday (1100-1300 LT) photolysis lifetimes of HCHO and MGLY for the three cases. Values shown are temporal (1100-1300 LT) averages, with plus and minus one standard deviation.

Appendix B

Supplementary Figures for Chapter 3

Contents of this file

Calculation of the LES chemical mechanism

Figures B1 to B3

Introduction

This supporting information introduces the calculation of the LES chemical mechanism and provides figures that analyze the production and loss rates of ISOPOOH (Figure B1) and segregations (Figure B2). Vertical cross sections of chemical species are shown to better understand segregation of isoprene and OH (Figure B3).

Calculation of the LES chemical mechanism

The LES predicts the transport, dry deposition, and chemical transformations of the total (gas + liquid) mixing ratio for each trace gas and partitions between gas and liquid phase. After the transport and dry deposition is calculated, chemical transformations are calculated. First, the total concentration is partitioned between the gas and aqueous phases based on a combination of the dimensionless, effective Henry's Law equilibrium (H_{eff}) and mass diffusion transfer limitation. The aqueous phase fraction (f_{liq}) of a trace gas total concentration is calculated as

$$f_{liq} = \frac{P_x}{1 + P_x} \frac{k_t \, dt}{H_{eff}},$$

where P_x is the equilibrium phase ratio of aqueous to gas phase concentrations [Barth et al., 2003; Lelieveld and Crutzen, 1991]. The diffusion-limited mass transfer rate constant, k_t, is found from the gas diffusivity and uptake at the gas-drop interface following Schwartz and White [1983], and modifies the partitioning if mass transfer from the gas phase into the drop is diffusion limited. This term is restricted to be less than or equal to 1. Once the gas and aqueous concentrations at the beginning of the time step and the rates of chemical reaction are known, the gas-aqueous chemical mechanism is solved with an Euler Backward Iterative (EBI) chemical approximation [Barth et al., 2003] using a convergence criterion of 0.01%. Gas-phase photolysis rates are calculated with offline NCAR Tropospheric Ultraviolet and Visible Radiation Model [Madronich and Flocke, 1999]. The effects of cloud scattering on photolysis rates are not considered, but aqueous-phase photolysis rates are increased (1.5 times the gas-phase photolysis rates) due to the pathlength increase inside the cloud drops caused by refraction [*Barth et al.*, 2003; *Madronich*, 1987]. A fixed pH value (4.8) is prescribed according to the pH distribution over Maryland based on the National Atmospheric Deposition Program (http://nadp.sws.uiuc.edu/ntn/annualmapsbyyear.aspx#2011).

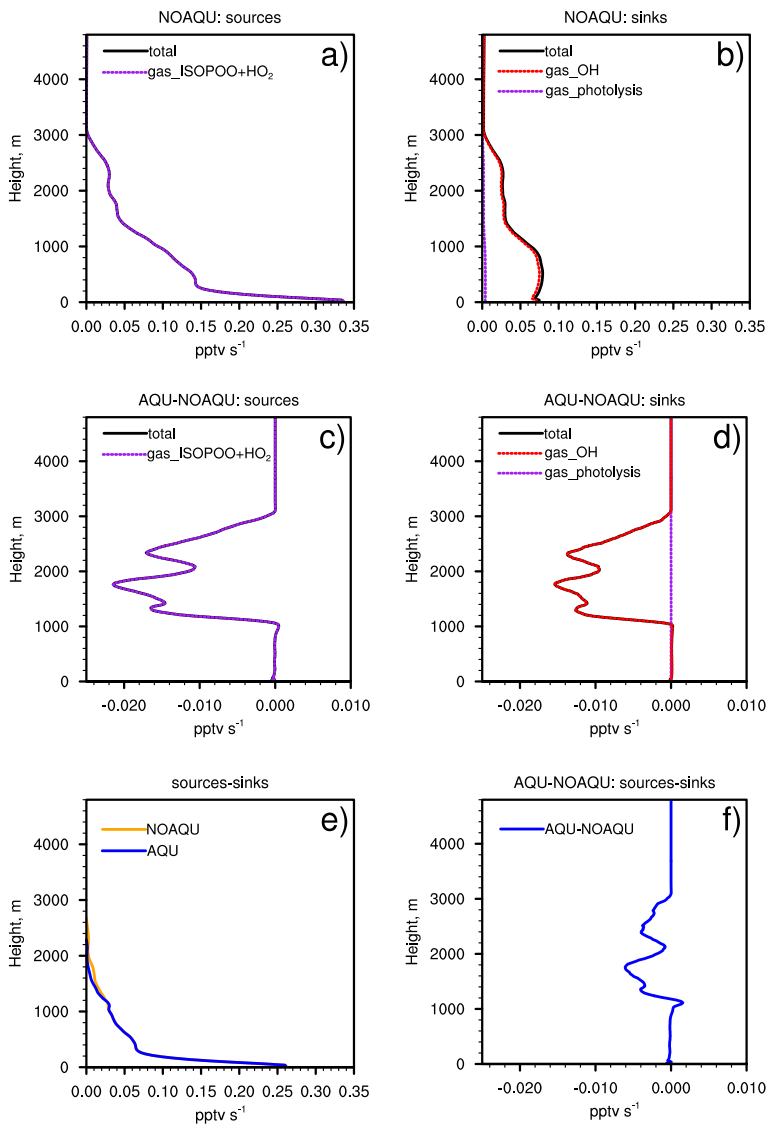

Figure B 1. Horizontally-averaged over the cloudy column production (a) and loss (b) rates of ISOPOOH in the cloudy column at 1200 LT for the NOAQU simulation (a, b), and the changes (AQU-NOAQU) in the production (c) and loss (d) rates after including aqueous phase chemistry (c, d) in the AQU simulation. The net production (sources-sinks) rates for the two simulations (e) and the change (AQU-NOAQU) in the net production rate after including aqueous phase chemistry (f) in the AQU simulation are also shown.

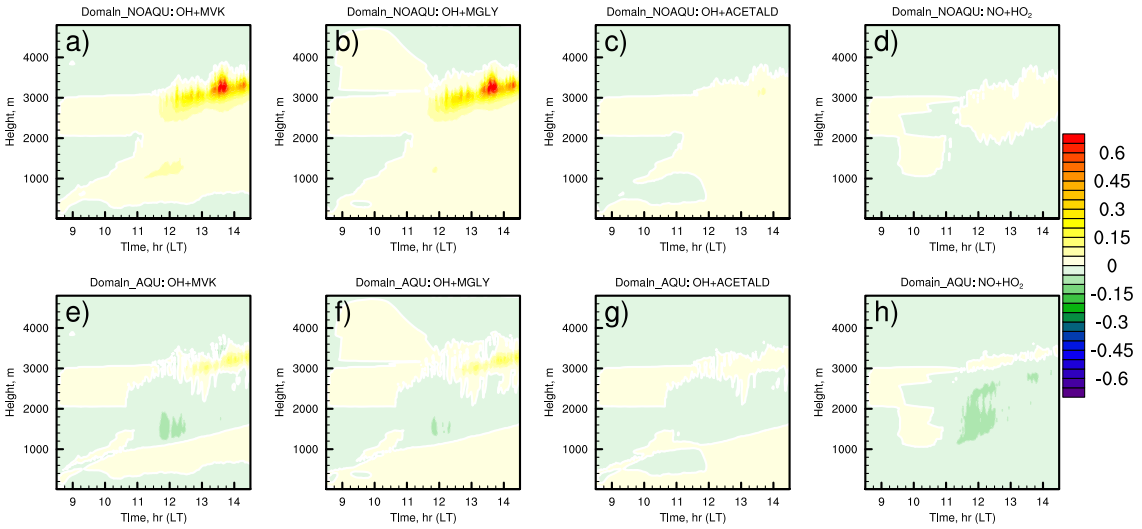

Figure B 2. Horizontally-averaged over the domain temporal evolution of Is for OH + MVK (a, e), OH + MGLY (b, f), OH + ACETALD (c, g) and NO+HO2 (d, h) for the NOAQU (a-d) and AQU (e-h) simulations.

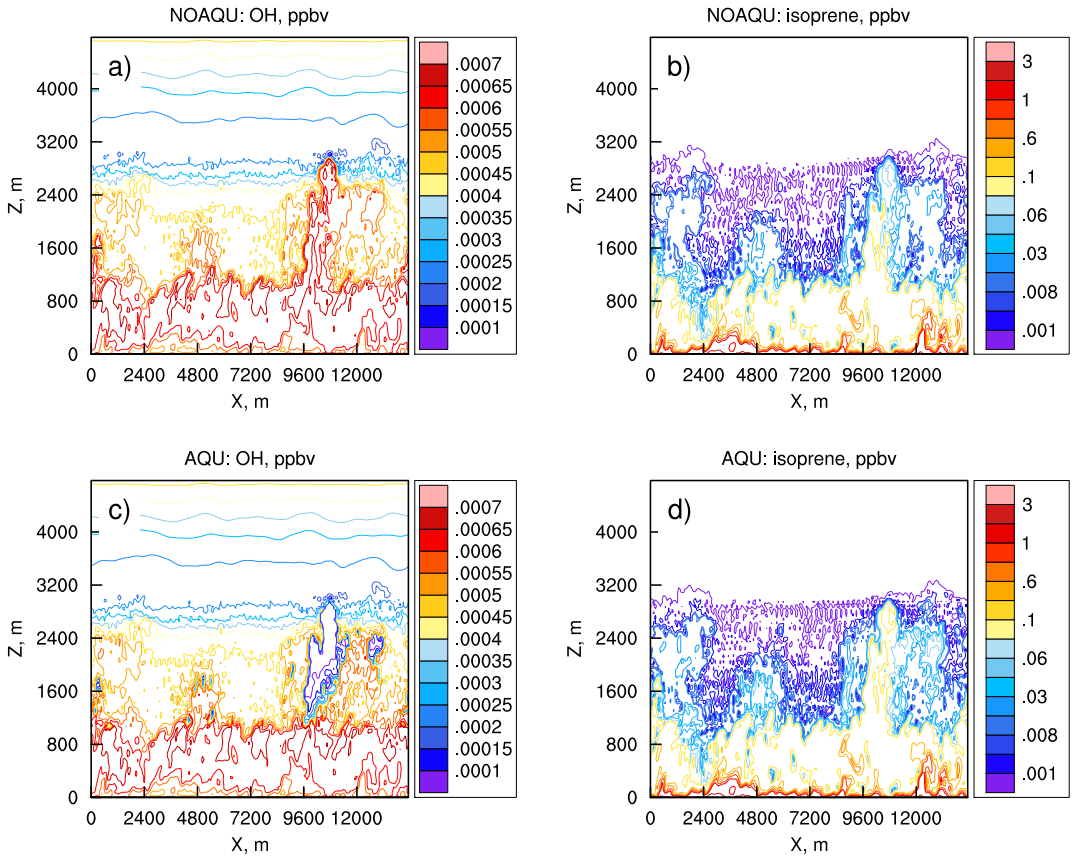

Figure B 3. LES simulated instantaneous vertical cross section of OH (ppbv) (a, c) and isoprene (ppbv) (b, d) in the middle of the domain (as marked by the grey dashed line in Figure 4a) at 1200 LT for the NOAQU (a, b) and AQU (c, d) simulations.

References

Barth, M., S. Sillman, R. Hudman, M. Jacobson, C. H. Kim, A. Monod, and J. Liang (2003), Summary of the cloud chemistry modeling intercomparison: Photochemical box model simulation, *Journal of Geophysical Research: Atmospheres*, *108*(D7).

Lelieveld, J., and P. Crutzen (1991), The role of clouds in tropospheric photochemistry, *J Atmos Chem*, *12*(3), 229-267.

Madronich, S. (1987), Photodissociation in the atmosphere: 1. Actinic flux and the effects of ground reflections and clouds, *Journal of Geophysical Research: Atmospheres*, *92*(D8), 9740-9752.

Madronich, S., and S. Flocke (1999), The Role of Solar Radiation in Atmospheric Chemistry, in *Environmental Photochemistry*, edited by P. Boule, pp. 1-26, Springer Berlin Heidelberg, doi:10.1007/978-3-540-69044-3_1.

Schwartz, S. E., and W. H. White (1983), Kinetics of reactive dissolution of nitrogen oxides into aqueous solution, *Advances in environmental science and technology*, *12*, 1-116.